Experimental and Theoretical Investigation of Transport Phenomena in Nanoparticle Colloids (Nanofluids)

by

Wesley Charles Williams

M.S. Nuclear Engineering (2002)
B.S. Mechanical Engineering (2000)
University of Tennessee, Knoxville

Submitted to the Department of Nuclear Science and Engineering
in partial fulfillment of the requirements for the degree of

Doctor of Philosophy in Nuclear Science and Engineering

at the

MASSACHUSETTS INSTITUTE OF TECHNOLOGY

December 2006

Author .....
Department of Nuclear Science and Engineering
December 13, 2006

Certified by .....
Jacopo Buongiorno
Assistant Professor of Nuclear Science and Engineering
Thesis Supervisor

Certified by .....
Lin-Wen Hu
Research Scientist of the Nuclear Reactor Laboratory
Thesis Co-Supervisor

Accepted by .....
Jeffery Coderre
Chairman, Department Committee on Graduate Students

Experimental and Theoretical Investigation of Transport Phenomena in Nanoparticle Colloids (Nanofluids)

by

Wesley Charles Williams

Submitted to the Department of Nuclear Science and Engineering
on December 13, 2006, in partial fulfillment of the
requirements for the degree of
Doctor of Philosophy in Nuclear Science and Engineering

Abstract

This study investigates the thermal transport behavior of nanoparticle colloids or *nanofluids*. The major efforts are: to determine methods to characterize a nanoparticle colloid's mass loading, chemical constituents, particle size, and pH; to determine temperature and loading dependent viscosity and thermal conductivity; to determine convective heat transfer coefficient and viscous pressure losses in an isothermal and heated horizontal tube; and finally to determine the feasibility for potential use as enhanced coolants in energy transport systems, with focus on nuclear application.

The efforts result in proving that the two selected nanofluids, alumina in water and zirconia in water, have behavior that can be predicted by existing single phase convective heat transfer coefficient and viscous pressure loss correlations from the literature. The main consideration is that these models must use the measured mixture thermophysical properties. With the acquired knowledge of the experiments, investigation into the potential use or optimization of a nanofluid as an enhanced coolant is further explored. The ultimate goal of contributing to the understanding of the mechanisms of nanoparticle colloid behavior, as well as, to broaden the experimental database of these new heat transfer media is fulfilled.

Thesis Supervisor: Jacopo Buongiorno
Title: Assistant Professor of Nuclear Science and Engineering

Thesis Co-Supervisor: Lin-Wen Hu
Title: Research Scientist of the Nuclear Reactor Laboratory

Acknowledgments

I would like to dedicate this entire work to my late grandfather, Willard Huffman Martin, you are the chief of my tribe. Mom, Dad, Bro, and Grandma you guys have been my support team for love, money, food, and lots of laughs. I would like to thank my advisors Jacopo and Lin Wen for being patient and kind towards me throughout this endeavor. I want to thank Prof. N.E. Todreas and Prof. M. Driscoll for helping me to get my foot in the door at MIT. I give great appreciation to the US Department of Energy and the taxpayers without whose monetary support none of this would have been possible. I would also like to include Idaho National Laboratory and the MIT Nuclear Reactor Laboratory.

I would like to personally thank Pete Stahle, Eric Forrest, Jianmai Che, Tom McKrell, Adam Grein, Bao Truong, Tim Lucas, and Judy Maro for their help with work in the laboratory. I would like to thank the collaboration with the laboratories of Prof. A. Hatton, Prof. G. McKinley, Prof. R. Piazza, and Prof. G. Chen and their respective students. Also, I acknowledge Calvin Li and Provost G.P. Peterson at RPI for their collaboration.

I salute my brothers In Cheol, Hyeongpil, Jeongik, Sung Joong, and Jacob; we have been thick as thieves over these years. I am sure half of this thesis has come from your ideas, most likely the better half. Last and definitely not least is the Progetto Rocca and Roberto Rusconi who helped to actualize most of the properties measurements and effectively shortened my Ph.D. duration by a year, mille grazie. I want to thank all the other members of my family who have helped keep me going and are too numerous to list. I would like to also thank all of the great teachers and friends I have had throughout my entire educational career who have helped me to dream big dreams, and in particular Maestro Larry Long my old guitar teacher.

Finally I would like to give this work up as an offering to appease the green lab demon, let me and my fellows rest in peace!

Contents

List of Figures

List of Tables

Nomenclature

Chapter 2

l	characteristic length of a single molecule
d_p	the particle characteristic length (the diameter for a spherical particle)
ΔG	the Gibbs free energy
σ	the surface tension
A_p	the surface area of a particle
ΔG^{att}	the attractive potential energy
F^{att}	the attractive force (mainly due to van der Waals force)
ΔG^{rep}	the repulsive potential energy
a, b, A', B'	energy equation constants
d	particle separation distance
F^{el}	the electrostatic force
$q_{1,2}$	electric charge
ε	dielectric constant
ε_0	permittivity of free space
Z	the number of electrons
e	the electron charge
κ	the inverse of the Debye-Hückel screening length
n	the concentration of simple ions
k_B	the Boltzmann constant ($1.3806503 \cdot 10^{-23} m^2 kg/s^2 K$)
T	temperature
PZC	point of zero charge
IEP	isoelectric point
μ_e	electric potential
η	the viscosity of the liquid
ζ	the zeta potential or surface potential of the particle
I	the ionic strength
N_A	Avogadro's number ($6.022x10^{23}$)

ε_r	the permittivity of the solution
e_f	the Faraday constant ($96485.3415 sA/mol$)
TEM	transmission electron microscopy
SEM	scanning electron microscopy
DLS	dynamic light scattering
NAA	neutron activation analysis
ICP	inductively coupled plasma spectroscopy
TGA	thermogravimetric analysis
$f(q, \tau)$	intermediate scattering function
q	scattering factor
τ	scattering time scale
$r(t) - r(0)$	particle displacement
D_0	mass diffusion coefficient

Chapter 3

THW	transient hot-wire
ΔT	change in temperature
q'	power per unit length
λ	thermal conductivity
E_1	exponential integral
κ	thermal diffusivity
t	time
a	wire radius
C	Euler's constant (1.781)
ΔT_∞	steady state temperature gradient
b	conductivity cell radius
I	current
L	wire length

R	electrical resistance
ρ	density
c_p	specific heat capacity
$J_{q'}$	heat flux
J_1	mass flux
μ_{11}^c	chemical potential
c_x	mass fraction of constituent x
L_{xx}	diffusion coefficient
λ_∞	steady state thermal conductivity
ϕ	volume fraction
λ^*	mixture thermal conductivity
MG	Maxwell-Garnett
M	shape factors
k_x	coefficients

Chapter 4

q"	heat flux
D_o	tube outer diameter
t	tube thickness
L	tube length
Re	Reynolds number
$\bar{v}$	average flow velocity
T_b	bulk fluid temperature
Gr	Grashof number
ζ	thermal expansion coefficient
$_{LM}$	log mean
NIST	National Institute of Standards
Nu	Nusselt Number

Pr	Prandtl Number
k	thermal conductivity
D_i	tube inner diameter
Q	heat
AV	volumetric flow rate
$\dot{m}$	mass flow rate
$T_{b,in}$	bulk inlet temperature
$T_{w,i}$	inner wall temperature
$T_{w,o}$	outer wall temperature
h	heat transfer coefficient
$_x$	local value
ΔP	viscous pressure loss
f_f	friction factor
$v\%$	volume percentage
$wt\%$	weight percentage
S	stopping distance

Chapter 5

P_{pump}	pumping power
S	cross sectional area of the flow
t_f	film temperature
t_c	coolant temperature

Chapter 1

Introduction

1.0.1 Thesis Objectives and Outline

This study investigates the potential use of nanoparticle colloids, *nanofluids*, as heat transfer enhancing coolants. Historically thermal transport properties of colloidal systems have been of little interest to the scientific world. Due to recent advancements in nanoparticle colloid production, such fluids are being explored for new non-traditional uses like heat transfer. This is due to the creation of ultra-fine particle colloids with the ability to remain in dispersion indefinitely. The aim of this study is to understand nanoparticle colloids under convective heat transfer conditions in tubes with the intent on utilizing them for enhanced heat transfer. Most modern large scale energy production systems are reliant on convective fluid heat transfer; therefore, any enhancement in convective heat transfer would directly impact current energy production in a positive way.

The discussion will begin with a review of existing work in the field of nanoparticle dispersions for heat transfer enhancement in Section 1.1. The study will follow with a description of colloid theory, preparation, and characterization techniques utilized in this study in Chapter 2. Experimental investigation of the thermal conductivity and viscosity of colloids is in Chapter 3. Experimental convective heat transfer measurements and their interpretation are discussed in Chapter 4. Chapter 5 assesses the merits of nanofluids as coolants. Final discussion and conclusions are given in

Chapter 6.

1.1 Background and Literature Review

The idea of using particulate dispersions as a method for augmenting thermal conductivity is not a recent discovery. Maxwell had dealt with the subject of increased electrical conductivity of liquids with particulate dispersions theoretically over 120 years ago [3]. Since then many studies have been done involving the suspension of milli- and micro-sized particles in various fluids. One such work by Ahuja [4][5][6], showed that by suspending 50-100μm sized polystyrene particles in glycerine, the thermal conductivity is lowered below that of the glycerine. The lowered thermal conductivity followed the predictions of existing heterogeneous mixed media models, like those of Hamilton-Crosser [7] and Maxwell Garnett [8]. However, convective heat transfer rate of the mixture in laminar flow increased by a factor of 2 without any increase in friction losses. The same work also investigated from a theoretical standpoint the effects of varying the particle size and density as well as other factors that might influence this enhancement. Ahuja suggested that the physical mechanisms of heat transfer enhancement for this mixture are due to the centrifugal fan-type churning due to rotation of the particles in the shear gradient, and good dispersion of the particles in the flow creating more of this churning. Application of such coolants to real systems proved difficult due to the inherent inability to keep these particles dispersed in fluids and the resultant settling and clogging potential. Therefore these fluids have never seriously been considered for industrial applications.

Since then, through the development of nanotechnology, methods have been created to produce mass amounts of nanoparticles of various shapes, sizes, and compositions; of importance is the ability to create nanophase materials of roughly spherical shape on the order of 5-10 nm in diameter [9]. Due to the rather large surface to volume ratios of such particles, the physical properties of these materials can vary significantly from that of the macro-sized base material [10]. The first experimental and theoretical investigation of the thermal conductivity enhancement in nanopar-

ticle suspensions is found in Japan by Masuda, et. al. [11] from 1993. This work showed that the thermal conductivity of alumina (Al_2O_3), silica (SiO_2), and titania (TiO_2) suspensions is enhanced above the base fluid water value upwards of 32% for a volume fraction under 5% (in the case of alumina). It was also found that the thermal conductivity increase and the viscosity decrease followed the same temperature trend as the base fluid. The conductivity enhancement was above that of the spherical mixed media models, but could be predicted by non-spherical models. Soon after, discussion of dispersing nanoparticles to increase thermal conductivity is introduced to the western world in the work of Choi [9] at the Argonne National Lab (ANL). The ANL group had done previous work on the mechanisms of fluid heat transfer enhancement and readily saw the heat transfer enhancement potential of using nanoparticle dispersions, which Choi coined and later patented [12] as *nanofluids*.

The initial work showed the enhancement of thermal conductivity in terms of existing traditional two-component system models and went on to show the potential heat transfer coefficient enhancement exclusively due to the change in properties[9]. The initial benefit was expected to be 20% enhancement of the heat transfer coefficient in laminar flow, exclusively due to the enhancement in thermal conductivity. The other key concept was that these nanofluids would remain dispersed simply due to the Brownian motion of the fluid and would therefore be less prone to encountering the problems incurred by larger particle suspensions.

The next logical step in the progression was to further investigate the thermal conductivity of nanofluids experimentally. Metallic-oxide-in-water-type nanofluids have already been examined to increase the conduction by 30% over the water alone [11] prior to the work of Choi. Since then various studies have been done measuring the thermal conductivity of nanoparticles in various liquids experimentally as well as attempting to explain the phenomenon theoretically. Choi and Eastman along with other colleagues have produced various works along these lines investigating and trying to describe the thermal conductivity of the nanofluids [13] [14] [15] [16] [17] [18] [19] [20] [21]. Other groups from India [22] [23] and China [24] [25] [26] [27] [28] [29] [30] have more recently contributed work in the conduction area. All of the

above works are focused on metal or metallic oxide particle dispersions. More recently the production of carbon nanotubes has increased the investigation of these types of nanofluids [31] [32].

All of the above mentioned studies suffer from one or more flaws in logic. Often the colloids were poorly classified or unstable. The measurements were later determined to be unrepeatable, even by the group which made the original measurement. Many groups reported enhancement of the colloid thermal conductivity to be anomalously above that predicted by the Maxwell-Garnett model. However, the Maxwell-Garnett equation is strictly for monodisperse spherical particles. Most of the anomalous enhancement is easily explainable through non-spherical mixed-media models. Likewise temperature dependence of the conductivity is presented in a misleading fashion. The increased conductivity value is compared to the base fluid value at room temperature. In the case of water, the thermal conductivity increases with temperature and this is often the "enhancement" which is reported but clearly cannot be attributed to the nanoparticles. Other types of studies have begun the investigation of the convective and transport behavior of nanofluids [33] [34] [35] [36] [37] [38] [2] [39] [40] [41] [42] [43]. Some have done studies involving pool boiling and two phase properties [44] [45] [46] [47] [48] [49] [50] [51]. It is found that nanofluids have a potential for enhancing the critical heat flux over that of the base fluid in pool boiling experiments. The enhancement can be upwards of 200%. The enhancement is most likely due to surface effects from either deposition of the nanoparticles or change in the surface energy. Flow boiling studies are yet to be considered, but could prove to be very beneficial to nuclear reactor applications. More physics based work has been done involving the surface wetting behavior of nanofluids [52] [53] which could also affect boiling and condensation.

The final result from investigating these previous works is that full characterization of the nanoparticle colloids and their thermophysical properties must be done in order to begin determination of the convective behavior. This will require that the particle amount and size, chemical composition, thermal conductivity and viscosity of each colloid be determined in order to fully understand the behavior and

therefore model it. It can be seen that the promise of nanofluids as an effective way to increase heat transfer capabilities of existing equipment opens a new horizon, not unlike the material science revolution has for structural mechanics, where fluids can be engineered in order to attain desired properties. This study has developed an experimental apparatus and methodology which can be used to investigate the convective heat transfer performance of nanoparticle colloids and shed more light on the underlying phenomenology behind their behavior.

Chapter 2

Preparation and Characterization of Nanofluids

The first step in studying nanofluids is their preparation and characterization. Only well characterized fluids can be considered if one wants to limit the unknowns in the experiments to be undertaken. It is also important to understand the behavior of nanofluids from a fundamental point of view in order to best realize them in an engineered system. An understanding of the preparation and characterization of a nanofluid begins with introductory colloid and surface science. Insight is given to some of the more complex issues of nanofluid characterization. Using this existing knowledge as the basis, techniques for characterizing colloids are used to investigate various nanofluids for potential use in the conductive and convective heat transfer experiments.

2.1 Colloid and Surface Science

An introduction to colloid and surface science is essential to the understanding of nanofluids. Some key definitions will be covered, followed by the ideas of colloidal stability and the methods for achieving it. It is not the intention to repeat the contents of the many existing books in the field, but to summarize them concisely for the introductory nanofluid scientist.

2.1.1 Definitions

The following definitions are useful when discussing nanofluids (or colloids)[10]:

Solvent - The base fluid containing the nanoparticles

Dispersant, Particles, or Solute - Nanoparticles dispersed in the solvent

Colloid or Dispersion - A class of materials that exists between molecular and bulk dispersion systems, where one of the solute dimensions is roughly between 1 and 1000 nm.

Laminated Dispersion - Dispersant with one dimension below 1000nm

Fibrillar Dispersion - Dispersant with two dimensions below 1000nm

Corpuscular Dispersion - Dispersant with three dimensions below 1000nm (most nanofluids)

Lyophobic - Dispersant strongly repels solvent

Lyophillic - Dispersant strongly attracts solvent

Hydrophobic - Lyophobic to water

Hydrophillic - Lyophillic to water

Surfactant - A surface active agent which lowers the interfacial tension, surface tension, or improves wettibility of a liquid

Monodisperse - Dispersion where all particles are relatively the same size

Polydisperse - Dispersion where particles have a range of sizes

Floc - An open, loosely connected grouping of particles (reversible)

Flocculation - the formation of flocs

Coagulum - A dense, strongly connected grouping of particles (not reversible)

Coagulation - the formation of coagulates

Sedimentation - the falling separation of flocs or coagulum to the bottom of the dispersion (particles which are denser than the liquid)

Creaming - the floating separation of flocs or coagulum to the top of the dispersion (particles which are less dense than the liquid)

Aggregates - Particles which have sedimented or creamed out of the dispersion

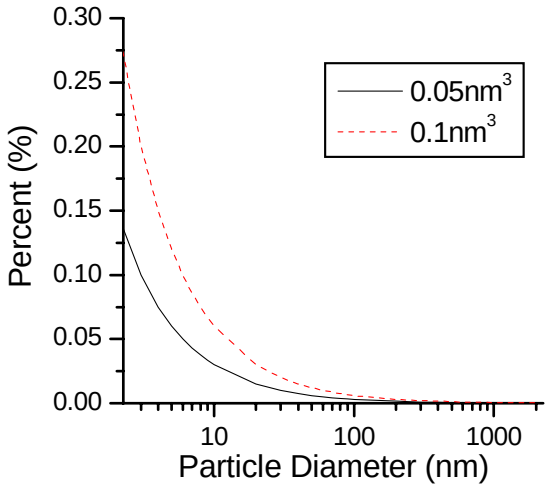

Figure 2-1: Percentage of molecules in the surface of particles depending on particle diameter for two characteristic molecular sizes

2.1.2 Surface Properties in Colloids

A key principle in dealing with colloids involves the notion of properties. It is seen from simple analysis that the number of molecules in the particle surface relative to the total molecules in the particle can be given by

$$Number\ fraction\ of\ particles \sim 6(l/d_p) \tag{2.1}$$

where l is the characteristic length of the single molecule and d_p is the particle characteristic length (the diameter for a spherical particle). A plot of this ratio gives insight into this property for nanofluids as shown in Figure 2-1. It is shown that below ~100nm the number of molecules in the surface can become significant. The implications of this are that the surface molecules do not behave thermodynamically in the same manner as the bulk material molecules. This is due to the interface between the solid and liquid. In large materials the surface effect is relatively unimportant in comparison to the bulk material present. In a small particle, the curvature and surface to volume ratio would allow for a surface molecule to see the bulk material on less than 50% of its sides. This can be seen conceptually in Figure 2-2. Material properties are strictly dependent on the molecular interactions and it is hard to think

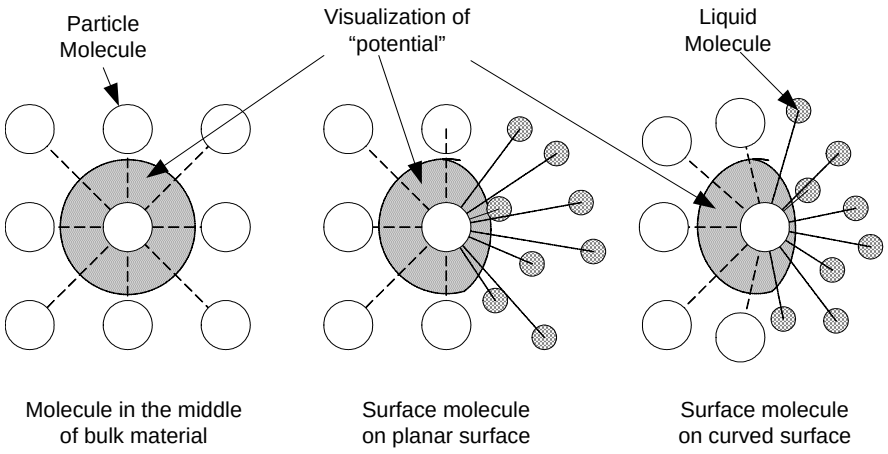

Figure 2-2: Visualization of surface molecules

of the particles as being thermodynamically homogenous. Also chemical reactions that occur at the surface can be increased by this increase in surface accessible to the fluid. Of these chemical effects the electrical double layer is of major importance to colloidal stability. Free energy arises due to the differences of the intermolecular forces “felt” by the molecules in the bulk material and those felt by the surface molecules as shown in Figure 2-2. This can be seen from the free energy due to the surface tension,

$$\Delta G = 2\sigma A_p \tag{2.2}$$

where ΔG is the free energy, σ is the surface tension, and A_p is the surface area. This free energy is due to the attraction of like molecules in the surface. Therefore the minimization of free energy comes through minimization of surface area. For this reason all particle surfaces will attract in both vacuum and in dispersion in an attempt to minimize this surface area. The effect of solvent in this situation is to slightly lower this attraction between surfaces due to the solvent/solute interaction and surface tension of the fluid. In general, the solvent is not enough to prevent flocculation and coagulation of the particles. Therefore all colloids are inherently unstable due to this free energy of attraction. In order to prevent flocculation or coagulation and hence achieve metastability or colloidal stability an energy barrier must be created to prevent the close contact of particle surfaces with one another.

2.1.3 Colloidal Stability

As mentioned above, colloidal stability is achieved through the creation of an energy barrier which would prevent the particles from coming in close proximity and thus aggregating. The concept can be visualized as the total interparticle potential energy of interaction curve. One can consider that the particles have multiple attractive and repulsive forces. The forces create more free energies similar to those shown in the previous section, where ΔG_{att} would be the attractive and ΔG_{rep} the repulsive free energy of interaction. These forces are a function of the separation distance between the particles. A summation of the forces would give a total interaction potential curve. The creation of a local maximum in this curve would amount to a barrier and thus create a metastable point. This can be seen relatively in Figure 2-3.

For spherical particles the attractive energy is found as

$$\Delta G^{att} = -\Delta W = \int_d^\infty F^{att} dr = -A \int_d^\infty 1/r^7 dr = -A'/d^6 \tag{2.3}$$

which is known as the London-van der Waals attraction, where A' depends on the specific particle properties and d is the seperation distance. Likewise the Born repulsion created by interaction of the electron clouds creates a repulsive energy of

$$\Delta G^{rep} = (B/a)e^{-ad} \tag{2.4}$$

where a and B are constants. One can use an approximate expression

$$\Delta G^{rep} = B'/d^{12} \tag{2.5}$$

where B' is a constant. Combination of these two terms into the total interaction energy is

$$\Delta G = G^{rep} + G^{att} = (B'/d^{12}) - (A'/d^6) \tag{2.6}$$

and is known as the Lennard-Jones potential. Of course this is overly simplified if one is considering colloidal particles where electrostatic repulsion, steric repulsion,

and other effects come into play. For example if one considers the particles as charged points then Coulomb's law gives the electrostatic interaction force as

$$F^{el} = q_1 q_2/(4\pi\varepsilon_0 d^2) \tag{2.7}$$

where q is the charge and ε_0 is the dielectric constant. This force would give a electrostatic repulsive energy of

$$\Delta G^{el} = q_1 q_2/(4\pi\varepsilon_0 d) \tag{2.8}$$

measured relative to that at infinite separation. This term could be added to the total interaction potential of Eq. 2.6 to give

$$\Delta G = G^{rep} + G^{att} + G^{el} = (B'/d^{12}) - (A'/d^6) + q_1 q_2/(4\pi\varepsilon_0 d) \tag{2.9}$$

If the additional electrostatic or steric energies are designed properly one can create an energy barrier which makes stable colloids.

The height of the energy barrier should be somewhat greater than $\mathrm{k}_B\mathrm{T}$ the thermal energy of the liquid, where k_B is the Boltzmann constant. This thermal energy of the liquid is what creates the Brownian motion. Brownian motion is the only force which can push the particle together over the energy barrier. Due to the probabilistic nature of Brownian motion, usually a barrier of $10k_BT$ is required to assure good stability. Barrier height is dependent on fluid and particle composition, temperature, and pressure. There are several methods for the creation of this energy barrier. Two major methods will be discussed here: surface charging and surfactant adsorption. The objective of these is to create repulsive forces to counteract the attraction of the particle surfaces.

Surface charging is typically achieved with the electrical double layer. The simplest way to visualize the double layer is as an ionic atmosphere around the particle which is created by the chemical reaction between the solvent and the particle. The surface of the particle will react with the solvent to create charged groups on the surface;

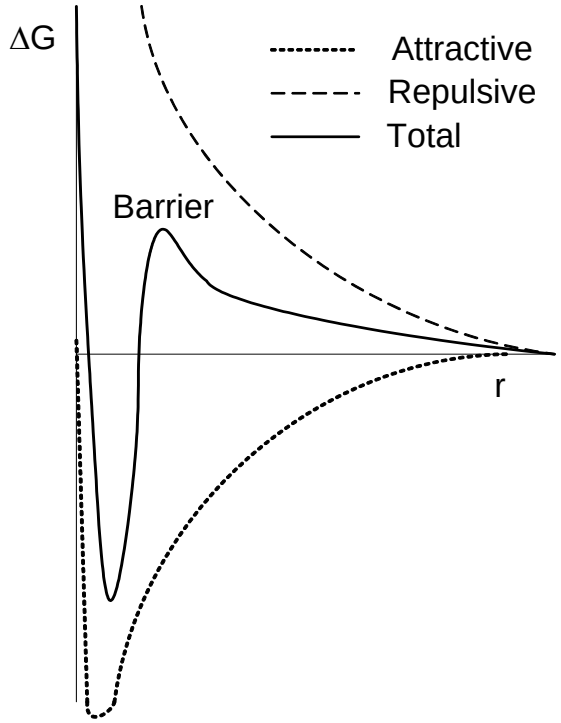

Figure 2-3: Potential energy of interaction curves

this in turn builds the atmosphere of oppositely charged ions to balance the overall charge. Conceptually the double layer is shown in Figure 2-4. The diffusive double layer better visualizes the actual physics. The size and charge concentration of the double layer directly affect the stability of colloids. The creation of like charges on the surfaces of the particles makes a strong repulsive force between particles which falls off exponentially as the interparticle distance is increased. This force is seen as the barrier in the total interaction potential as shown in Figure 2-3. At long distances the double layer covered particle would be seen as neutral, however when two particles approach the interaction potentials overlap.

The common theory used to understand the force between charged surfaces interacting through a liquid medium is known as DLVO theory, named after the developers Derjaguin, Landau, Verwey, and Overbeek. This theory considers the Van der Waals attraction and charged double layer repulsion between to particles in a vacuum or fluid media. The theory also considers the charge screening due to the material between

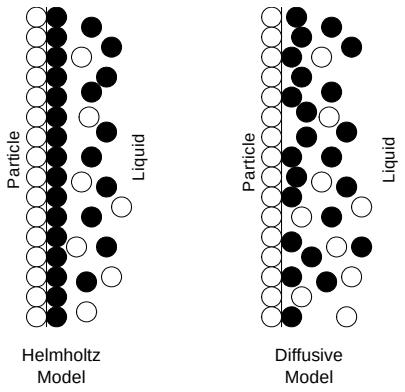

Figure 2-4: Electrical Double Layer (Colors represent positively and negatively charged ions

the particles. The potential is described as

$$U(r) = \frac{Z^2 e^2}{\epsilon} \left[\frac{\exp(\kappa d_p)}{1+\kappa d_p}\right]^2 \frac{\exp(-\kappa d)}{d} \tag{2.10}$$

where ϵ is the dielectric constant of the liquid, d is the separation distance from center to center of particle, d_p is the sphere radius, Z is the number of electrons, e is the electron charge and κ is the inverse of the Debye-Hückel screening length defined as

$$\kappa^2 = \frac{4\pi}{\epsilon k_B T} \sum_{\alpha} n q^2 \tag{2.11}$$

where n is the concentration of simple ions of charge q.

However, DLVO theory is an approximation and does not consider non-continuum effects which may be more prominent for short range particle interactions and dispersion interactions. Therefore the main assumption is that the particles are well dispersed monosized spheres. Experimentally the interparticle potential is traditionally understood through electrophoretic measurement and the zeta potential. More recently atomic force microscopy (AFM) has been used for understanding these interactions. The work of El Ghazaoui investigates both methods for the measurement on alumina and zirconia double layer potentials [1]. Figures 2-5 and 2-6 show the surface charge of zirconia and alumina for different pHs and concentration of NaCl.

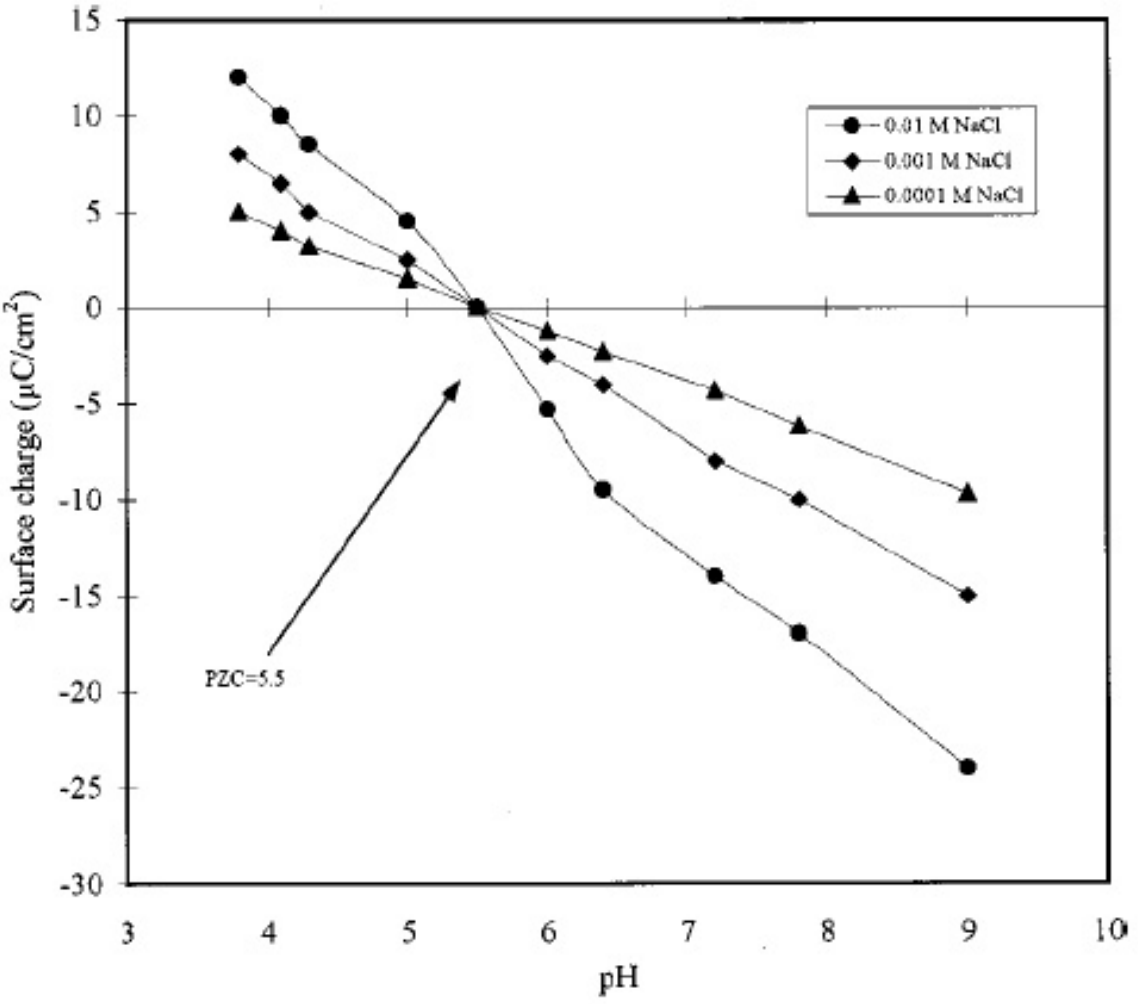

Figure 2-5: Surface charge of crystalline zirconium dioxide as a function of the pH and the concentration of NaCl solution at 298 K [1].

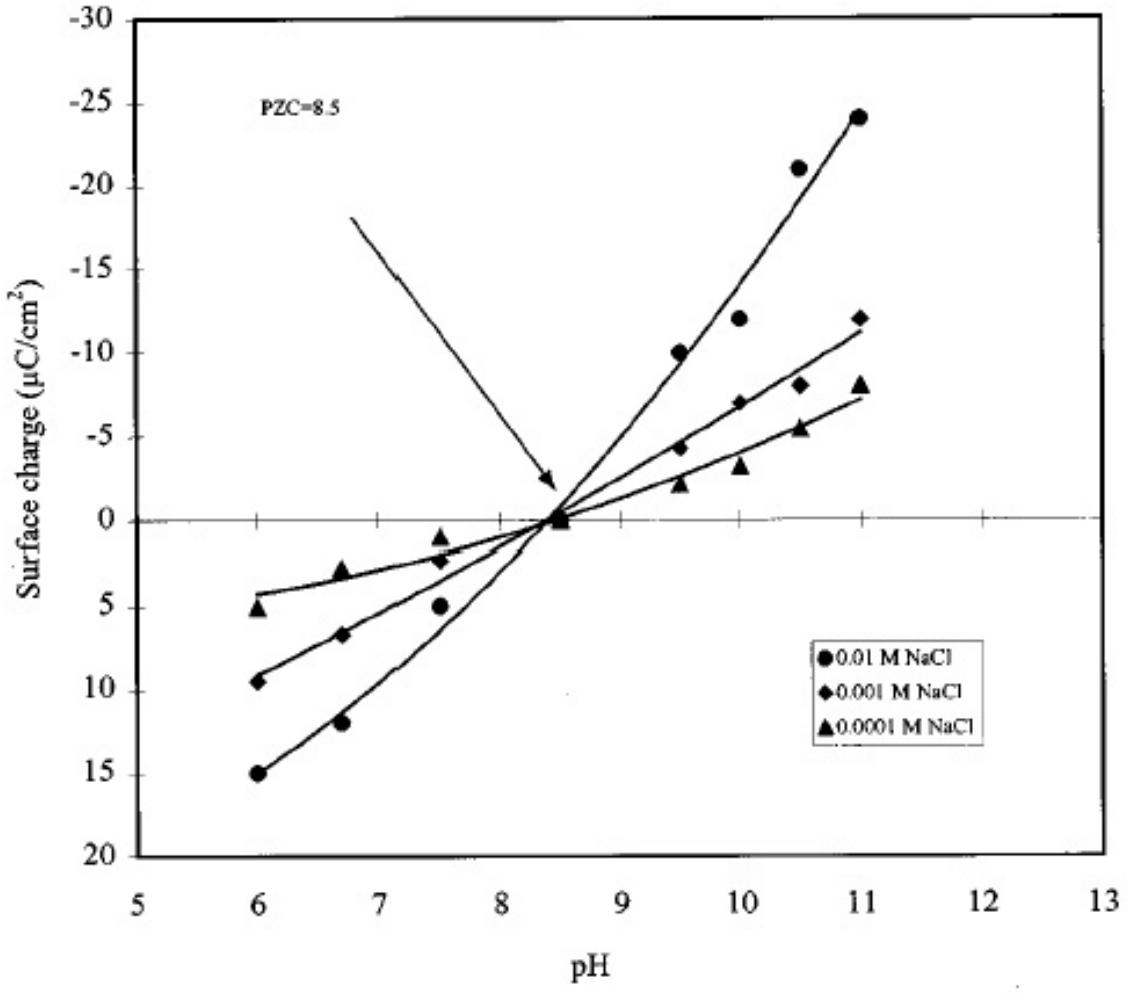

Figure 2-6: Surface charge of α-alumina as a function of the pH and the concentration of NaCl solution at 298 K [1].

Electrophoresis is the movement of a charged material, in this case the particles, under the influence of an electric field. Mobility of the particle depends on the surface properties and solution properties. This can be approximated at high ionic strengths through the Smoluchowski equation

$$\mu_e = \frac{\epsilon\epsilon_0\zeta}{\eta} \tag{2.12}$$

where ϵ is the dielectric constant of the liquid, ϵ_0 is the permittivity of free space, η is the viscosity of the liquid, and ζ is the zeta potential or surface potential of the particle. The situation where the particle has no surface charge and hence no electrophoretic mobility is known as the isoelectric point (IEP) or the point of zero charge (PZC), respectively. These values are the same if there are no adsorption of other ions at the surface of the particle. Figures 2-7 and 2-8 show the zeta potential of zirconia and alumina for different pHs and concentration of NaCl. Since colloidal stability is achieved through the charging of the particles, the pH should be far from the IEP and/or PZC as possible. In metal oxide nanofluids a formation of this double layer can be controlled by adjusting pH of the colloid. The low or high pH creates a protonated or deprotonated surface group like the hydroxyl ligand. This is dependent on the ionic concentrations in the fluid, if a metal oxide is dispersed in the fluid then the metal ions can move into the solvent due to the creation of the hydroxide layer. However, if the particles are dispersed in a fluid with a larger ionic group such as a citric acid or nitric acid group then these ions will create the double layer around the particles. Often it is seen that most commercial nanofluids are created in the first method. For manufacturers it is important that the fluids should be as pure as possible with only the dispersant and solvent. The overall goal is that the fluid should have fast coagulation and sedimentation of the fluid when the pH is changed. However, if one uses other ionic groups to stabilize the nanofluids, the stability becomes less dependent on the pH of the fluid.

The second method of colloid stabilization is the adsorption of surfactants or steric repulsion. Surfactants are wetting agents that lower the surface tension of a liquid,

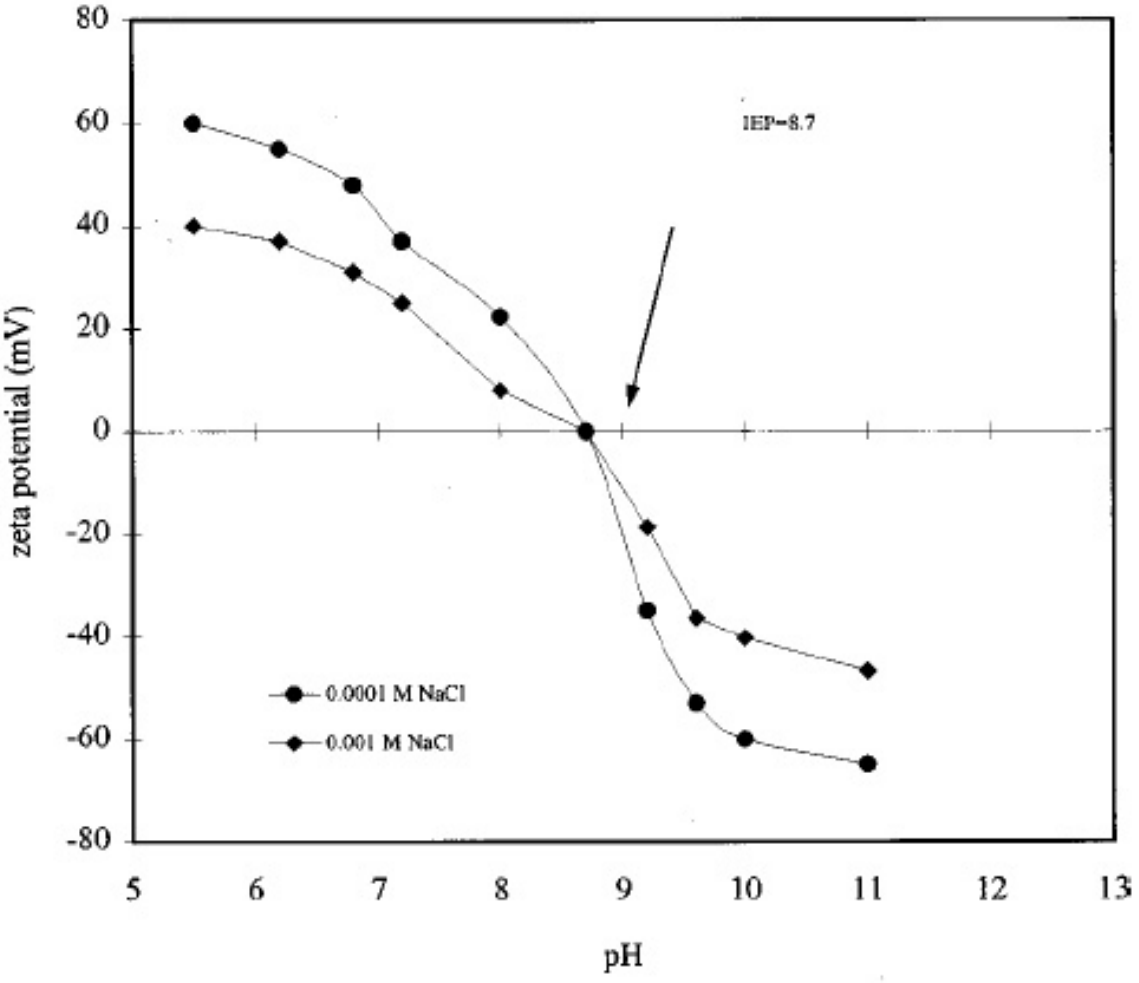

Figure 2-7: Zeta potential of crystalline zirconium dioxide as a function of the pH and the concentration of NaCl solution at 298 K [1].

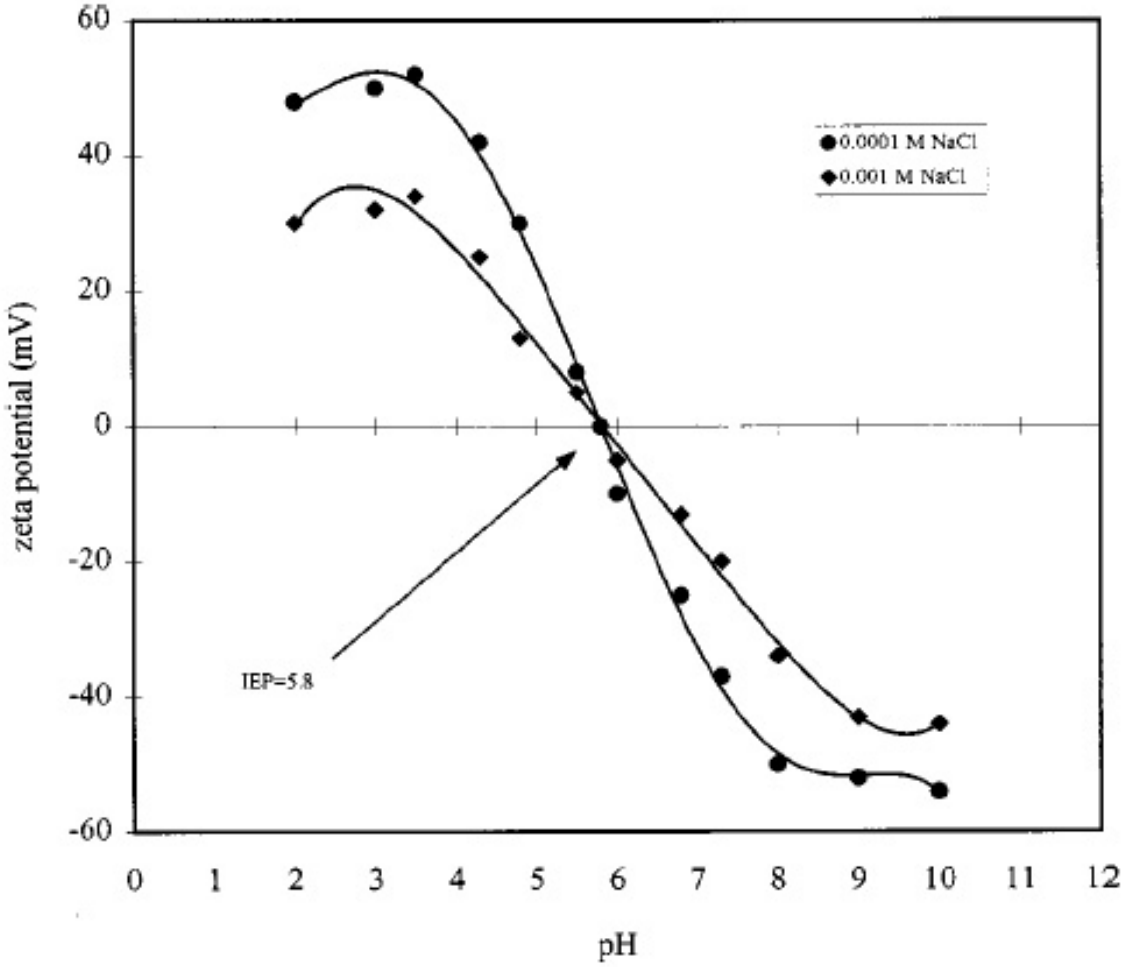

Figure 2-8: Zeta potential of α-alumina as a function of the pH and the concentration of NaCl solution at 298 K [1].

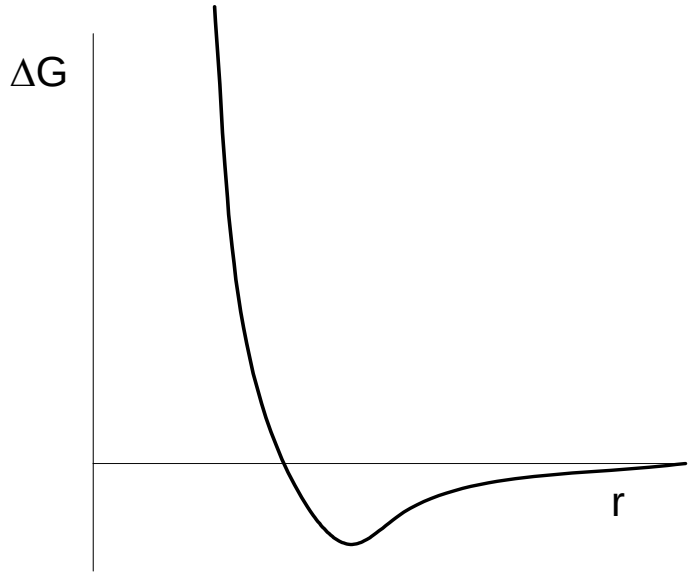

Figure 2-9: Total interaction potential for steric repulsion

allowing easier spreading, and lower the interfacial tension between two liquids. They can be seen simply as string-like materials with hydrophobic heads and hydrophillic tails. The concept is similar to the double layer, except that the surfactants are anchored to the surface and the tails of the surfactants reach out into the fluid. The tails prevent the particles from approaching each other close enough to agglomerate. The total interaction potential can be seen in Figure 2-9 and an illustration of the technique in Figure 2-10.

Steric repulsion allows for more stability of a colloid under variable pH or concentration conditions. However the adsorbed layers due to their organic nature have low temperature and chemical resistance. It is often difficult to match the surfactants that adhere to the particle and do not react with the solvent. It has been seen from other works in the literature, like Krishnakumar [54], that steric repulsion stability can be highly dependent on the dielectric constant of the fluid. The dielectric constant will alter the amount of surfactant that can be adsorbed on the particle surface. The amount of absorbtion determines the stability of the resultant colloid. It is therefore very important to select the proper surfactant for the particular fluid/particle combination which often times requires trial and error. The work of Krisnakumar showed

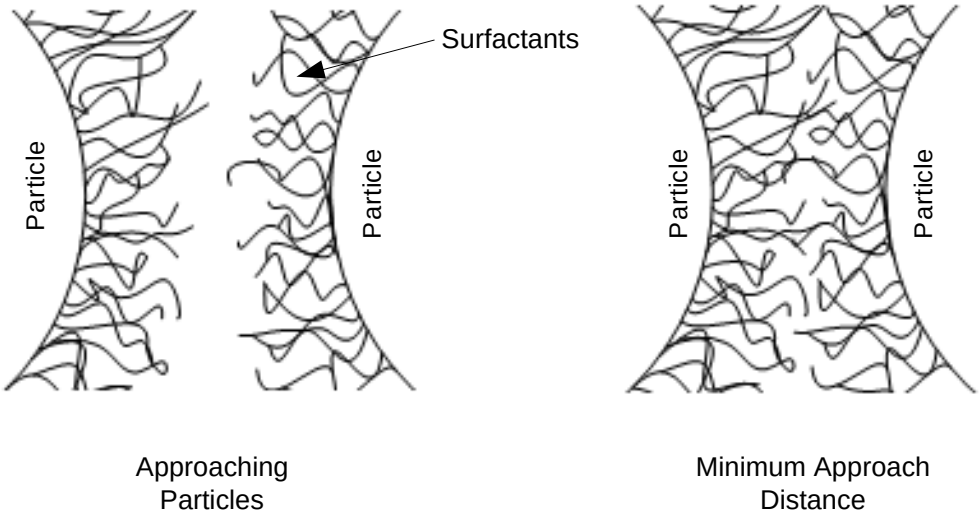

Figure 2-10: Conceptual image of steric repulsion

that Aerosol-OT (AOT) can effectively help to stabilize dispersions of alumina in non-polar solvents, where surface charge stabilization is not possible.

2.1.4 Volume and mass fraction

In most all of the nanofluid thermal conductivity and heat transfer literature the particle loadings of the colloids are given in terms of volume fraction. Volume fraction is desired in order to utilize the existing models for mixed media thermal conductivity like the Maxwell-Garnett[8] or Hamilton-Crosser[7] models. However from an experimental standpoint the exact volume fraction is quite difficult to determine. Due to the large number of surface molecules in the particles, the macroscopic bulk material density is not appropriate when calculating volume fraction. When the particles are placed into solution the formation of oxide or other surface groups also changes the volume being displaced by the particles.

Amorphous surfaces like the hydroxide layers on the outside of the particles can be more porous, than the inner bulk material thus altering the effective volume as well. Due to these chemical effects it is not possible to directly use weight and density measurements in order to determine volume fraction. If one looks at the

mixed media thermal conductivity models, it is found that the resulting conductivity is highly dependent on the volume fraction of the material. It is the author's belief that some of the discrepancies of the measured experimental values and the values predicted by the models could be partially attributed to this effect. The adsorbed ion layer effectively dilates the outer layers of the particle and hence increases its volume, the outer layers thus becoming less dense. The models are strictly volume based.

Most studies are using the weight loading and density of the respective materials in order to determine the volume loading for the modeling. This work follows the same trend as the previous works, however regard is taken to the fact that volume fraction can be misleading and that what might appear to be an anomalous change in properties is potentially explainable through this effect. It however has no bearing on the validity of the experimental results under flow conditions, if one realizes that the properties are only interpreted through the weight fractions. Therefore the loadings in the loop are compared directly with the properties of the samples taken from the loop and the reference to volume fraction is the same as a reference to weight fraction divided by the respective bulk density of the particle material.

Another interesting phenomenon is the alteration of the volume fraction of the colloid by changing the temperature. The density (volume) of some liquids is strongly dependent on the temperature. The volume and hence density of the solid particles is usually much less dependent on the temperature. For this reason one must consider the fact that volume loading of a colloid actually can decrease as the system is heated up. This temperature effect should be accounted for if one wants to use volume averaging models to predict conductivity. There are other effects due to the temperature which will be described in the next section. Once again this effect comes out of the analysis of the flow situation due to the comparison with the exact samples taken from the loop.

Finally, one study has mentioned that there is a potential to have liquid layering at the surface of the particles and how this would affect the modeling of thermal conductivity using volume weighting [28]. Molecular dynamics modeling of nanofluids has shown that this liquid layering is not a structure but more like an ordered higher

density region created by the strong particle/fluid interaction, see the work of Eapen [55]. Eapen showed this region could also potentially have higher thermal conductivity due to other energy transport pathways, i.e. potential energy flux. This molecular dynamics view fits closely with the concept of the interfacial shell model.

2.1.5 Temperature effects

Temperature can have some minor effects on nanofluid behavior beyond the simple density effect discussed above. Due to the chemical nature of the double layer there is a mild sensitivity to temperature change. The approximate thickness of the double layer can be seen from the reciprocal of the Debye-Huckel parameter

$$\kappa^{-1} = \sqrt{\varepsilon_0 \varepsilon_r k_B T / 2 N_A e_f^2 I} \tag{2.13}$$

where I is the ionic strength, N_A is Avogadro's number, ε_0 is the permittivity of free space, ε_r is the permittivity of the solution, T is the temperature and e_f is the Faraday constant. The change in the charge density, which is due to the change in the Debye-Huckel parameter, can alter the stability of the nanofluid as well as the apparent volume of the particles from a hydrodynamic viewpoint. This is a combined effect with the increase in Brownian motion due to the temperature change which would allow a slightly larger percentage of particles to "jump" the total potential barrier. The ionic strength and permittivity is also affected by the temperature change. It might be possible for an increase in temperature to destabilize a colloids because the increase in the Brownian motion causes more jumping and the increase in Debye Length effectively lowers the charge density around the particles if they are in the same chemical equilibrium state. Likewise, surfactant hydrophilia can increase or decrease with temperature as well. Therefore the change of temperature could create a more or a less stable fluid. However it is typical that these effects are minimal and most likely would not effect the fluid over moderate temperature ranges.

2.2 Preparation or purchase of nanofluids

Three main types of nanofluids are studied here: those made from purchased powders mixed with water, those made from chemical precipitation in the liquid, and those which are purchased. Other methods for the creation of nanofluids exist, i.e. plasma arch deposition; but have not been studied in this project. It is very important to understand fully the constituents of any nanofluid under investigation in order to draw significant conclusions as to the heat transfer phenomena. It is common practice to add various chemicals or surfactants in order to maintain nanofluid stability and size distribution. These additional chemicals could also play an important role in the transport phenomena as well as the potential to be used in the nuclear reactor environment.

2.2.1 Preparation

The first attempt to make nanofluids consisted in purchasing nanoparticle powders available from Sigma-Aldrich, see Tables 2.1 and 2.2, and mixing them with a base fluid. Since the purity of the nanofluid is important, attempts were made to mix the particles directly with water with no additives. The metallic oxide nanopowders are not chemically reactive in atmosphere; however they do tend to form loose micro-sized agglomerates in atmosphere and in fluid suspension over time. The most effective method of breaking and evenly dispersing the powder in a fluid is through application of ultrasonic vibration. It has been previously observed, by Das et al.[22], that this technique will maintain fluids with less than 2% volume of particles in suspension indefinitely and suspensions up to 4% by volume with only minor sedimentation. The ultrasonic vibration was done for over 12 hours for each fluid by Das et al. with effective results.

Using this methodology the nanofluids were created using the two oxide nanopowders and ultrasonic vibration was applied for 12+ hours. The resulting nanofluids initially looked promising, but were not stable for longer periods of time. Although some particles remained dispersed, the majority formed larger agglomerates and set-

Table 2.1: Sigma-Aldrich Zirconium(IV) oxide nanopowder (www.sigmaaldrich.com)

Product No.	Description
544760	**Zirconium(IV) oxide** nanopowder
Identifiers	
Molecular Formula	O_2Zr
Molecular Weight	123.22
CAS Number	1314-23-4
EG/EC Number	2152272
MDL number	MFCD00011310
Properties	
Form	solid
diameter	26 nm (calculated)
surface area	39.4 m^2/g
Density	5.89 g/ml

tled out of the liquid. It is mentioned in the work of Das et al. that due to the short duration of their testing, stabilizing agents such as surfactants or pH control were not used. It is believed that the cause of the differences in stabilities of our nanofluids and those of Das et al. could either be due to poor sonication of our samples or nanoparticles from Nanophase Technology Corporation are better dispersed than those from Sigma-Aldrich. This remains to be verified.

As stated earlier, the small particle size gives the potential for the particle to escape settling due to gravity. The Brownian motion of the fluid keeps the particles aloft. However this small particle size dramatically increases the surface to volume ratio of the system. In order to increase the surface area of a material energy must be input into the system. This energy is input by breaking and dispersing the particles. Standard methods for breaking and dispersing are high speed stirring, ball milling, ultrasonication, and high shear nozzles. Therefore the distance from the point of energy stability is increased by increasing the surface area of the particles with these methods. The fully suspended system is either unstable or metastable at best, as found in colloid and surface science.

The other method for creating nanofluids tried in this study is through chemical precipitation with the addition of surfactants. It is theoretically possible to

Table 2.2: Sigma-Aldrich Aluminum oxide nanopowder (www.sigmaaldrich.com)

Product No.	Description
544833	**Aluminum oxide** nanopowder
Identifiers	
Synonyms	Alumina
Molecular Formula	Al_2O_3
Molecular Weight	101.96
CAS Number	1344-28-1
EG/EC Number	2156916
MDL number	MFCD00003424
Description	
mean particle size	40-47 nm
surface area	35-43 m^2/g
description	For column chromatography
Properties	
mean particle size	40-47 nm
surface area	35-43 m^2/g
description	For column chromatography

make any metal oxide nanofluid in this manner. Making of the Fe_3O_4 nanofluid is described as follows: To begin, excess oxygen is removed from deionized water by bubbling through nitrogen. Then, a 1:2 molar ratio of Iron (II) Chloride Tetrahydrate ($FeCl_2 \cdot 4H_2O$) and Iron (III) Chloride Hexahydrate ($FeCl_3 \cdot 6H_2O$) are added to the water. The mixture is stirred and heated to 80°C and becomes yellowish in color. Next, the polymer/surfactant Poly(4-styrenesulfonic acid-co-maleic acid) sodium salt $[CH_2CH(C_6H_4SO_3R)]x[CH(CO_2R)CH(CO_2R)]y$, (where R = H or Na) is added to the mixture until it is foaming.

In order to precipitate the particles a solution of Ammonium Hydroxide ∼28% is added and the solution immediately turns black with the iron oxide nanoparticles. The nanometer size of the particles is created due to the equilibrium between the amount of materials in the mixture. The quick adsorption of polymer surfactant on the particle surfaces is what prevents them from growing into larger macro particles. This solution is allowed to stir and fully react at 80°C for 30 minutes. The resulting nanoparticles are cleaned with acetone and separated from the liquid by using an electromagnet (particles are magnetite). If particles were not magnetic i.e. Al_2O_3 or ZrO_2, then centrifuging could be used. The cleaning process is repeated with deionized water, acetone, and the magnet several more times. The final particles are then heated to boil off the excess acetone and can then be dispersed in water. The final dispersion has been found to be stable indefinitely.

2.2.2 Purchase

Purchase of nanofluids has become more prevalent and cost effective over the past few years. Several companies list nanofluids as products. However it has been found, as will be shown later, that some contain overly contaminated products or products that do not meet specifications. Several companies were approached for samples in this project: Nyacol, Sigma-Aldrich, Nanophase Technologies, Applied Nanoworks and Meliorum Technologies, to name a few. These companies produce many nanofluid products with varying quality. The major candidates for this project which are purchased are water-based with zirconia and alumina particles, however some other fluids

have also been investigated.

2.3 Characterization

As stated above, it is important to be able to fully characterize the nanofluids under inspection for heat transfer enhancement. The first steps are to quantify the composition, size and loading of the nanoparticles, pH, and search for impurities in the nanofluids. Methods for finding these experimentally are discussed along with the results of these experiments.

2.3.1 Characterization methods

Some common tools are utilized to characterize and qualify nanofluids these include: neutron activation analysis (NAA), inductively-coupled plasma spectroscopy (ICP), transmission electron microscopy (TEM) imaging, thermogravimetric analysis (TGA) and dynamic light scattering (DLS). These will be described below.

Transmission electron microscopy (TEM)

TEM is the primary technique to verify single particle dimensions and to identify agglomerations of particles. The electron beam can be used to see features on the nanometer level. A major drawback to the use of TEM is that samples must be dried out of solution in order to be attached to the carbon matrix and placed in the vacuum chamber of the TEM; therefore the particles are not exactly in the colloid state and agglomeration might occur during drying. However, TEM can be used in combination with dynamic light scattering to acquire exact sizing in nanofluid form.

Another drawback of TEM is the cost and time investment needed to prepare and view the sample. It was decided that only some initial imaging will be done as a feasibility study. Later dynamic light scattering, which is a much simpler and less time consuming technique, will be used to first quantify the nanofluids and then selected samples will be viewed with the TEM. An example of one of the nanofluids (Sigma-Aldrich Al_2O_3 in water) can be seen in Figure 2-11. As seen in Figure 2-11

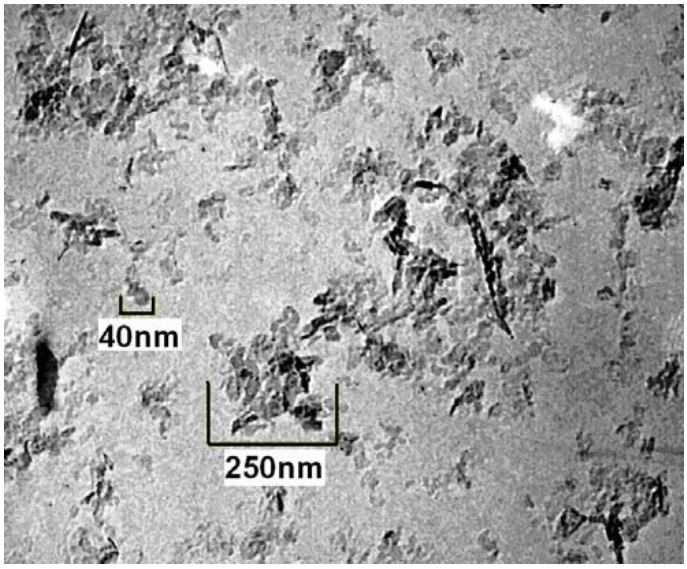

Figure 2-11: TEM image of Sigma-Aldrich Al_2O_3 nanofluid

the smallest particles are on the order of 40-50nm and are slightly oblong in shape. The larger loose agglomerations of particles are in the 250nm range. The time of agglomeration cannot be told from the images and may have occurred during the drying process on the slide. The mean particle size appears to be in agreement with the specifications of Sigma-Aldrich. It is therefore shown that TEM is a useful tool for particle sizing, but has limitations as discussed above.

Dynamic light scattering (DLS)

The dynamic light scattering technique used in this work is described in the work of Kim [56] as follows:

> Dynamic light scattering (DLS) theory is a well established technique for measuring particle size over the size range from a few nanometers to a few microns. The concept uses the idea that small particles in a suspension move in a random pattern. A microbiologist by the name of Brown first discovered this effect while observing objects thought to be living organisms, by light microscopy. Later it was determined that the "organisms" were actually particles, but the term has endured. Thus,

the movement of small particles in a resting fluid is termed "Brownian Motion" and can easily be observed for particles of approximately 0.5 to 1.0 microns bounce a microscope at a magnification of 200 to 400X. Observation of larger particles compared to smaller particles will show that the larger particles move more slowly than the smaller ones given the same temperature. According to Einstein's developments in his Kinetic Molecular Theory, molecules that are much smaller than the particles can impart a change to the direction of the particle and its velocity. Thus water molecules (0.00033 microns) can move polystyrene particles as large as a couple of microns. The combination of these effects is observed as an overall random motion of the particle.

When a coherent source of light such as a laser having a known frequency is directed at the moving particles, the light is scattered, but at a different frequency. The change in the frequency is quite similar to the change in frequency or pitch one hears when an ambulance with its wailing siren approaches and finally passes. The shift is termed a Doppler shift or broadening, and the concept is the same for light when it interacts with small moving particles. For the purposes of particle measurement, the shift in light frequency is related to the size of the particles causing the shift. Due to their average velocity, smaller particles cause a greater shift in the light frequency than larger particles. Thus, the difference in the frequency of the scattered light among particles of different sizes is used to determine the sizes of the particles present.

The DLS equipment used for this study consists of mainly three components. A laser purchased from Spectra-Physics emits a 514 nm wavelength of argon. A goniometer from Brookhaven preserves any scattering between the incident laser and present nano-size particle, which is placed onto a bath. Finally, a detector from Brookhaven detects a laser scattered in 90 degrees from the incident laser since the angle between the goniometer

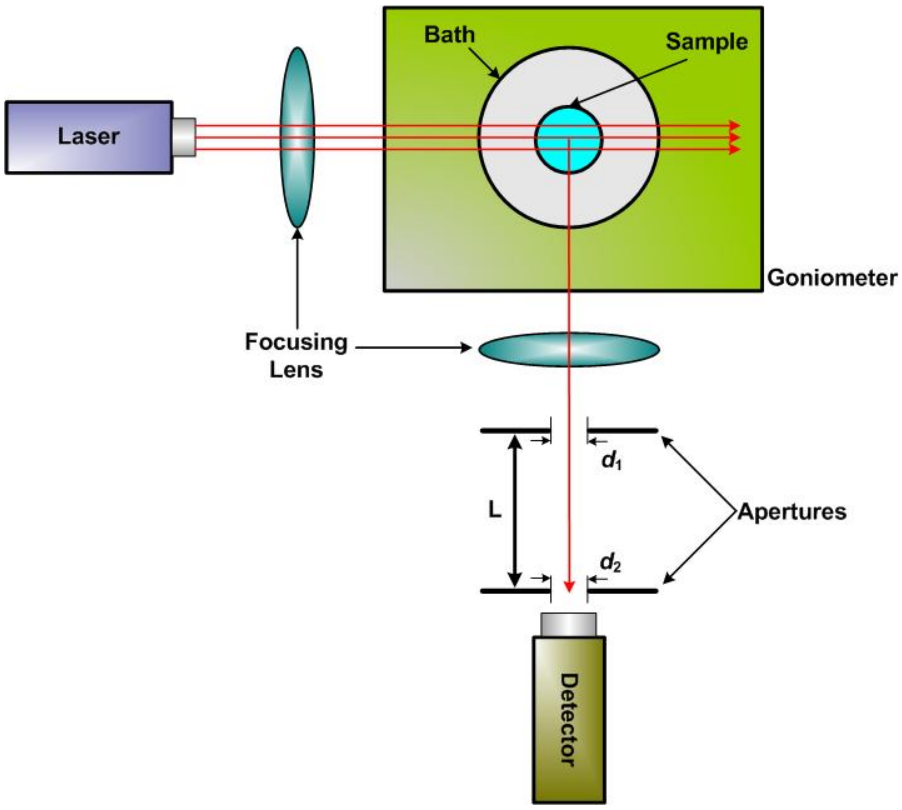

Figure 2-12: Schematic Diagram of light scattering measurement with a dynamic mode

and detector is fixed as 90 degrees. This configuration is well reflected in the Figure 2-12. It is of importance to clarify the physical situation upon this scattering measurement. Since the expected particle size will be smaller than the wavelength of the incident laser, this kind of scattering can be categorized as the Rayleigh scattering, which is defined as the scattering of light, or other electromagnetic radiation, by particles much smaller than the wavelength of the light.

In addition, an alternative mode of light scattering measurement, static light scattering, is also viable if the configuration allows the goniometer to rotate automatically. In such a case, scattered lasers will be detected according to the angle change, which gives the angular distribution of particle size. In either modes of dynamic or static, hydrodynamic or

gyration particle sizes can be obtained, respectively. When we measure a particle size, in practice, it is necessary to start with several assumptions. First the particles can be assumed to be in Brownian motion. Second, it assumed that the particle do not interact with each other. In a practical measurement, the second assumption can be valid when the fluid contains a small number of particles. With those assumptions, the average motion of a particle can be described by using an intermediate scattering function

$$f(q,\tau) = exp[-ip(r(0) - r(\tau)] = exp(iq\Delta r(\tau)) \tag{2.14}$$

where $p = (4\pi/\lambda)sin(\theta/2)$ is a scattering factor, λ is a wavelength of scattered light, θ is an angle between incident and scattered lights, τ is the time scale during the scattering, and $\Delta r(t) = r(t) - r(0)$ is displacement of particle in time t. For particles in Brownian motion, $\Delta r(t)$ is a real 3-D Gaussian variable and therefore $f(q,\tau)$ and the mean square displacement $< \Delta r^2(t) >$ becomes

$$f(q,\tau) = exp\left[-\frac{q^2}{6} < \Delta r^2(t) >\right] \tag{2.15}$$

and

$$< \Delta r^2(t) >= 6D_0\tau \tag{2.16}$$

which when combined form

$$f(q,\tau) = exp\left[-q^2 D_0 \tau\right] \tag{2.17}$$

where D_0 is the mass diffusion constant defined by the Stokes-Einstein theory as

$$D_0 = \frac{k_B T}{6\pi\eta d_p} \tag{2.18}$$

where η is the viscosity of the fluid and R is the radius of the particle. In the measurement, the measured quantity is the diffusion constant based

Sample ID	Alumina 2
Operator ID	Eric
Elapsed Time	00:03:52
Mean Diam.	192.0 (nm)
Rel. Var.	0.022
Skew	-3.174
RmsError	8.0311e-04

d	G(d)	C(d)	d	G(d)	C(d)	d	G(d)	C(d)
30.89	0	0	67.91	0	2	149.29	0	2
33.18	0	0	72.95	0	2	160.37	9	5
35.65	0	0	78.37	0	2	172.27	48	19
38.29	2	1	84.18	0	2	185.06	84	44
41.14	3	2	90.43	0	2	198.80	100	74
44.19	2	2	97.15	0	2	213.56	61	92
47.47	0	2	104.36	0	2	229.41	25	100
51.00	0	2	112.10	0	2	246.44	0	100
54.78	0	2	120.43	0	2	264.74	0	100
58.85	0	2	129.37	0	2	284.39	0	100
63.22	0	2	138.97	0	2	305.50	0	100

Figure 2-13: DLS analysis of Sigma-Aldrich Al2O3 nanofluid (d is particle diameter and G(d) is the intensity of the light)

on the known applied power and time. Using the obtained $f(q,t)$, from which it is viable to induce the diffusion constant by a simple algebra to determine the radius of the particle. It should be noted that this is the Stokes or hydrodynamic radius of the particle. This radius can differ from the actual radius due to the surface charging, as described above.

An example of the raw output for Sigma-Aldrich Al_2O_3 nanofluid measured with DLS is shown in Figure 2-13. It can be seen that the majority of the intensity is around the 200nm sizing, but there are some counts at the ~40nm size. This seems to be in good comparison to the results of the TEM imaging. However one of the main drawbacks of DLS is the measurement of very polydisperse systems. The intensity of the light scattered increases with the diameter of the particle. Therefore the sizes measured are correct, but the distribution of the particles in these size bins needs to be weighted according to their diameters. If this is corrected for in the analysis (which is automatically done by the software), then the majority of the

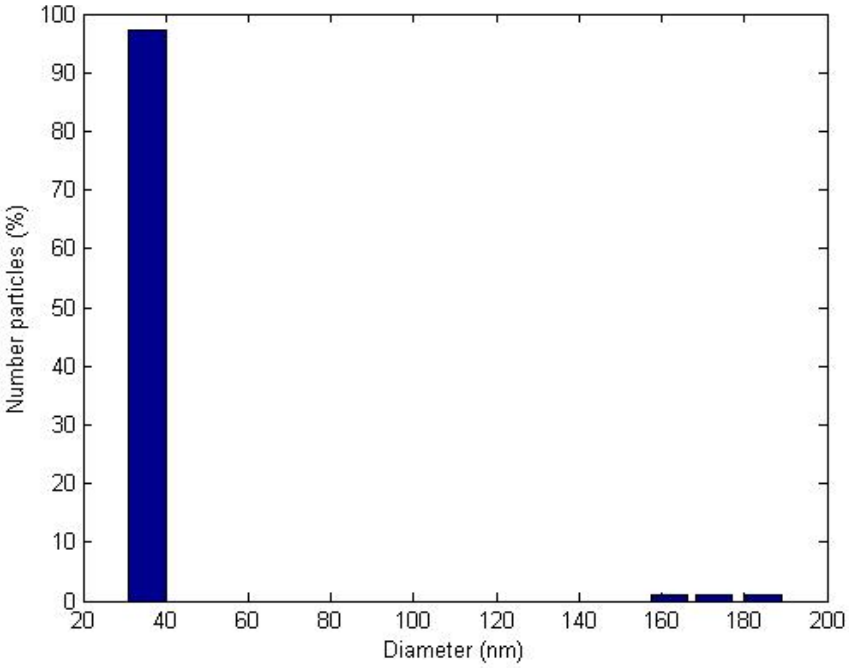

Figure 2-14: DLS analysis of Sigma-Aldrich Al2O3 nanofluid after correction

particles are in the 40nm range with a few larger agglomerations, see Figure 2-14, which reinforces previous findings and the technical specifications of the fluid. The pH of the Sigma-Aldrich is around 4 in order to maintain the particles in dispersion. If the pH is allowed to rise to 7, the agglomerations are seen to increase significantly. Therefore care must be taken to maintain the nanofluid pH stable during dilution for the DLS measurement, this will be shown later. Other DLS measurements are made on Nyacol alumina and zirconia, see Figures 2-15 and 2-16 and the Fe_3O_4 nanofluids with reasonable results. It has been determined that DLS is an effective way of determining nanofluid particle sizes in solution and in combination with TEM, full characterization of particles sizes and distributions is possible.

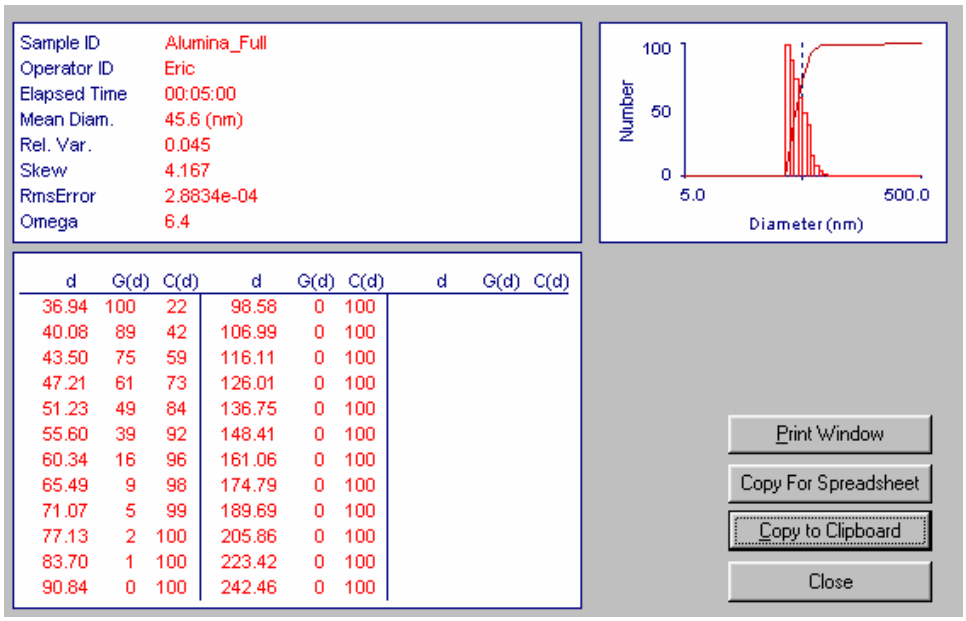

Figure 2-15: DLS analysis of Nyacol Al2O3 nanofluid

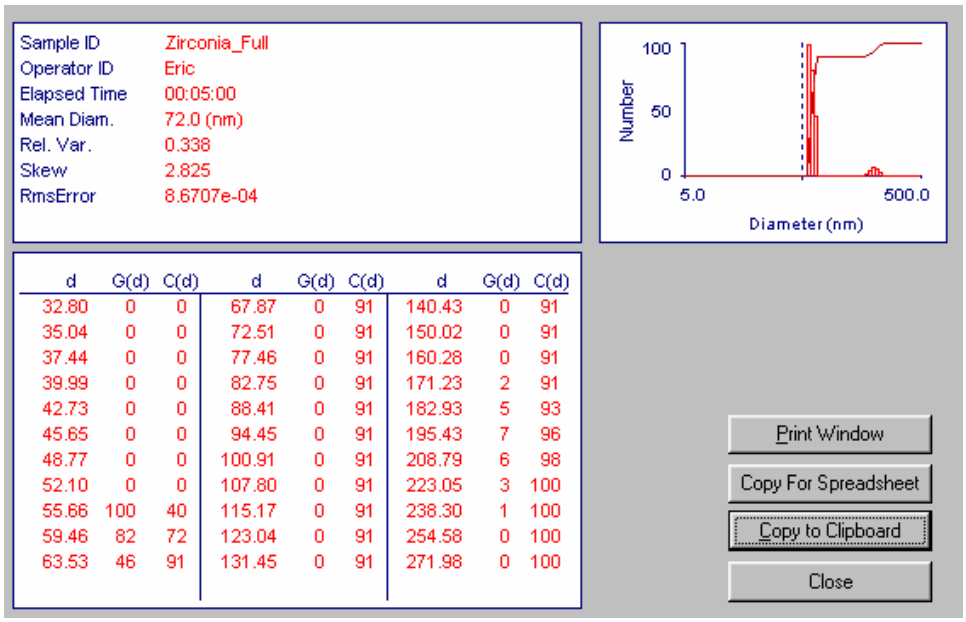

Figure 2-16: DLS analysis of Nyacol ZrO2 nanofluid after correction)

Table 2.3: Elements detectible by neutron activation analysis

Aluminum	Dysprosium	Lanthanum	Potassium	Tellurium
Antimony	Erbium	Lutetium	Praseodymium	Terbium
Arsenic	Europium	Magnesium	Rhenium	Thorium
Barium	Gadolinium	Manganese	Rubidium	Thulium
Bromine	Gallium	Mercury	Ruthenium	Zirconium
Tin	Cadmium	Germanium	Molybdenum	Samarium
Titanium	Cerium	Gold	Neodymium	Scandium
Tungsten	Cesium	Hafnium	Nickel	Selenium
Uranium	Chlorine	Indium	Niobium	Silver
Vanadium	Chromium	Iodine	Osmium	Sodium
Ytterbium	Cobalt	Iridium	Palladium	Strontium
Zinc	Copper	Iron	Platinum	Tantalum

Neutron activation analysis (NAA)

Particle concentration in the nanofluid solution is another problem of characterization. The capabilities of MIT's research reactor to perform neutron activation analysis are utilized for determining nanoparticle and other impurity concentrations in the nanofluids. NAA is a method that uses the gamma decay emissions of the samples after having undergone neutron irradiation to identify elements and their concentrations. Irradiation times depend on the materials under investigation and the half life of the gamma decay modes. Table 2.3 lists all of the elements detectible using NAA. Two zirconia nanofluid samples are irradiated, because of the long zirconium half life the samples have been irradiated for 6 hours. Both samples are supplied as 10 percent zirconia by weight in water from the vendors. Samples are from Sigma-Aldrich and Applied Nanoworks. The measurements were conducted by experienced NRL staff, so the details will not be reported here. The results found that both nanofluids contained zirconium, 0.076gm/gm in the Sigma-Aldrich and 0.0203gm/gm in the Applied Nanoworks. In order to determine the amount of zirconia, it is assumed all of the zirconium is in the form of the oxide and contains two oxygen atoms. By addition of this extra weight it is found that the Sigma-Aldrich has 0.1027gm/gm or 10.27wt% zirconia and the Applied Nanoworks has 0.0274gm/gm or 2.74wt% zirconia. Therefore it is concluded that the Sigma-Aldrich is very close to the manufacturer specifications;

the Applied Nanoworks is dramatically different than the specifications.

Also, there is as much zinc as zirconium in the Applied Nanoworks sample; the zinc has been found at 2.6wt%, which is a significant contamination. The Sigma-Aldrich sample only has 6.5e-3wt%, which is insignificant. It is believed that the Applied Nanoworks specifications are either unreliable or that the batch is overly contaminated. Trace amounts (ppm levels) of other elements (K, Cl, Na) are found and assumed to be as additives for pH control or just in the water used for dispersion.

Some alumina nanofluids have also been considered. Nyacol at 20wt% (NY), Meliorum (ML) and Sigma-Aldrich (SA) at 10wt% were the three measured fluids. For the alumina both short and long irradiations are required. The long (6 hours) is for the majority of elements and the short (5 mins) is for the aluminum due to the short half life. The results of the long show that the samples all contained nearly insignificant levels (ppm) of Na, K, and a few other earth elements like Zn.

The results of the short irradiations gave the loading of the aluminum and thus alumina for the nanofluids. It is seen that the NY has 19.37wt%, specs gave 20wt%. The ML has 9.74wt% and the SA has 8.68wt% for 10wt% in the specs. These seem to be in good agreement with the specifications of the vendors. The discrepancy of the SA is assumed to be due to settling of the nanofluid, because it was an older sample. Further tests would be required to make certain that the SA discrepancy was due to settling. It is concluded that NAA can be used for quality control of nanofluids. The major limiting factors of NAA is the time and cost of the procedure. It also involves handling of radioactive materials.

Inductively-coupled plasma spectroscopy (ICP)

A more cost and time effective approach has been selected for determining the nanoparticle loading and composition, i.e., the ICP spectrometer. ICP spectrometry uses the light spectrum released from injecting materials into an extremely high temperature plasma. The list of elements detectible by ICP is listed in Table 2.4. In general the sensitivity of the ICP is lower than that of the NAA.

Each sample analysis takes only a few minutes once the ICP is calibrated for the

Table 2.4: Elements detectible by ICP

Ar	Ca	Eu	In	Na	S	Ta	Y
Ag	Cd	Fe	K	Nb	Sb	Th	Yb
Al	Ce	Ga	La	Nd	Sc	Ti	Zn
As	Co	Gd	Li	Ni	Se	Tl	Zr
B	Cr	Ge	Lu	P	Si	Tm	Ba
Cu	Hf	Mg	Pb	Sm	U	Be	Dy
Hg	Mn	Pr	Sn	V	Bi	Er	Ho
Mo	Re	Sr	W	-	-	-	-

element of interest. Two samples are tested using the ICP: Al_2O_3 (Sigma-Aldrich) and Fe_3O_4 in water. One key to the analysis is that the nanofluid samples need to be diluted to stay below the maximum concentration of the calibration standards. Therefore the Al_2O_3 which was initially at 10wt% is diluted to 0.05wt% (200:1) and the Fe_3O_4 which was initially at 3.5wt% (polymer & iron oxide) is diluted to 0.035wt% (100:1), both using deionized water. The Al_2O_3 is found to be at a concentration of 0.047wt% which is within ∼5% of the specified value. This is somewhat closer result than that from the NAA. Sodium and potassium are also found, which is consistent with the NAA results. These are used to stabilize the nanofluid using the pH method. The Fe_3O_4 is seen to have a concentration of 0.034wt% which is within ∼10% of the specified value (∼0.031wt%). The sodium of the stabilizing polymer could also be seen by the ICP. These results are determined to be valid. The advantage of ICP is its speed. It is more accurate than the NAA with respect to the alumina sample. However, the nanoparticles may not be effectively introduced in the nebulizer if large agglomerations occur. Therefore care must be taken to prevent agglomeration when diluting pH stabilized nanofluids.

Thermogravimetric analysis (TGA)

Thermogravimetric analysis of nanofluids provides another means of analyzing different components of a nanofluid by weight. This may be desirable when one needs to know an accurate weight percentage of nanoparticles in solvent, or when the amount of polymer (added to improve the nanoparticle stability) in a nanofluid must be known.

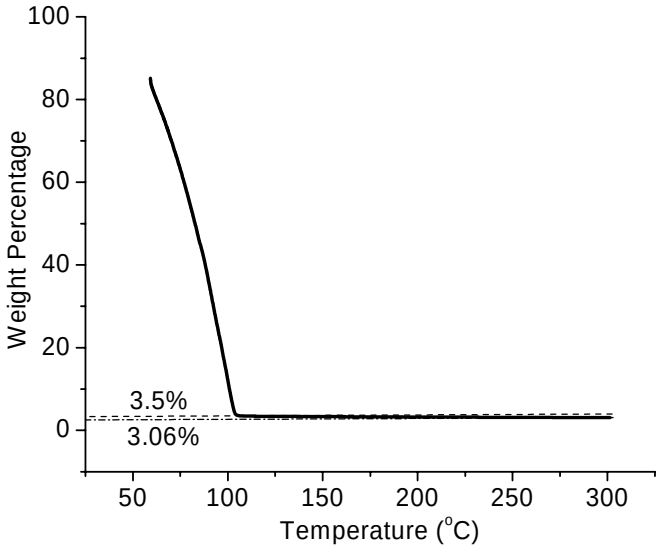

Figure 2-17: Thermal gravimetric analysis of Fe3O4 nanofluid in water with surfactants

Thermogravimetric analysis works by heating a small sample on an extremely sensitive balance in a high temperature furnace. The weight vs time curve combined with knowledge of the boiling point of the species in the samples provide the sample composition. The specific equipment to be used is the Perkin Elmer TGA7. Samples, typically less than 40mg, are placed on a platinum balance and can be heated to over 1000°C.

Figure 2-17 shows outputs from the TGA7 for the Fe_3O_4 nanofluid produced. Weight percentage remaining is plotted on the y-axis, with temperature on the x-axis. The polymer poly(4-styrenesulfonic acid-co-maleic acid) did not completely "cook off" until higher temperatures, around 300°C or 400°C. Results have shown that this polymer, by weight, makes up about 12% of the polymer coated Fe_3O_4 nanoparticles, whereas the rest is composed of Fe_3O_4. The weight loading of a nanofluid can easily be determined in this fashion, 3.5wt% for the iron oxide plus surfactant and 3.06wt% for the iron oxide alone. A sample of the Nyacol Al_2O_3 nanofluid was also tested at 20wt%. The results of the TGA showed that the particles consisted of 21.8wt%, which is slightly higher than the specified value. However further heating to the maximum temperature found that the alumina is at 20.070wt%. It is believed that this extra

weight could possibly be due to the left over hydroxide groups on the surface of the particles.

TGA has been found to be a simple way of measuring particle loading in nanofluids. It is inexpensive and uses very little of the sample. However it is not obvious what constituents are producing the final weight results. If the nanofluids have severe contamination, this could be incorrectly seen as additional particles in the final weight loading. It is therefore intelligent to use both the ICP and TGA in order to fully understand the loading of the nanofluid.

KD2 thermal conductivity analyzer

An important property to be characterized in this study is the thermal conductivity of the nanofluid. In order to select the desired fluids to be fully characterized, enhanced thermal conductivity is possibly the most important element in this study, because it points to the nanofluid with high heat transfer potential. There is an inexpensive commercially available system for the measurement of the thermal conductivity. The Decagon Devices KD2 thermal properties analyzer, after some initial testing, is used on all nanofluids at room temperature as a first check. In later sections, the transient hot wire method, on which the KD2 operates, will be described in full along with the true thermal conductivity measurement apparatus.

The accuracy of the KD2 is given as 5% by the manufacturer over a span of temperatures of 0 to 60°C. However it is found, through trial and error, that the KD2 operates very accurately if the probe is setup perfectly vertical and an isothermal bath is used to maintain the sample at 25°C. These measures prevent convection problems and the external boundary effect problems. A schematic of the KD2 setup with the isothermal bath is shown in Figure 2-18.

In order to test the accuracy of the KD2, mixtures of water and ethylene glycol are prepared and tested against existing data in the literature from Bohne, Fischer, and Obermeier [57]. The results of the measurement are shown in Figure 2-19. It can be seen that the KD2 is quite accurate in measuring the values of the mixtures. This is a reassurance of the KD2's operation and it is therefore acceptable as an initial

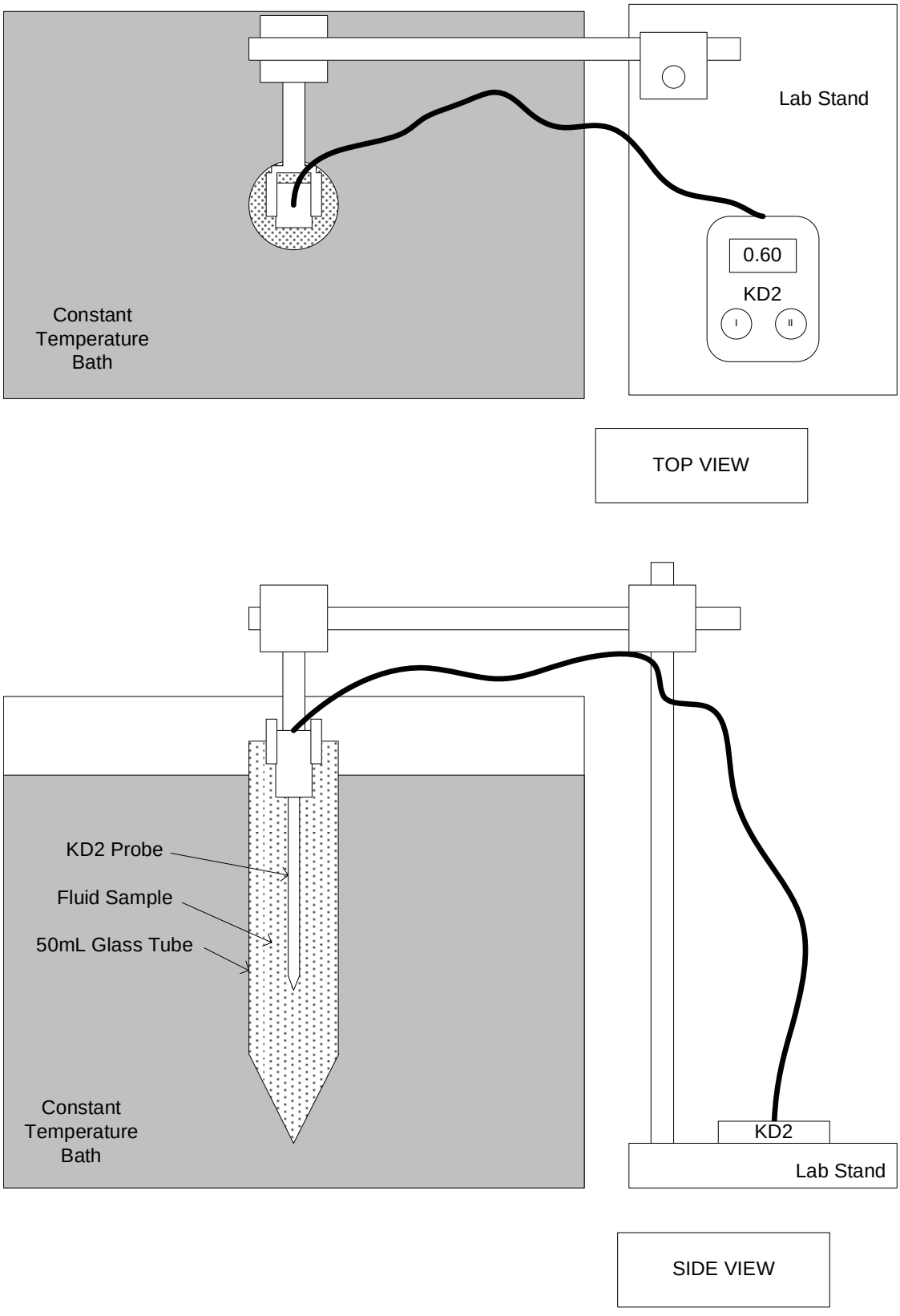

Figure 2-18: Schematic setup of KD2 thermal properties analyzer

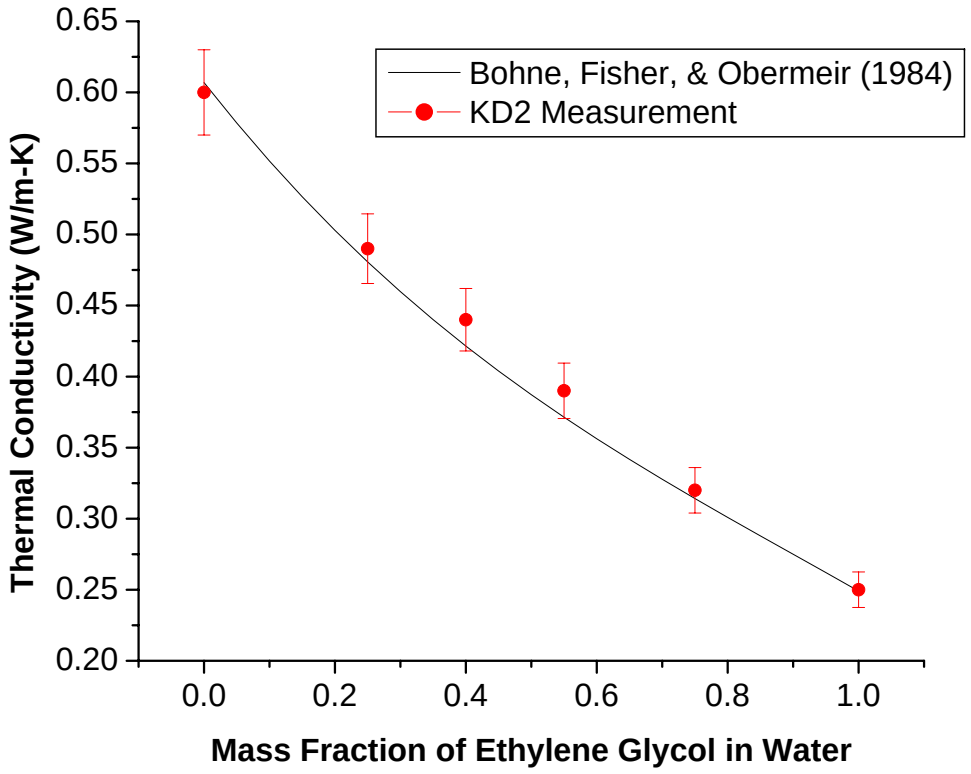

Figure 2-19: Thermal conductivity of water and ethylene glycol mixtures

scoping tool for thermal conductivity.

2.3.2 Experimental selection of nanofluid samples

Using the characterization techniques as described above many nanofluids have been tested as potential candidates for further experimental investigation. The key properties used as criteria to eliminate the bad candidates are thermal conductivity enhancement, stability, and contamination.

Thermal conductivity at room temperature

Initially both water and ethylene glycol nanofluids are considered due to the availability of the data in the literature for these fluids. It has been previously decided that

the scope of this work would be limited to water based nanofluids. The measured thermal conductivity at room temperature for the nanofluids can be seen in Table 2.5 along with the loadings, manufacturers, and measured pH values. It is seen that few fluids have enhancement in the conductivity and none of the fluids have what would be considered anomalous enhancement beyond that of the mixed media model, like Maxwell-Garnett, as shown. From this list, a short list of good candidates is compiled which includes primarily alumina in water fluids from Sigma-Aldrich, Meliorum, and Nyacol. Secondary candidates are zirconia in water fluids from Sigma-Aldrich and Nyacol, diamond in water fluid from the University of Florida and Applied Nanoworks, silica in water fluid from Applied Nanoworks. Due to time constraints only the Nyacol Alumina and Zirconia are selected for the full experiments.

Investigation of colloidal stability

Further investigation of the Nyacol and Sigma-Aldrich alumina is done because of alumina nanofluid being of primary interest for the experiments. Some of the colloidal stability properties can be easily shown experimentally with particle sizing techniques. A small experiment on the size/stability of oxide particles with pH was done. Two loadings of alumina are created from 10% by weight alumina in water nanofluids from Sigma-Aldrich and another two from 20% by weight. The Sigma-Aldrich fluid has a pH value of 4.3, thus during dilution with water the pH was allowed to change towards neutral. The size and stability effects are highly visible using dynamic light scattering. The initial Sigma-Aldrich fluid is shown in Figure 2-20 where the mean diameter is 51.32nm with some minor flocs at higher diameters. The samples are diluted to 0.01% and 0.001% by weight and allowed to sit for 1 hour. It can be seen in Figures 2-21 and 2-22 that the mean diameter has increased to 90.09nm and 181.15nm, respectively.

The samples are then allowed to sit for 1 day. It can be seen in Figures 2-23 and 2-24 the mean diameter has increased to 129.02nm and 224.51nm, respectively for 0.01%wt and 0.001%wt. The pH change due to dilution is a very important parameter to the overall size and stability of the nanofluid. This was predictable

Table 2.5: List of samples which have been investigated for thermal conductivity enhancement

Particle	Liquid	Maker	Preparation	Loading		pH	Conductivity	
				wt%	vol%		Measured	Predicted
	EG						*0.25*	*0.25*
Ag	EG	MIT	No Surfact/No pH	0.029	-	-	0.25	0.25
Al_2O_3	EG	MIT	No Surfact/No pH	-	~3	8.5	0.28	0.27
Au	EG	Meliorum	Surfactants	-	1	-	0.25	0.26
CuO	EG	MIT	No Surfact/No pH	-	~1	4.15	0.27	0.26
SiO_2	EG	MIT	No Surfact/No pH	-	1.6-3.3	-	0.28	0.26
ZrO_2	EG	MIT	No Surfact/No pH	-	4	-	0.28	0.27
	H_2O						*0.59*	*0.59*
Al_2O_3	H_2O	SA	pH	10	-	4.3	0.63	0.64
Al_2O_3	H_2O	RPI	Surfactants	-	2 (0.5)	8.15 (7.05)	0.64 (0.62)	0.63 (0.60)
Al_2O_3	H_2O	Nyacol	pH	20	-	4	0.68	0.70
Al_2O_3	H_2O	Meliorum	pH	10	-	3.9	0.62	0.64
Au	H_2O	Meliorum	Surfactants	-	5	-	0.58	0.68
Cu	H_2O	MIT	No Surfact/No pH	-	0.5	6.5	0.59	0.60
CuO	H_2O	MIT	No Surfact/No pH	-	<5	7.12	0.59	0.61
Diamond	H_2O	UF	No Surfact/No pH	1.7	-	6.67	0.62	0.60
Diamond	H_2O	MIT	No Surfact/No pH	0.1	-	6	0.60	0.59
Fe_3O_4	H_2O	MIT	Polymer Surfactant	-	1	8.54	0.56	0.60
Pt	H_2O	Meliorum	?	0.0486	-	-	0.57	0.59
SiO_2	H_2O	Applied Nano	pH	10	-	10.17	0.63	0.62
SiO_2	H_2O	Polimi	?	34	18.6	7.13	0.63	0.69
SiO_2	H_2O	MIT	No Surfact/No pH	5	-	-	0.57	0.60
Teflon	H_2O	Polimi	No Surfact/No pH	10.2	5	3.35	0.58	0.57
ZnO_2	H_2O	MIT	No Surfact/No pH	-	0.4	7.15	0.59	0.59
ZrO_2	H_2O	SA	pH	10	-	2.7	0.62	0.60
ZrO_2	H_2O	MIT	No Surfact/No pH	17	4	5.27	0.62	0.62
ZrO_2	H_2O	Applied Nano	pH	10	-	4.17	0.59	0.60
ZrO_2	H_2O	Nyacol	pH	20	-	4.17	0.61	0.62

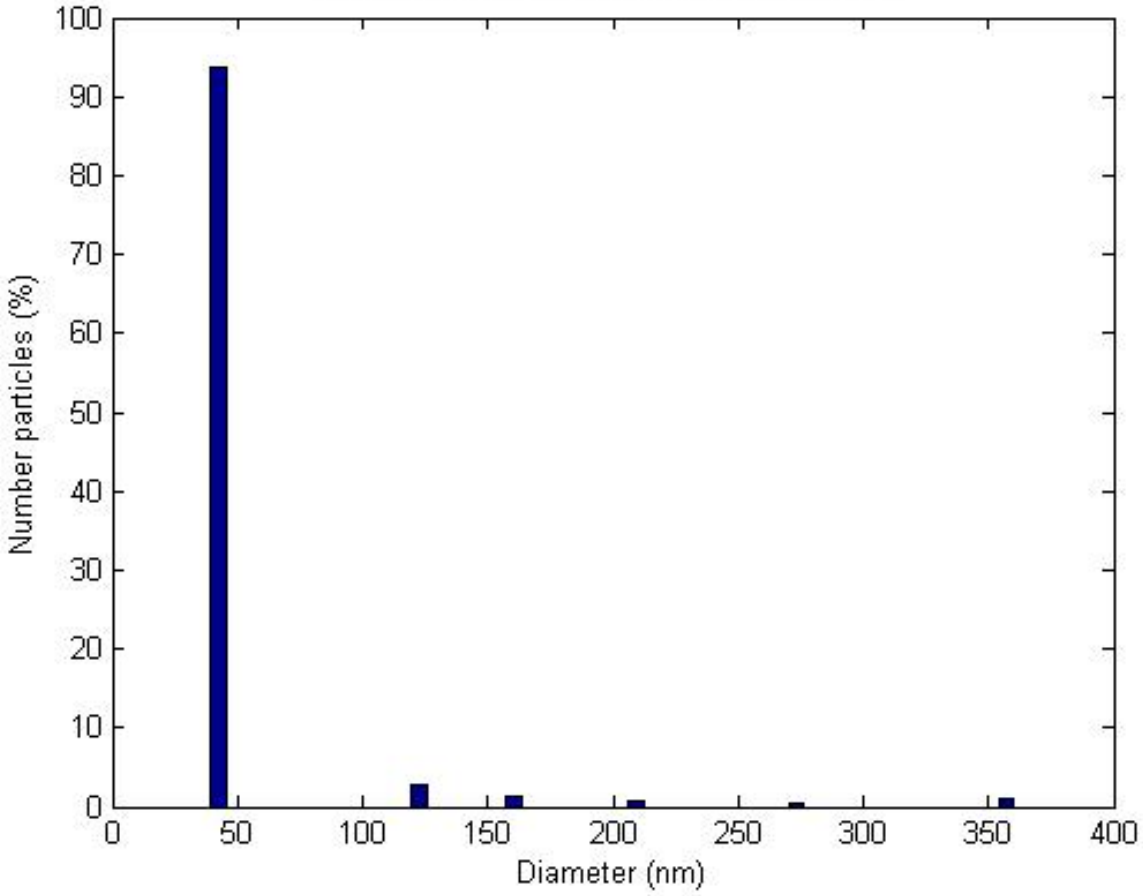

Figure 2-20: Particle size distribution for pH 4.3 alumina Sigma-Aldrich nanofluid at 10wt%

from the dependence of the double layer on the pH, and the concentration of charged groups on the surface of the particles. It is believed that many of the studies in the literature do not give ample information about the dilution techniques and pH control, so it is hard to assess whether the initial particle size distribution can be assumed to persist throughout the experiments. This is very important because the conductivity appears to have a strong size and chemical effect.

However different results are found for the Nyacol nanofluid. The Nyacol uses nitrate as the surface ion group as opposed to the alumina hydroxide group used in the Sigma-Aldrich. The initial Nyacol fluid has a pH value of 4, thus during dilution with water the pH was allowed to change towards neutral. The size distribution

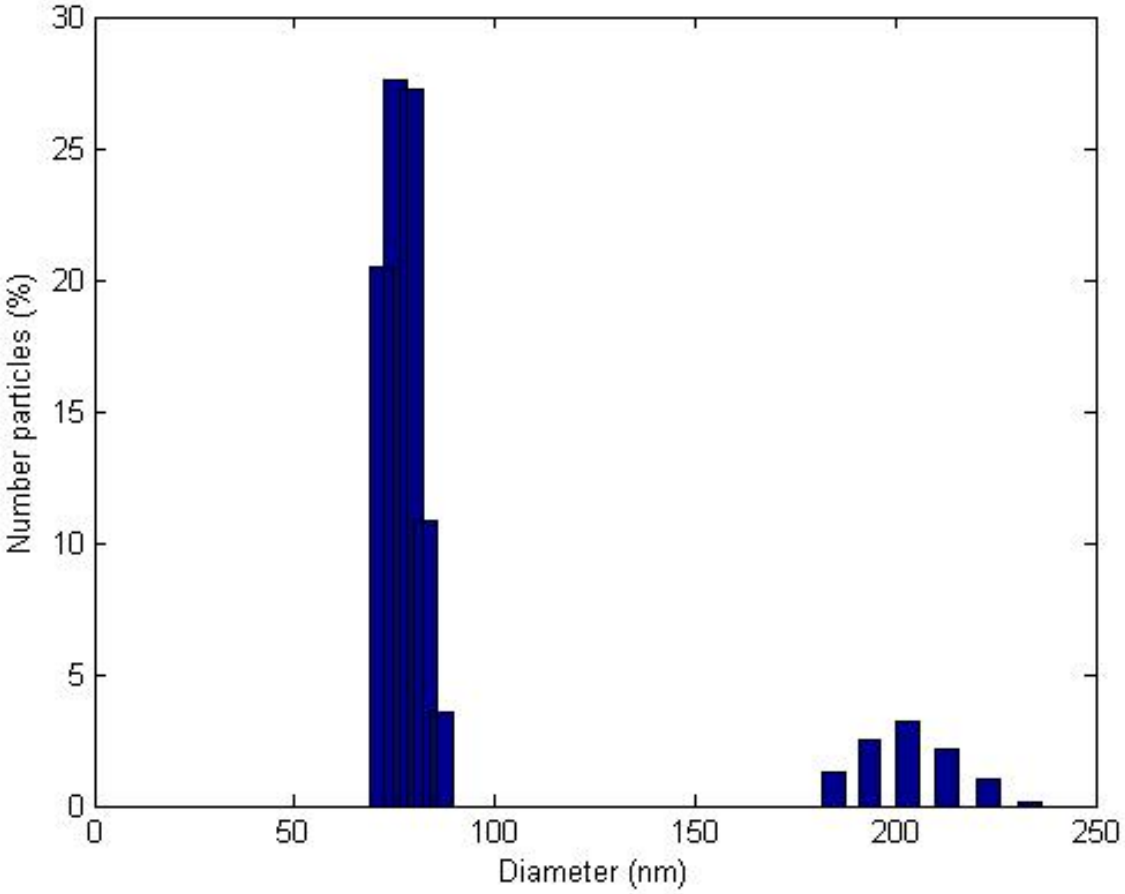

Figure 2-21: Particle size distribution for 0.01%wt alumina Sigma-Aldrich nanofluid at one hour

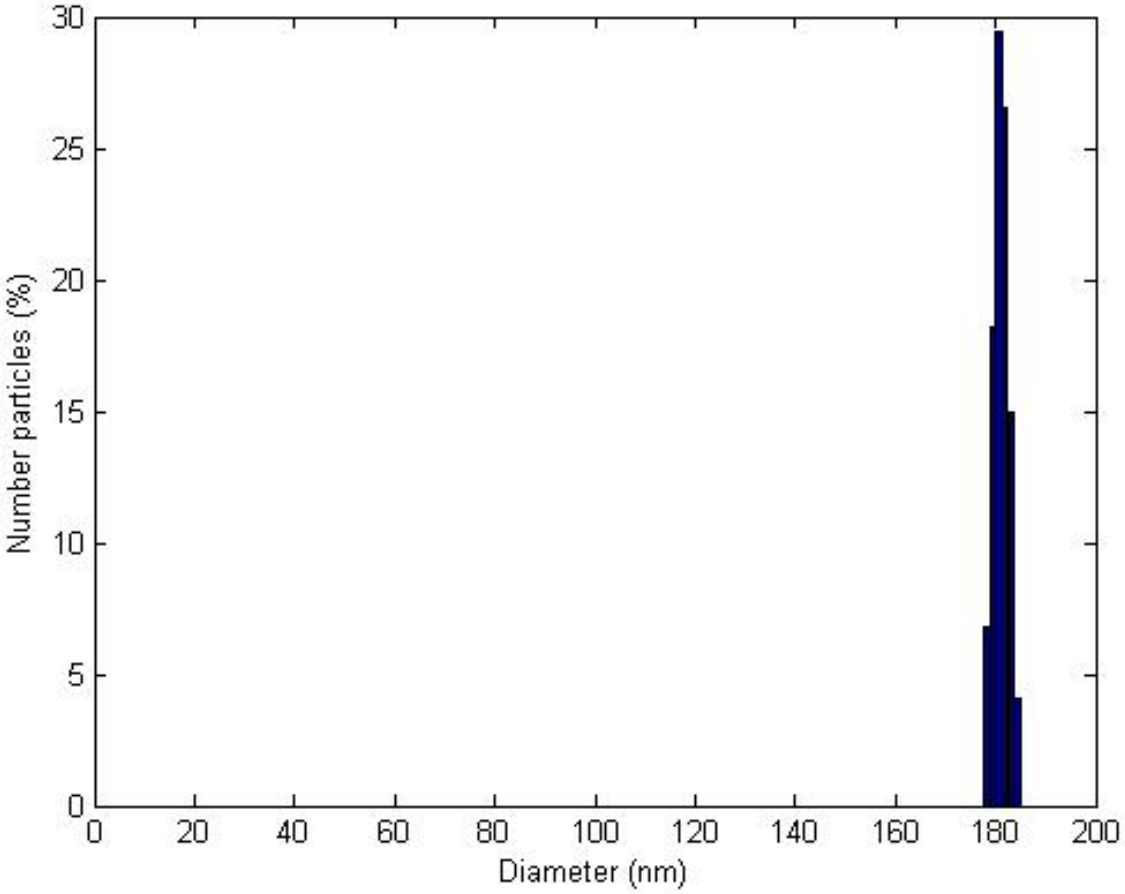

Figure 2-22: Particle size distribution for 0.001%wt alumina Sigma-Aldrich nanofluid at one hour

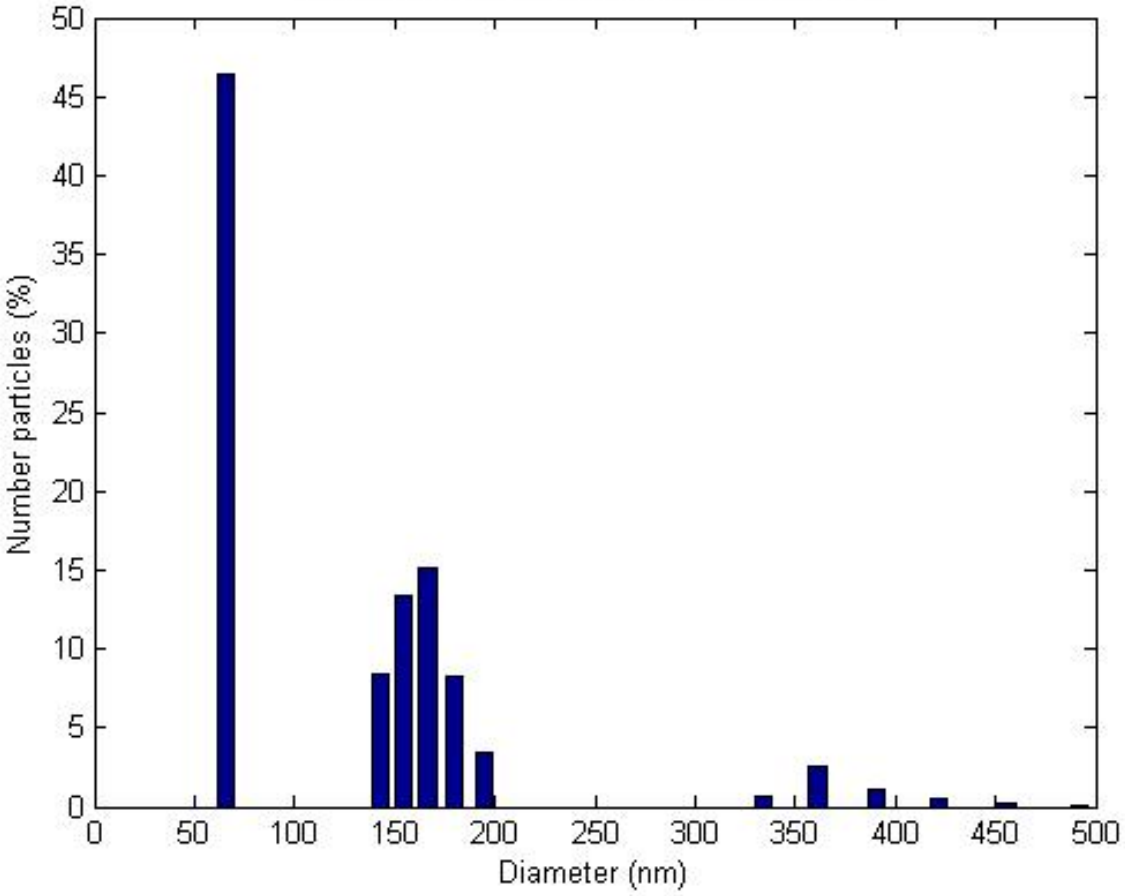

Figure 2-23: Particle size distribution for 0.01%wt alumina Sigma-Aldrich nanofluid at one day

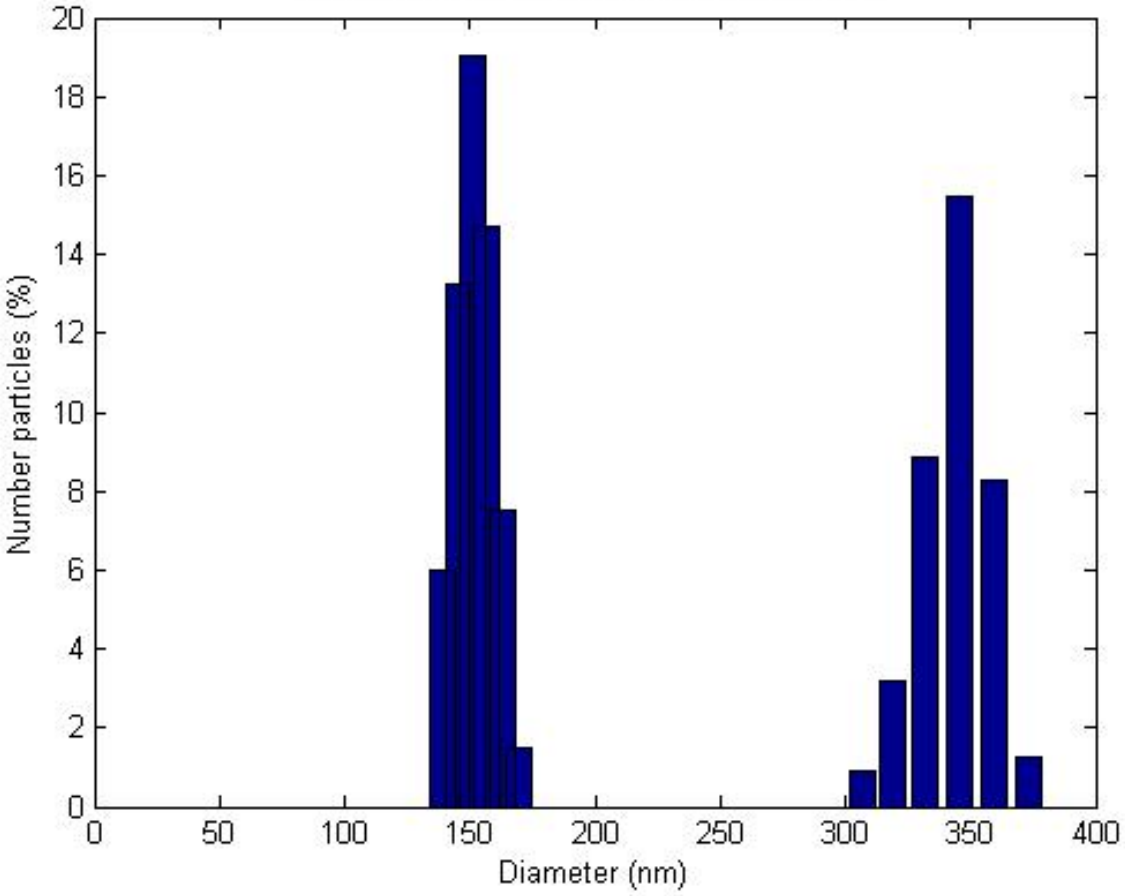

Figure 2-24: Particle size distribution for 0.001%wt alumina Sigma-Aldrich nanofluid at one day

is shown in Figure 2-25 where the mean diameter is 37.8nm with some minor flocs at higher diameters. The samples are diluted to 0.04% and 0.004% by weight and allowed to sit for 1 hour. It can be seen in Figures 2-26 and 2-27 the mean diameter has increased slightly to 42.6nm and 52.3nm, respectively. The samples were then allowed to sit for 1 day. It can be seen in Figures 2-28 and 2-29 the mean diameter is basically unchanged at 46.7nm and 46.7nm, respectively for 0.04%wt and 0.004%wt. The pH change due to dilution is less important for the nitrate stabilized nanofluid. Salt concentration plays an important role in the double layer size and strength. Because the size distribution of its particles is not strongly affected by dilution the use of Nyacol nanofluid should be easier in an engineering system. For this reason the Nyacol nanofluids (alumina and zirconia) were the final selections to be used in the experimental loop.

2.3.3 Conclusions

In conclusion, there are many variables that must be accounted for when dealing with nanofluid (colloid) experiments. The conceptual and theoretical developments of colloid and surface science lead to a far better understanding of nanofluid properties and behavior. Some properties such as size and stability are easily altered by concentration, pH, and temperature modifications.

It is determined that nanofluids can be purchased or made in a variety of ways. Surfactant addition and/or pH control are the standard techniques for the production of stable nanofluids. Ultrasonication is the selected method for breaking up larger agglomerations and homogenizing the fluids. It is also found that care should be taken when using purchased nanofluids, due to the possibility for contaminants and variation from the specified properties. Nevertheless, there are some reliable nanofluids which can be purchased and used after full in-house characterization.

A description of the techniques to quantify nanofluids has been given. Of these techniques, DLS and TEM have been selected for particle and agglomeration sizing of the nanofluids. It is determined that DLS should be the primary method of particle sizing, due to its ease of use and low cost. However, TEM imaging must be used

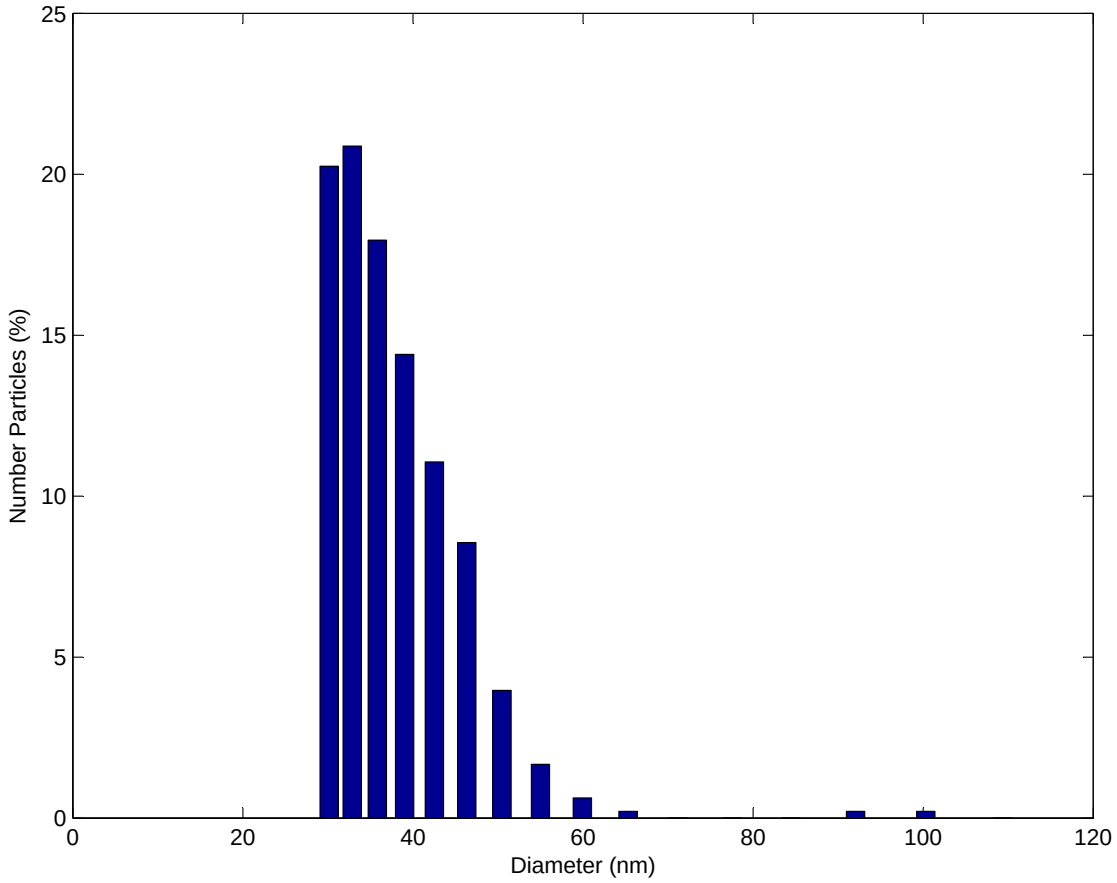

Figure 2-25: Particle size distribution for pH 4 alumina Nyacol nanofluid at 0.01wt%

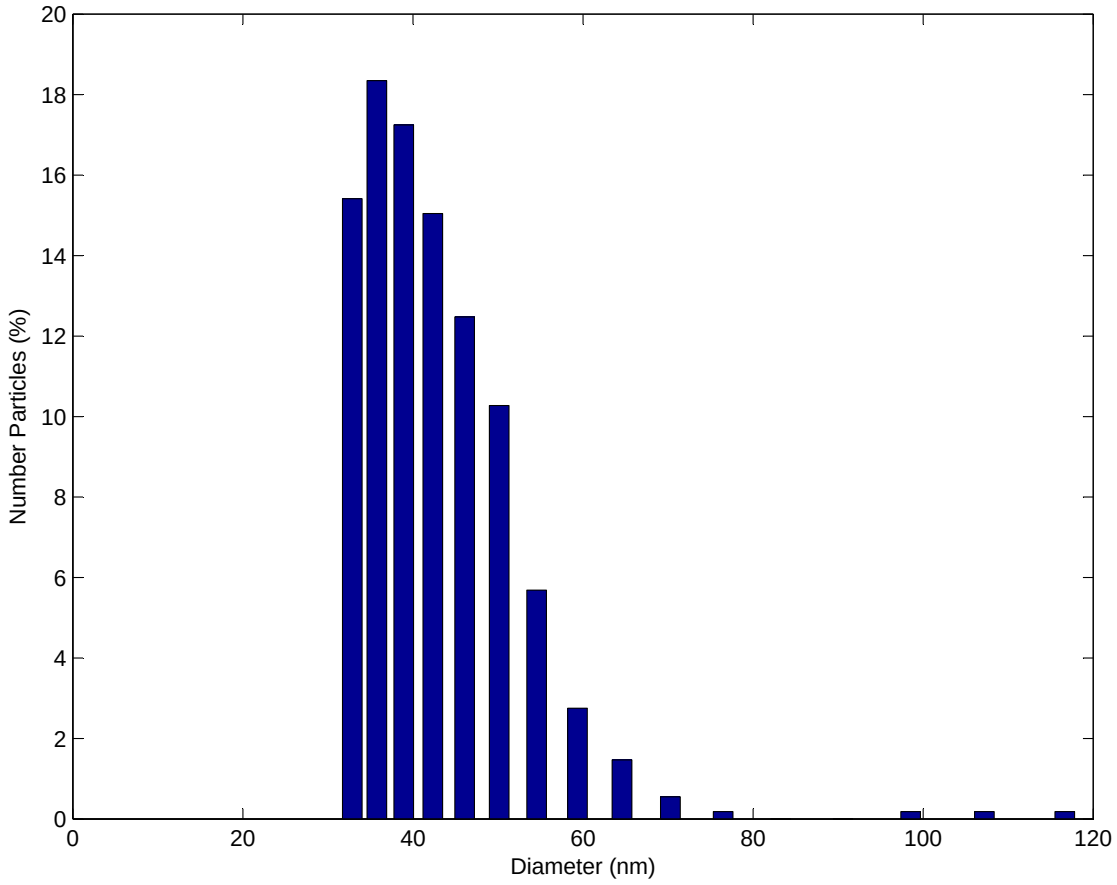

Figure 2-26: Particle size distribution for 0.04%wt alumina Nyacol nanofluid at one hour

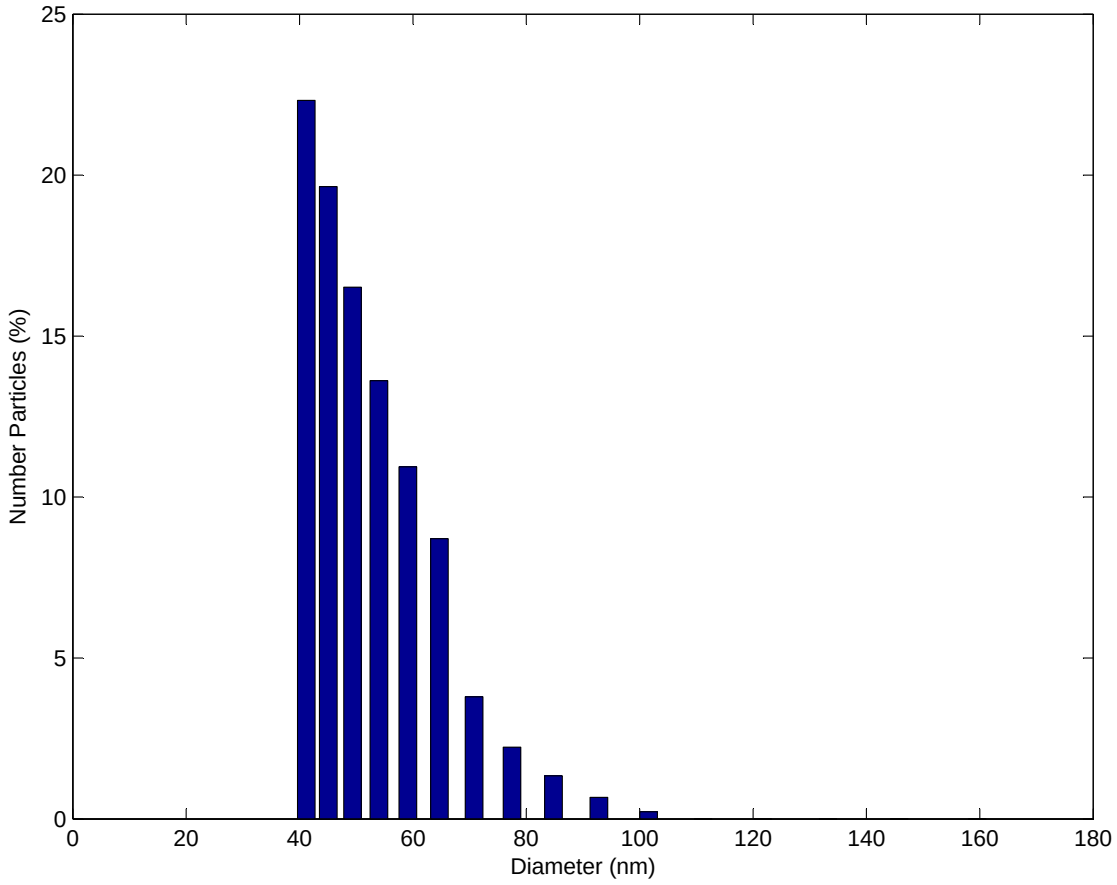

Figure 2-27: Particle size distribution for 0.004%wt alumina Nyacol nanofluid at one hour

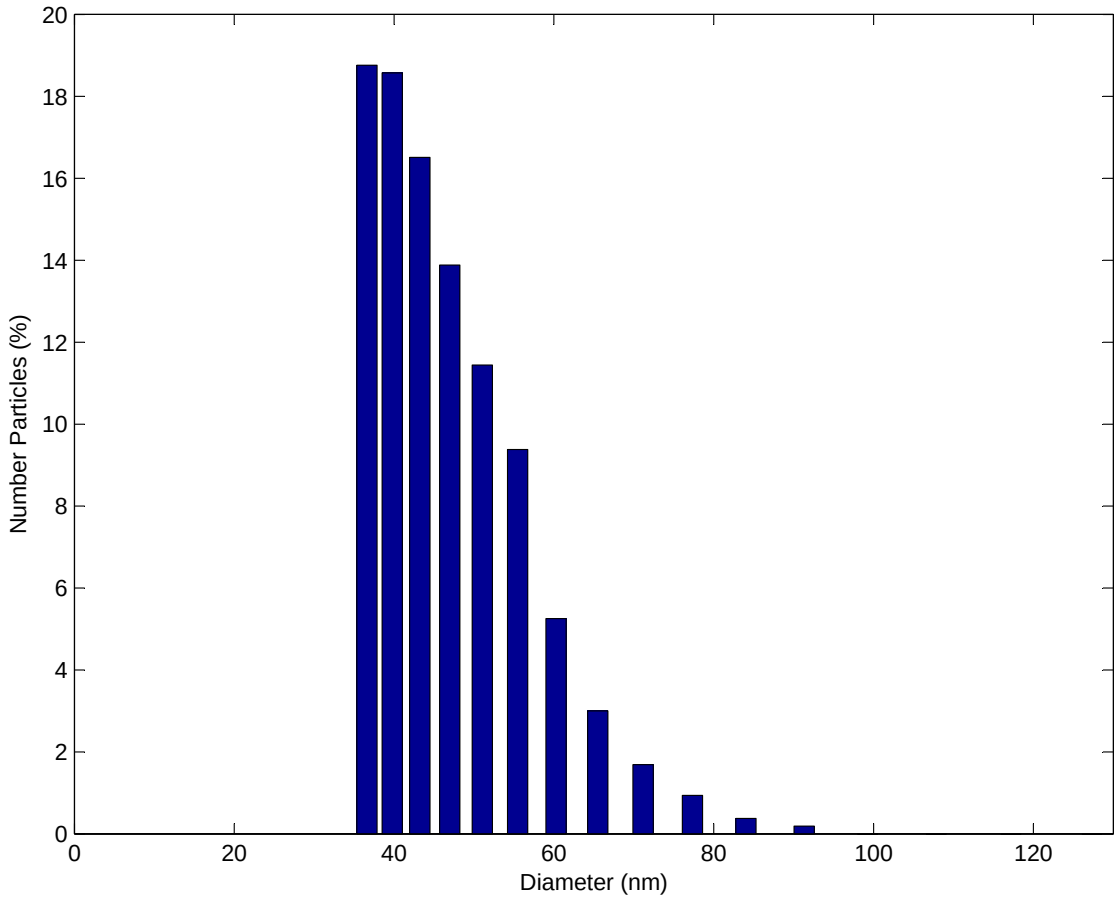

Figure 2-28: Particle size distribution for 0.04%wt alumina Nyacol nanofluid at one day

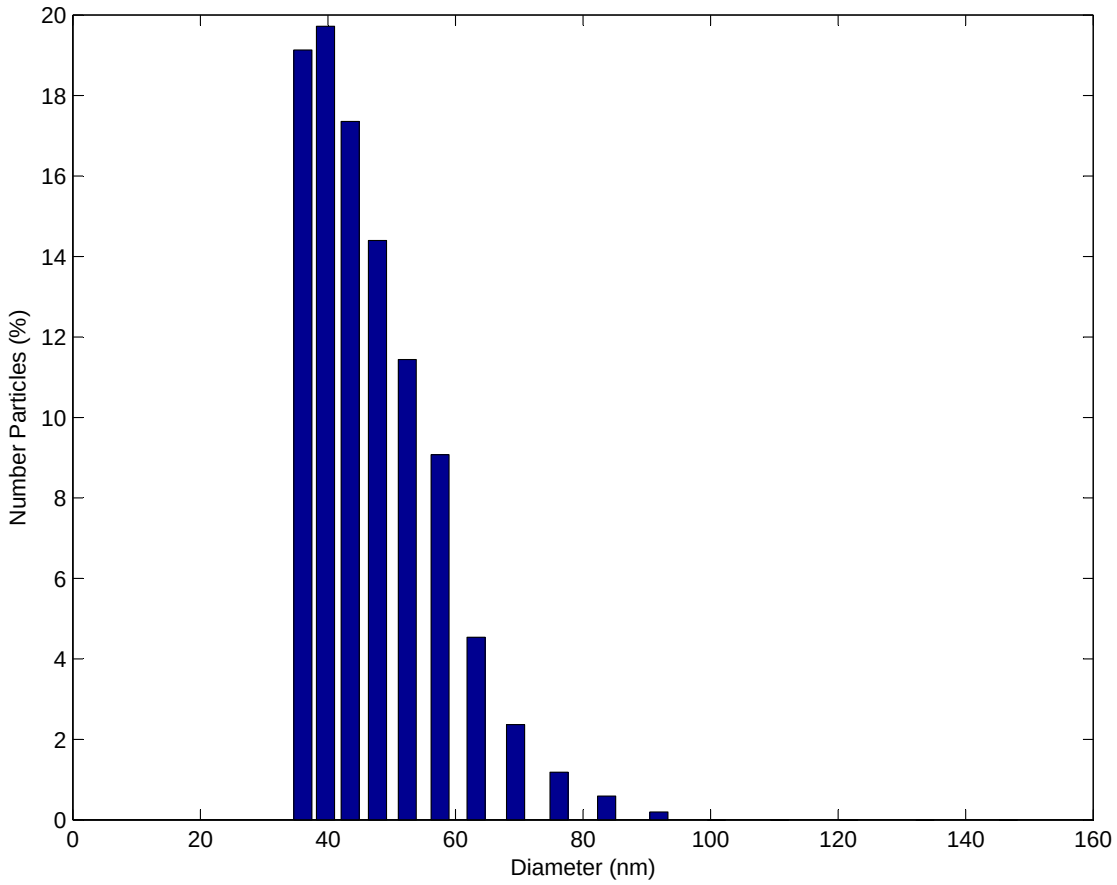

Figure 2-29: Particle size distribution for 0.004%wt alumina Nyacol nanofluid at one day

in order to certify the results because of the potential for error due to non-spherical particles and polydispersity in the system.

ICP and TGA are selected for the determination of nanofluid concentration. ICP is very effective in determining the exact elemental constituents of the system. It can be used to find contamination down to the ppb level of multiple elements with great ease. The major drawback of ICP is that it only determines elemental makeup of the system and not the molecular/chemical makeup. Therefore some calculation must be done in order to determine weight loading of nanoparticles. For this reason TGA is a quick and easy method of determining particulate loading of a system. The "cooking off" of constituents allows one to see surfactant weight loading, as well as, the particle loading. Therefore a combination of the two techniques is recommended for nanofluid characterization.

Alumina in water nanofluid is selected as the primary candidate for further experimentation, Nyacol fluid in particular. The Nyacol zirconia in water nanofluid is the secondary candidate. The Nyacol nanofluids are exceptionally stable, have thermal conductivity enhancement, and are inexpensive and readily available. The fluids will be sampled throughout the convective experimentation in order to reverify the properties at the specific loadings under investigation, specifically the size distribution and the loadings.

Chapter 3

Thermophysical properties

Thermophysical properties of nanofluids are quintessential to the understanding of their convective behavior. Experimental determination of their thermophysical properties is a major part of the overall scope of this project. Properties of interest are the density, heat capacity, thermal conductivity, and viscosity. The viscosity and thermal conductivity cannot be predicted a priori; the heat capacity and density are easily found from weighted averaging as shown in this chapter. This chapter will cover the experimental techniques for measuring the viscosity and thermal conductivity for nanoparticle colloids and the results of these measurements.

3.1 Description of the transient hot-wire method

The transient hot-wire (THW) technique is the most used method to measure the thermal conductivity of fluids [58, 59, 60, 61, 62, 63]. This is probably due to its relative simplicity and to the possibility, theoretically, of eliminating convective contributions to the heat transfer from the measurements. This method is based on applying a constant current to a thin wire, usually made of platinum or tantalum with a diameter of around 25 μm or less, and measuring the time evolution of its electrical resistance due to the temperature increase.

The hot-wire is at the same time the heater and the probe (knowing the resistance-temperature relation). In electrical conducting liquids the wire is also coated with a

thin insulation layer, e.g. telfon, to prevent stray current losses. One of the advantages of this technique is that, within certain approximations, there's a simple analytical expression between the temperature rise of the wire and the thermal conductivity of the medium. In fact the basic solution of the Fourier equation in case of

- infinite wire with infinite thermal conductivity and specific heat
- constant power per unit length (q')
- infinite incompressible medium with constant thermal conductivity (λ) and diffusivity (κ)

is

$$\Delta T = \frac{q'}{4\pi\lambda} E_1\left(\frac{a^2}{4\kappa t}\right) \tag{3.1}$$

where E_1 is an exponential integral $E_1(x) = -\gamma - \ln(x) + x + o(x^2)$ with $\gamma = 0.577$ and a is the wire radius. For

$$t \gg \frac{a^2}{4\chi} \quad (\sim ms) \tag{3.2}$$

we have

$$\Delta T \simeq \frac{q'}{4\pi\lambda}\left[\ln(t) + \ln\left(\frac{4\kappa}{a^2 C}\right)\right] \tag{3.3}$$

where $C = \exp(\gamma) = 1.781$.

The THW technique can be used to measure simultaneously both thermal conductivity and thermal diffusivity. However the uncertainty of the thermal diffusivity is about an order of magnitude higher than that of the thermal conductivity.

3.1.1 Corrections due to the finite thermal conductivity and heat capacity of the wire

If one considers the thermal conductivity λ_w and heat capacity $(\rho c_p)_w$ of the wire, the analytic solution is then [58]:

$$\Delta T \simeq \frac{q'}{4\pi\lambda}\left\{\left[1 - \frac{(\rho c_p)_w - (\rho c_p)}{2\lambda t}\,a\right]\ln\left(\frac{4\kappa t}{a^2 C}\right) + \frac{a^2}{2\kappa t} - \frac{a^2}{4\kappa_w t} + \frac{\lambda}{2\lambda_w}\right\} \tag{3.4}$$

where κ_w is the thermal diffusivity of the wire. Due to the high value of thermal conductivity and the small size of the wire, all these corrections become negligible after few tens of ms.

3.1.2 Corrections due to the finite boundary

For sufficiently long times the heat flux at the boundary of the cell is no longer negligible as during the initial phase and this must modify the temperature history. This is a very complex problem from the theoretical point of view and the only analytical expression that can be used is in the limit of the steady-state [58]:

$$\Delta T_\infty = \frac{q'}{2\pi\lambda}\ln(b/a) \tag{3.5}$$

where b is the radius of the cell. Compared to the other approximations, in this case the effect of the finite boundary is negligible for a sufficient short time given by:

$$t \ll \frac{b^2 C}{4\kappa} \quad (\sim ms) \tag{3.6}$$

which is around $70s$ for a cell with a radius of $5mm$. Anyway, to better understand the effect of a finite boundary on the measurements in the transient hot-wire one necessarily needs to use numerical simulations. A computational approach is above all fundamental to verify the effect of natural convection, which is unavoidable due to the horizontal density gradients, on the heat transfer in simple fluids. Finally other corrections to be considered are:

- the effect of axial conduction: this should be negligible for a sufficiently long wire ($\sim cm$);
- the applied power $q' = I^2 R/L$, where the input current I and the length L of

the wire are constant but the resistance R depends on temperature, is in turn a function of time: however for small temperature increments (few $°C$) it can be considered as nearly constant;

- if the fluid is a gas at low density, corrections due to Knudsen effects (when the mean free path becomes of the same order of magnitude as the wire diameter) must be considered;

- in the case of absorbent liquids also the influence of radiative heat transfer is not negligible.

3.2 Experimental Setup

The experimental setup is essentially made from a fine wire placed in a cell as shown in Figure 3-1. Two different kinds of wire are typically used: Tantalum wire ($\rho = 16.69\, g/cm^3$, $\kappa = 57.5\, W/m - K$, $c_p = 0.14\, J/g - K$), with a diameter of $25\mu m$ and without external insulation and Platinum/Isonel-coated wire ($\rho = 21.45\, g/cm^3$, $\kappa = 71.6\, W/m - K$, $c_p = 0.1325\, J/g - K$) with a bare diameter of $25\mu m$ ($28\mu m$ with the insulating coating). The tantalum wire can be oxidized in order to prevent stray currents, however this proved very difficult to maintain and was not as rugged as the teflon coated platinum wire. The length of the wire used is variable between 25 and $40mm$. The supporting leads are two tantalum rods to keep the wire straight and to connect it to the electrical system; these rods are also electrically insulated. The electrical system is composed by a current source (*Keithley - 6221*) and a nanovoltmeter (*Keithley - 2182A*): using these instruments is a key-factor in the development of this setup, because the variations of resistance of the wire are usually really small ($< mV$) and so it is extremely important to have a voltage meter with a very high degree of sensitivity. The vessel is made of stainless steel with an external diameter of around 2.5 cm and it is placed in a bigger container that can be used to circulate water from a thermostatic bath in order to control the temperature at which the experiments are performed.

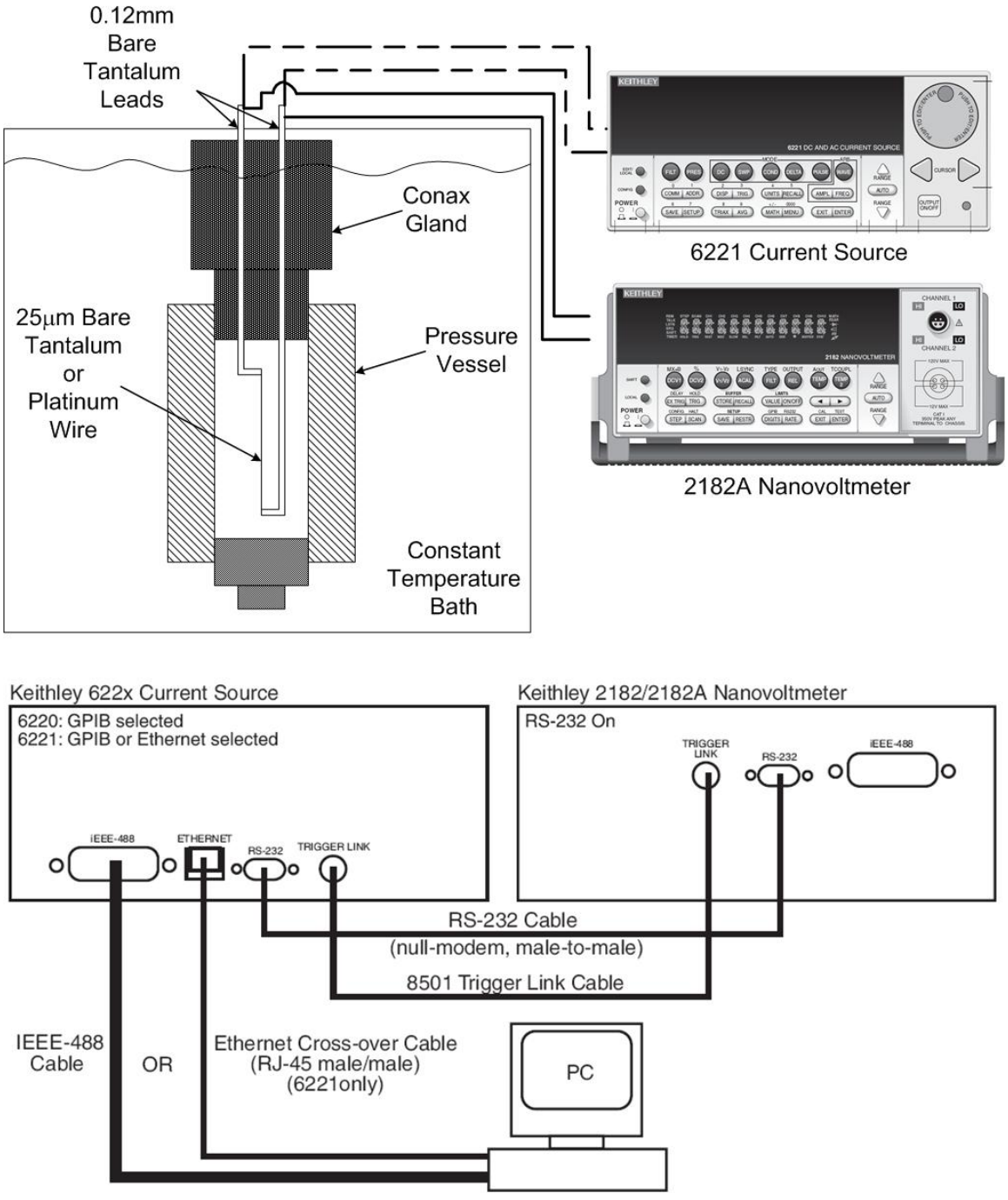

Figure 3-1: Schematic of transient hot-wire test setup.

3.2.1 The acquisition system

The current source and the voltmeter provide the possibility to use a remote control via a *GPIB* port utilizing a *Matlab* code to interface the instruments with a PC. The *Matlab* code routines can be found in Appendix B. One peculiar parameter to set is the acquisition rate, because, as found from the numerical simulations, it is important to have very fast measurements (around few seconds) to prevent the onset of convection. The range of acquisition rates for these instruments should go from 0.01 to 60 $NPLC$, where NPLC means "Number of Power Line Cycles" and 1 $NPLC \simeq 16.7\ ms$. However it is actually found out (figure 3-2) that, turning off the analog and digital filter, there is no difference in terms of number of points per seconds between $NPLC = 0.01$, 0.1 or 1; but also in the first case the measurements are too noisy while in the latter it seemed that the rate is too slow to correctly follow the time evolution of the signal. So in the measurements $NPLC = 0.1$ is used, which corresponds to an acquisition rate of about 17 ms.

Each measurement takes around $20s$, in this partition. In the first $5s$ the system acquires the voltage signal at a very low input current (usually $1mA$) in order to measure the resistance of the wire before the heating (R_0): in this way, using the resistance-temperature relation, the temperature of the sample is known and compared to the thermostatic bath. In the last $15s$ the input current switches to higher values (in the range of $50 - 100mA$) and the wire starts heating; at the end the current source is turned off and the collected data are transferred to the software. So the *modus operandi* is: performing a series of runs and taking the average for different input currents (from 50 to $100mA$).

3.2.2 Calibration measurements and comparison with the simulations

Each wire used in the measurements is calibrated as reported in Figure 3-3, and they are verified for the linear dependence of the resistance with temperature, through a coefficient of 0.00367 Ω/K which is very close to the tabulated value for platinum

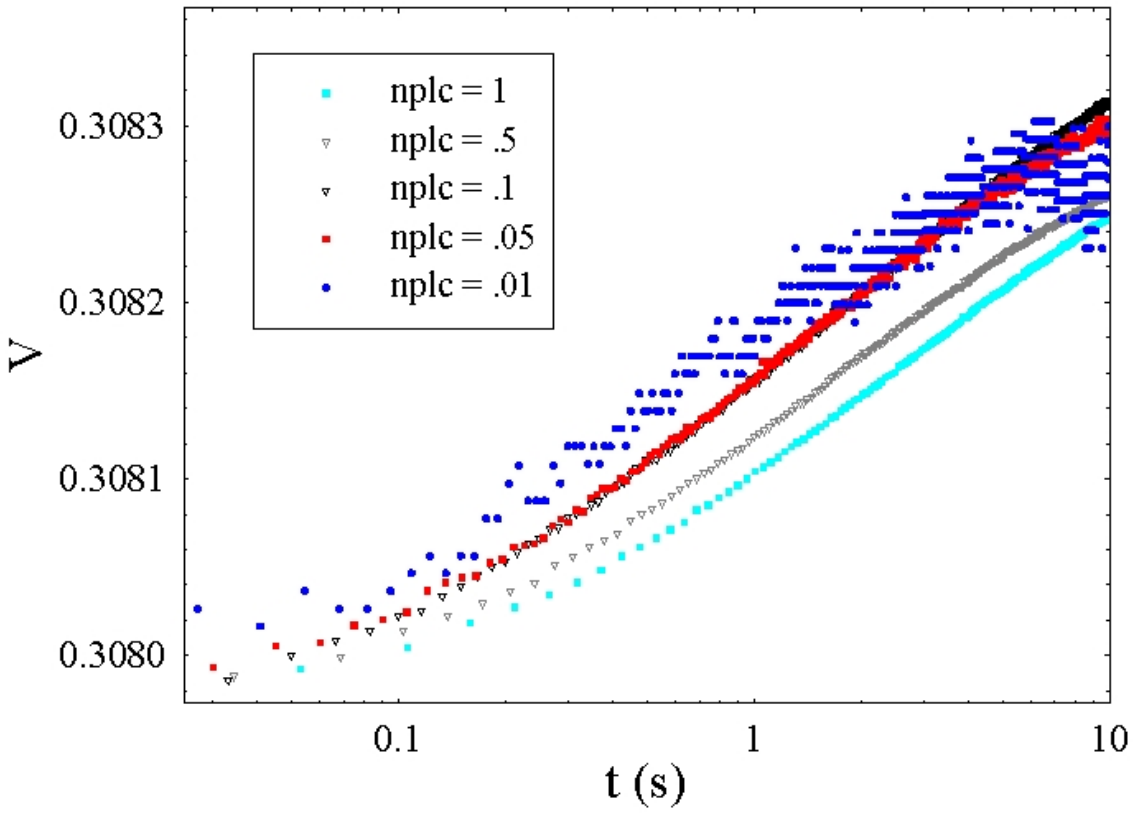

Figure 3-2: Effect of the acquisition rate on the measurements.

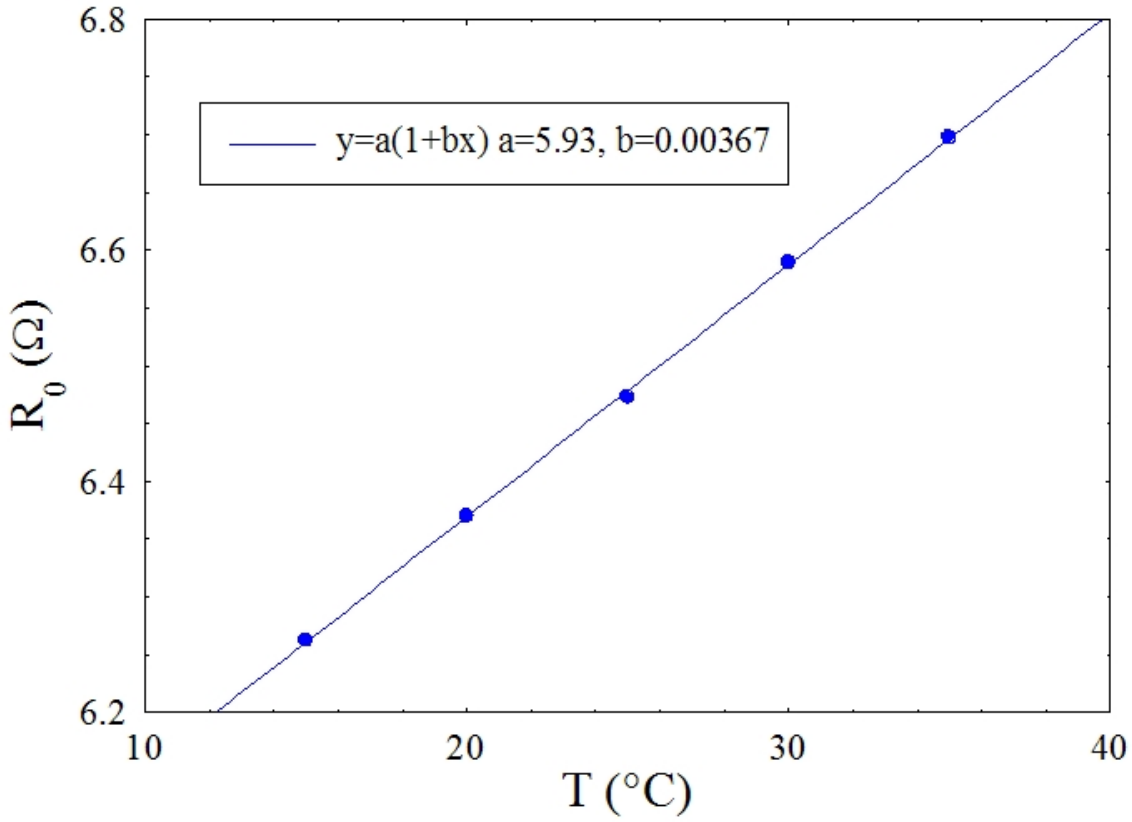

Figure 3-3: Resistance-temperature relation for the platinum wire.

($0.0039\ \Omega/K$). In Figure 3-4 measurements of thermal conductivity of water at $25°C$ are plotted. First of all it is noticed that the experimental data are linear (in a log scale) almost along the whole measurement time, as expected from the numerical simulations, see Appendix A. However the curves at different powers don't overlap, even if the slope is roughly the same. It is found that this off-set is related to the time immediately after activation of the current source. Considering the resistance increment (and so the temperature increment), with respect to the first point, all the curves do in fact overlap as shown in the inset.

Anyway in both cases the thermal conductivity from fitting the logarithmic trend is almost the same. This value (considering also the correction factor for a finite-length wire obtained from simulations) is around 15% higher than the real one for water. This value is used as a calibrating factor for the length of the wire (a correction of 15% for a $25mm$-long wire gives $28.75mm$, which is not much larger than the uncertainty

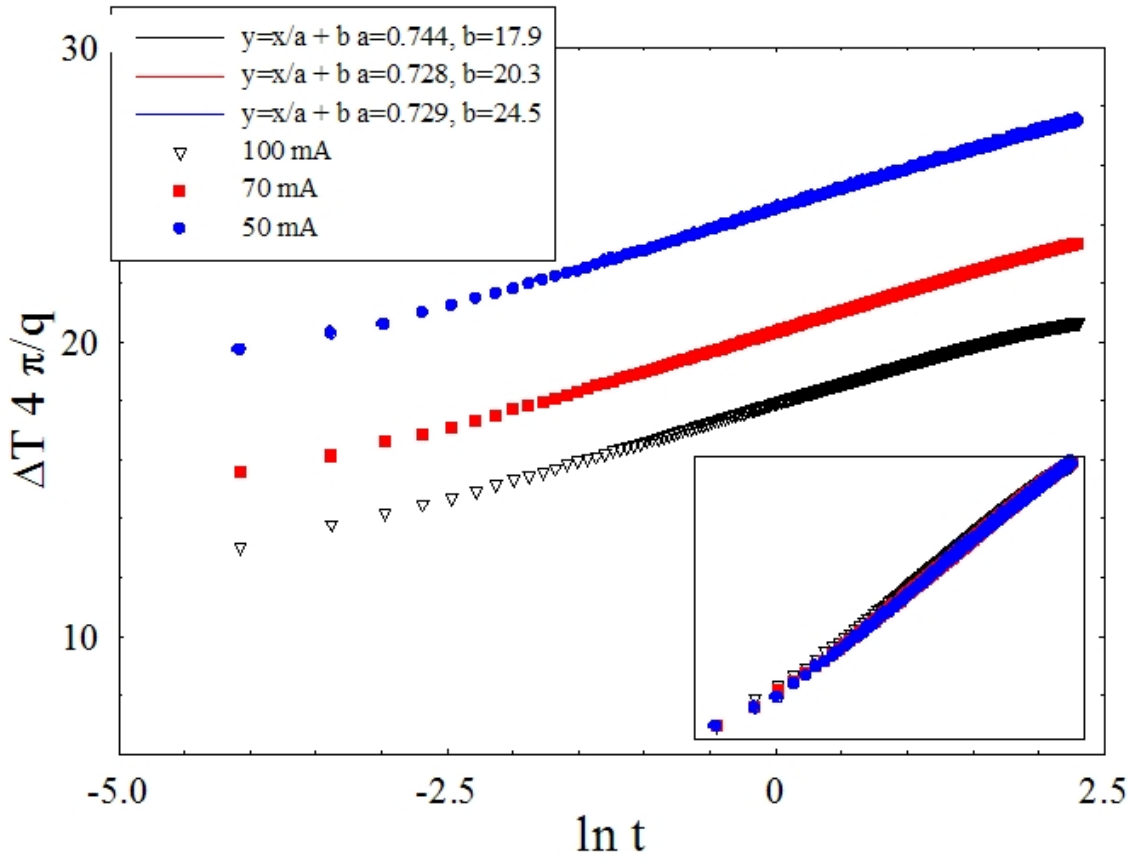

Figure 3-4: Measurements of thermal conductivity of water at different input currents.

of the Vernier calipers). The problem of the off-set should be solved if one were to also measure the thermal diffusivity of the fluid (given by the intercept of the linear-log fit); anyway, as said before, the uncertainty for thermal diffusivity in the THW is an order of magnitude higher than for conductivity and usually it is not considered.

In Figure 3-5 the temperature dependence of the experimental results for the thermal conductivity of water is displayed and one can notice a very good agreement with the data available in literature. Error bars are not due to the uncertainty, but the actual variation in experimental measurements.

Another important feature is the excellent agreement between the experimental data and numerical results, see Appendix A, for the effect of convection in this method, see Figure 3-6. In both cases at $25°C$, the trend is slightly affected by the buoyancy, at $50°C$ this effect is much more evident and the simulation correctly predicts the onset of convection. As a further verification of the reliability

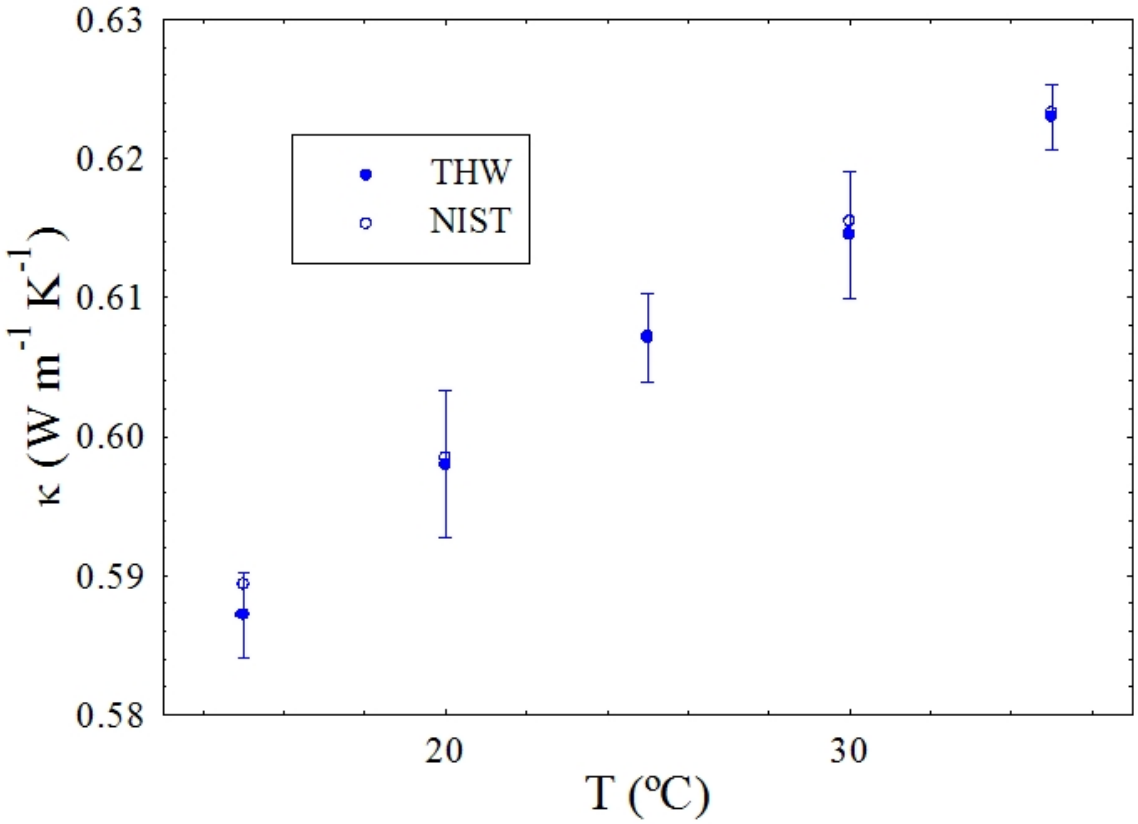

Figure 3-5: Measurements of thermal conductivity of water at different temperatures, compared to the tabulated values (from NIST).

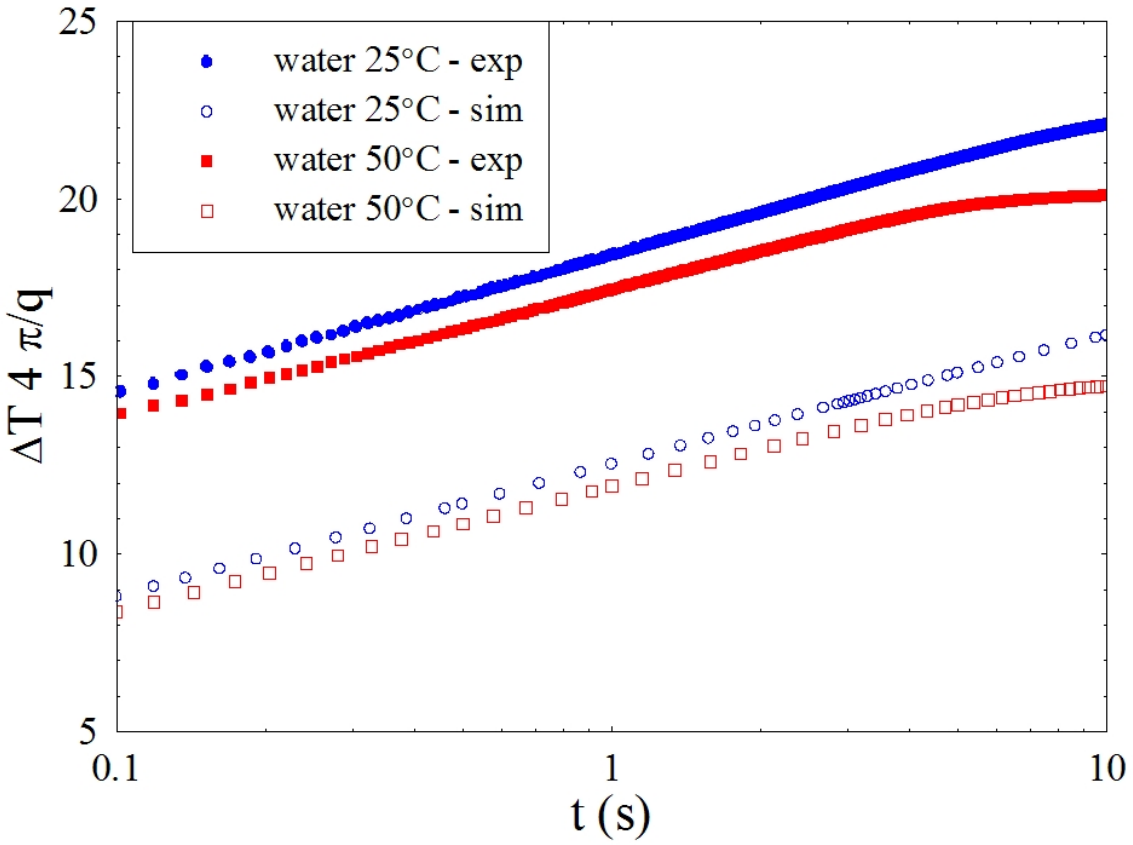

Figure 3-6: Comparison between the measurements and numerical simulations for water at $25°C$ and $50°C$.

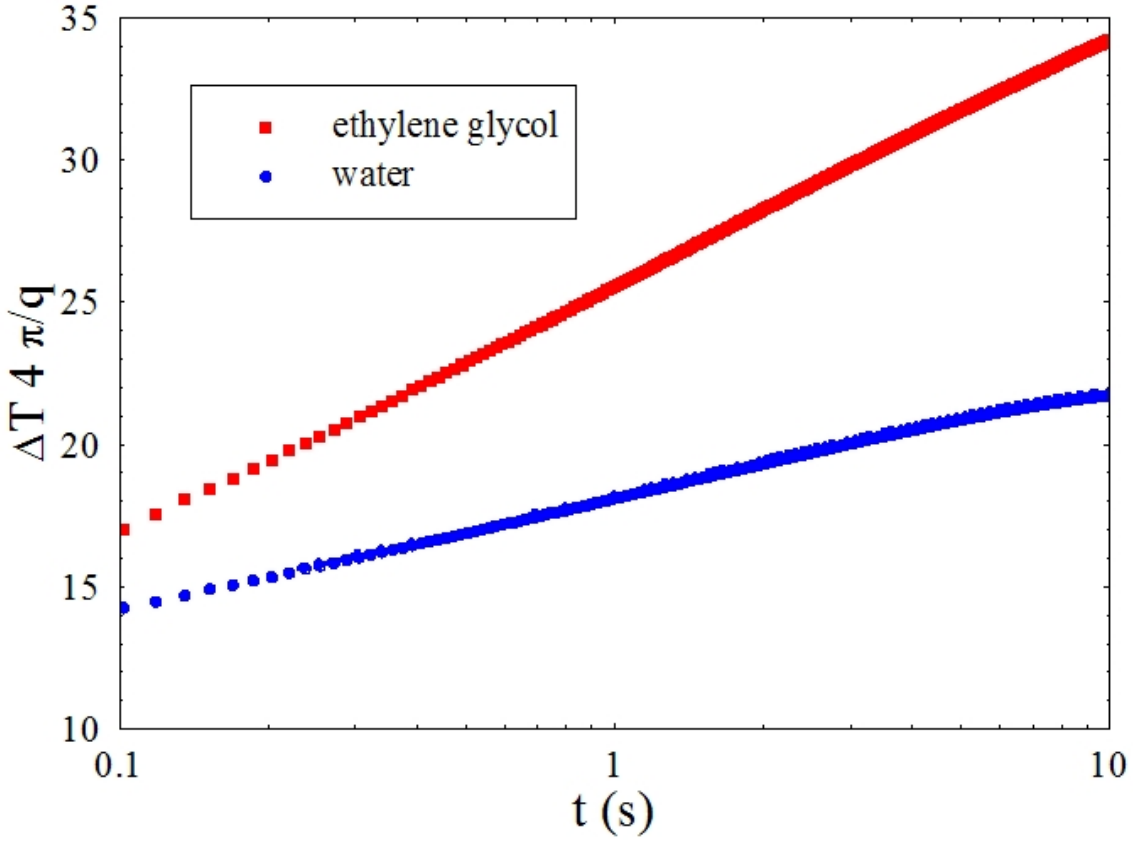

Figure 3-7: Comparison between the measurements of thermal conductivity of water and ethylene glycol at room temperature.

of this setup the thermal conductivity of ethylene glycol is measured, Figure 3-7. The value obtained, 0.265 $Wm^{-1}K^{-1}$, is very close to that reported in literature (0.257 $Wm^{-1}K^{-1}$).

3.2.3 Conclusions for liquid thermal conductivity measurement

It is concluded that this simplified transient hot-wire is effective for the measurement of thermal conductivity in liquids. The computational modeling described in the appendix gives insight into the potential for convective and geometrical effects on the measurement system. The simplification of the system through removal of the Wheatstone bridge and shrinking of the wire's axial dimensions allows for ease in setup. Wheatstone bridges were typically used to measure the wire resistance, however the Kiethley instrumentation allows for direct measurement of the resistance. The smaller dimensions of the wire are beneficial in the reduction of sample size which is of importance to the desired future application of this method.

3.3 Binary System Thermal Conductivity

It is stated in [62] that for the case of mixtures further phenomenon can occur due to the imposition of thermal gradients in the system. These phenomenon, most commonly thermal diffusion or the Soret effect, can potentially cause additional modes of energy transfer due to the non-zero thermal-diffusive flux of mass which arises in the transient method. However, the thermal conductivity is defined using Fourier's law for the steady state situation. Thus, the measured thermal conductivity of the binary system during transient heating is not strictly the same as that which is defined from Forier's law.

3.3.1 Non-reacting systems

The general conservation equations for the mass and energy of a non-reacting binary system can be found in [64] as follows:

$$\mathbf{J_{q'}} = -L_{qq}\frac{\nabla T}{T^2} - L_{q1}\frac{\mu_{11}^c}{c_2 T}\ \nabla c_1, \tag{3.7}$$

$$\mathbf{J_1} = -L_{1q}\frac{\nabla T}{T^2} - L_{11}\frac{\mu_{11}^c}{c_2 T}\nabla c_1, \tag{3.8}$$

$$\mu_{11}^c = (\partial \mu_1/\partial c_1)_{P,T}, \tag{3.9}$$

where ρ_1, c_1, and μ_1 are respectively the density, mass fraction, and chemical potential of constituent 1, $\rho = \rho_1 + \rho_2$ is the mixture density and through the Onsager relation

$$L_{1q} = L_{q1}. \tag{3.10}$$

The coefficient L_{1q} is characteristic for the thermal diffusion or flow of matter caused by a temperature gradient. This is commonly known as the Soret effect in liquids. Likewise, the reciprocal, i.e. flow of heat caused by a mass gradient, is known as the Dufour effect and is characterized by the L_{q1} coefficient. In order to satisfy the entropy source strength as positive definite then

$$L_{qq} \geq 0, \quad L_{11} \geq 0, \quad L_{qq}L_{11} - L_{1q}^2 \geq 0. \tag{3.11}$$

By defining

$$\lambda = \frac{L_{qq}}{T^2} \qquad \text{(heat conductivity)}, \tag{3.12}$$

$$D'' = \frac{L_{q1}}{\rho c_1 c_2 T^2} \qquad \text{(Dufour coefficient)}, \tag{3.13}$$

$$D' = \frac{L_{1q}}{\rho c_1 c_2 T^2} \qquad \text{(thermal diffusion coeff.)}, \tag{3.14}$$

$$D = \frac{L_{11}\mu_{11}^c}{\rho c_2 T^2} \qquad \text{(diffusion coefficient)}, \tag{3.15}$$

the cross correlation terms can be easily seen in the modified equations as:

$$\mathbf{J_{q'}} = -\lambda \nabla T - \rho_1 \mu_{11}^c T D'' \nabla c_1, \tag{3.16}$$

$$\mathbf{J_1} = -\rho c_1 c_2 D' \nabla T - \rho D \nabla c_1. \tag{3.17}$$

and the Onsager relation implies that

$$D' = D'' \tag{3.18}$$

and the inequality of (3.11) changes to

$$\lambda \geq 0, \quad D \geq 0, \quad (D')^2 \leq \frac{\lambda D}{T \rho c_1^2 c_2 \mu_{11}^c}. \tag{3.19}$$

Therefore the apparent thermal conductivity of the system is

$$\lambda_\infty = \lambda + \rho_1 \mu_{11}^c T D'' \frac{\nabla c}{\nabla T}. \tag{3.20}$$

In Eq. 3.20 shows that in principle the measured (apparent) thermal conductivity can be different from the conductivity purely due to heat conduction.

3.3.2 Reacting systems

The nature of colloidal systems makes them somewhat different than binary mixtures of non-reacting components. Colloids have the potential for not only thermal/mass diffusion, but also for chemical reaction due to the non-uniform temperature distribution. Outside the presence of thermal or mass gradients, colloidal particle surfaces

are in chemical equilibrium with the base fluid. Alteration of the local temperature or concentration can alter this chemical equilibrium and hence affect the apparent thermal conductivity. The modification of the thermal diffusion due to these effects is developed in detail in ([64]) and is similar in nature to the non-reacting situation. It is found that the chemical reaction can increase the steady state thermal conductivity over that of the intrinsic value as

$$\lambda_\infty \simeq \lambda + \frac{\rho_2 D(\Delta h)^2}{T\mu_{11}^c} \tag{3.21}$$

where (Δh) is the chemical reaction heat at constant temperature and pressure. Chemical equilibrium requires that $\mu_{11}^c \geq 0$ and thus the increase in thermal conductivity.

It is not readily apparent whether or not this effect is significant and is strictly dependent on the chemical constituents of the system under investigation. Due to the poor understanding of reaction energies at the surfaces in colloidal systems, numerical estimates of this effect are not pursued here. Furthermore they are not considered in the modeling or in the experimental effort at hand. It is hoped that further investigation could shed more light on this interesting coupling phenomenon.

3.4 Coupled effects on hot-wire thermal conductivity measurement

One study [65] investigated the effects of thermal diffusion in binary gas mixtures on the apparent thermal conductivity measured by the hot-wire technique. For the case of a stationary binary gas mixture the transient equations were derived as

$$\rho C_p \frac{\partial T}{\partial t} = -\nabla \cdot \mathbf{J_{q'}} = \nabla \cdot \{\lambda \nabla T + \rho_1 \mu_{11}^c T D'' \nabla c_1\}, \tag{3.22}$$

$$\frac{\partial c_1}{\partial t} = -\nabla \cdot \mathbf{J_1}/\rho = \nabla \cdot c_1 c_2 D' \nabla T + \rho D \nabla c_1, \tag{3.23}$$

where

$$\mu_{11}^{c} = RT/[c_1(c_1M_2 + c_2M_1)] \tag{3.24}$$

for an ideal gas using R as the universal gas constant and M_i as the molar value of constituent i. For the case of gas mixtures it can be assumed that D is the same as the binary diffusion coefficient, D_{12}, obtained by kinetic theory.

(3.22) and (3.23) allow for two extreme values of the thermal conductivity to be found: λ_o the intrinsic thermal conductivity and λ_∞ the apparent steady state thermal conductivity. In the case of zero mass flux, i.e. steady state, it can be found that

$$\lambda_\infty = \lambda_0 - c_1c_2\rho_1\mu_{11}^{c}TD'^2/D. \tag{3.25}$$

Once again deriving the working equation, (3.3), using (3.22) and (3.23) it was found in [65] that the working equation becomes

$$\Delta T \simeq \frac{q'}{4\pi\lambda_\infty}\left[\ln(t) + \ln\left(\frac{4\kappa_m}{a^2C}\right)\right] \tag{3.26}$$

where κ_m is the effective thermal diffusivity of the mixture as described in [65].

It cannot be presumed a priori that the hot-wire measures the steady state value of the thermal conductivity, λ_∞. However, the zero mass flux condition at the wire surface does create the ability to measure the steady state value, because the mass would have to be passing through the surface of the wire to cause the thermal conductivity modification. Therefore, because of the boundary condition, it is concluded that the hot-wire will always measure the correct steady state value of the conductivity for a fluid mixture with consideration of thermal/mass diffusion. Non-reacting liquid mixtures, gas-liquid, or solid-fluid mixtures should follow suit, due to the similar nature of the systems.

However, the potential for the thermal/mass diffusion to create convective effects on the measurement technique has not been considered. The density gradients created by the diffusion of particles in the system can alter the threshold for the onset of

natural convection. Natural convection can strongly distort the measured thermal conductivity found by the hot-wire. Therefore convection effects are given great consideration in the computational modeling, shown in the Appendix. The convection effects are found to be minimal for the short time scale of the measurements and hence do not alter the measured value.

Finally, consideration of measurement of a reacting system with the hot-wire technique is forgone here due to the lack of understanding of the complex and numerous chemical reactions occurring at colloidal particle surfaces. There are no studies found in the literature about the chemical potential of nanoparticles in liquids. It is therefore hard to verify the order of magnitude of the thermal conductivity shift caused by Equations 3.21 and 3.25. Nevertheless, it could be a potential cause of unusual or erroneous thermal conductivity values measured in colloids. It is mentioned here due to the large number of recent works involving *anomalous* enhancement of thermal conductivity in colloids, i.e. nanofluids, see [16]. If there were anomalous behavior, chemical reactions might be the first logical place to look for explanation, rather than Brownian motion or micro convection.

3.5 Measurements of thermal conductivity in nanoparticle colloids

3.5.1 Aluminium oxide

Utilizing the experimental apparatus described above (see Figure 3-1), the thermal conductivity of a suspensions of aluminium oxide (also commonly referred to as *alumina*) particles (Nyacol Nano Technologies, Inc.) are measured at different volume fractions and external temperatures. The physical properties are the same as those used in the numerical simulations, see Appendix A. From SEM and TEM pictures (Figure 3-8 and Figure 2-11) a rough idea of the morphology of these particles is found and determined to be non-spherical.

In Figure 3-9 the measurements and the simulations for water and for a dispersion

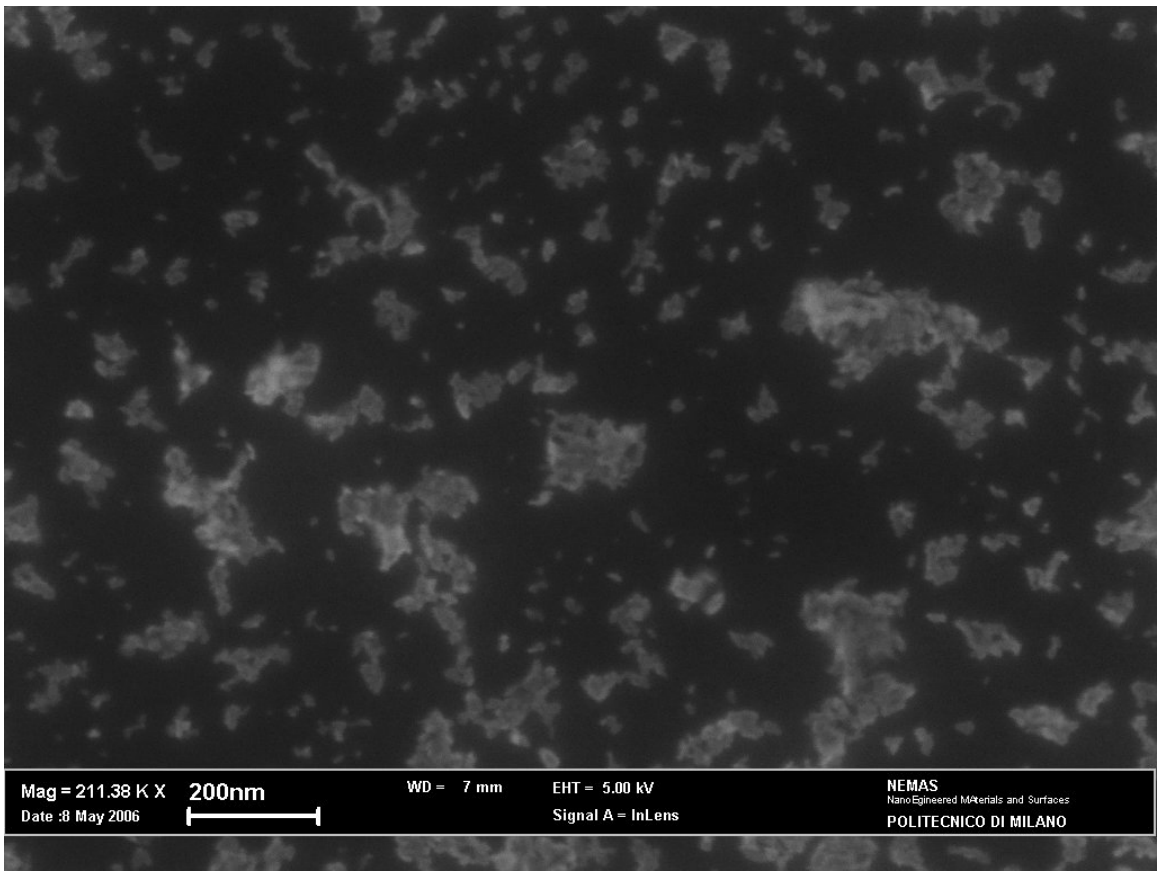

Figure 3-8: SEM picture of the alumina particles in the Nyacol nanofluid.

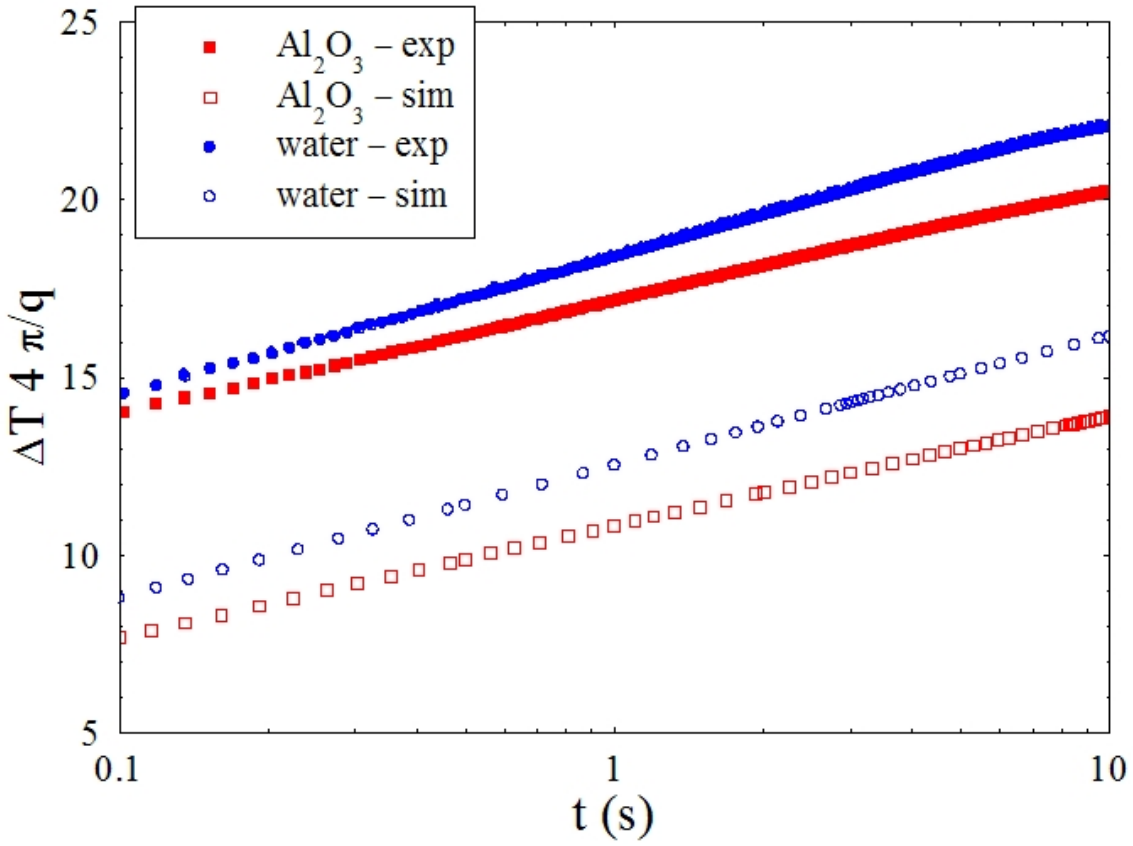

Figure 3-9: Measurements and simulations for water and a suspension of alumina ($5.14\%vol$) at $25°C$.

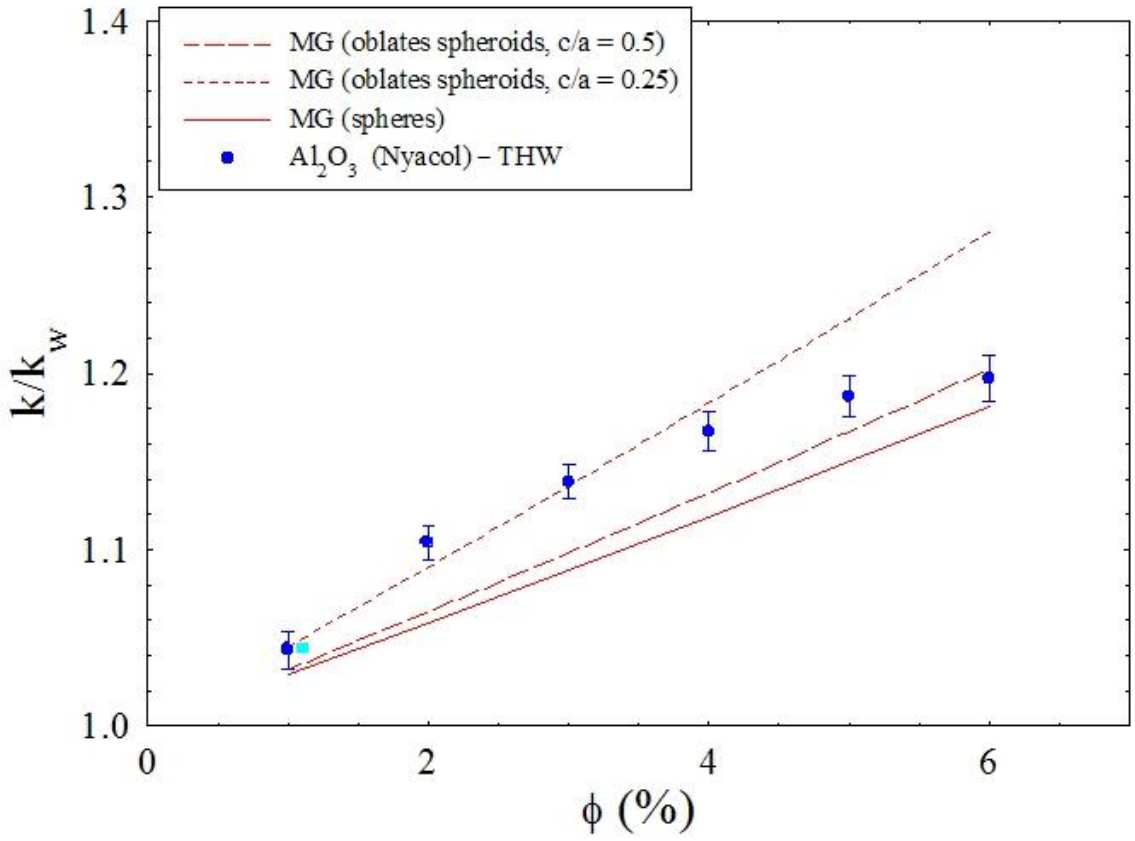

Figure 3-10: Dependence on the volume fraction for the thermal conductivity of alumina suspensions at $25°C$.

of alumina (at 20%wt) are compared and also in this case it's evident the agreement between experimental and numerical results. An investigation of the dependence of the conductivity on the volume fraction, from 1% to 6% at 25°C is shown in (figure 3-10). The experimental data are reported in comparison with an "effective medium theory" for heterogeneous media ([66]). According to this model, the thermal conductivity of a dispersion of randomly oriented and isotropic *spheroids*, which are ellipsoids having two axes of equal length (a,a,c), immersed into a matrix of different conductivity, is given by:

$$\frac{\lambda^*}{\lambda_1} = 1 + \frac{1}{\lambda_1}\frac{\alpha[\lambda]\phi}{1 + (\alpha - 1)\phi}$$

where $[\lambda] = \lambda_2 - \lambda_1$ (2 is the dispersed phase and 1 is the matrix) and

$$\alpha = \frac{\lambda_1}{3}\left(\frac{2}{\lambda_1 + [\lambda]M_\perp} + \frac{1}{\lambda_1 + [\lambda]M_\parallel}\right)$$

with

$$M_\parallel = \frac{1}{e^2}\left(1 - \frac{\sqrt{1-e^2}}{e}\arcsin e\right)$$

if $c < a$ (that means *oblate* spheroids, as disks) or

$$M_\parallel = \frac{1-e^2}{2e^3}\left(\ln\frac{1+e}{1-e} - 2e\right)$$

if $c > a$ (that means *prolate* spheroids, as fibers),

$$M_\perp = \frac{1 - M_\parallel}{2}$$

where $e = \sqrt{1-\xi^2}$ is the eccentricity and $\xi = c/a$ (if oblate) or $\xi = a/c$ (if prolate). In case of spheres:

$$M_\perp = M_\parallel = 1/3$$

and

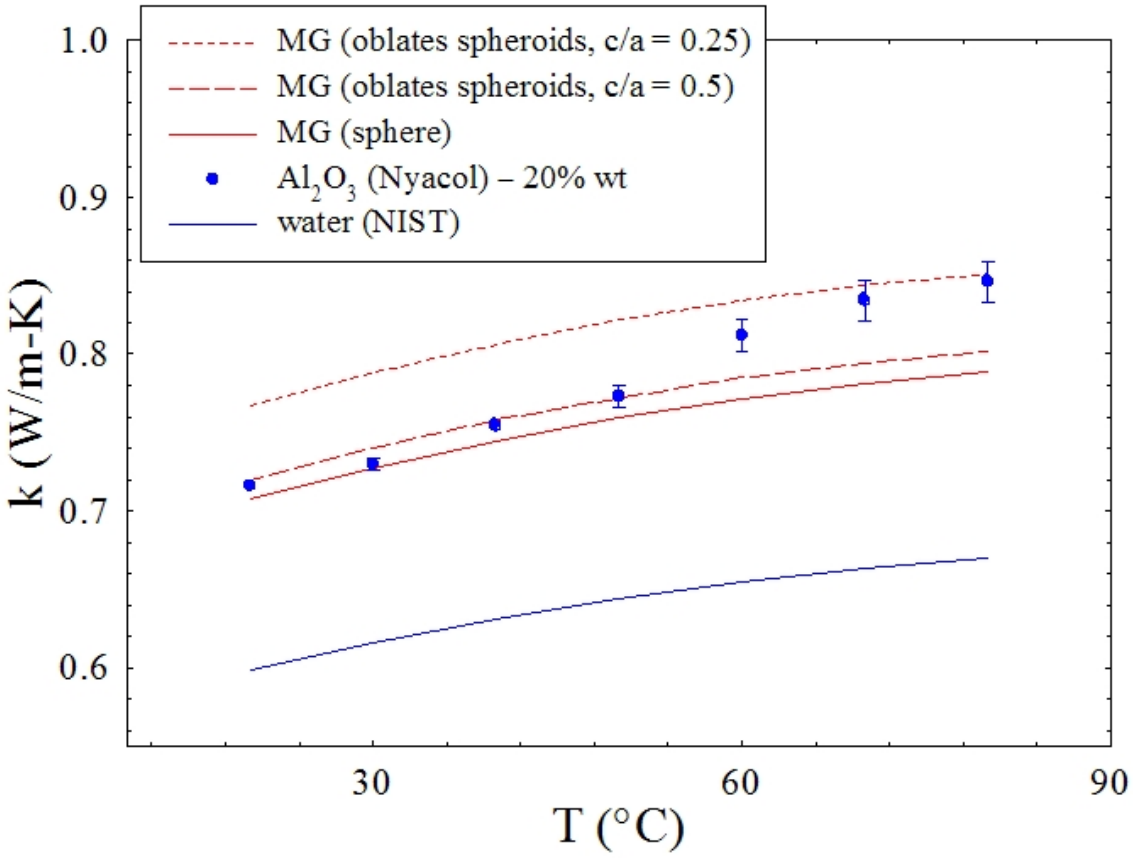

Figure 3-11: Dependence on temperature for the thermal conductivity of a 20%*wt* (5.1%*vol*) alumina suspension.

$$\frac{\lambda^*}{\lambda_1} = 1 + \frac{3(\lambda_2 - \lambda_1)\phi}{\lambda_2 + 2\lambda_1 - (\lambda_2 - \lambda_1)\phi}$$

which is the Maxwell-Garnett (MG) model.

It can be seen in Figure 3-10 that the measurements are in between the model for oblate spheroids with an axial ratio of 0.5 and 0.25: this is not, of course, an explanation of the experimental trend but rather a highlight that the particle shape is an important factor to be considered and should be well-known before comparing measurements with theoretical predictions. The same analysis can be applied also to the experimental data for the thermal conductivity of an alumina suspension as a function of temperature, see Figure 3-11. Moreover in this case, it is quite evident that this dependence is simply due to the behavior of water.

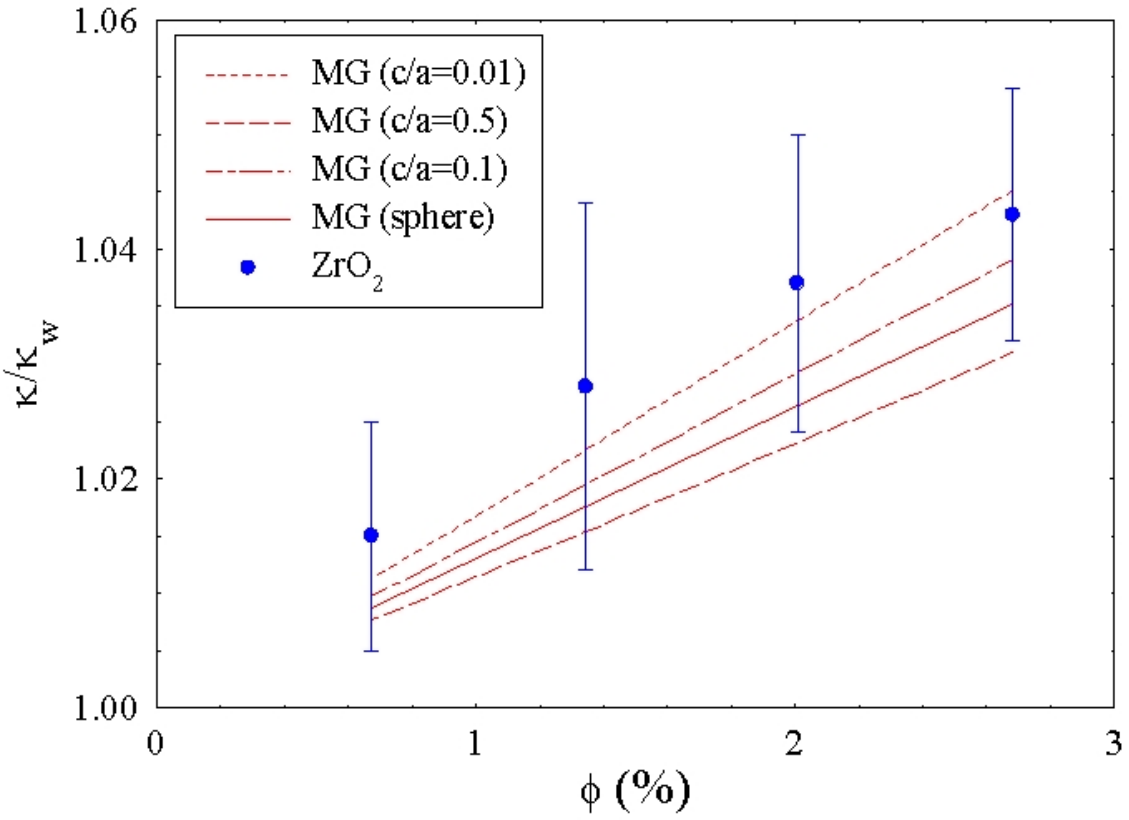

Figure 3-12: Dependence on the volume fraction for the thermal conductivity of zirconia suspensions at $25°C$.

3.5.2 Zirconium oxide

The dependence on the volume fraction and temperature for a dispersion of zirconium oxide (*zirconia*) particles (Nyacol Nano Technologies, Inc.) is investigated. The physical properties of zirconia are: $\rho_p = 5.89\ g\ cm^{-3}, c_p = 0.418\ J\ g^{-1}\ K^{-1}, \lambda_p = 2\ W\ m^{-1}\ K^{-1}$ and a diameter of about $50nm$ is given as the manufacturer's specification and confirmed by DLS as about $65to75nm$.

In Figure 3-12 it is shown that the dependence on the volume fraction is very close to the model. Due to a quite low value of thermal conductivity for zirconia, the shape factor is not as relevant as in the case of alumina suspensions. Furthermore the temperature dependence, shown in Figure 3-13, is similar to that of water.

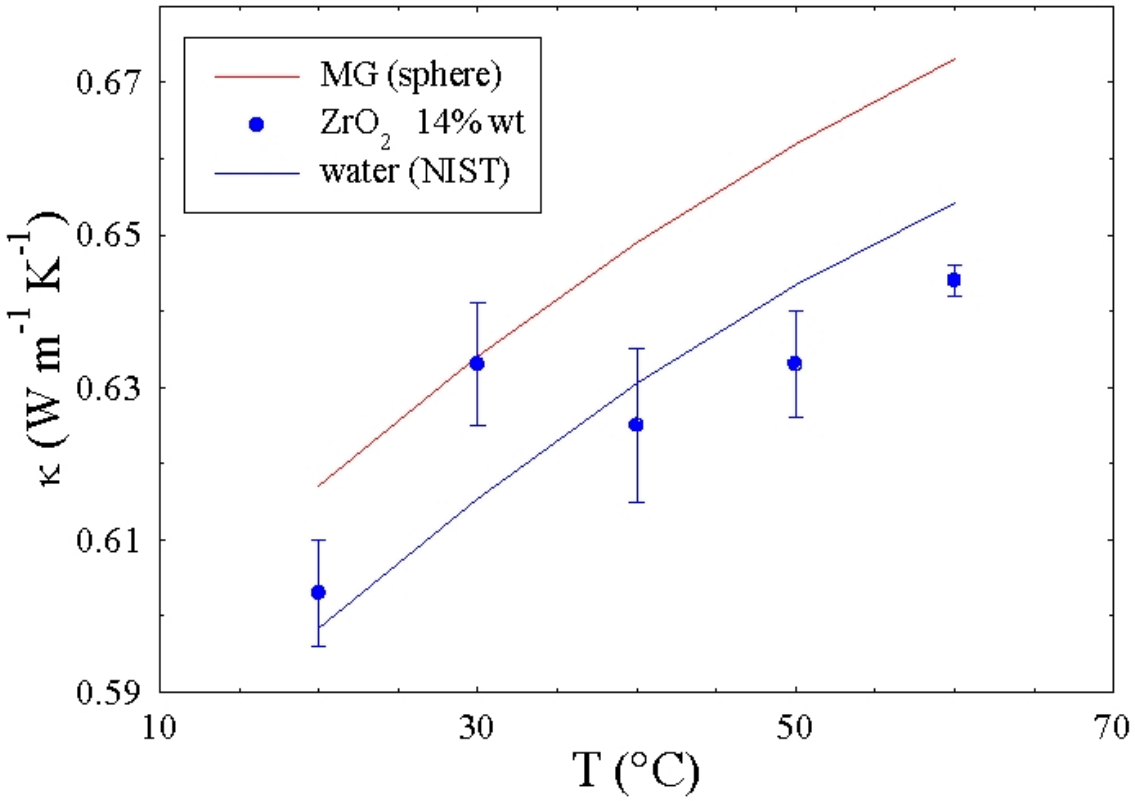

Figure 3-13: Dependence on temperature for the thermal conductivity of a 14%*wt* (2.4%*vol*) zirconia suspension.

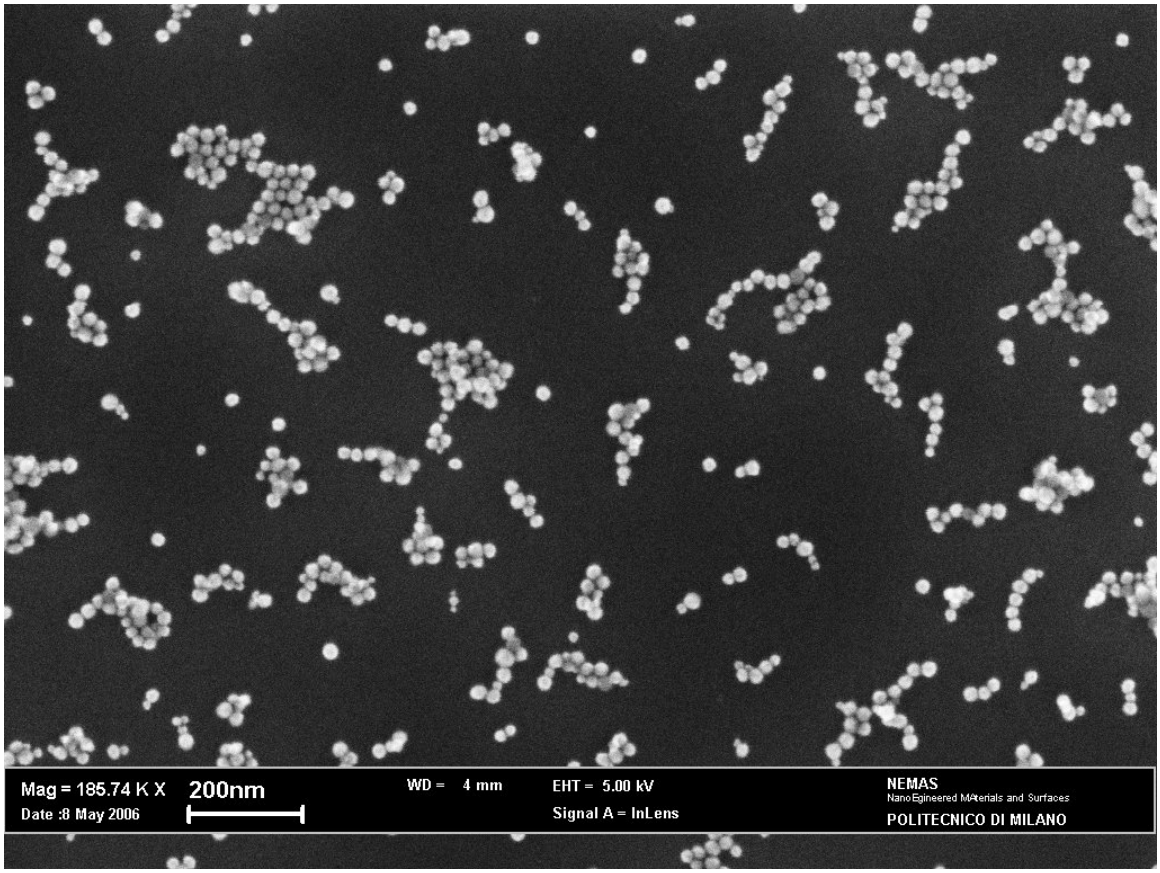

Figure 3-14: SEM picture of the Ludox particles.

3.5.3 Ludox

Ludox (Grace Davison) is a colloidal silica; the physical properties used to analyze the measurements are: $\rho_p = 2.2\ g\ cm^{-3}, c_p = 0.814\ J\ g^{-1}\ K^{-1}, \lambda_p = 1.4\ W\ m^{-1}\ K^{-1}$. These particles are found to be very spherical (see the SEM picture in Figure 3-14) with a diameter of about $16nm$ measured with Dynamic Light Scattering (DLS). It can be noticed in Figure 3-15 that the experimental data are in quite good agreement with the MG model for spheres.

3.5.4 Gold

A measurement of the thermal conductivity of a dispersion of gold particles prepared by the University of Florence is done. These particles are spherical and small (see the SEM picture in figure 3-16) with a diameter of about $5nm$ and a weight fraction

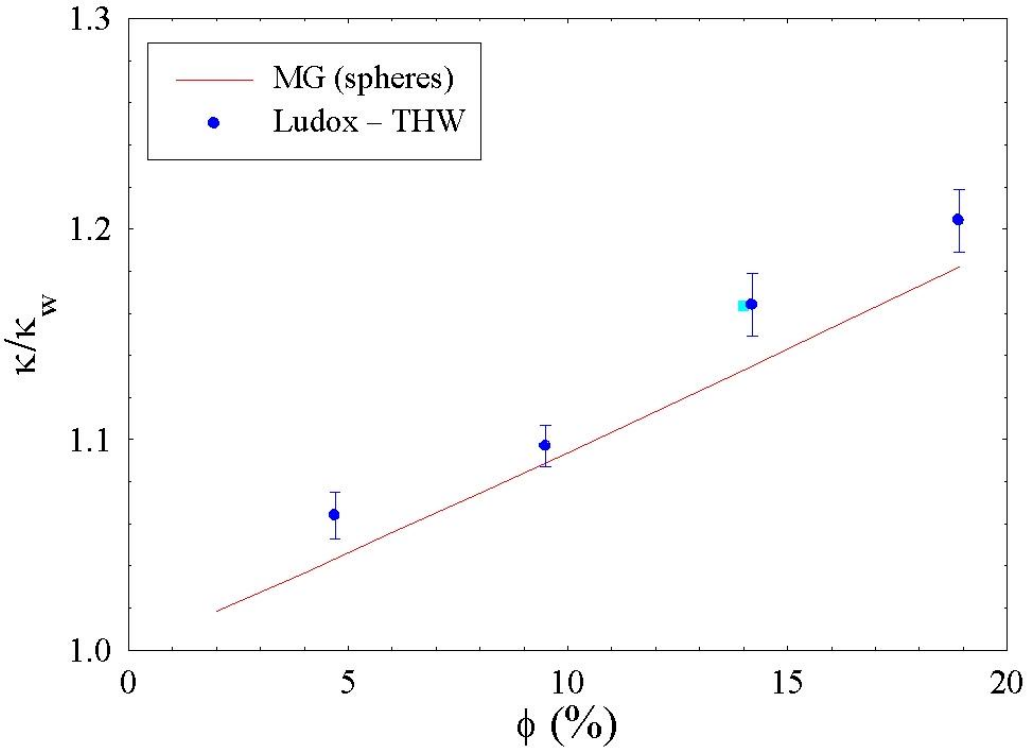

Figure 3-15: Dependence on the volume fraction for the thermal conductivity of ludox suspensions at $25°C$.

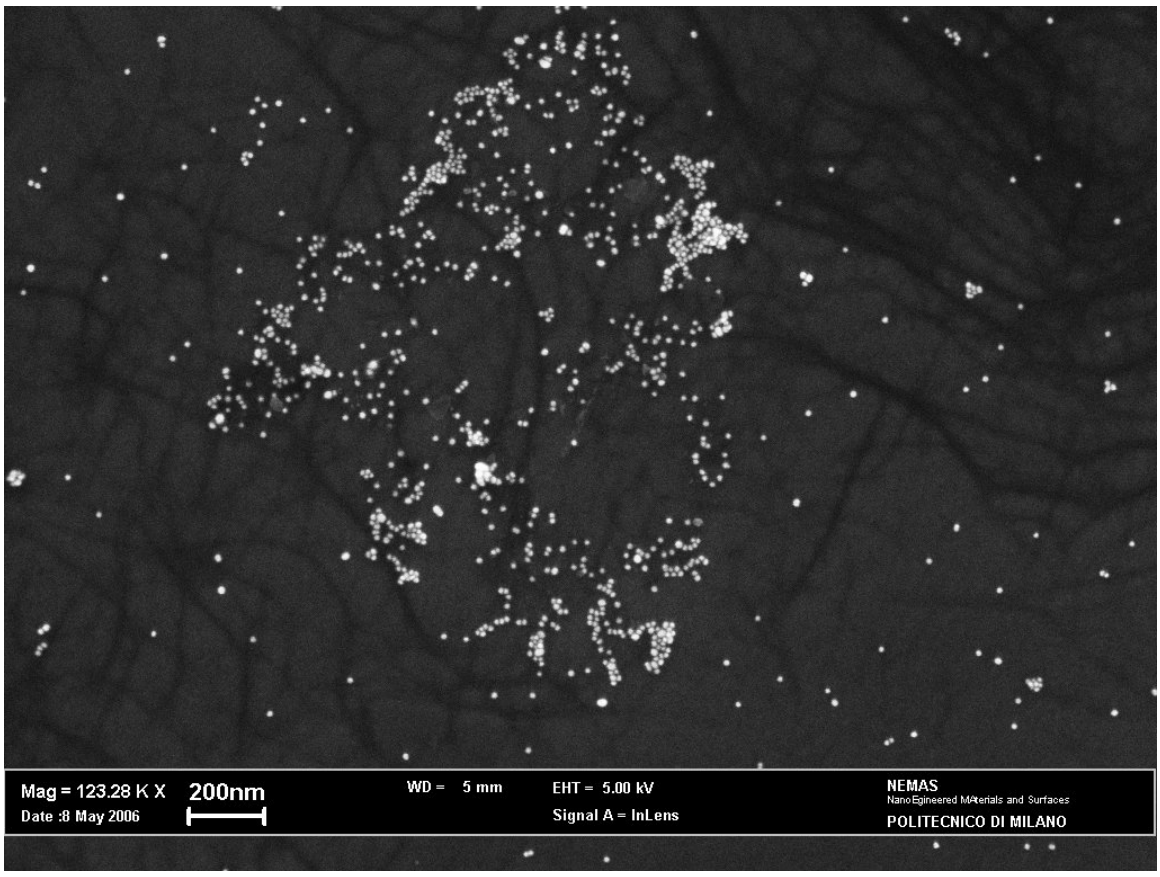

Figure 3-16: SEM picture of the gold particles.

around 0.01% (which means around $5 \cdot 10^{-6}$ in volume fraction). At this low loading, no difference in thermal conductivity could be seen between the suspension and the pure solvent. This is contrary to reports of gold at a similar concentration in [23] which were found to have an "anomalous" higher value.

3.5.5 Teflon

Finally, a measurement of the thermal conductivity is performed for a suspension of PFA particles (Solvay Solexis), that are fluorinated polymers as the PTFE which is generally known to the public by DuPont's brand name *Teflon*. An interesting feature of these particles is that they are really quite monodisperse and spherical (the radius measured by DLS is about $22nm$) and the thermal conductivity is lower than water ($0.195 W m^{-1} K^{-1}$). In figure 3-17 the thermal conductivity for this dispersion as a function of the volume fraction is plotted. The data are in fairly good agreement with the model for spheres.

3.6 Comparison of methodologies for thermal conductivity measurement

A collaboration between several groups has been made in order to verify the accuracy and validity of the transient hot wire technique to measure nanoparticle colloids. The short transient hot wire method (STHW) and the KD2 from above, two other hot wire methods of Lee [14](THW1) and Ma [67](THW2), the thermal lens method of Rusconi, et al. [68](TL), and the steady-state cut bar technique of Li and Peterson [69](CB) are all compared for the exact same fluid sample, water and Nyacol alumina in water at the maximum loading 5.14 vol% or 20 wt%. The results of this comparison are shown in Table 3.1. It is seen from the table that all the values are roughly the same. The steady state cut-bar (CB) is slightly lower, however the uncertainty is much higher in that experiment. The maximum value is 24% enhancement and the minimum is 12% with an average of 23%. Other fluids such as Nyacol zirconia, teflon,

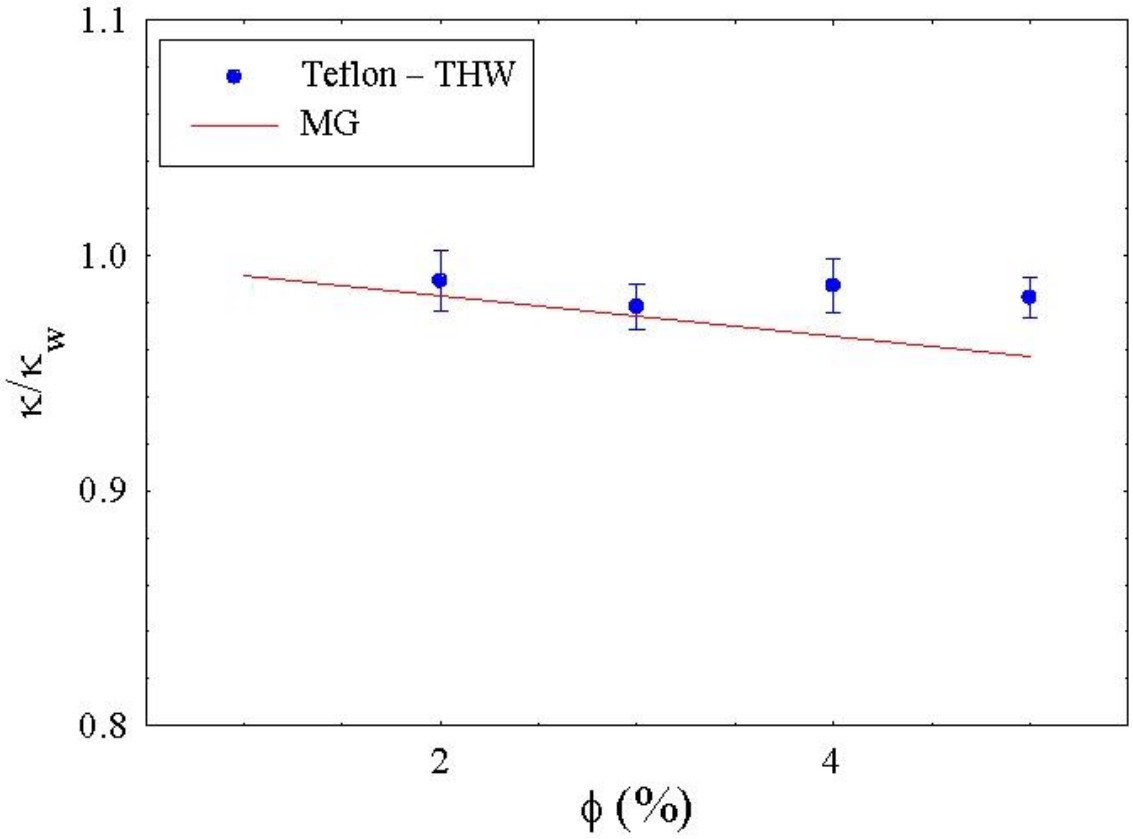

Figure 3-17: Dependence on the volume fraction for the thermal conductivity of teflon suspensions at $25°C$.

Table 3.1: Thermal Conductivity Measurement Technique Comparison

Method	Water	Alumina	Enhancement
KD2	0.58	0.68	17%
STHW	0.59	0.71	20%
THW1	0.58	0.72	24%
THW2	0.58	0.71	22%
TL	0.59	0.71	22%
CB	0.58	0.65	12%

Ludox silica and diamond in water were also compared with a similar outcome. It is thus concluded that the short transient hot wire is capable of measuring the thermal conductivity of nanoparticle colloids.

3.7 Conclusions for colloidal thermal conductivity

It is concluded that the simplified transient hot-wire apparatus is effective for the measurement of colloidal thermal conductivity. However depending on the system composition additional contributions to the heat transfer are possible with binary mixtures in general, including colloids. These should be considered in the modeling and measurement of colloidal thermal conductivity. The convective and thermal diffusion contributions are computationally simulated and verified to be of minimal consequence in the above measurements.

Five colloids have been measured and found to give alterations in thermal conductivity which correspond with the values predicted by effective medium theories. These fluids were compared with different setups and methodologies to ensure the validity. The short transient hot wire technique can allow for the investigation of many colloids and help resolve some of the open issues with regard to their thermal conductivity behavior.

3.8 Experimental viscosity measurement

Various methods can be used for the experimental determination of viscosity. Concentric cylinders or cone and plate methods are very similar to the parallel plate visualization which can be found in the textbooks describing the meaning of shear viscosity. Falling sphere viscometry uses Stokes flow to determine the viscosity. The method which is chosen for this work is the capillary viscometer and more specifically the Cannon-Fenske Opaque (Reverse-Flow) Viscometer as shown in Figure 3-18. Opaque or reverse flow glass capillary viscometers are used when the meniscus of the fluid is not able to be seen due to the opacity of the fluid. It must therefore be run

backwards. The capillary viscometer follows Ostwald flow where

$$\nu = \frac{\pi r^4 g h / 8l}{dv/dt} \tag{3.27}$$

r is the capillary radius, h is the free surface elevation difference, l is the length of the capillary section, g is the acceleration of gravity, and dv/dt is the velocity of the fluid. Each glass viscometer size has a coefficient of calibration. The coefficient is multiplied by the time it takes for the fluid sample to pass between the different marks on the viscometer. This value determines the kinematic viscosity, which can be converted to the dynamic viscosity by multiplying with the density of the fluid.

3.8.1 Viscosity of suspensions

Hydrodynamic interactions and particle-particle interaction of the particles within a suspension can cause the viscosity to be different than that of the base fluid. Quite often the particles lead to volume exclusion effects which gives increased viscous dissipation even at low concentration. For spherical particles at low volume fractions Einstein developed the equation

$$\eta/\eta_s = 1 + 2.5\phi \tag{3.28}$$

where η_s is the base fluid viscosity and ϕ is the volume fraction. This equation however only considers the liquid particle interactions and is hence valid only to volume fractions of about 0.01 [10]. At higher loadings one must consider the effect of particle pairs coming in close proximity. Second and third order corrections must be made to account for this behavior, the equation appears as

$$\eta/\eta_s = 1 + k_1\phi + k_2\phi^2 + k_3\phi^3 + \ldots \tag{3.29}$$

where $k_1 = 2.5$ and $k_2 = 6.2$ and the higher order coefficients are as of yet not fully understood. If one continues to higher volumetric loadings the fluids exhibit strongly non-Newtonian behavior and is not describable in a simple fashion. Nonspherical

Figure 3-18: Cannon-Fenske Opaque (Reverse-Flow) Viscometer (height 8 inches)

particles also add to the difficulty of modeling. The coefficients of Equation 3.29 must be modified depending on the aspect ratio of the particles. For example, if the spheres are replaced by rods with an aspect ratio of 15, the value of k_1 will be modified to 4.0. Most nanofluids have particles of varying shapes, sizes, and size distributions. For this reason it has been decided that the viscosity of the fluids in this study must be determined experimentally.

3.8.2 Measurements of viscosity in nanofluids

An investigation of the dependence of viscosity on temperature and particle loading for the nanofluids discussed in Section 3.5 was conducted using the *Cannon-Fenske Opaque* capillary viscometer. With this instrument it is possible to measure the kinematic viscosity of a fluid in a range from 1 to 15cSt ($1cSt = 1mm^2/s$) with an uncertainty of 0.5%. In order to have experimental data at different temperature the viscometer can be placed in a closed transparent container where water from a thermostatic bath is flowing (see picture in Figure 3-19). The instruments come

Figure 3-19: Picture of the setup used to measure viscosity.

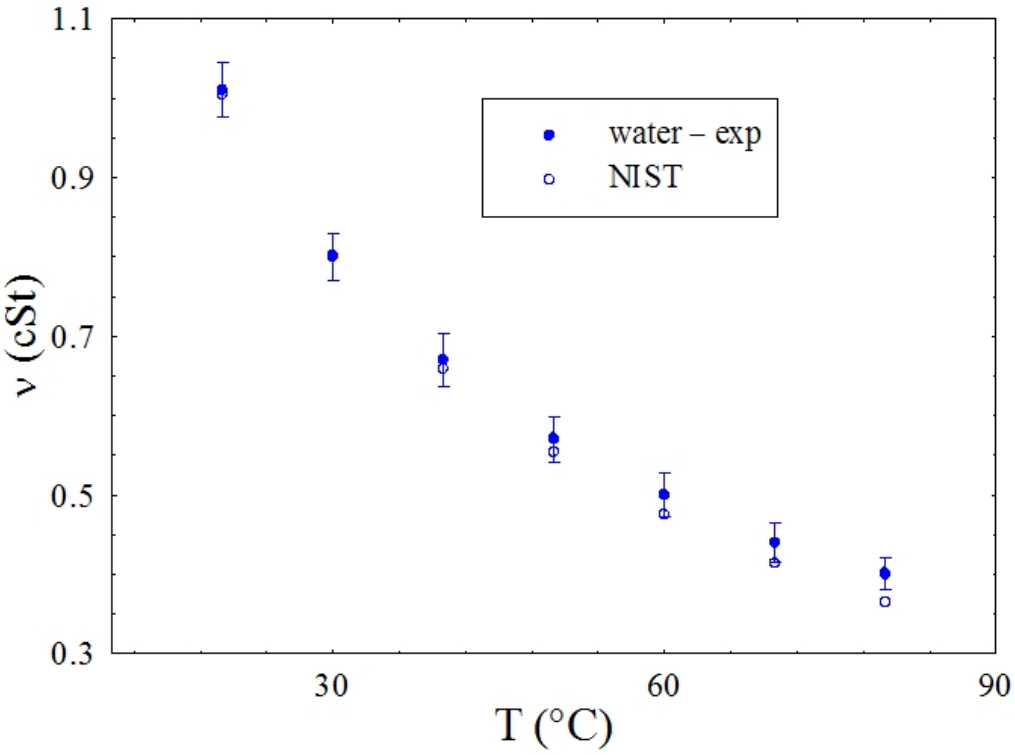

Figure 3-20: Kinematic viscosity as a function of temperature for water.

NIST calibrated from the vendor but as a check it is retested with the viscosity of a standard liquid (ISO 17025 Viscosity and density standard - S3 by Koehler) obtaining the correct value of 3cSt. Also the temperature dependence for water is checked and it is found to be in good agreement with the values available in literature (see Figure 3-20).

In Figure 3-21 and Figure 3-22 the experimental results for kinematic viscosity of alumina and zirconia suspensions are displayed: one can notice a similar behavior to water for all the samples at different particle loadings. This effect is much more evident (Figure 3-23 and Figure 3-24) considering the relative dynamic viscosity or the ratio between the viscosity of the suspension and the solvent. (Dynamic viscosity is found by multiplying the kinematic viscosity by the density of the respective nanofluid) One can see that all the curves at different temperatures overlap and have the same dependence on the volume fraction. This dependence is fitted using a model

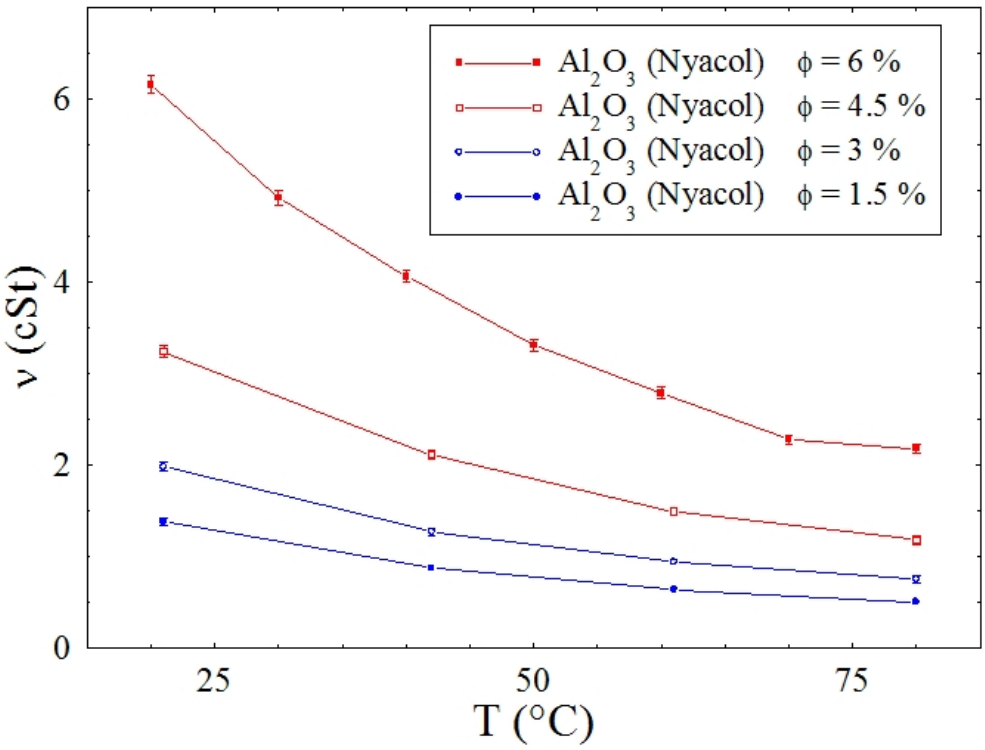

Figure 3-21: Kinematic viscosity as a function of temperature and particle loading for alumina suspensions.

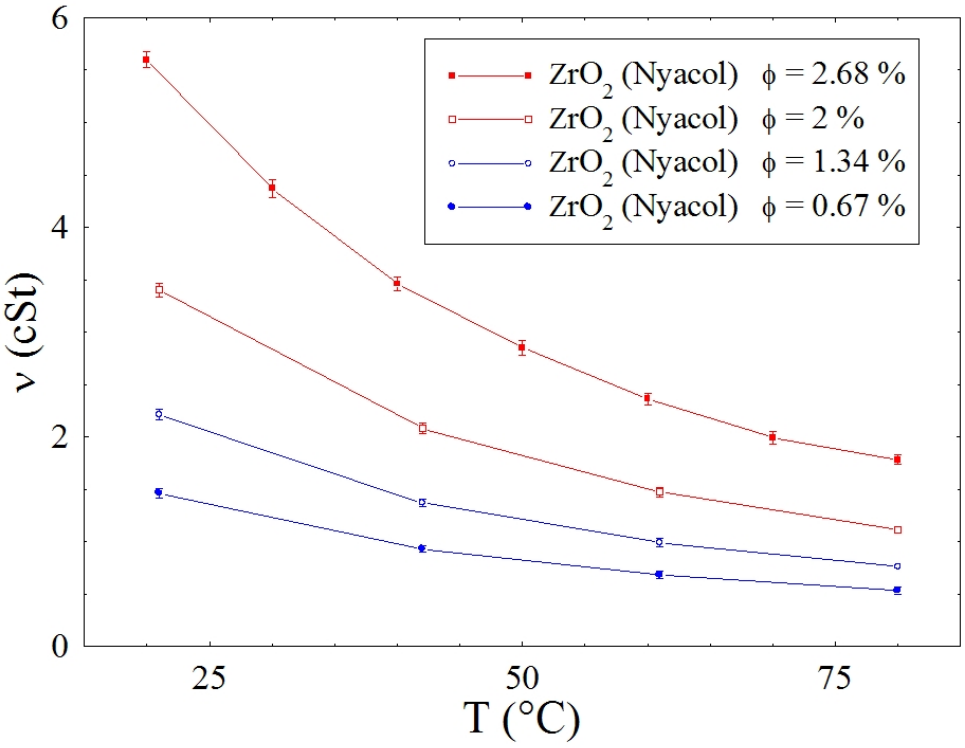

Figure 3-22: Kinematic viscosity as a function of temperature and particle loading for zirconia suspensions.

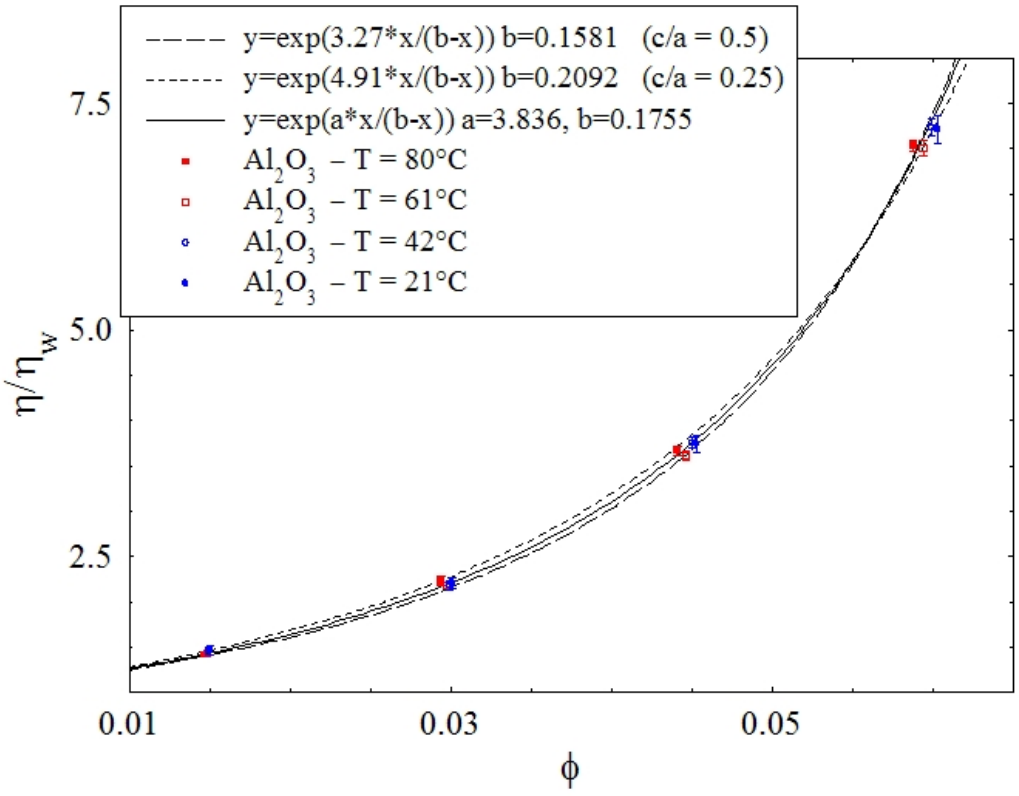

Figure 3-23: Relative viscosity as a function of volume fractions for alumina suspensions at different temperatures.

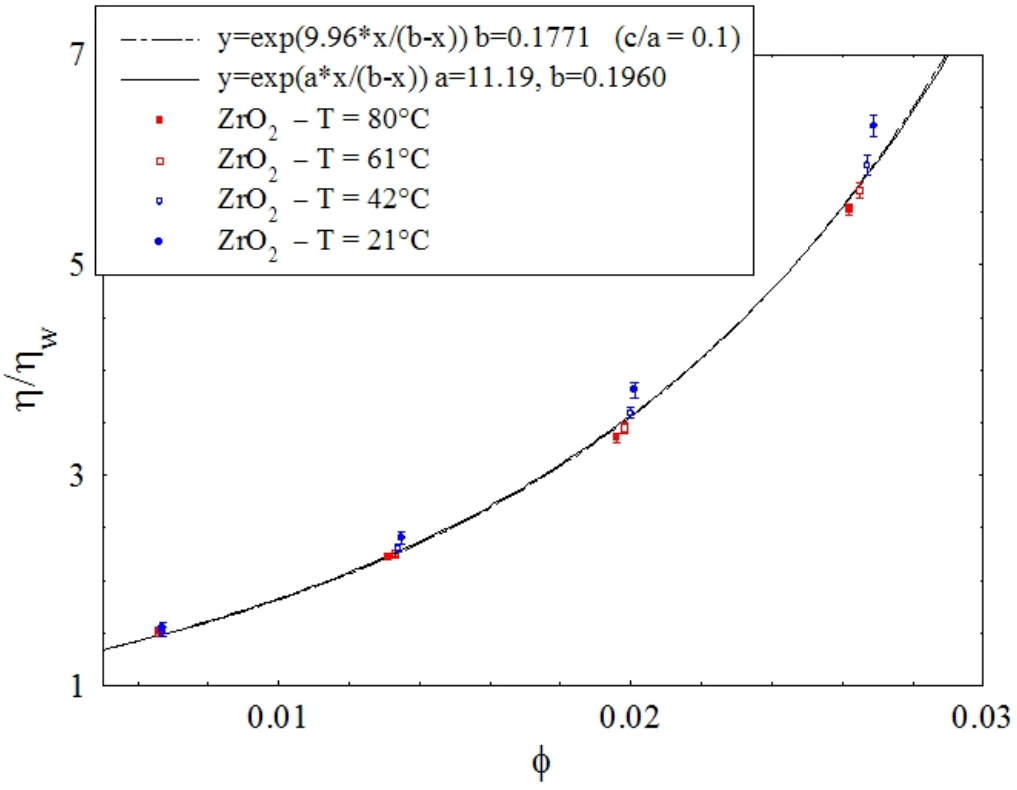

Figure 3-24: Relative viscosity as a function of volume fractions for zirconia suspensions at different temperatures.

for concentrate dispersions of oblate spheroidal particles derived from [70][1] :

$$\frac{\eta}{\eta_0} \;=\; \exp\left[[\eta]\,\frac{\phi}{\phi_p - \phi}\right]$$

where ϕ_p is the close-packing volume fraction and $[\eta]$ is the intrinsic viscosity defined as

$$[\eta] \;=\; \lim_{\phi \to 0} \frac{\eta - \eta_0}{\phi\,\eta_0}$$

and for spheres is equal to 2.5. For spheroids it is related to the shape tensor S_{ijij} with the relation

$$[\eta]_{ij} \;=\; \frac{1}{2S_{ijij}}$$

for which there are two independent shear components:

$$S_{1212} \;=\; \frac{1}{4}\left[1 \;-\; \frac{1-J}{1-\xi^2}\right]$$

and

$$S_{1313} \;=\; \frac{1+\xi^2}{2}\,\frac{1-J}{1-\xi^2}$$

where $\xi = c/a$ and

$$J \;=\; \frac{3\xi}{2(1-\xi^2)^{3/2}}\,\left[\arccos\xi \;-\; \xi(1-\xi^2)^{1/2}\right]$$

for $\xi < 1$. In the fitting curves, the first component of the shape factor is important because it is the cause of the higher viscosity. One can see that for alumina the best fit is between the models for an axial ratio of 0.5 and 0.25, the same as that found for the thermal conductivity. Anyway, as said before, this is not an explanation for the viscosity of these samples (due to lack of knowledge of the real value of the close-packing volume fraction) but rather a suggestion for trying to understand this behavior. Although, the intrinsic viscosity could also be related to the charge of the particles. This is called *electroviscous effect* and it is expressed by the relation $[\eta] = 2.5 + f(c)\,\zeta^2$, where $f(c)$ is a function of the ionic concentration and the particle

[1] In the referred paper the authors used a model with 1 instead of ϕ_p

size and ζ is the zeta-potential as defined in Equation 2.12. The measured dynamic viscosity for a Ludox suspension at the higher volume fraction (18.6%) is $4.29cP$: this value can be obtained from the model used before in case of spherical particles and with a close-packing fraction of around 0.5. Moreover the viscosity of the highest loading of Teflon particles (around 5% in volume fraction) is $1.25cP$ which is the expected value for a dilute dispersion of spheres.

3.9 Conclusions for thermophysical properties

Implementation of a simplified hot wire thermal conductivity probe has been successful in the determination of the thermal conductivity of basic liquids and more importantly the nanoparticle colloids. These measurements could be made for different loadings and more importantly different temperatures. Likewise, the glass capillary viscometer is found to be effective in the measurement of the viscosity of nanoparticle colloids at different loadings and temperatures. The two major colloids under investigation, alumina and zirconia, have been measured at various loadings and temperatures. Using these values, the following models will be used in the determination of nanofluid properties for the data analysis of the convective heat transfer loop.

- Specific heat capacity:

$$c_{p,mixture} = \frac{((1-\phi) * \rho_{water} * c_{p,water}) + (\phi * \rho_{solid} * c_{p,solid})}{((1-\phi) * \rho_{water}) + (\phi * \rho_{solid})}$$

- Density:

$$\rho_{mixture} = ((1-\phi) * \rho_{water}) + (\phi * \rho_{solid})$$

- Viscosity for Alumina:

$$\mu_{mixture}(T) = \mu_{water}(T) * exp(4.91 * \phi/(0.2092 - \phi))$$

- Viscosity for Zirconia:

$$\mu_{mixture}(T) = \mu_{water}(T) * exp(11.19 * \phi/(0.1960 - \phi))$$

- Thermal conductivity for Alumina:

$$k_{mixture}(T) = k_{water}(T) * (4.5503 * \phi + 1)$$

- Thermal conductivity for Zirconia:

$$k_{mixture}(T) = k_{water}(T) * (-29.867 * \phi^2 + 2.4505 * \phi + 1)$$

It can be seen that the viscosity and thermal conductivity models are multipliers utilizing only the temperature dependence of the base fluid water as found in these experiments. The heat capacity and density are volume weighted averages.

Chapter 4

Convective heat transfer

As stated in the introduction, the primary objective of this work is to investigate the convective heat transfer capabilities of nanoparticle colloids. In order to do this a convective heat transfer experimental loop is designed and constructed. The design, calibration of instrumentation, water testing, and finally the nanofluid experimentation is described in this chapter.

4.1 Design and Construction

Some basic requirements are developed as design considerations for the convection loop. These requirements are generated in order to meet certain goals: some to mimic nuclear reactor conditions, some to meet existing equipment and lab requirements, and finally some arbitrary conditions. In order to best mimic the conditions of a pressurized water reactor, the hydraulic diameter is selected roughly as $0.5in$ $(0.0127m)$ and the desired heat flux is greater than $100kW/m^2$, though the effect of heat flux on non-boiling heat transfer is expected to be limited. A 24kW ($40V$ and $600A$) EMHP 40-600 DC power supply from Lambda Americas is available for use in the laboratory, as shown in Figure 4-1. Joule heating is selected as the best way of producing the uniform heat flux condition in the test section. The amount of heat produced by Joule heating is I^2R where I is the current and R the resistance across the test section. The heat flux can be roughly predicted from a tube outer diameter D_o and

Figure 4-1: EMHP 40-600 DC power supply from Lambda Americas

thickness t as:

$$q" = \frac{I^2 \rho_0}{\pi^2 * t(D_o^2 - 3D_o t + 2t^2)}. \tag{4.1}$$

If one uses, $\rho_0 = 7.4 * 10^{-7} ohm \cdot cm$, a typical value for the electrical resistivity of stainless steel 316 and a standard tube diameter and thickness of $0.5in$ $(0.0127m)$ and $0.065in$ $(0.00165m)$, respectively, then the heat flux should be $157kW/m^2$, which is more than the desired value as stated above. In order to achieve a fully developed region in turbulent flow, the test section length should be at a minimum of about $L \sim 25 - 40D_o$, which is greater than $0.3m$. The length of the tube is also somewhat constrained by the bulk temperature rise, $\triangle T_b$. Due to the limitations of thermocouple uncertainties ($\sim 1^oC$), it is desired to maximize the bulk temperature rise as much as is reasonable. If Reynolds number, $Re = \rho D\bar{v}/\mu = 4\dot{m}/\pi D\mu$, where D is the inner tube diameter, is assumed as 50,000 (turbulent), then one can find an approximate value of the needed length for a designated bulk temperature rise as:

$$L = \frac{Re\mu C_p \triangle T_b}{4q"}, \tag{4.2}$$

from which it is determined that roughly $3m$ would be required to get 10^oC of bulk temperature rise, which is deemed sufficient.

It is also important to mention the potential for mixed convection effects in the horizontal tube flow. High heat fluxes and the resulting large film temperature gradient could give rise to buoyant mixing and radial tube temperature variation. The amount of buoyancy contribution to the overall flow is determined through a ratio of Grashof and Reynolds number as follows:

$$\frac{Gr}{Re^2} = \frac{\frac{g\rho^2\zeta(T_w - T_b)_{LM}D^3}{\mu^2}}{\left[\frac{\rho D\bar{v}}{\mu}\right]^2}, \tag{4.3}$$

where the log mean temperature difference is used. If this ratio is greater than around 0.1 then the effects of buoyancy will begin to alter the flow. This value is calculated during operation in order to assure proper operation. Initial estimations show that buoyancy at the minimum flow Reynolds (around 20,000) and maximum heat flux ($180W/m^2$) gives a ratio of less than 0.01 and thus should not alter the flow.

Furthermore, pump requirements must be able to achieve turbulent flow conditions in the loop. In the lab is a Berkeley SS1XS1-1 pump with $1HP$, shown in Figure 4-2, with a frequency speed controller. The pump is capable of operation with water up to 120^oC and $8bars$, due to the shaft seal limitations. After rough estimation of the total loop pressure losses, assuming $0.5in$ ($0.0127m$) diameter tubing throughout, and from knowledge of the pump characteristic curve, it is found that the pump should be capable of producing around 4 GPM (0.252 l/s) which is equivalent to a mass flow rate for water at room temperature of around 0.25 kg/s. This will deliver a significantly turbulent flow rate for water at room temperature, up to Reynolds of 60,000. Therefore, the pump is deemed usable for the experiment. Finally, selection of the data acquisition system is of essential importance. The available HP3852A Data Acquisition and Control Unit is used in this experiment as shown in Figure 4-3. The unit has the ability to control and acquire data from several card slots which are interchangeable. The cards installed in the unit are as follows:

Slot 0 Empty

Figure 4-2: Berkeley SS1XS1-1 pump

Slot 1 5 1/2 to 3 1/2 Digit Integrating Voltmeter HP44701A Directly measures: dc voltage; ac voltage; Resistance

Slot 2 Relay Multiplexer HP44708A Directly multiplexes: Thermocouples

Slot 3 Relay Multiplexers HP44705A Directly multiplexes: Voltage

Slot 4 8-Channel Relay Actuator HP44728A Directly provides: Solid state relay actuation for control

Slot 5 5-Channel Counter / Totalizer HP44715A Directly provides: Count measurements Period measurements Frequency measurements Interrupts

Slot 6 Empty

Slot 7 Empty

The system is used to measure system thermocouples, pressure gauge voltages, power supply current and voltage, flow meter frequency, and to control the pump and power supply. These features are implemented into a Visual Basic user interface, as shown in Figure 4-4. The convective loop setup is shown in Figure 4-5. There are two test

Figure 4-3: HP3852A

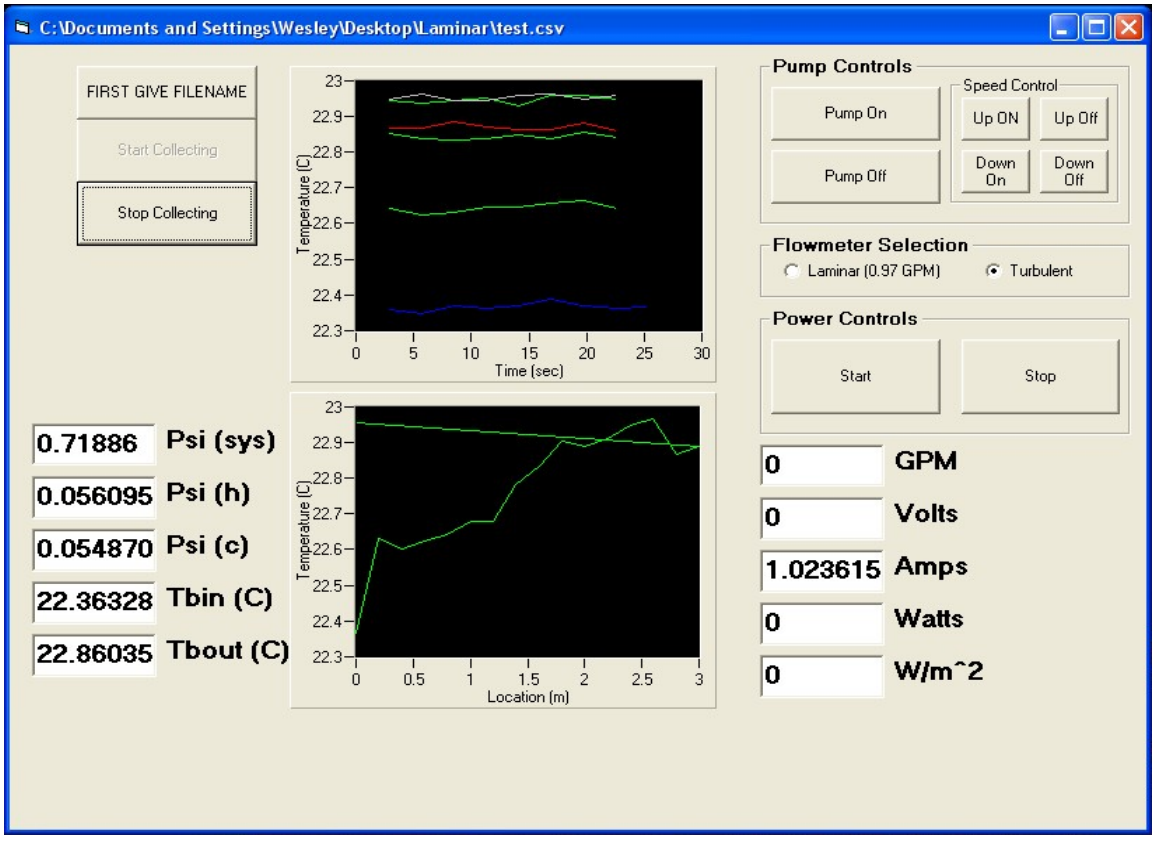

Figure 4-4: Visual Basic user interface for the convective loop control and data acquisition

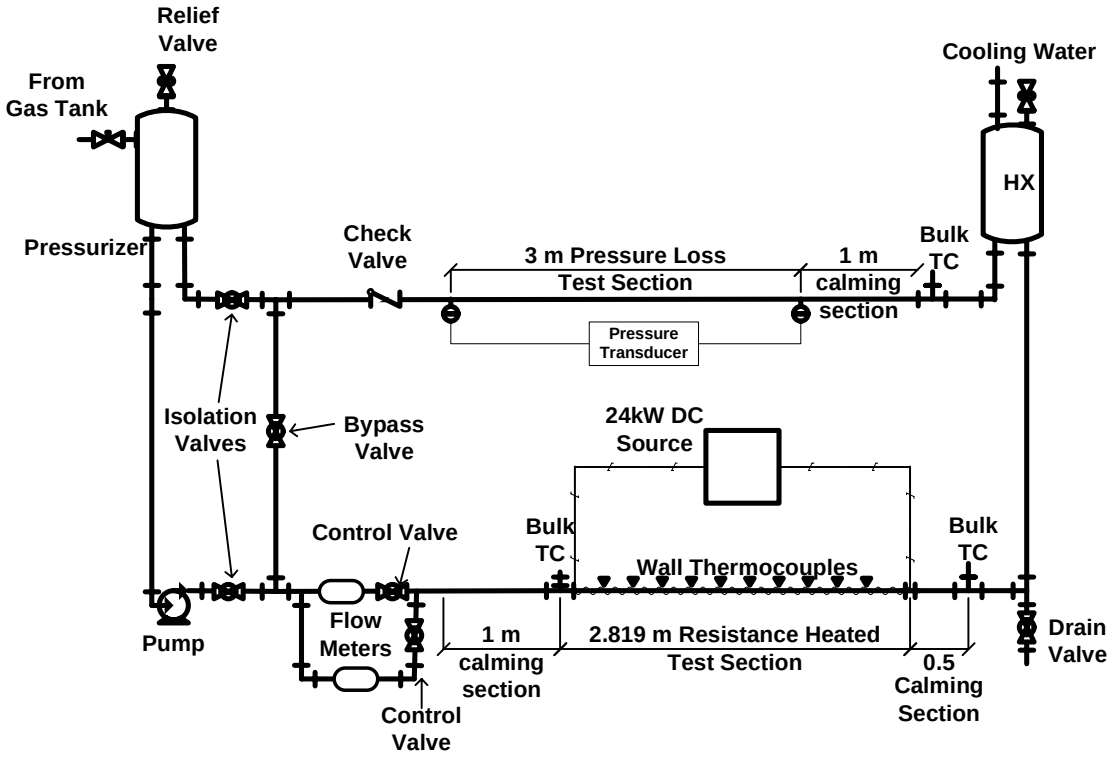

Figure 4-5: Schematic of convective loop facility

sections, one heated for the convective heat transfer coefficient measurement and a second for isothermal viscous pressure loss measurement. The heated section is Joule heated as stated earlier with 14 T-type wall thermocouples every 0.2m on the section. There are also two T-type thermocouples submerged in the flow channel at the inlet and outlet of the heated section. The heated and the isothermal sections both have pressure transducers tapped at the inlet and outlet in order to measure viscous pressure losses in the tube. Finally, the loop has the pump for circulation, a pressurizer/inventory tank, a tube and shell heat exchanger for heat removal (McMaster Carr 35185K55, Stainless Steel Shell-and-Tube Heat Exchanger 9.1 Sq ft Surface Area, 76 GPM Flow Capacity), and various valves for control and removal of the fluid.

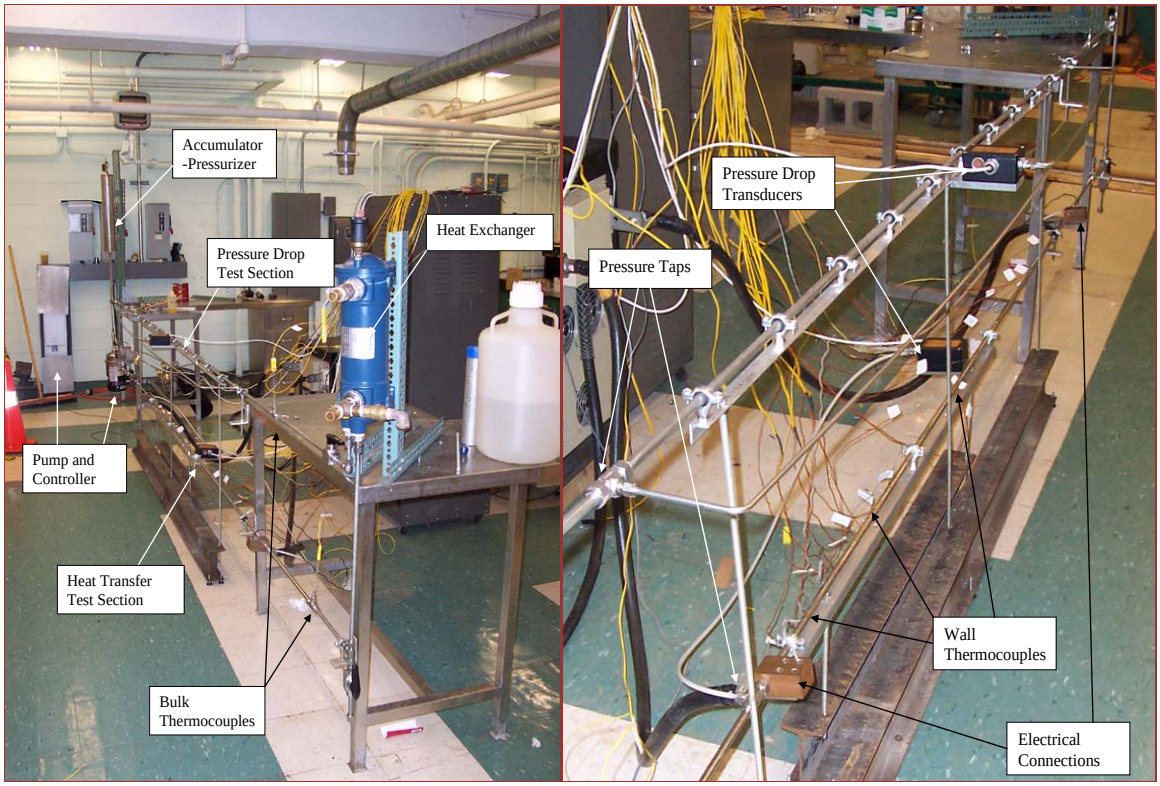

Figure 4-6: Pictures of convective loop facility without insulation

4.2 Calibration

The next step is the calibration of the many sensors on the convective heat transfer loop. The flow meters come calibrated from the vendor and their curves are presented here. The digital voltmeter, power supply current, and thermocouples require calibration to verify proper function. This is described below.

4.2.1 Flow Meters

As stated above, the flowmeters come calibrated from the manufacturer. Two flow meters are used in the system the Omega FTB-902 has the range from $0.75GPM$ to $5GPM$ for the turbulent flows and the FTB-9510 has range from $0.07GPM$ to $0.95GPM$. Both flow meters are accurate to within 0.5% of the reading. The meters output a frequency signal corresponding to the volumetric flow rate. These curves are presented in Figures 4-7 and 4-8, respectively. Fluid viscosity can become an issue if the viscosity is higher than that of water. The deviation of the flow meter reading becomes an issue when the meter is running in the lower 25% of its operating range for fluids of viscosity less than 30 times that of water. Nanofluids that will be run in this loop are typically only 5 times more viscous than water, therefore the calibration should not be an issue.

4.2.2 Digital Voltmeter

The digital voltmeter is the single most important piece of the data acquisition system. All of the voltage, current, pressure transducer, and thermocouple signals are measured by this instrument. The system is calibrated against the laboratory's NIST certified HP3245A universal source standard. A high range calibration is performed at 0 to 10V and a low range calibration is performed at 0 to 10mV. These calibration curves are shown in Figures 4-9 and 4-10, respectively. It can be seen that the digital voltmeter does a sufficiently accurate job and does not require extra consideration.

4.2.3 Power Supply Current

The EMHP 40-600 DC power supply by Lambda Americas provides an internal shunt for current measurement. Due to the age of the power supply this shunt must be calibrated to insure proper function. A NIST certified shunt is borrowed from the Plasma Science and Fusion Center and placed between the power supply leads. The current calibration curve is shown in Figure 4-11. This calibration curve is implemented in the Visual Basic program for data acquisition.

4.2.4 Thermocouples

The T-type thermocouples, Omega TJC36-CPSS-032-U, come specified from the manufacturer to have an uncertainty of 0.5^oC or 0.4% from $0 - 350^oC$. Thermo-

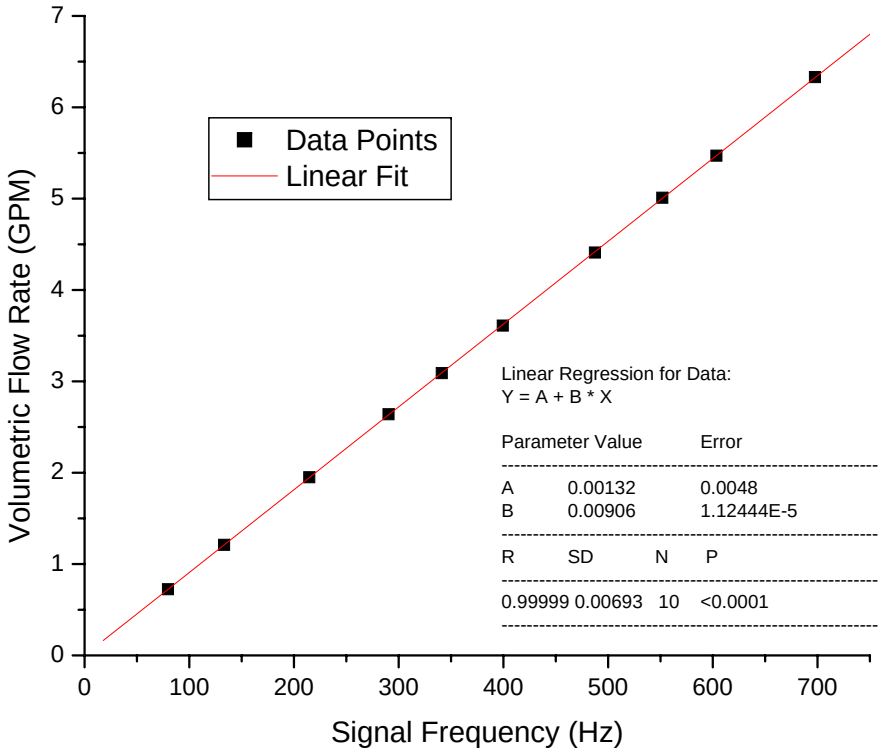

Figure 4-7: High range flow meter calibration

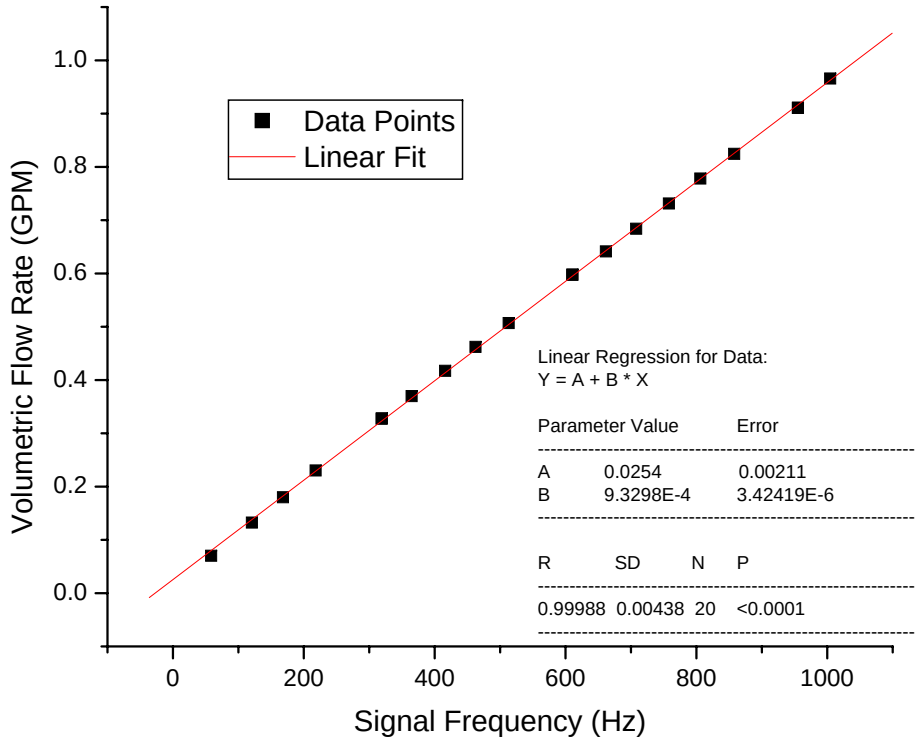

Figure 4-8: Low range flow meter calibration

couples are not calibrated in the technical sense as this is done automatically by the instrumentation with the NIST calibration curves; rather, they are tested with standard temperatures to ensure no manufacturing or connection flaws are creating erroneous readings. The thermocouples are immersed in well mixed boiling-water bath which is at 100.16^oC for the laboratory pressure and a well mixed ice-water bath which is at 0^oC. The resulting histograms for the measurements are given in Figure 4-12. The figures show the aggregate of all of the thermocouples' readings over 100 seconds. It can be seen that the offset and the standard deviations are below the specifications for the thermocouples and that the distribution is somewhat Gaussian.

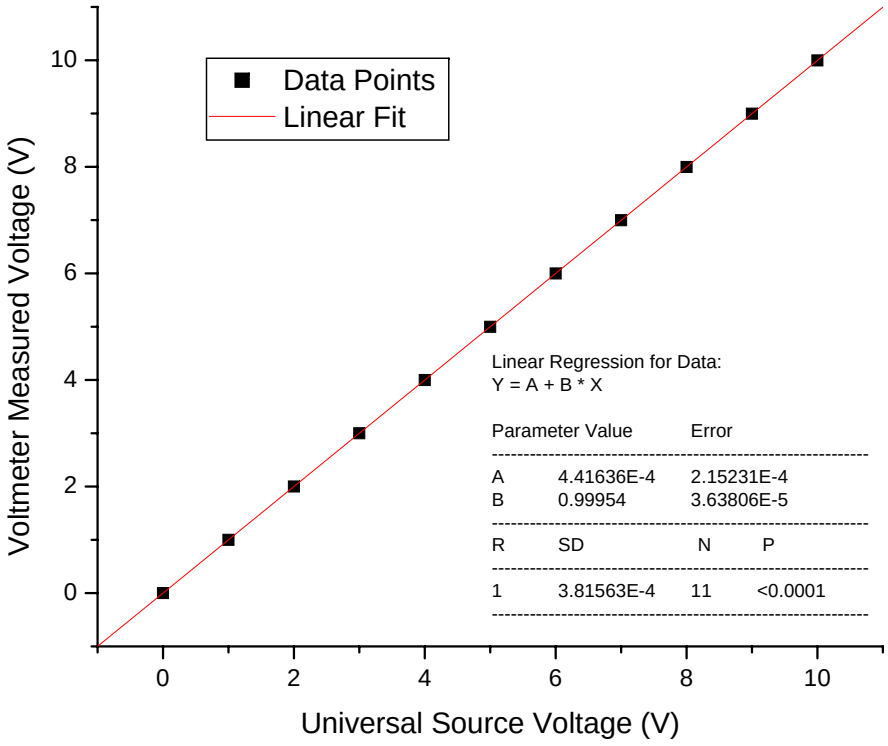

Figure 4-9: High range voltage calibration

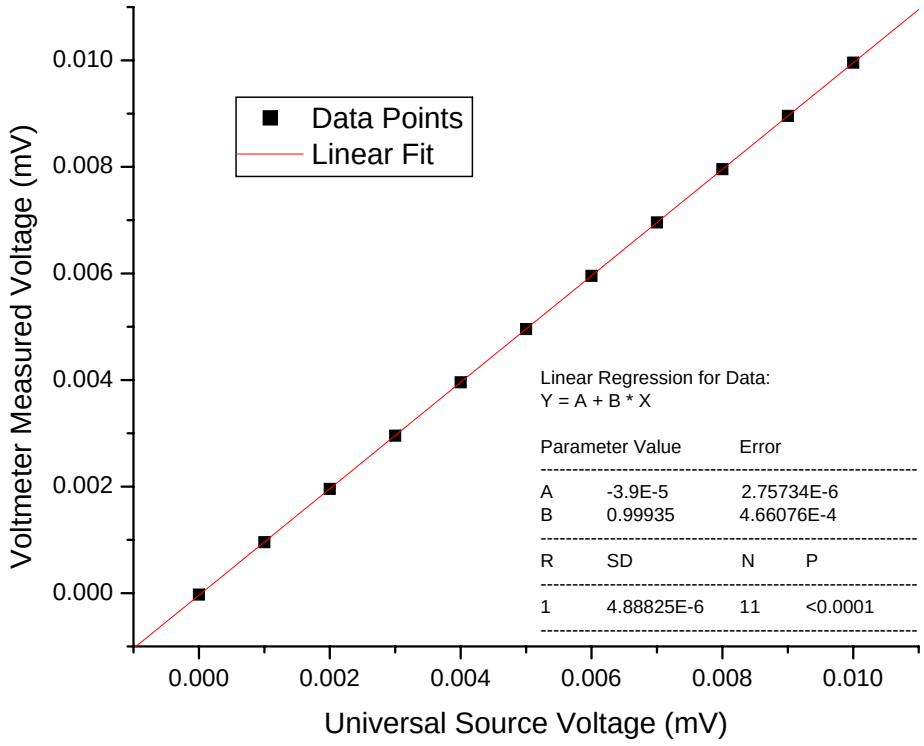

Figure 4-10: Low range voltage calibration

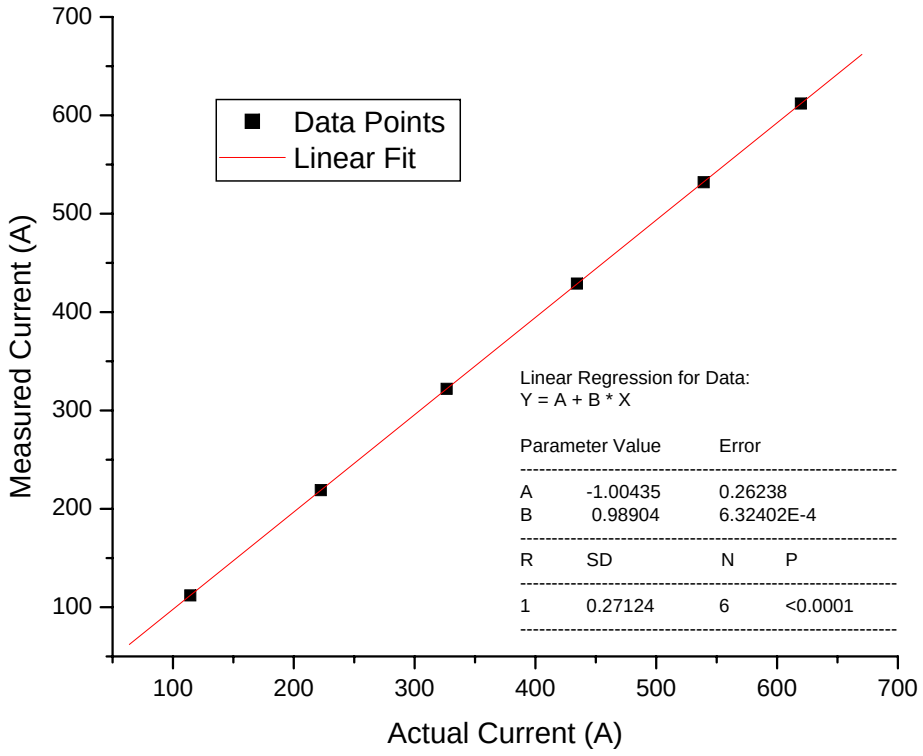

Figure 4-11: Current calibration

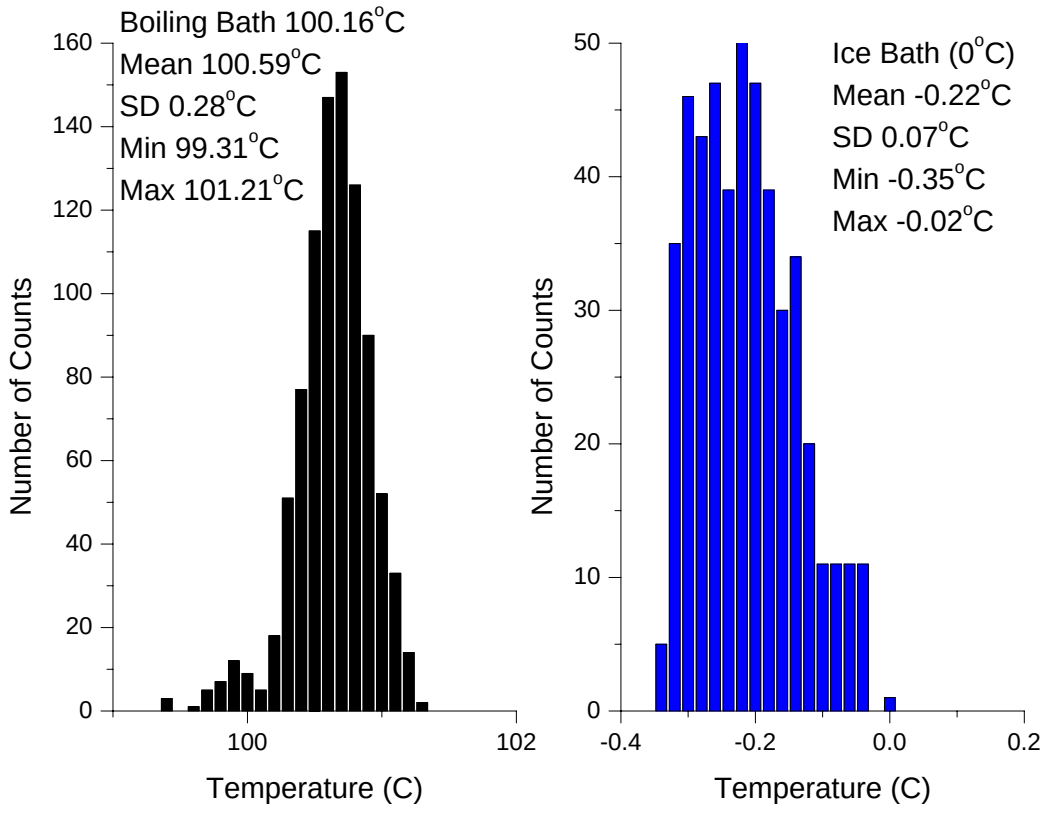

Figure 4-12: Thermocouple testing

4.2.5 Differential Pressure Transducer

The differential pressure transducer, Omega PX293-030D5V, operates over a range of $0-30psid(0-207kPa)$ with accuracy to within 0.5% of the reading as calibrated by the manufacturer. The output is a linear curve scaled from $0-5DCV$ for the full scale pressure. No additional calibration is required.

4.3 Water convection testing

After completion of construction and calibration of the flow loop, testing of the loop's functionality for measuring heat transfer coefficient and viscous pressure loss is required. The initial test is done with water, whose performance and properties are well known from literature. Six initial tests are run with various flow rates and inlet temperatures. The test are operated for Reynolds numbers betwenn 18,000 and 65,000 with heat flux of $100kW/m^2$. Inlet temperatures are varied between 20^oC and 60^oC to maintain the wall temperature below the boiling point. All tests are performed at atmospheric pressure. These tests prove the apparatus for heated turbulent flows against existing friction factor and heat transfer coefficient correlations found in the literature. All raw data for the test is given in Appendix D.

4.3.1 Heat transfer coefficient water test

First the heat transfer coefficient is compared by means of the local Dittus-Boelter-type correlation for Nusselt number,

$$Nu_x = 0.023Re_x^{0.8}Pr_x^{0.4} = 0.023\left(\frac{\rho D\bar{v}}{\mu}\right)_x^{0.8}\left(\frac{\mu c_p}{k}\right)_x^{0.4}, \tag{4.4}$$

where D is the tube inner diameter, $\bar{v}$ is the average velocity, ρ is the density, c_p is the specific heat capacity, and μ is the viscosity all evaluated at the local axial position. The following steps are used in the calculation of the heat transfer coefficient:

Power

Power is measured directly from the test section current, I, and voltage difference, V, assuming no heat losses $Q = IV$ and heat flux on the tube inner wall as

$$q" = \frac{Q}{\pi D_{in} L}$$

. The heat loss assumption is proven through the energy balance and the bulk temperature rise in the next step.

Bulk and Wall Temperature

The flow rate is measured from the volumetric flow rate, AV, and the bulk inlet temperature, $T_{b,in}$, for the density, ρ, as $\dot{m} = \rho AV$. Local bulk temperature is interpolated using the conservation of energy as $T_b(x) = Q/\dot{m}c_p + T_{b,in}$. This value is compared with the bulk outlet temperature which is also measured to assure minimization of heat loss. All the experiments determined that this error is usually less than 1% for the heat fluxes under investigation and therefore it is assumed that heat losses will not alter the results substantially.

Wall temperature is measured on the outer surface, $T_{w,o}$, of the tube and the inner wall temperature, $T_{w,i}$, is found through the analytical solution for the conduction through the tube as

$$T_{w,i} = T_{w,o} - \frac{Q}{2\pi k_w L}\left[\frac{D_o^2}{(D_o^2 - D_i^2)} log\left(\frac{D_o}{D_i} - 1/2\right)\right]$$

where the temperature dependent thermal conductivity of stainless steel is found from a linear curve fit of data found in the ASM Handbook [71], as shown in Figure 4-13. The resulting linear fit for the temperature dependent is the following funtion

$$k_w(T) = 0.0127 * T + 13.23188.$$

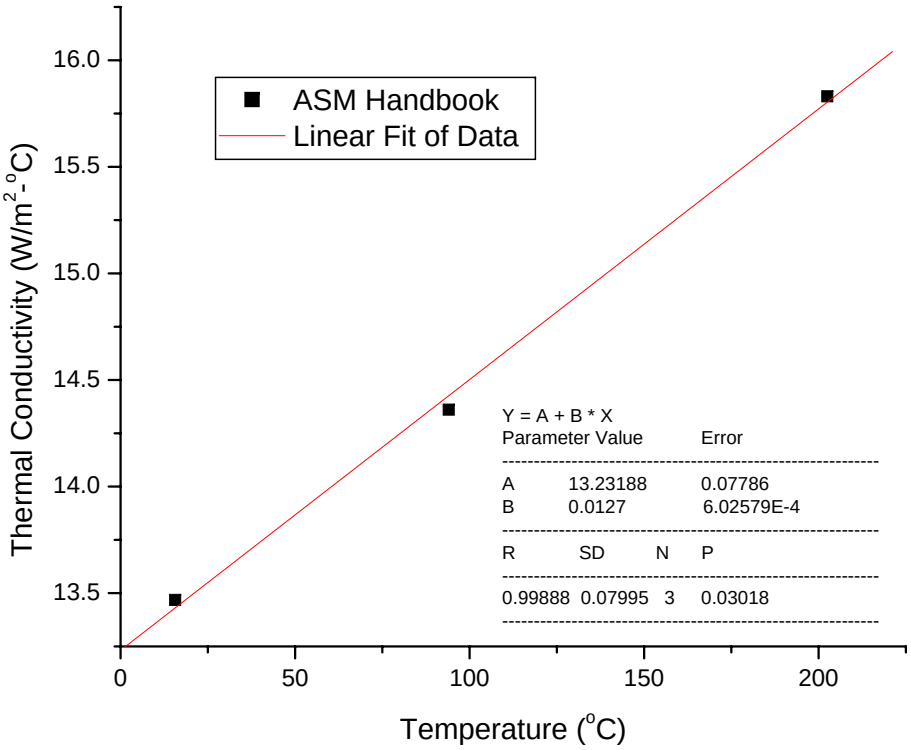

Figure 4-13: Temperature dependence of stainless steel 316 thermal conductivity

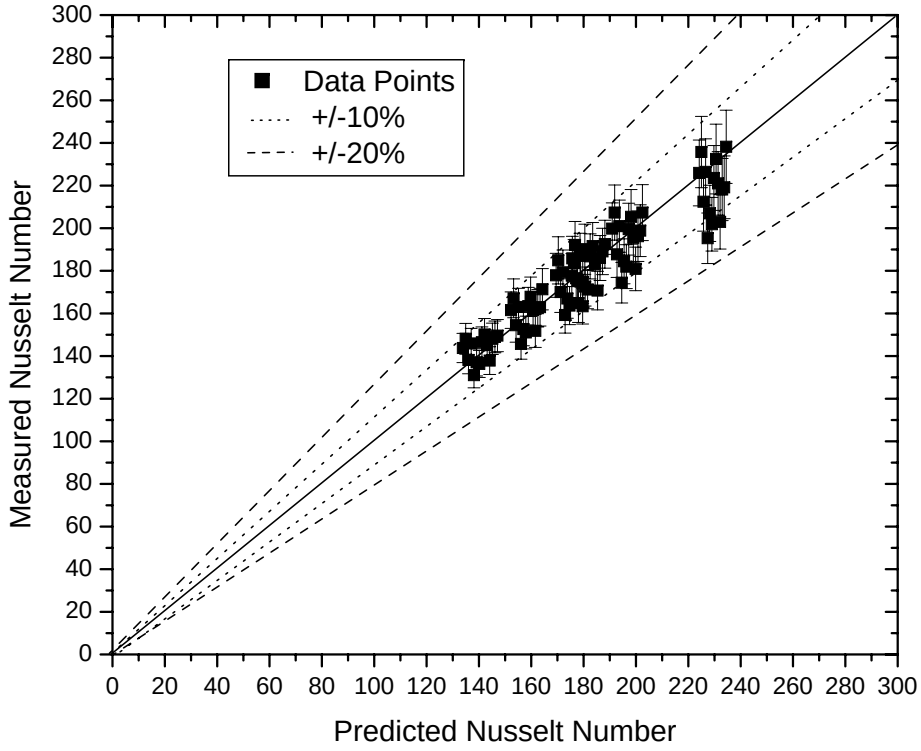

Figure 4-14: Water test Nusselt number comparison to theory

Heat transfer coefficient

The local heat transfer coefficient is defined as

$$h_x = \frac{q"}{(T_{w,i} - T_b)_x}$$

where all of the terms are defined above. This can be compared with the value predicted by equation where $h_x = Nu_x k_{b,x}/D_i$ with $k_{b,x}$ as the bulk liquid thermal conductivity. It can be seen in Figure 4-14 that most of the data land within 10% of the predicted values and all of the data including the uncertainty land within 20% of the prediction. Uncertainty analysis can be found in Appendix C. A sample wall temperature profile is provided for one of the cases in Figure 4-15. Each case records around 40 points in time over around 100 seconds. This assures that the system

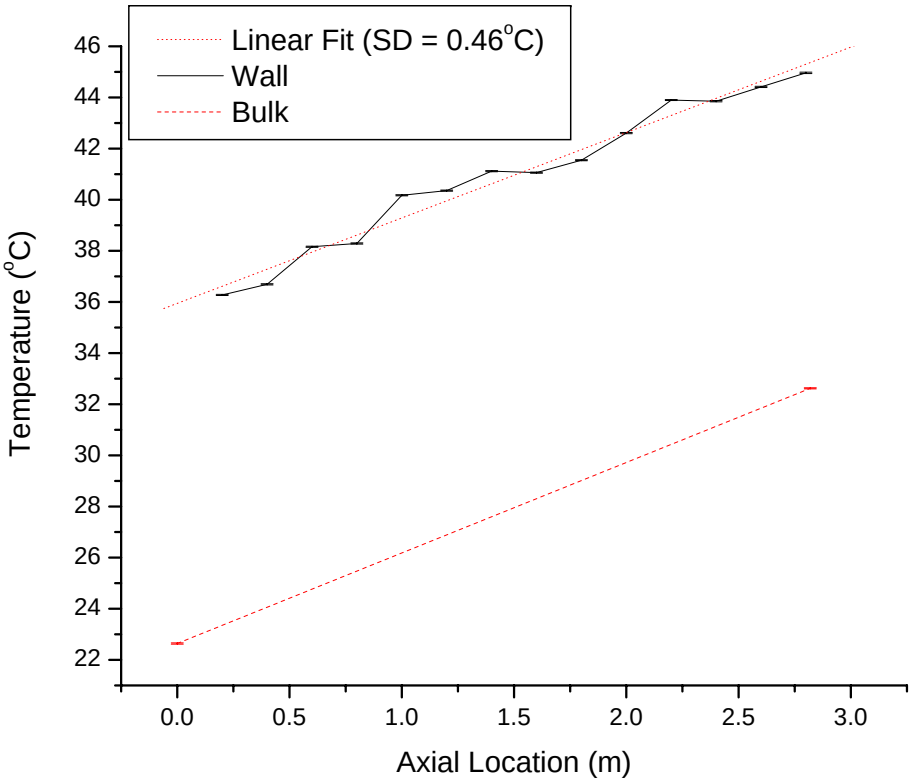

Figure 4-15: Test wall temperature profile

has achieved steady state. It can be seen that the time dependence (error bars) are insignificant. However, it is noticed that there is a small axial temperature variation on the wall. It is assumed this is due to contact resistance and normal thermocouple offsets. If one makes a line fit it can be seen that the values standard deviation is less than the specified value of 0.5^oC. For this reason and for ease of comprehension of data, the tube average heat transfer coefficient and Nusselt number will be used, as shown in Figures 4-16 and 4-17. It is found that this reduces clutter and shows the desired results in an easier to comprehend fashion, without loss of information.

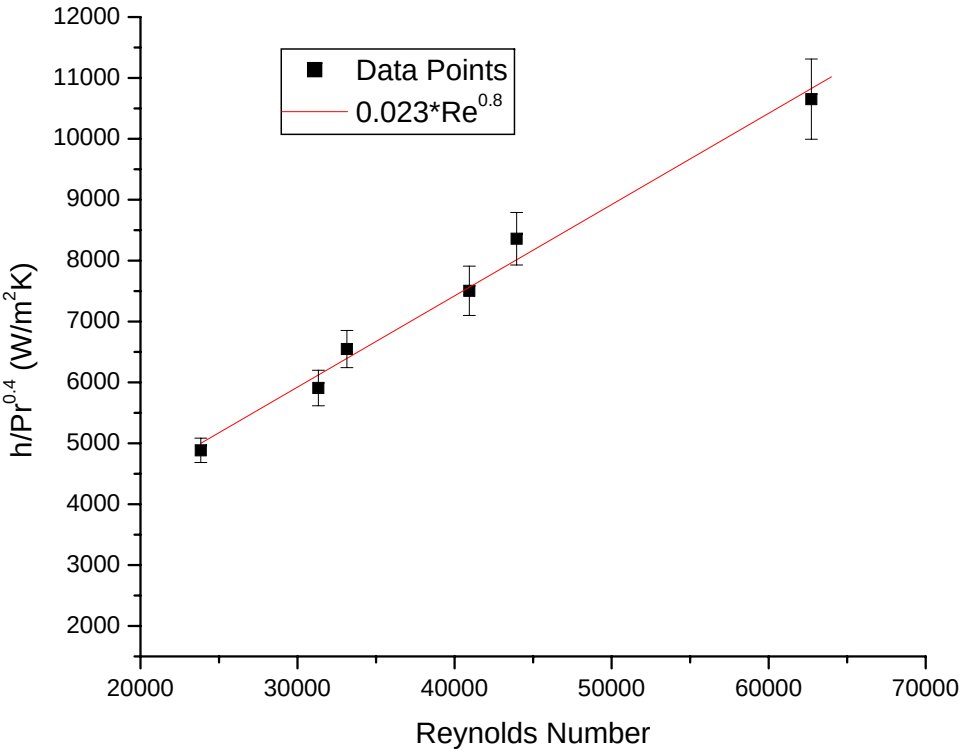

Figure 4-16: Normalized heat transfer coefficient

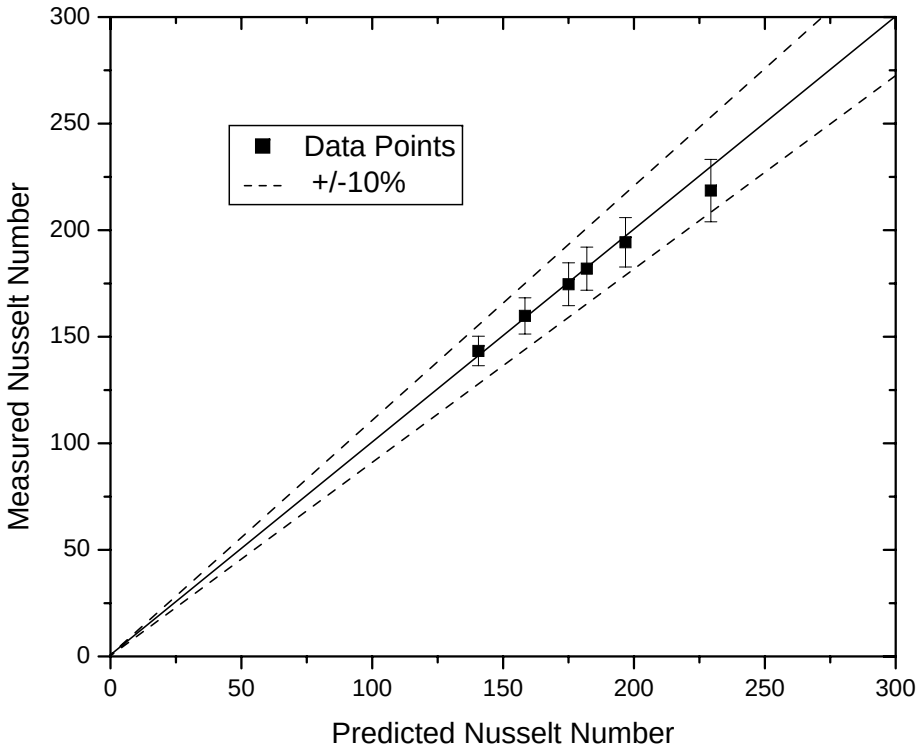

Figure 4-17: Water test tube-average Nusselt number comparison to theory

4.3.2 Viscous pressure loss water test

The heated and isothermal sections are used to provide viscous pressure loss data for the six cases investigated above. Values measured can be compared to the correlated theory where pressure loss is

$$\Delta P = f_f \frac{L}{D} \frac{\rho \bar{v}^2}{2} \tag{4.5}$$

where L and D are the length and diameter of the tube and the friction factor f_f can be determined in the fully developed turbulent flow regime from

$$f_f = 0.316 Re^{-0.25}, \tag{4.6}$$

the Blasius relation, if $Re < 30000$ or else

$$f_f = 0.184 Re^{-0.2}, \tag{4.7}$$

the McAdams relation. The test section is horizontal and has a constant flow area, thus gravitational, acceleration and form pressure terms can be neglected in Eq. 4.5. Also, a calming section at the entrance of the test section ensures that fully-developed flow is achieved before the pressure drop is measured. The results can be seen in Figure 4-18. The measured values land to within 10% of the predicted values. If one considers the friction factors, the results can be seen in Figure 4-19. The friction factors and the uncertainty land well within 20% of the predicted values. Uncertainty analysis is presented in Appendix C. From these results, it is presumed that the experiment is functioning properly. Completion of the water testing proved the apparatus is capable of measuring heat transfer coefficient and viscous pressure drop for liquids effectively. The testing also allowed for the development of operation practices, software, and data reduction methodology. The data reduction software developed in *MATLAB* is presented in Appendix D.

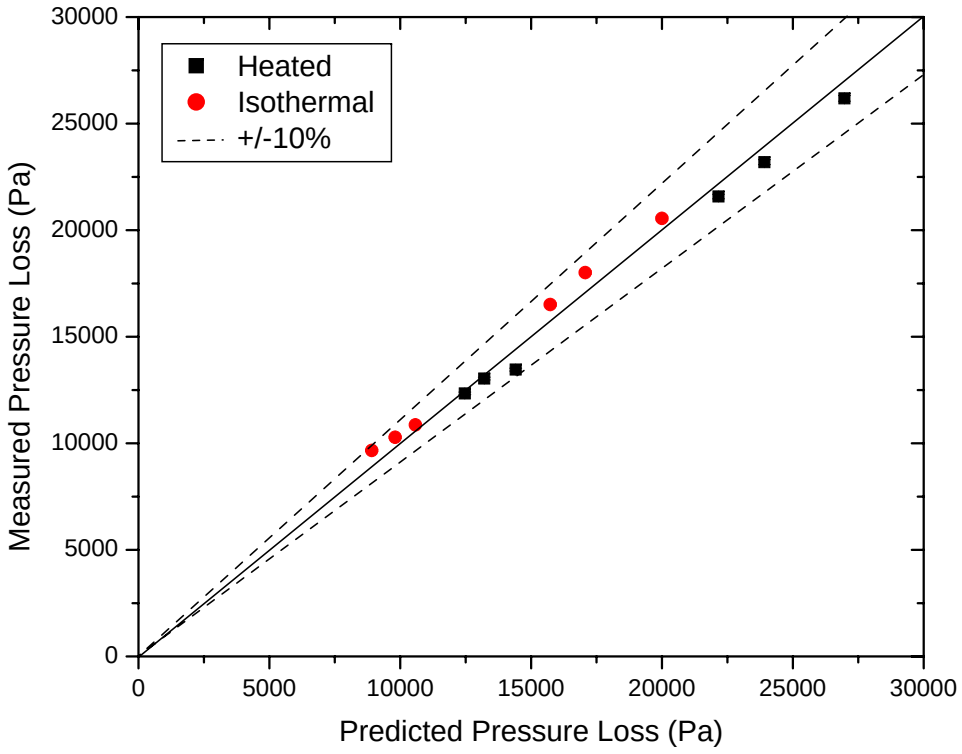

Figure 4-18: Water test viscous pressure loss comparison

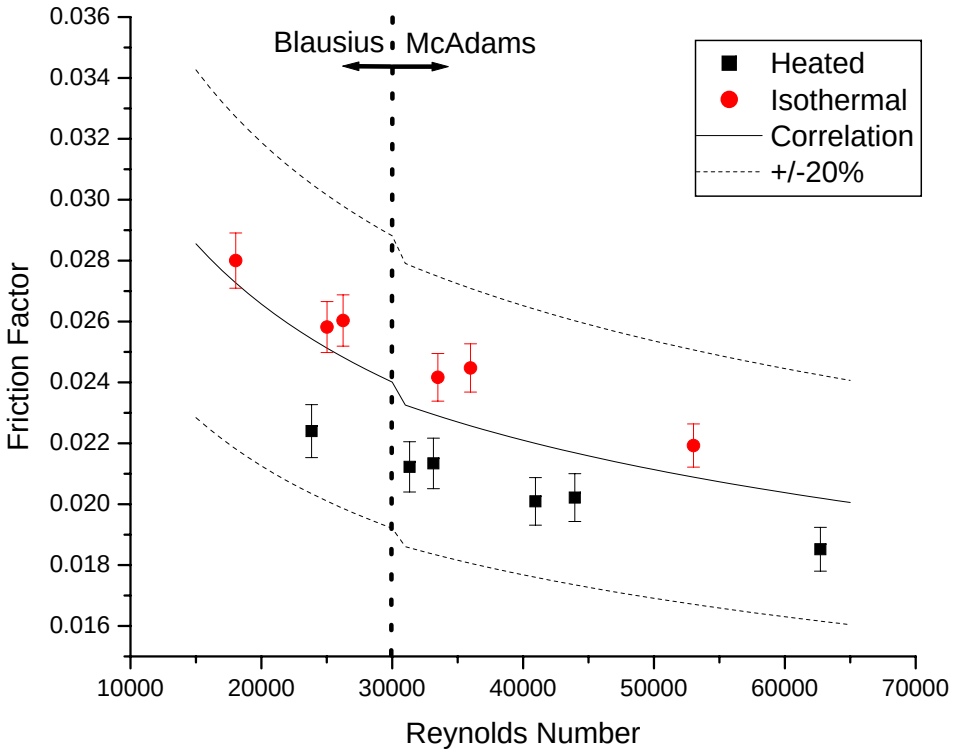

Figure 4-19: Test friction factor comparison

4.4 Nanofluid Convection Experiments

This section covers the most important piece of this work, which is the nanofluid convective heat transfer and viscous pressure loss experiments. The methodology is discussed below and the experiments follow. First, the alumina nanofluid from Nyacol will be tested. After this run, the loop will be cleaned using water and then tested with water to assure no deposition will alter the outcome. Finally, the zirconia will be tested. These results are interpreted through some theoretical analysis. All raw data for the test is given in Appendix D.

4.4.1 Methodology

The implementation of nanofluids in the loop requires some additional actions. It is desired to run the loop with different nanoparticle loadings and with different nanoparticles (Al_2O_3 and ZrO_2). It is key to know the loadings in order to utilize the correct properties in the evaluation of the data. For this reason the loop will be loaded with the maximum desired loading and then diluted to lower loadings. In order to get the desired loadings, an approximate loop volume is required. The loop volume is estimated to be roughly 7 liters. Therefore, the loop will be loaded at the maximum and then 3.5 liters will be removed and replaced with water between experimental runs. Three loadings are measured for each nanofluid. The removed nanofluids are kept for verification of the nanofluid properties, most especially the loading.

Each nanofluid is investigated at various flow rates, bulk inlet temperatures, and heat fluxes. The heat flux should have only limited effect on the nanofluid (via change in the wall viscosity) if it is behaving like a normal fluid. Bulk inlet temperature variation should catch if there is any temperature enhancing effect on the nanofluid. The flow rates should determine if there is any turbulent mixing effect of the nanofluid.

4.4.2 Alumina Results

The Nyacol alumina is run for three different loadings as follows: 0.9 vol% (3.53 wt%), 1.8 vol% (7.06 wt%), and 3.6 vol% (14.11 wt%). The weight loadings were verified

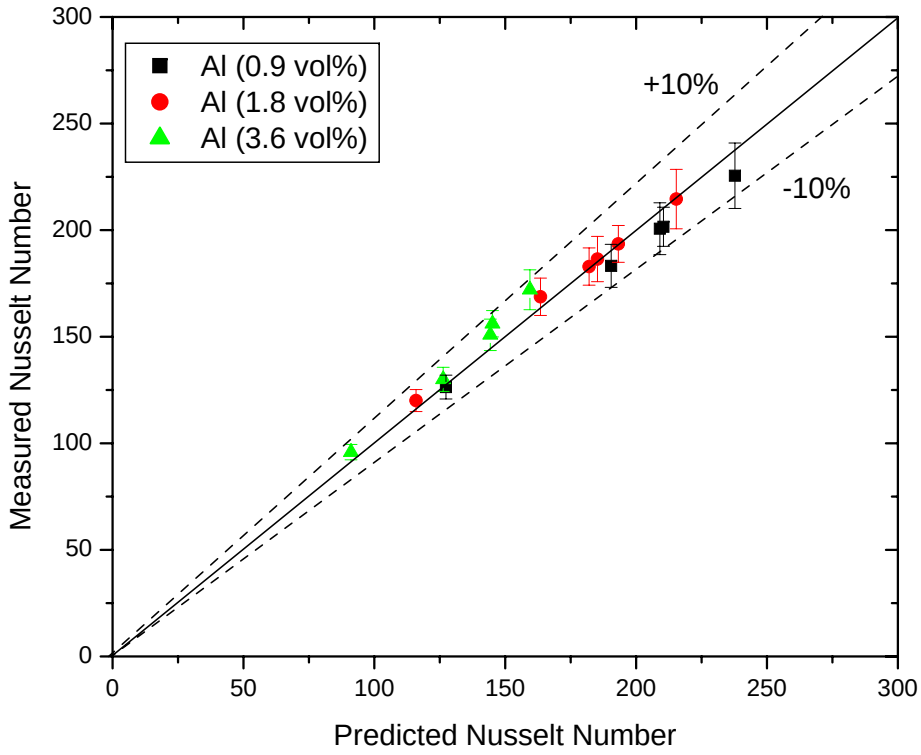

Figure 4-20: Nyacol alumina tube-average Nusselt number comparison to theory

after the experiment using TGA. The conversion between weight and volume fraction is done through the assumed density of 3920 kg/m^3 for the alumina.

Nyacol Alumina Nusselt Number

The measured Nusselt number is compared to that of the predicted Nusselt number of the Dittus-Boelter equation, as defined in Equation 4.3.1, which predicts most fluids to within ±20% of experiment. Properties of the nanofluid are determined from the temperature and loading dependent properties as defined in Section 3.9. The resulting plot is shown in Figure 4-20. It can be seen in the figure that the Nusselt number is effectively predicted by the Dittus-Boelter equation to within ±10%, if the properties of the nanofluid are used.

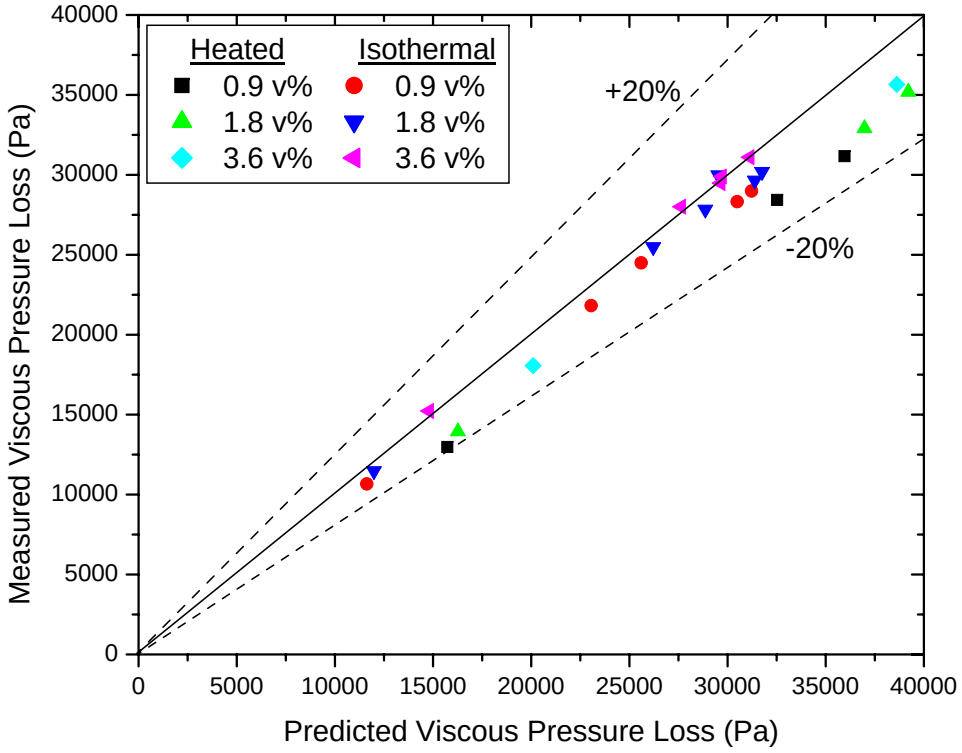

Figure 4-21: Nyacol alumina viscous pressure loss comparison

Nyacol Alumina Viscous Pressure Losses

The viscous pressure loss is also compared to the theoretical loss predicted by Blasius and McAdams correlations, Equations 4.6 and 4.7, which predict most fluids to within ±20% of experiment. The heated and isothermal pressure drop sections are both investigated and compared to theory. The viscous pressure losses are compared in Figure 4-21 and the friction factors in Figure 4-22. It can be seen in the figures that the viscous pressure losses and friction factors are effectively predicted by the theory within ±20%, if the properties of the nanofluid are used.

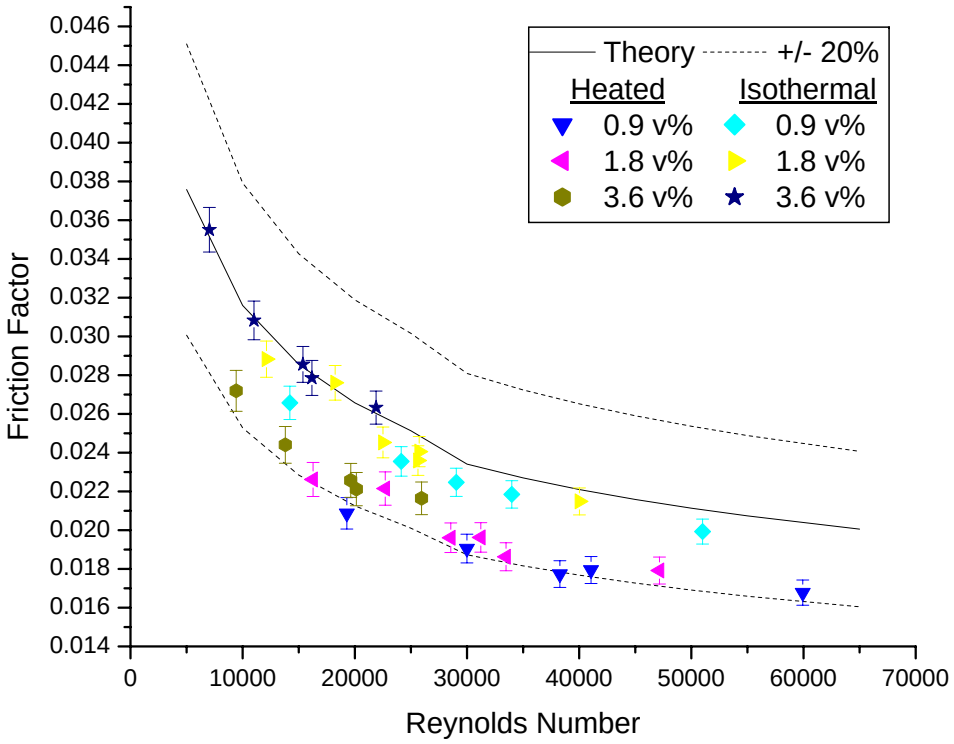

Figure 4-22: Nyacol alumina friction factor comparison

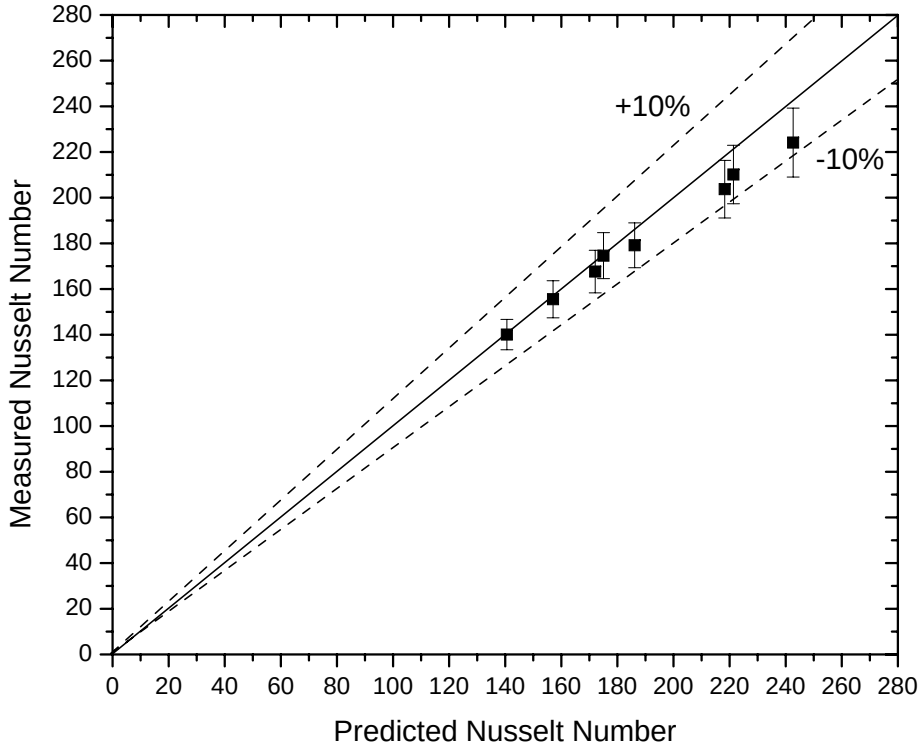

Figure 4-23: Water retest tube-average Nusselt number comparison to theory

4.4.3 Water Retest Results

After completion of the alumina testing, the loop is drained completely and flushed several times to remove the remaining nanoparticles. However in order to insure there are no surface modifications or fouling in the system, water is once again run and compared to theory. The tube average Nusselt number is shown in Figure 4-23 and the viscous pressure losses are shown in Figure 4-24 It is found that the results are similar to those of the initial tests. It is therefore concluded that no major modification of the tube surface occurred due to the usage of nanofluids.

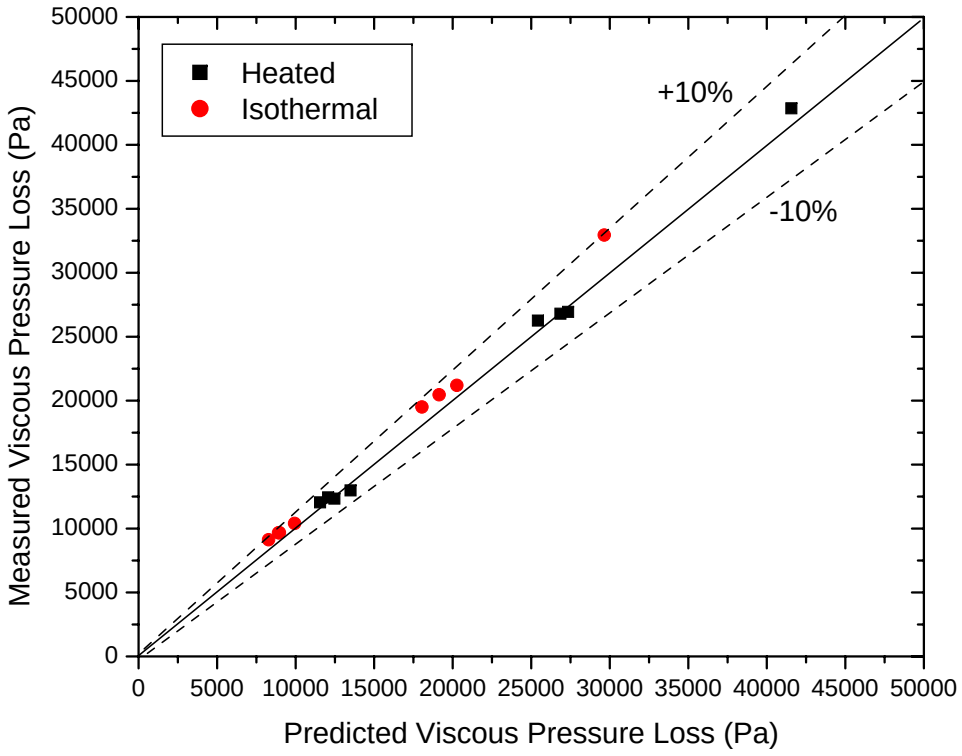

Figure 4-24: Water retest viscous pressure loss comparison

4.4.4 Zirconia Results

The Nyacol zirconia is run for three different loadings as follows: 0.2 vol% (1.1 wt%), 0.5 vol% (2.75 wt%), and 0.9 vol% (4.95 wt%). The weight loadings were verified after the experiment using TGA. The conversion between weight and volume fraction is done through the assumed density of 5500 kg/m^3 for the zirconia.

Nyacol Zirconia Nusselt Number

As earlier, measured Nusselt number is compared to that of the predicted Nusselt number of the Dittus-Boelter equation, as defined in Equation 4.3.1, which predicts most fluids to within ±20% of experiment. The temperature and loading dependent properties in Section 3.9 are used to calculate the non-dimensional groups. The resulting plot is shown in Figure 4-25. It can be seen in the figure that the Nusselt number is effectively predicted by the Dittus-Boelter equation to within ±10%, if the properties of the nanofluid are used.

Nyacol Zirconia Viscous Pressure Losses

The viscous pressure loss is also compared to the theoretical loss predicted by Blasius and McAdams correlations, Equations 4.6 and 4.7, which predict most fluids to within ±20% of experiment. The heated and isothermal pressure drop sections are both investigated and compared to theory. The viscous pressure losses are compared in Figure 4-26 and the friction factors in Figure 4-27. It can be seen in the figures that the viscous pressure losses and friction factors are effectively predicted by the theory within ±20%, if the properties of the nanofluid are used.

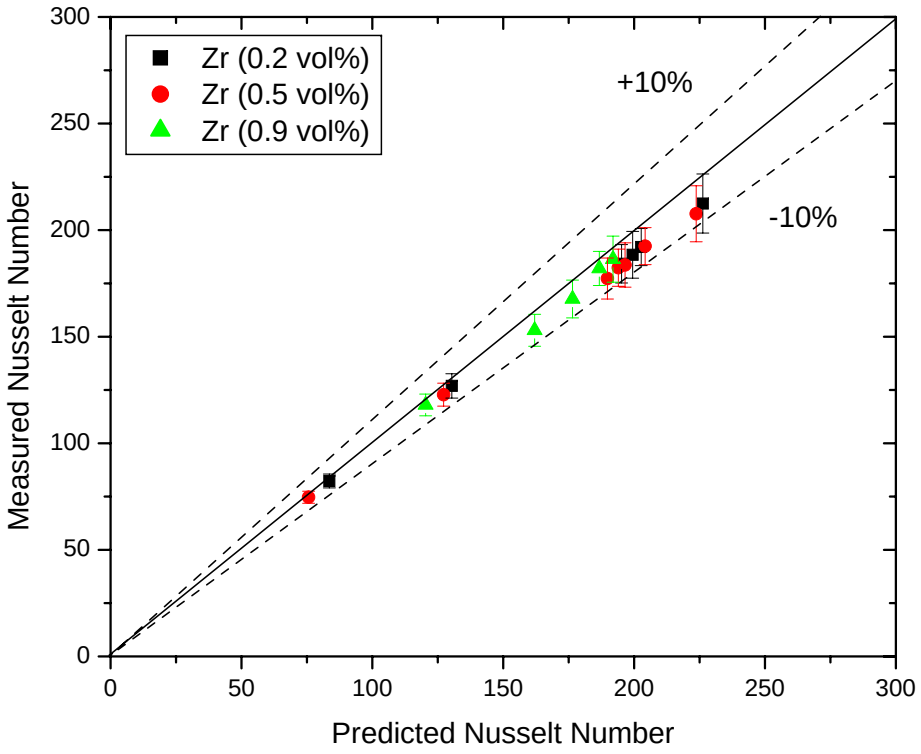

Figure 4-25: Nyacol zirconia tube-average Nusselt number comparison to theory

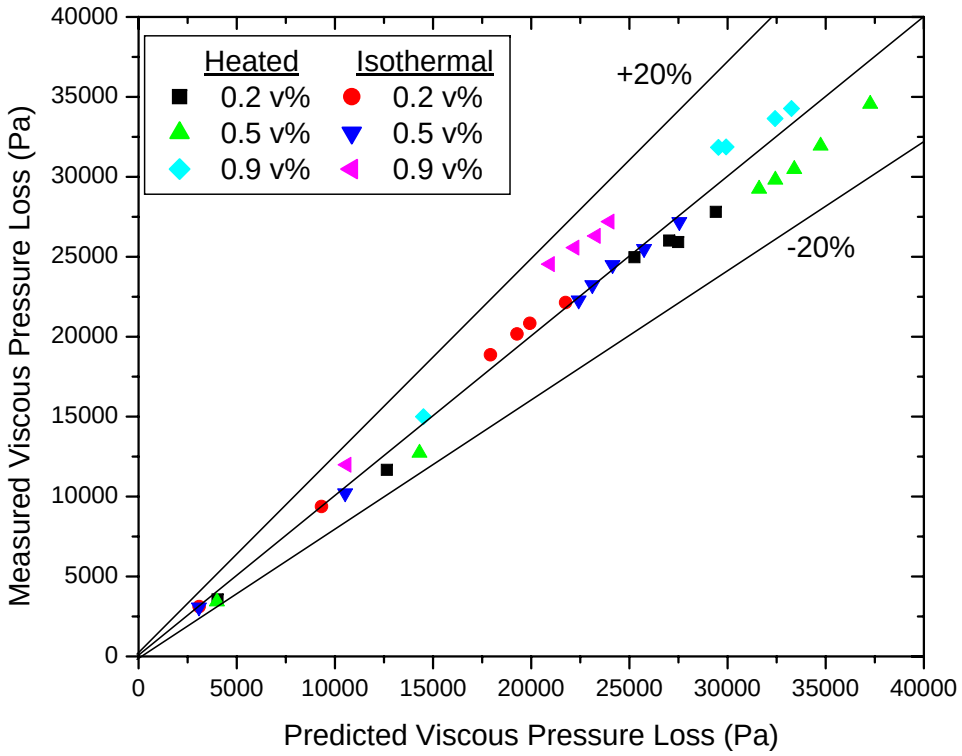

Figure 4-26: Nyacol zirconia viscous pressure loss comparison

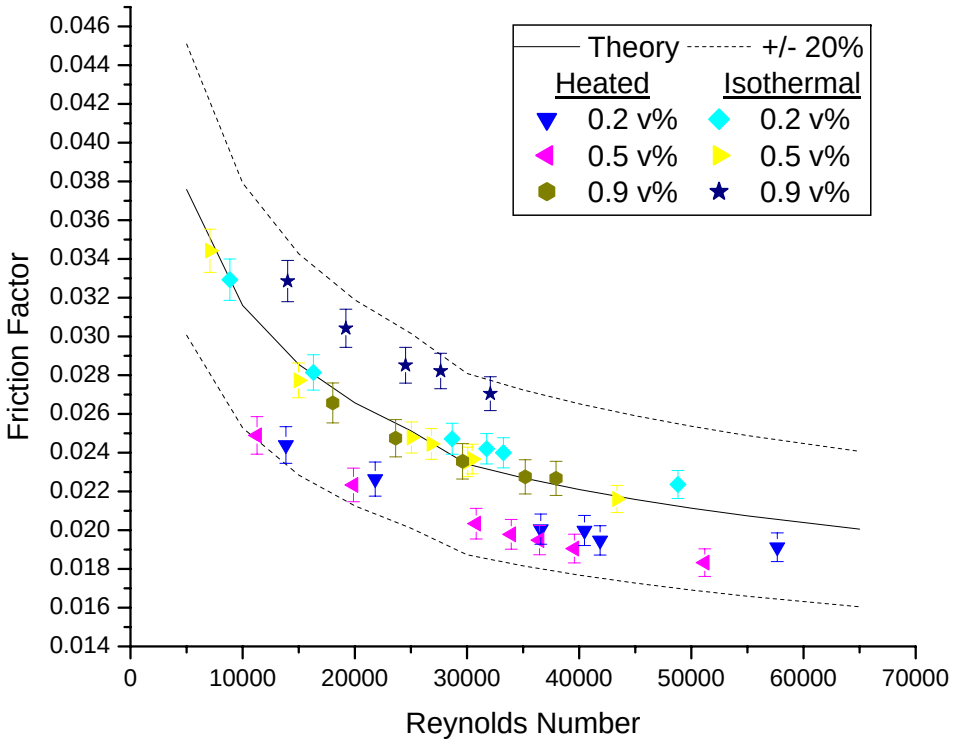

Figure 4-27: Nyacol zirconia friction factor comparison

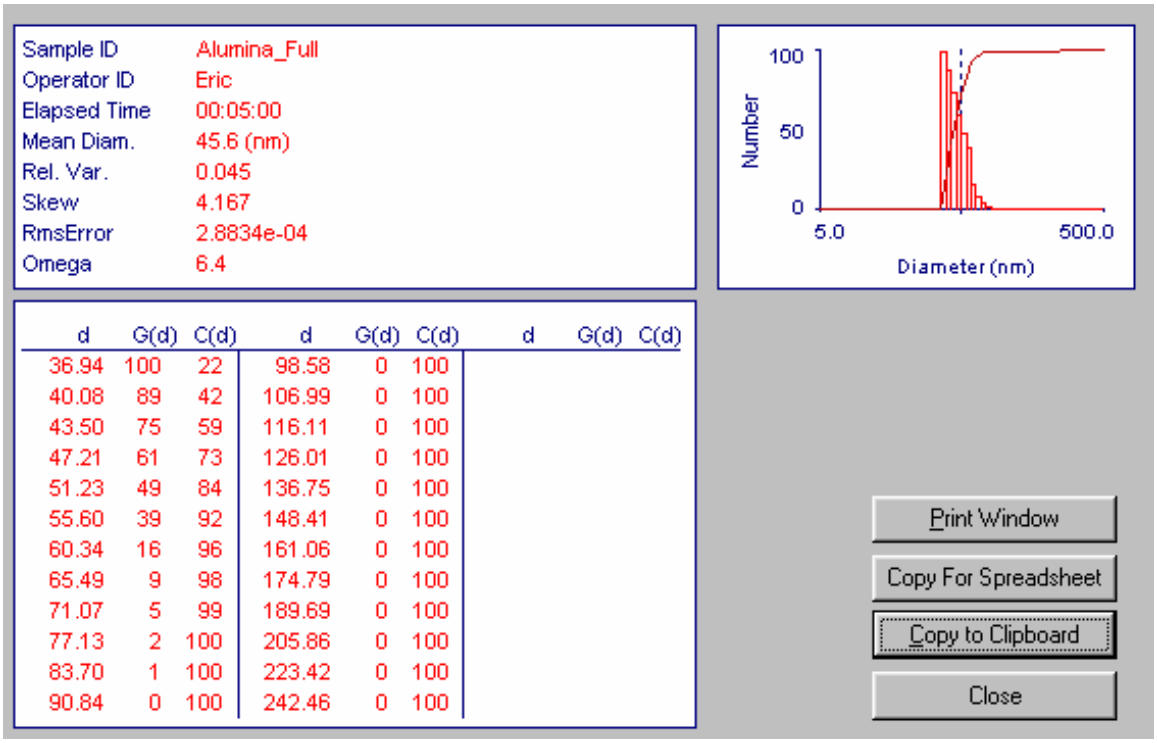

Figure 4-28: DLS of Nyacol alumina 3.6 vol%

4.5 Post Test Nanofluid Characterization

It is important to recheck the particle diameters using DLS after the experiment is completed to reassure the nanometer scales have been retained. It can be seen in Figures 4-28, 4-29, 4-30, 4-31, 4-32, and 4-33 that the particle size remained relatively the same as the initial size in the fully loaded colloid. Therefore it is determined that no major agglomeration occurred during the testing.

4.6 Data Interpretation

In their experiments with and analyses of nanofluids, Pak and Cho [34], Xuan and Roetzel [35] and Xuan and Li [2] assumed that convective heat transfer enhancement could come from dispersion of the suspended nanoparticles. However, a mechanistic description of particle dispersion in nanofluids has shown that this effect is very small by Buongiorno [43].

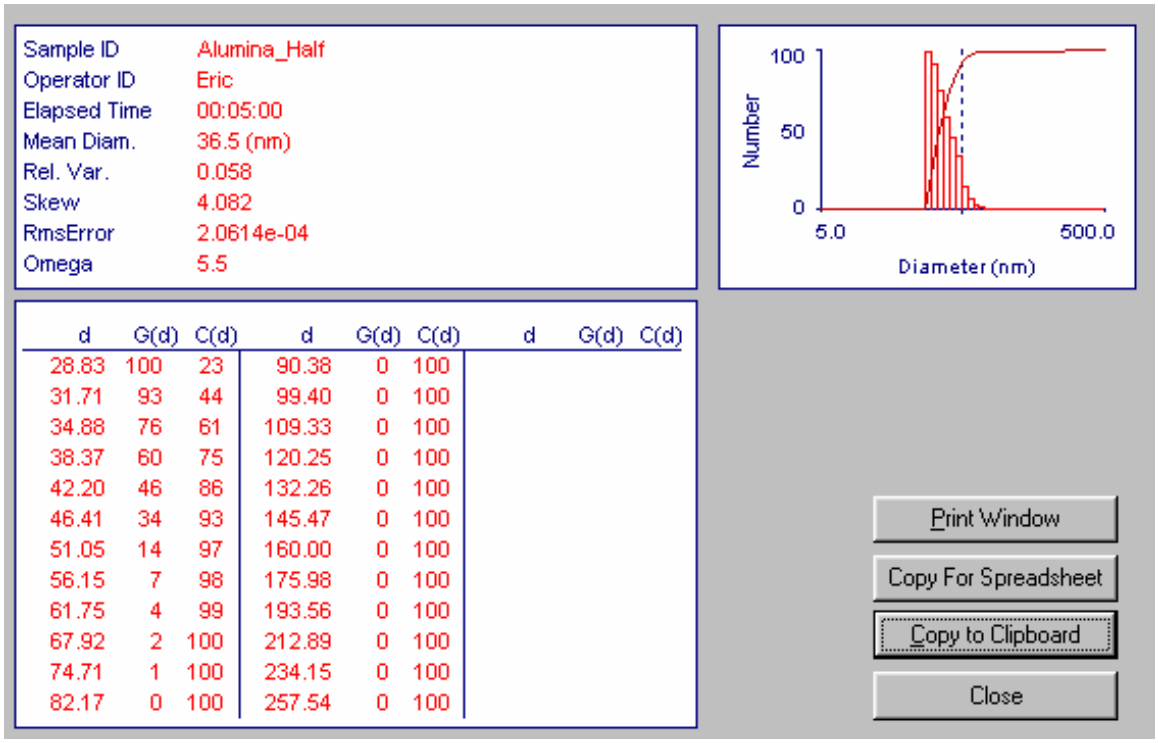

Figure 4-29: DLS of Nyacol alumina 1.8 vol%

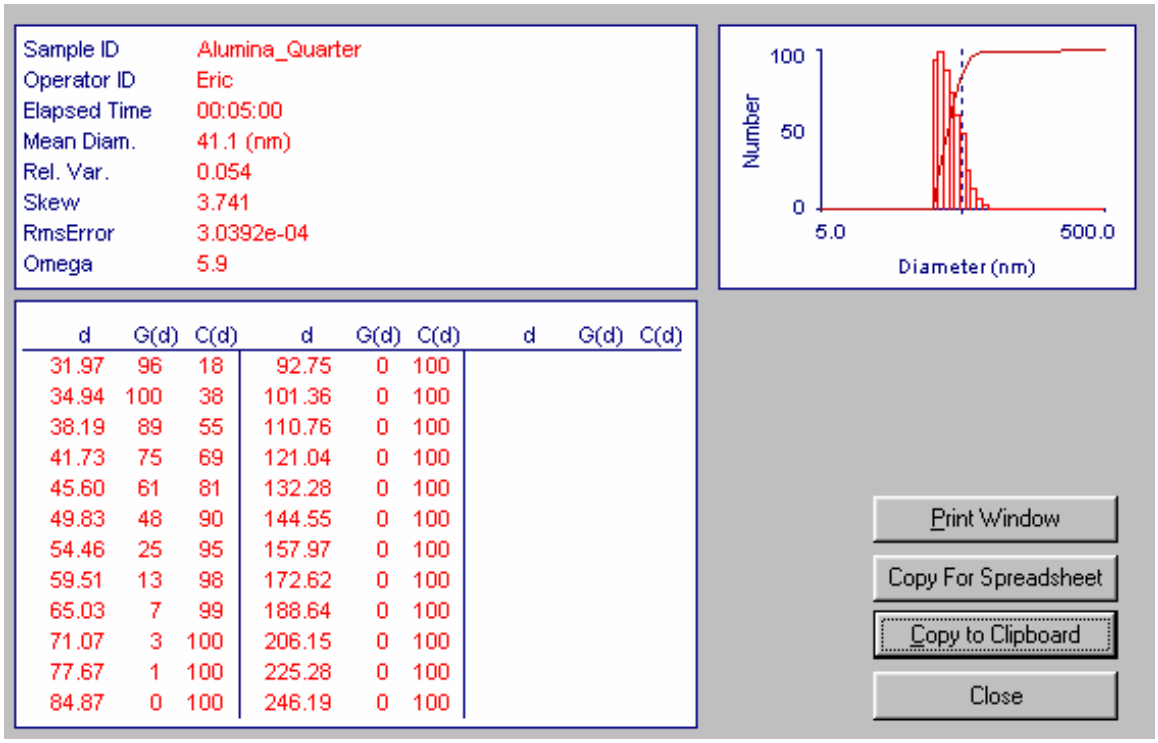

Figure 4-30: DLS of Nyacol alumina 0.9 vol%

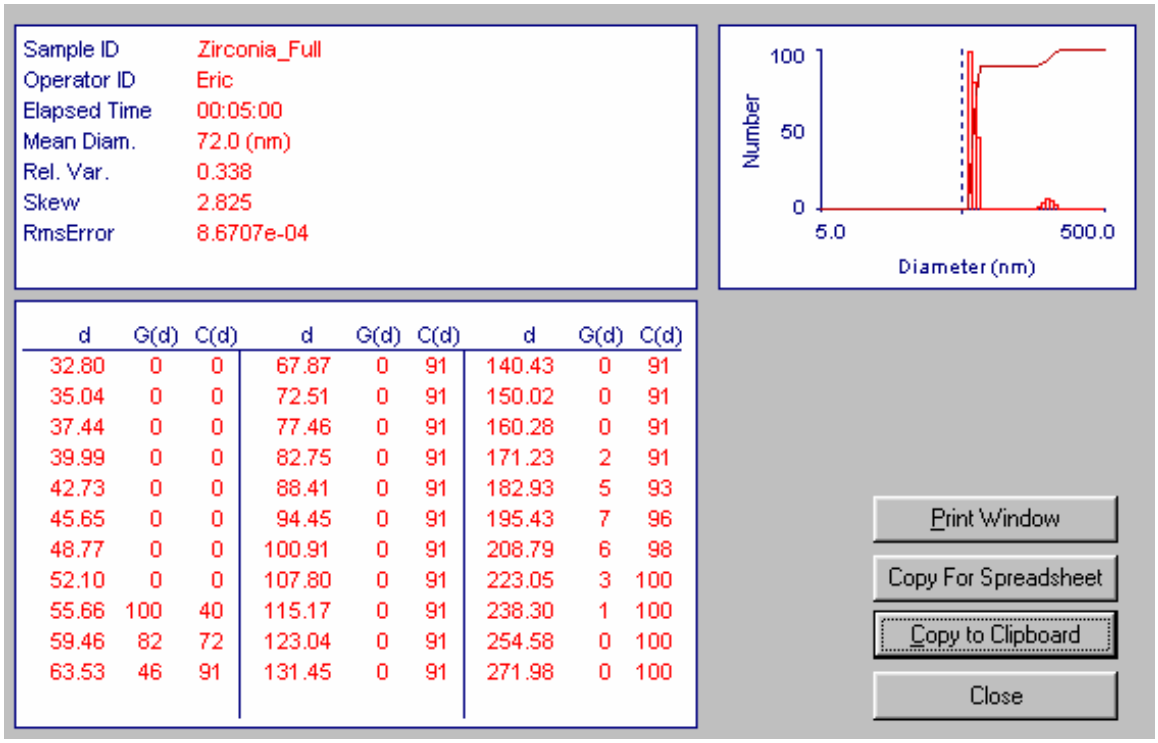

Figure 4-31: DLS of Nyacol zirconia 0.9 vol%

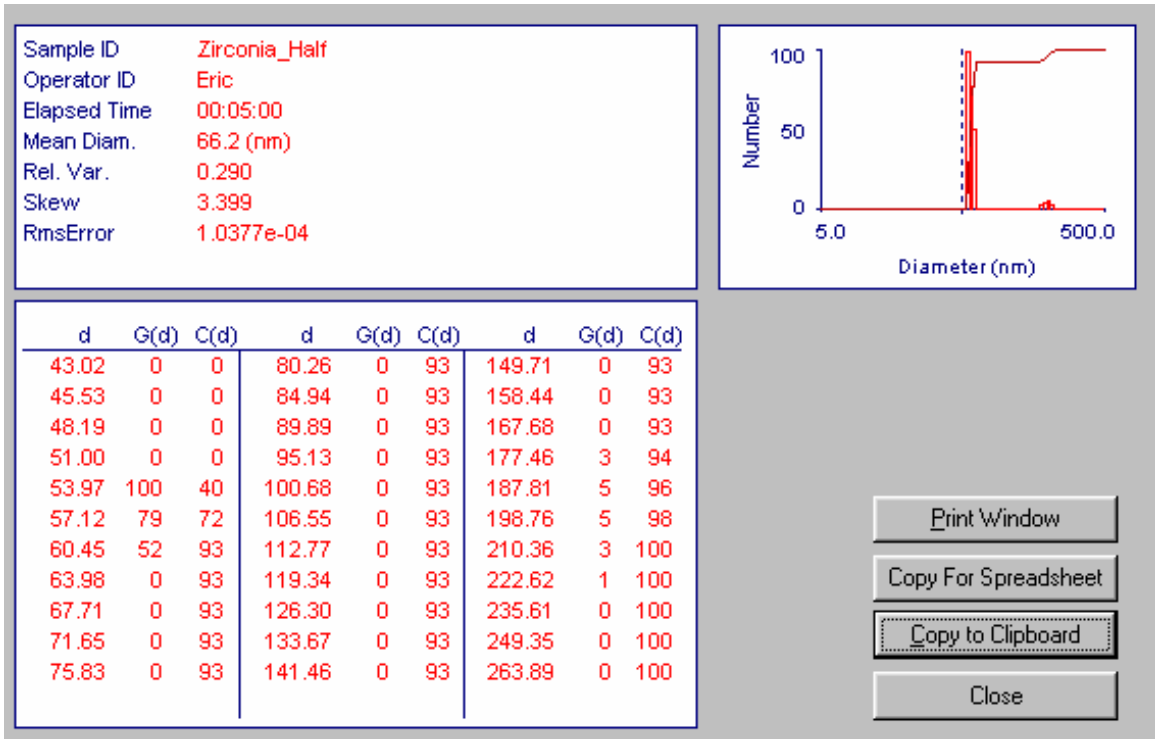

Figure 4-32: DLS of Nyacol zirconia 0.5 vol%

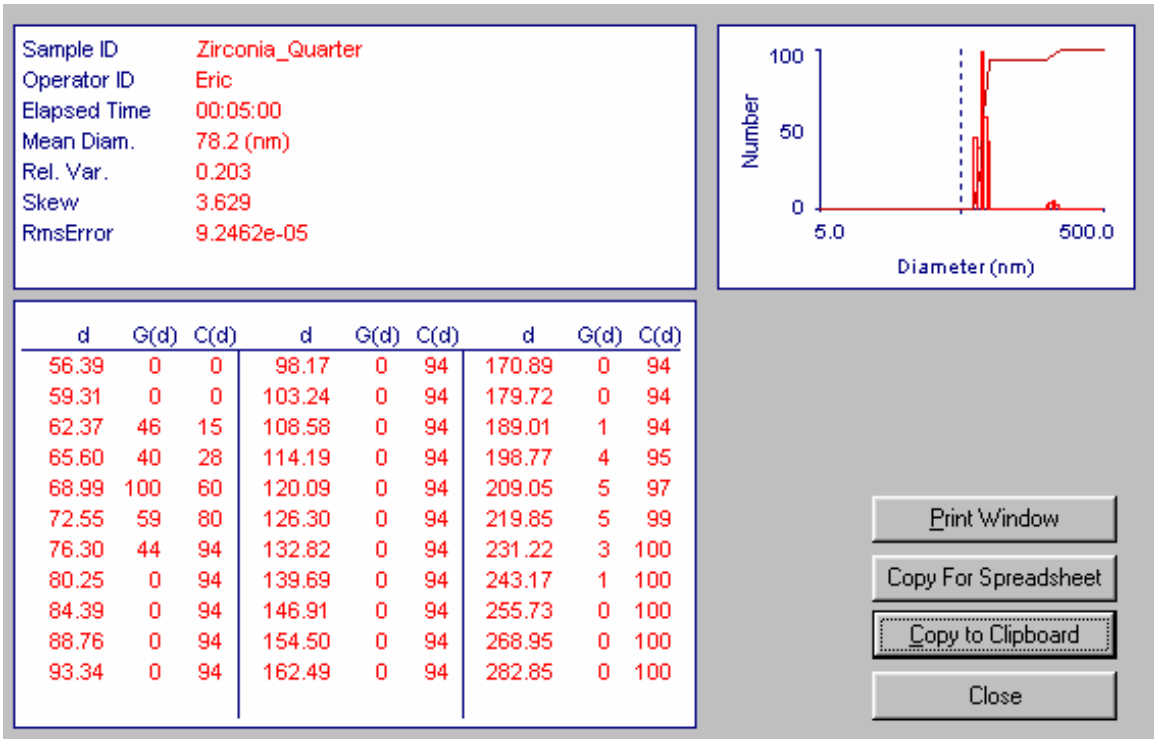

Figure 4-33: DLS of Nyacol zirconia 0.2 vol%

Xuan and Li [2] also proposed that the enhancement could come from intensification of turbulence due to the presence of the nanoparticles. However, our pressure drop measurements as well as measurements by Xuan and Li [2] and Pak and Cho [34] clearly show that turbulent friction factors in nanofluids can be very well predicted by the traditional friction factor correlations for pure fluids, if the measured nanofluid viscosity is used. This suggests that, beyond the obvious viscosity effect, turbulence is not affected by the presence of the nanoparticles. This conclusion is corroborated by a comparison of the time and length scales for the nanoparticles and the turbulent eddies, as explained next.

A comparison of the time scale of the heat transfer from the particle to the gas with the time scale of the particle slip motion in the water can be used to determine the thermal equilibrium characteristics of the mixture. The heat transfer time scale is mainly dependent on the particle to fluid conduction (τ_{con}). The values for τ_{con} are found to be on the order of 10^{-9} to 10^{-7} seconds in gases, see Figure F-3. These

values are expected to be even smaller in a liquid due to the higher density of the surrounding liquid. In turbulent flow the dominant slip mechanism is from inertial flight following the abrupt stop of an eddy. The time scale for this process is the so-called relaxation time of the particle

$$\tau_{rel} = \frac{\rho_p d_p^2}{18\mu} \tag{4.8}$$

Evaluation finds that $\tau_{con} \ll \tau_{rel}$, it is concluded that particles can exchange energy very effectively as they fly within the liquid; therefore we can assume that there is local particle/liquid thermal equilibrium.

Heat transfer enhancement due to turbulence strengthening is quantified analytically to justify why the results of our experiments above are logical. Due to their small size, nanoparticles can be entrained in both large and small turbulent eddies. This is shown by the size (l), velocity (V) and time scales (τ) of the eddies as follows:

Scales for *large* eddies:

- $l_o \sim 0.07 \cdot D = 0.07 \cdot 9.4mm = 0.658mm$
- $V_o \sim V_{shear} \sim 0.9 - 3.6m/s$ where $V_{shear} = \frac{\tau_w}{\mu}$
- $\tau_o \sim l_o/V_o \sim 1.9 - 7.3 \cdot 10^{-4} sec$

Scales for *small* eddies (using Kolomogorov's scaling laws [72]):

- $l_s/l_o \sim Re^{-3/4} \Rightarrow l_s \sim 0.17 - 0.69\mu m$
- $\tau_s/\tau_o \sim Re^{-1/2} \Rightarrow \tau_s \sim 0.8 - 7.5 \cdot 10^{-6} sec, V_s \sim l_s/\tau_s \sim 0.09 - 0.22m/s$

It is seen that the particles (40-75nm) are smaller than the eddy sizes (0.658mm and 0.17-0.69μm). Therefore, turbulent eddies can in principle carry nanoparticles.

The next step is to determine the stopping distance (S) for the particles entrained in the small and large eddies in order to see how far they can be thrown by the eddy velocities. It is found that [73]

$$S_o = \frac{\rho_p d_p^2}{18\mu} V_o \sim 0.4 - 1.5\mu m \tag{4.9}$$

for particles entrained by large eddies and

$$S_s = \frac{\rho_p d_p^2}{18\mu} V_s \sim 40 - 99nm \tag{4.10}$$

for particles entrained by small eddies. This suggests that nanoparticles do not significantly project out of the eddies with the possible exception of those entrained by small eddies. That is, the nanoparticles move with the turbulent eddies. Thus, contribution of inertial slip to nanoparticle dispersion is probably negligible. Regarding the question of turbulence intensification, the presence of the nanoparticles does increase viscosity, which will delay the onset of turbulence for given mean velocity.

Moreover, the stopping distance suggests that particles entrained by large eddies may interact with (i.e., break up) small eddies, since their length scales are comparable. Based on order-of-magnitude estimates of the kinetic energy carried by each eddy and using Kolomogorov's scaling laws, one finds that the ratio of the number of small eddies generated per unit time and volume to the number of large eddies generated per unit time and volume is proportional to $Re^{11/4}$, which in our case is greater than 10^{10}. Therefore, small eddies are much more numerous than large eddies. This means that nanoparticles being projected out of large eddies will affect only a very limited number of small eddies due to their vast numbers. In summary, an effect of the nanoparticles on turbulence beyond the obvious effect via the change in viscosity seems unlikely.

Finally, a major logic flaw will be discussed involving the previous works on turbulent convective heat transfer in nanofluids. The other major works [2], [34] pronounce enhancement of the convective heat transfer coefficients for nanofluids in tubes. The major issue is the plotting of heat transfer coefficient as a function of dimensionless Reynolds number. The nanofluids do have a higher heat transfer coefficient when compared at the same Reynolds number as a water flow. This is due to the increase in the Prandtl number. If one replots the existing data in the literature with heat transfer coefficient normalized by $Pr^{0.4}$ evaluated with the nanofluid properties, then it is obvious that this is the cause of the higher heat transfer coefficients as reported

in the literature.

The increase of Prandtl number comes from an increase in viscosity. What is not reported by the previous works is the large penalty in pumping power incurred by this increased viscosity. If one analyzes the data from a prospective of the ratio of increased heat transfer to the increase of the pumping power, it is found that the nanofluids are not an enhancement over the use of the pure water base fluid.

4.7 Conclusions

It is concluded that the nanofluids behave in a similar fashion to single-phase fluids, if one considers the temperature and concentration dependent nanofluid properties. It is therefore proven that the existing empirical correlations for viscous pressure drop and convective heat transfer coefficient in a tube describe the behavior of the nanofluids investigated. Nanoparticles in the fluids do remain at their original size, even through dilution. It is also shown theoretically how the nanoparticles would not be expected to modify the large turbulent eddies nor large numbers of small eddies and hence modify the structure of turbulence. This is confirmed by the experiments where friction factors behave under the same Reynolds dependence as typical single-phase fluids. Therefore nanofluid efficacy can be considered through properties evaluation alone.

Chapter 5

Efficacy of Nanofluids as Coolants

It has been seen that the nanofluids under investigation behave as single-phase liquids in turbulent flow and convective heat transfer in a heated tube. This creates the ability to directly compare nanofluid performance with the performance of other coolants, in particular water, through consideration of the fluid properties. Comparison of coolant performance has been studied previously for nuclear reactor and other applications. It usually involves investigation of the pumping power required to achieve certain heat removal goals under certain constraints, for example, a limited maximum temperature in the system. The methodology to be described and utilized here is that of Bonilla from the Nuclear Engineering Handbook [74]. However, this methodology can be applied also to non-nuclear systems where convective heating or cooling is involved, such as, electronic devices, chemical reactors, engines, etc. It will be shown that nanofluids can be optimized and that under certain conditions will outperform water.

5.1 Comparison of Coolants

Various factors can be considered for the selection of coolants, i.e. economics, hazards, neutronic effects, etc. An initial rough comparison can be done through consideration of the thermophysical properties of the coolant. This is most directly seen as a ratio of the required pumping power for two coolants under certain constraints. The most relevant constraints to consider for practical applications are a fixed is coolant

temperature rise (Δt_c) and a fixed coolant-film temperature difference (Δt_f).

5.1.1 Pumping power

The pumping power or work required to circulate a coolant can be calculated as

$$\mathbf{P}_{pump} = \Delta P \frac{\dot{m}}{\rho} \tag{5.1}$$

where ΔP is the pressure drop, $\dot{m}$ is the mass flow rate and ρ is the coolant density. The viscous pressure loss is

$$\Delta P_f = \frac{f_f \dot{m}^2 L}{2 D \rho S^2} \tag{5.2}$$

where D is the effective diameter of the flow geometry, S is the cross sectional area of the flow, and f_f is the friction factor and can be calculated from Eq. 4.7. If Eqs. 5.1, 5.2, and 4.7 are combined one can find the pumping power for an incompressible fluid is

$$\mathbf{P}_{pump} = \frac{0.092 L}{D^{1.2} S^{1.8}} \left[\frac{\mu^{0.2}}{\rho^2} \right] \dot{m}^{2.8} \tag{5.3}$$

where L is the effective length of the flow channel. In the case of laminar flow the equation can be modified with the friction factor defined as $f_f = C/Re$ where for round tubes $C = 64$ thus making

$$\mathbf{P}_{pump} = \frac{128 L}{D^2 S} \left[\frac{\mu}{\rho^2} \right] \dot{m}^2 \tag{5.4}$$

It can be seen that under the same constraints the coolant performance can be compared through the properties groups contained in the brackets of Eqs. 5.3 and 5.4. A ratio of these groups for two different coolants is a rough direct comparison of their performance. However further constraints must be supplied to make the comparison more definitive.

5.1.2 Constant coolant temperature rise

First consider a system that has a large bulk temperature difference from inlet to outlet as compared to the film temperature difference ($\Delta t_c >> \Delta t_f$), which would be the case for small diameter, long channels with low heat flux. If the bulk temperature difference is held to be constant. The substitution of $q/c_p\Delta t_c$ for $\dot{m}$ in Eqs. 5.3 and 5.4 gives

$$\mathbf{P}_{pump} = \frac{0.092Lq^{2.8}}{D^{1.2}S^{1.8}\Delta t_c^{2.8}}\left[\frac{\mu^{0.2}}{\rho^2 c_p^{2.8}}\right] \tag{5.5}$$

for turbulent flow and

$$\mathbf{P}_{pump} = \frac{128L}{D^2 S}\frac{q^2}{\Delta t_c^2}\left[\frac{\mu}{\rho^2 c_p^2}\right] \tag{5.6}$$

for the case of laminar flow. The groups contained in the brackets contain the effects due to the coolant properties. It can be seen that viscosity, density, and heat capacity are the only important properties and thermal conductivity is of no importance under the sole constraint of fixed Δt_c.

5.1.3 Constant coolant-film temperature difference

Now consider a system that has a large film temperature difference as compared to the bulk temperature difference from inlet to outlet ($\Delta t_f >> \Delta t_c$), which would be the case for larger diameter, short channels with high heat flux. If the film temperature difference is held constant (i.e. heat transfer coefficient is held constant). Utilizing the Dittus-Boelter correlation $Nu = hD/k = 0.023Re^{0.8}Pr^{0.4}$ to find the average velocity (or mass flow rate) it is found that

$$\mathbf{P}_{pump} = \frac{49850LSh^{3.5}}{D^{0.5}}\left[\frac{\mu^{1.835}}{\rho^2 c_p^{1.167}k^{2.4}}\right] \tag{5.7}$$

for fully developed turbulent flow in a tube of non-metallic coolants and

$$\mathbf{P}_{pump} = 5.66L^3D^2h^6\left[\frac{\mu}{\rho^2 c_p^2 k^4}\right] \tag{5.8}$$

for the case of laminar flow.

Transport properties	Volume fraction of nanoparticles						
	0.3%	0.5%	0.8%	1.0%	1.2%	1.5%	2.0%
k_{nf} (W/m·°C)	0.6054	0.615	0.6252	0.6306	0.633	0.663	0.702
$\upsilon_{nf} \times 10^6$ (m^2/s)	0.91	0.915	0.945	0.96	1.012	1.044	1.125

Figure 5-1: Properties of copper water nanofluids from Xuan and Li [2]

5.2 Efficacy of Nanofluids

Using the above described methodologies we will define the efficacy of a coolant as the ratio of the property parameters in brackets with that of water. For example, for the constant coolant temperature rise in turbulent flow case as given in Equation 5.5 the efficacy would be defined as

$$\frac{\left[\frac{\mu^{0.2}}{\rho^2 c_p^{2.8}}\right]_{water}}{\left[\frac{\mu^{0.2}}{\rho^2 c_p^{2.8}}\right]_{coolant}} \tag{5.9}$$

Therefore if the coolant has better performance than that of water (which is nominally the best selection) then the efficacy would be greater than unity. Properties of zirconia and alumina nanofluids are calculated using the models proposed in Section 3.9. The properties for copper in water are determined from curve fits of the properties given by Xuan and Li [2], which was only to a volume fraction of 2%, see Figure 5-1. The efficacy for each fluid under the above constraints is calculated and plotted in Figures 5-2, 5-3, 5-4, and 5-5. It can be seen that the only potentially beneficial nanofluid is the copper under the laminar constant film temperature case. The major issue is that the dominating factor is typically the viscosity and not the conductivity. The product of density and heat capacity remains relatively constant for all materials, except for porous insulators. However there is also a mild dependence on heat capacity, $C_p^{0.8}$, which is typically lower for the water nanofluid than the base water. The other main issue is the large increase in viscosity associated with the nanoparticle

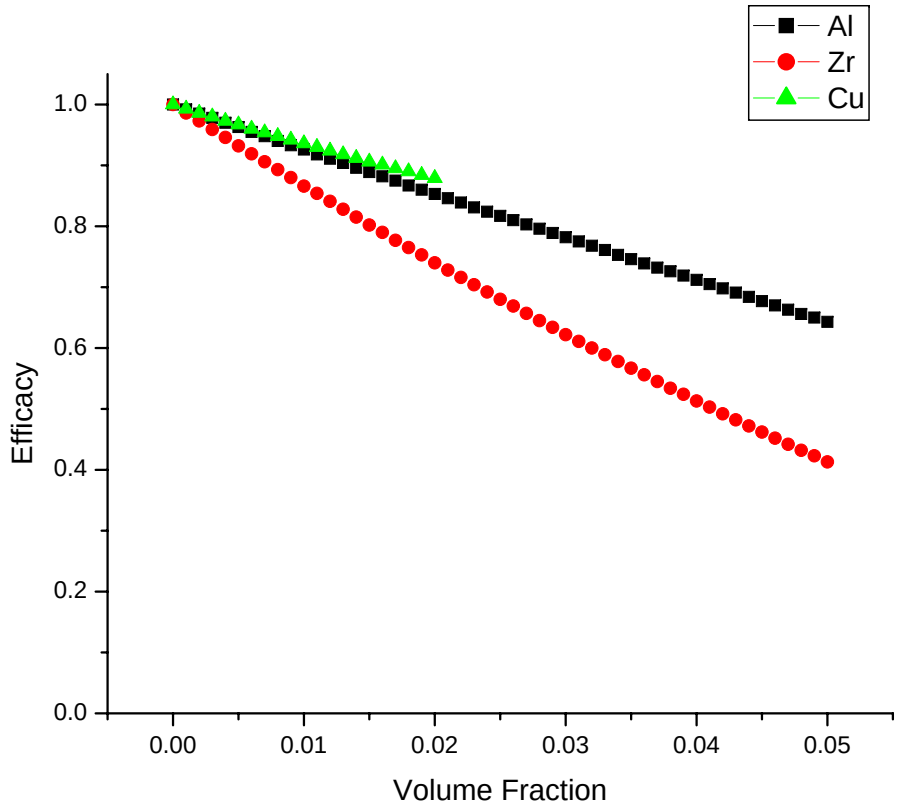

Figure 5-2: Efficacy of nanofluids under laminar bulk temperature rise constraint

dispersions. Likewise in order to increase the stabilization requires increasing surface charge density, which in turn increases the viscosity. The thermal conductivity effect may become important in the constant film temperature cases, primarily for laminar flow and only in the case for nanofluids with high thermal conductivity enhancement such as Cu based nanofluids..

5.3 Conclusions

Assuming that nanofluids behave in the same fashion as single-phase fluids, it was shown that the efficacy for these fluids can be determined theoretically if the properties are known. It is determined that the nanofluids tested in this study afford no enhancement for turbulent convective heat transfer enhancement at a given pump-

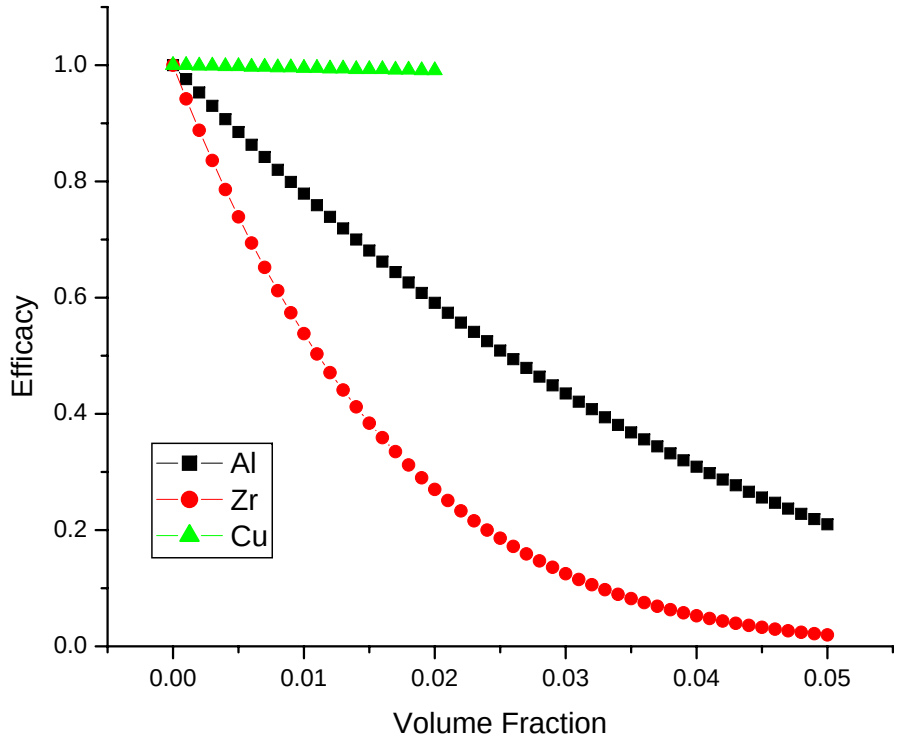

Figure 5-3: Efficacy of nanofluids under turbulent bulk temperature rise constraint

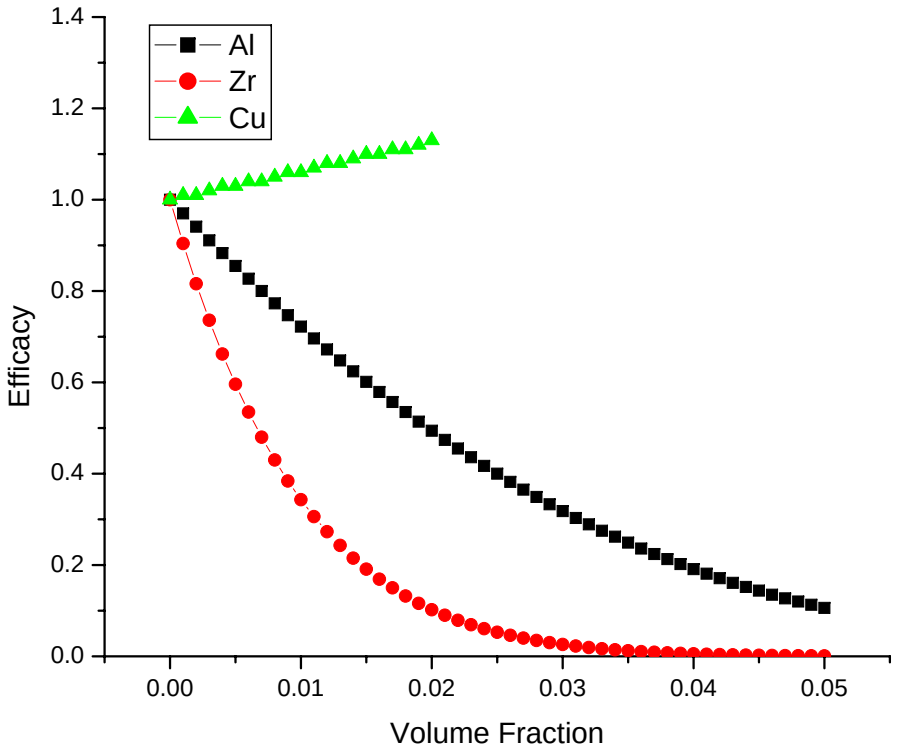

Figure 5-4: Efficacy of nanofluids under laminar film temperature rise constraint

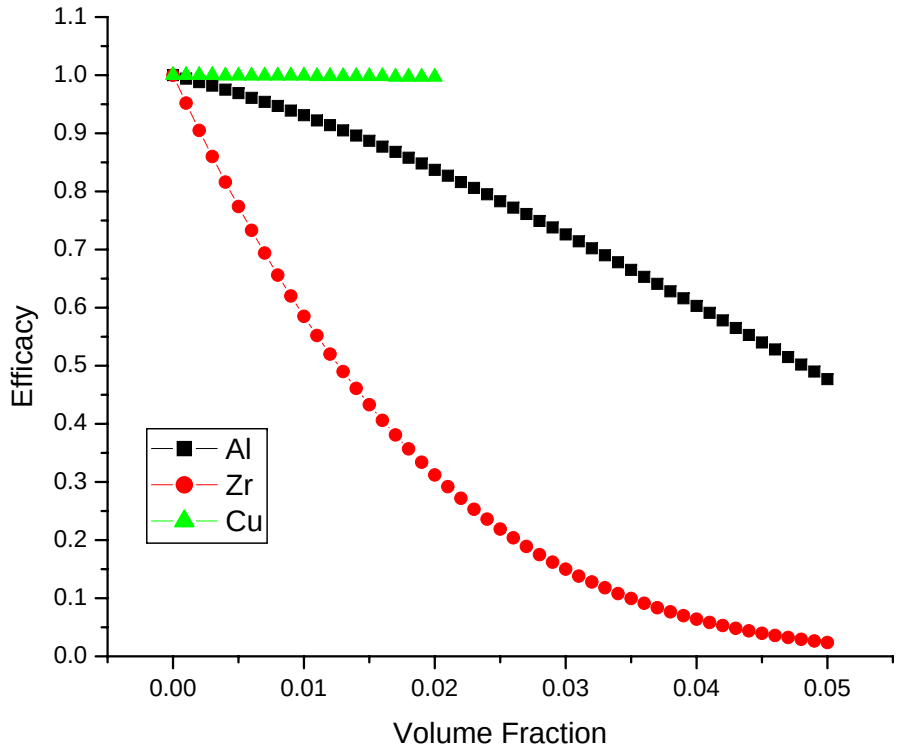

Figure 5-5: Efficacy of nanofluids under turbulent film temperature rise constraint

ing power. However fluids could possibly be beneficial to short channel high heat flux laminar flow situations. It is very important to maintain the viscosity as low as possible, while obtaining the thermal conductivity enhancement, which is intuitive.

Our experiments suggest that nanofluids convective heat transfer can be accurately described using traditional homogenous-medium theories. However such theories do not account for potential enhancement of heat transfer in the developing length, which has been shown to be important in laminar flows in recent works on nanofluids, like Ding et al. [75].

Another problem is the usage of nanoparticles in the enhancement of the thermal properties of other coolants like ethylene glycol or refrigerants. It is important to remember that these coolants are used for particular purposes besides their heat transfer capability. Water is a superior heat transfer medium typically, however other coolants are better under certain temperature constraints. Ethylene glycol is typically used when the operating temperature is expected to drop below the freezing point of water. Likewise refrigerants are used for their higher volatility or ability to evaporate. It is yet to be seen how the addition of particles would affect evaporation and freezing. Studies in this area are ongoing at MIT.

Chapter 6

Conclusions

In conclusion, there are many variables that must be accounted for when dealing with nanofluid (colloid) experiments. The conceptual and theoretical developments of colloid and surface science lead to a far better understanding of nanofluid properties and behavior. Some properties such as size and stability are easily altered by concentration, pH, and temperature modifications. ***Nanofluids are colloids*** and should be investigated as such.

A description of the techniques to characterize nanofluids quantitatively has been given. Of these techniques, DLS and TEM have been selected for particle and agglomeration sizing of the nanofluids. It is determined that DLS should be the primary method of particle sizing, due to its ease of use and low cost. However, TEM imaging must be used in order to certify the results because of the potential for error due to non-spherical particles and polydispersity in the system. ***DLS and TEM are the best techniques to characterize particle sizes.***

ICP and TGA are the best techniques for the determination of nanofluid concentration. ICP is very effective in determining the exact elemental constituents of the system. It can be used to find contamination down to the ppb level of multiple elements with great ease. The major drawback of ICP is that it only determines elemental makeup of the system and not the molecular/chemical makeup. Therefore some calculation must be done in order to determine weight loading of nanoparticles. For this reason TGA is a quick and easy method of determining particulate loading of

a system. The "cooking off" of constituents allows one to see surfactant weight loading, as well as, the particle loading. Therefore a combination of the two techniques is recommended for nanofluid characterization.

Implementation of a short hot wire thermal conductivity probe has been successful in the determination of the thermal conductivity of basic liquids and more importantly the nanoparticle colloids. Likewise, the glass capillary viscometer is found to be effective in the measurement of the viscosity of nanoparticle colloids at different loadings and temperatures. It is concluded that ***nanofluids behave in a similar fashion to equivalent single-phase fluids, if one considers the temperature and concentration dependent nanofluid mixture properties.***

It is proven that the traditional empirical correlations for viscous pressure drop and convective heat transfer coefficient in a tube describe the behavior of the nanofluids investigated. It is also shown by means of order-of-magnitude estimates that the nanoparticles would not be expected to modify the large turbulence eddies nor large numbers of small eddies and hence modify the flow structure. This is reiterated by the experiments where friction factors behave under the same Reynolds dependence as typical single-phase fluids.

Nanofluid efficacy can be considered through properties evaluation alone. Assuming that nanofluids behave in the same fashion as single-phase fluids, it is shown that the efficacy for these fluids depends only on their thermophysical properties. It is determined that the current nanofluids are of no interest for turbulent convective heat transfer enhancement. However fluids could possibly be beneficial to short channel high heat flux laminar flow situations. It is very important to maintain the viscosity as low as possible, while obtaining the thermal conductivity enhancement, which is somewhat intuitive.

It is recommended that future nanofluids could be easily investigated using theory and properties measurement. However the theory does not account for potential enhancement of heat transfer in the developing length, which is important in laminar flows. However, theory can be a guide for the development of future engineering coolants like nanofluids.

Appendix A

Hot-Wire Numerical Studies by Roberto Rusconi

A.1 The transient hot-wire method: numerical simulations

Numerical simulations have been performed for the THW method using a commercial finite-elements solving routine, *FlexPDE Professional 3D* (PDE Solutions Inc.), which requires a direct implementation of the governing equations. By exploiting the symmetry of the problem, a 2D cylindrical model is chosen (see Figure A-1) and a self-adapting mesh of triangular elements (derived from an analogue problem [68]).

The Navier-Stokes equations are used along with the Boussinesq approximation, the so-called "Poisson pressure" equation, and the heat diffusion equations as:

$$\nu\nabla\cdot\nabla v_r = \frac{1}{\rho}\frac{\partial p}{\partial r} + v_r\frac{\partial v_r}{\partial r} + v_z\frac{\partial v_r}{\partial z} + \frac{\partial v_r}{\partial t}$$

$$\nu\nabla\cdot\nabla v_z = \frac{1}{\rho}\frac{\partial p}{\partial r} + v_r\frac{\partial v_z}{\partial r} + v_z\frac{\partial v_z}{\partial z} + \frac{\partial v_z}{\partial t} - g\alpha\Delta T$$

$$\nabla\cdot\nabla(p/\rho) = \delta\left[\frac{1}{r}\frac{\partial r v_r}{\partial r} + \frac{\partial v_z}{\partial z}\right] + 2\left(\frac{\partial v_r}{\partial r}\frac{\partial v_z}{\partial z} - \frac{\partial v_r}{\partial z}\frac{\partial v_z}{\partial r}\right) - g\alpha\frac{\partial\Delta T}{\partial z}$$

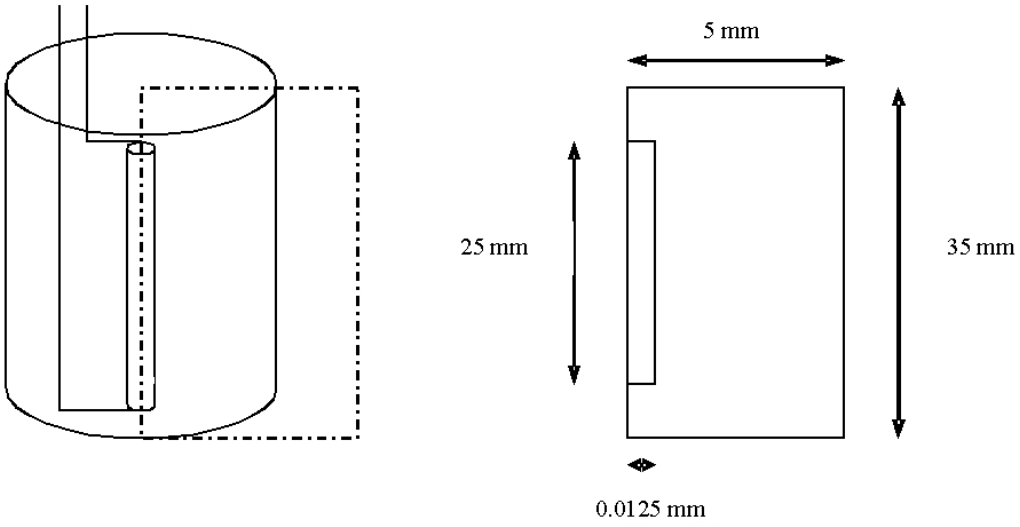

Figure A-1: Computational domain used in the numerical simulations.

$$\kappa \nabla \cdot \nabla(\Delta T) \;=\; v_r \frac{\partial \Delta T}{\partial r} + v_z \frac{\partial \Delta T}{\partial z} + \frac{\partial \Delta T}{\partial t}$$

where v_r and v_z are the radial and axial components of momentum, ρ is the density and δ is the penalty coefficient which numerically enforces the incompressibility of the velocity field, for more details see [68]. In contrast with [68], this case has two different areas: the wire (solid) and the sample (liquid). As the routine doesn't allow the implementation of distinct equations for different regions, a parameter `m` which is equal 1 in the liquid area and 0 in the solid one is used. In this way only the Fourier equation has been solved for the wire and it was checked that this imposition didn't affect the solution of the other equations in the liquid part.

A.1.1 Case: simple fluid without convection

First, the results obtained by the numerical simulations for pure water (at room temperature) in absence of natural convection ($g = 0$) with the theoretical analysis are given.

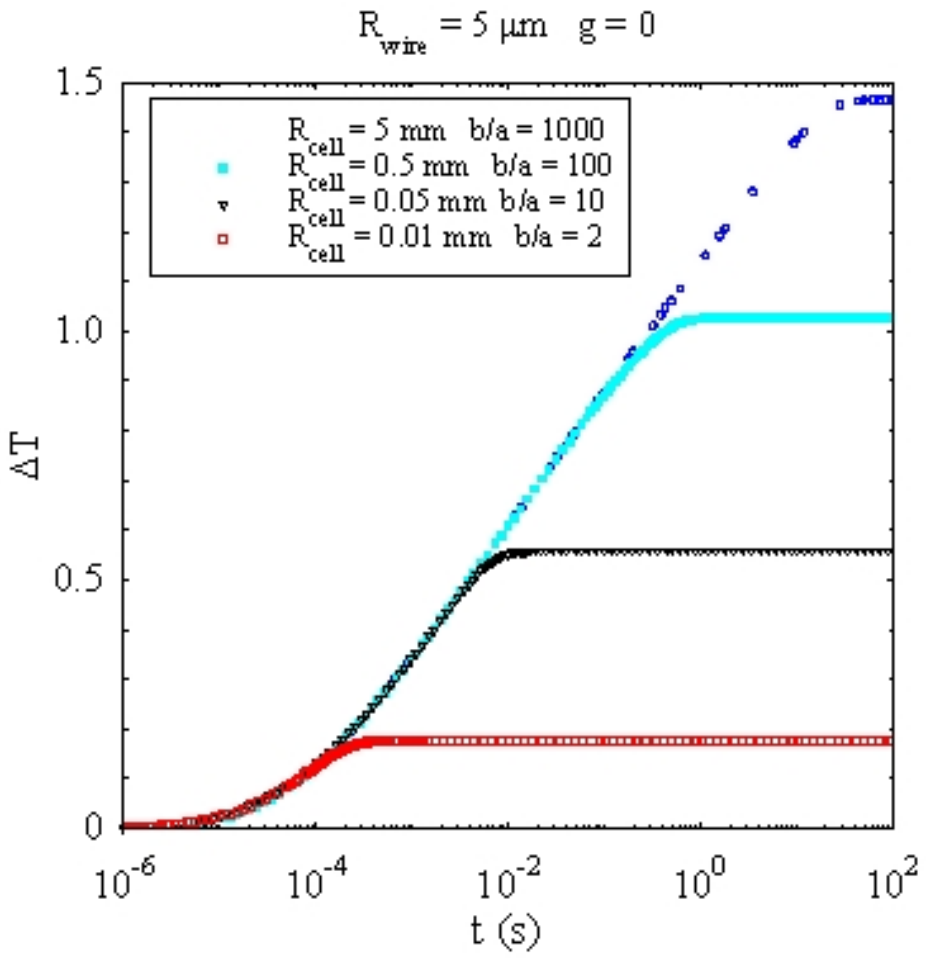

Figure A-2: Effect of the finite boundary on the temperature rise.

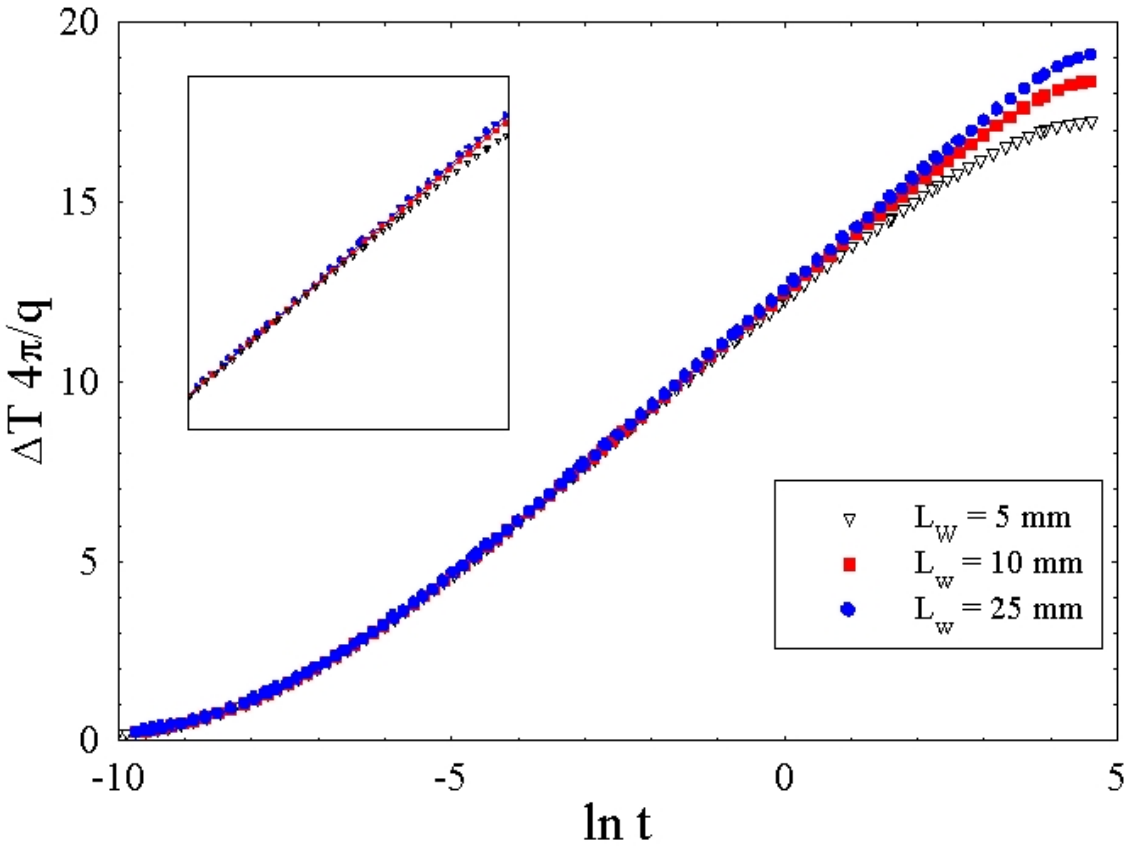

Figure A-3: Temperature increase for different lengths of the wire.

In Figure A-2 the temperature increments (ΔT is meant as an average of the temperature field over the entire wire) are displayed for distinct ratios between the outer radius and the radius of the wire: it is clearly seen that the logarithmic growth, which is independent of the size of the cell but is longer for larger outer radii, and the steady-state value, which is proportional to $\ln(b/a)$.

In Figure A-3 the results for different lengths of the wire are given: in case of $L = 25mm$ a value of thermal conductivity is obtained (the inverse of the slope of the curves) equal to $0.621\,Wm^{-1}K^{-1}$, which slightly higher of the real value $0.607\,Wm^{-1}K^{-1}$. It is noticed that with shorter wires the difference from the theoretical model is stronger. Moreover it can seen in Figure A-4 that the temperature rise divided by the applied power is not dependent on the input current, as expected.

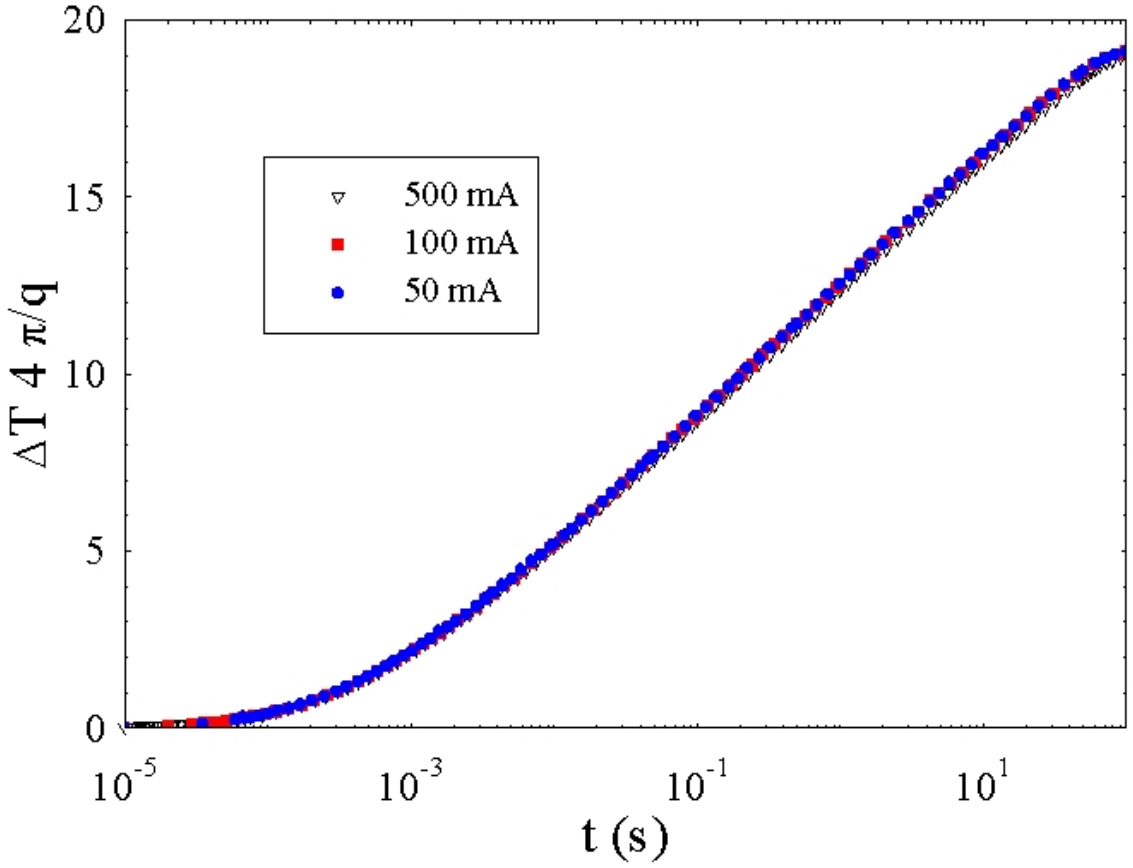

Figure A-4: Temperature increase for different input currents.

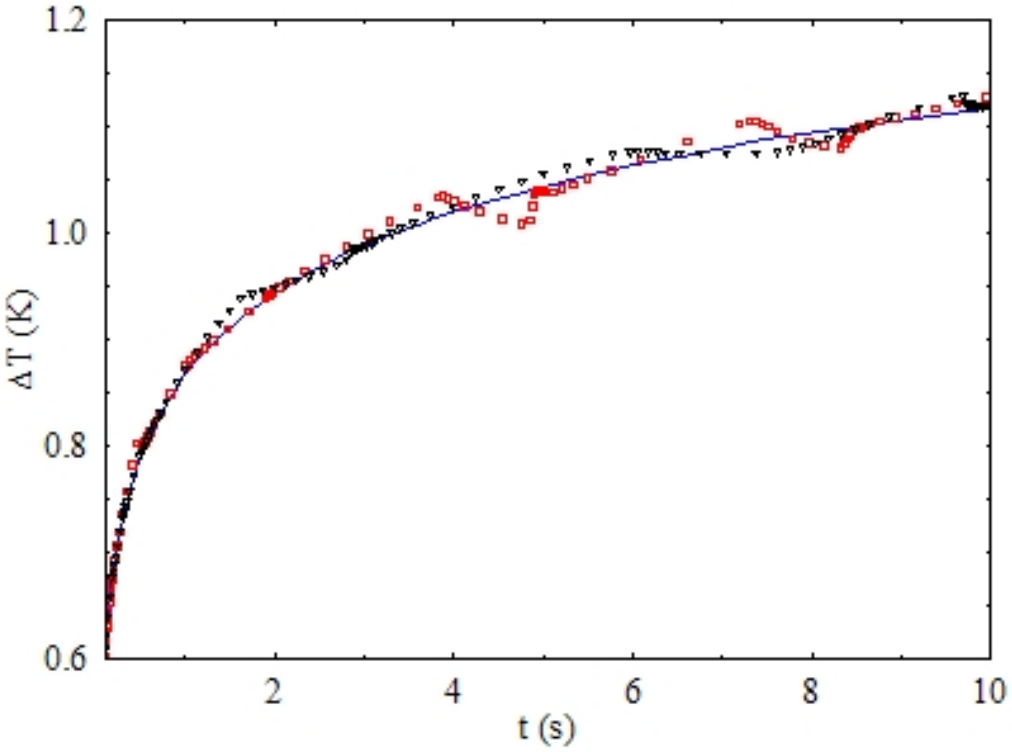

Figure A-5: Numerical instabilities in the solution.

A.1.2 Case: simple fluid with convection

After verifying that the model used in the simulations is consistent with the theory of THW, the effect of natural convection is analyzed by the same method. In order to reduce computational times, but at the same time to preserve the accuracy of the solution, the influence of some numerical parameters (mesh size, solution controls and penalty factor) are investigated for their effect on the numerical results. In Figure A-5 it is noticeable that in some cases the simulations can have an oscillatory behavior, while the full line is the accurate and mesh-independent solution.

In Figure A-6 it is seen how the temperature field after $100s$ is distorted by the presence of the convective rolls in Figure A-7. In Figure A-8 the time-dependent temperature increments with or without natural convection are compared. The presence of a velocity field produces a sensible deviation from the logarithmic trend after some seconds. This is much more evident if it is considered that instead of taking the

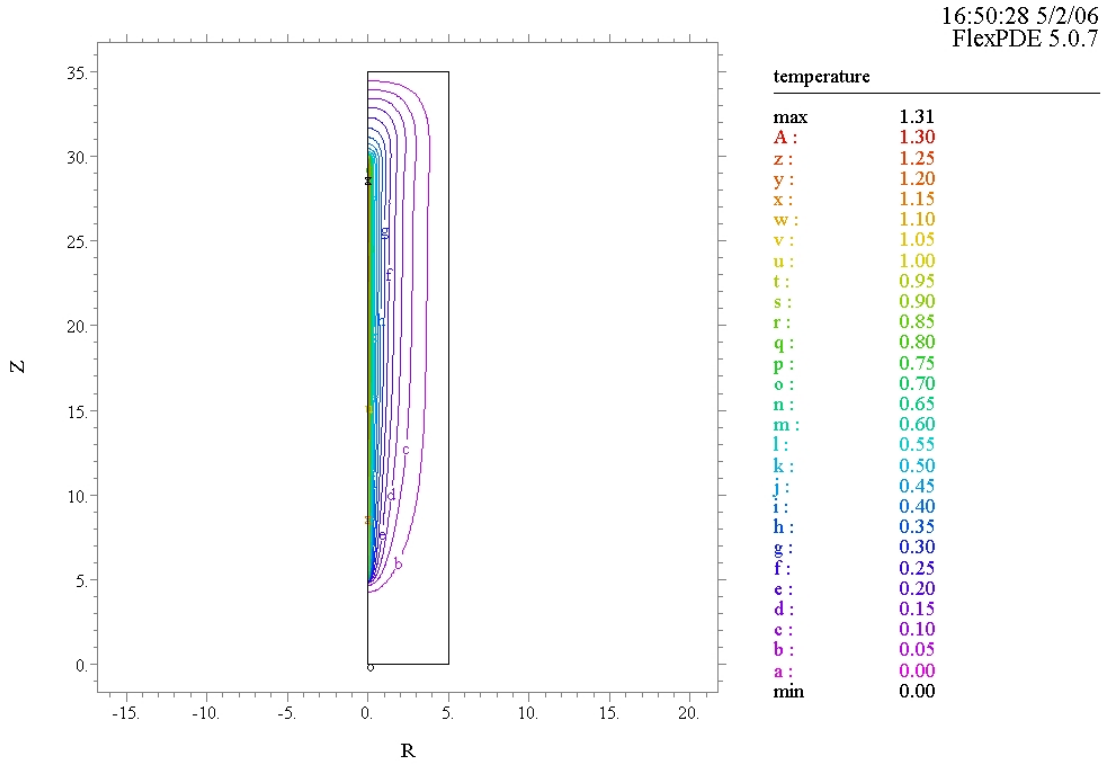

Figure A-6: Temperature field after 50s for water.

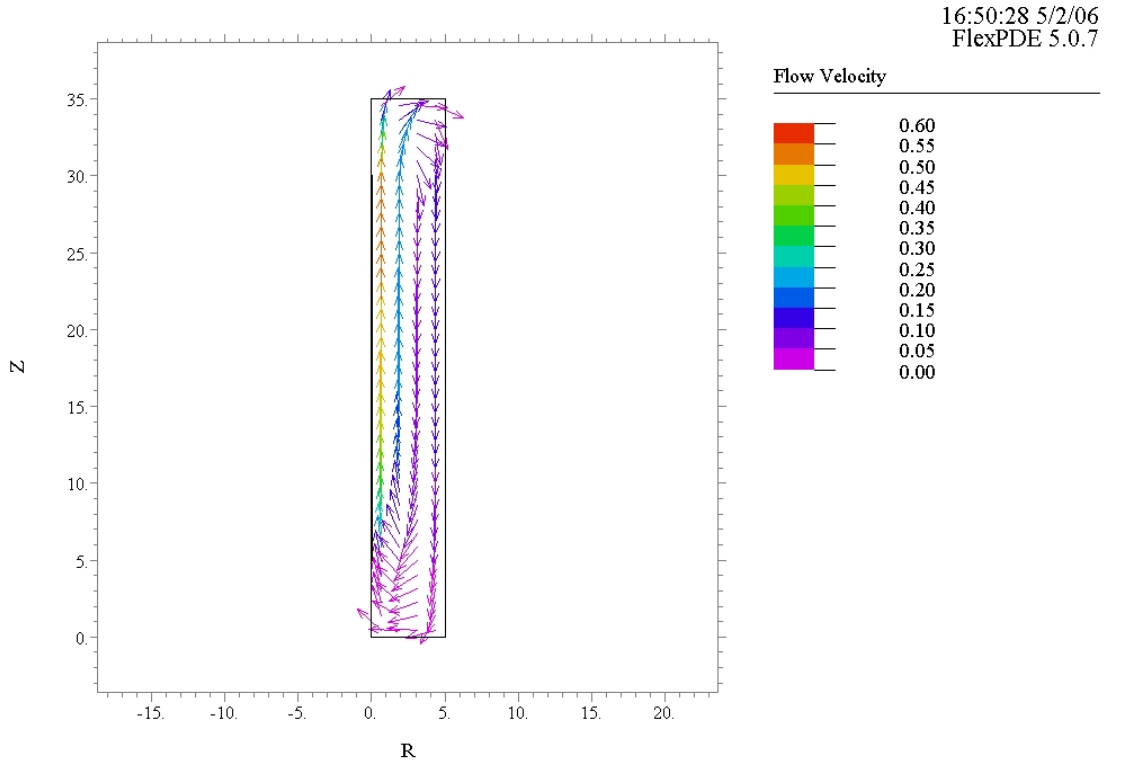

Figure A-7: Velocity field after 50s for water.

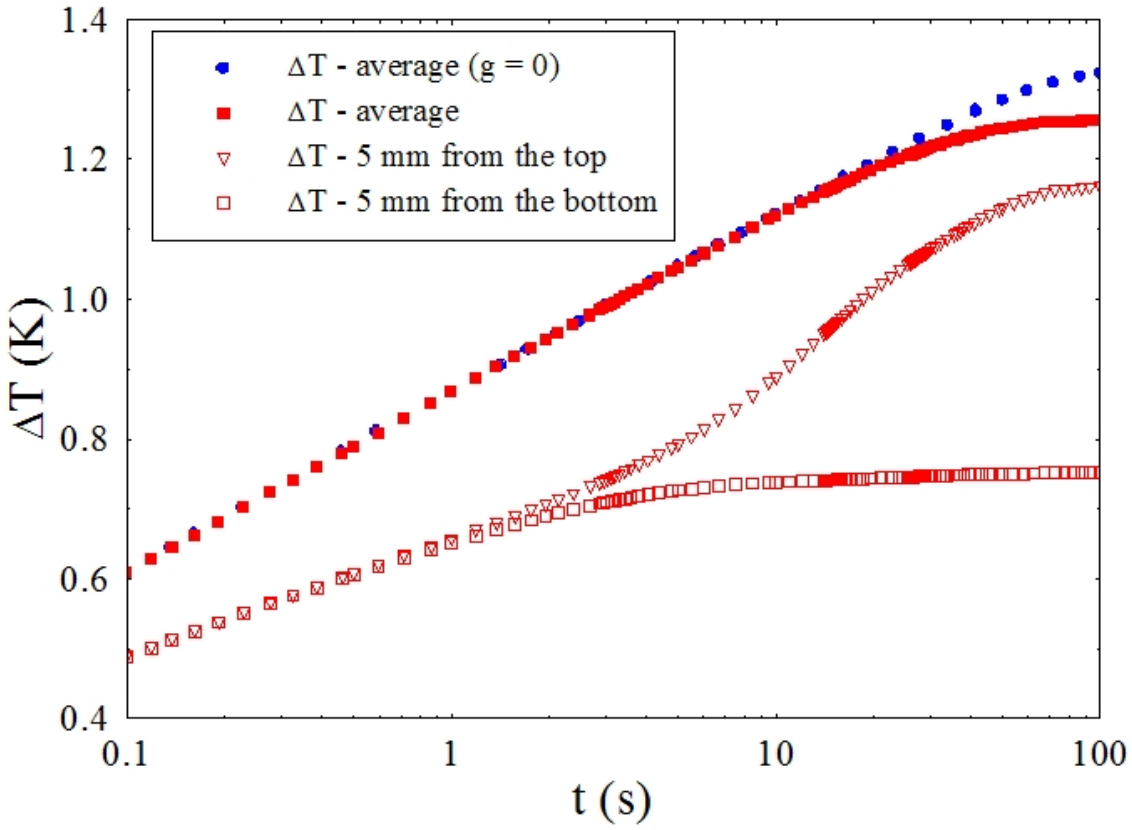

Figure A-8: Temperature increments for a wire of $25mm$ with and without natural convection.

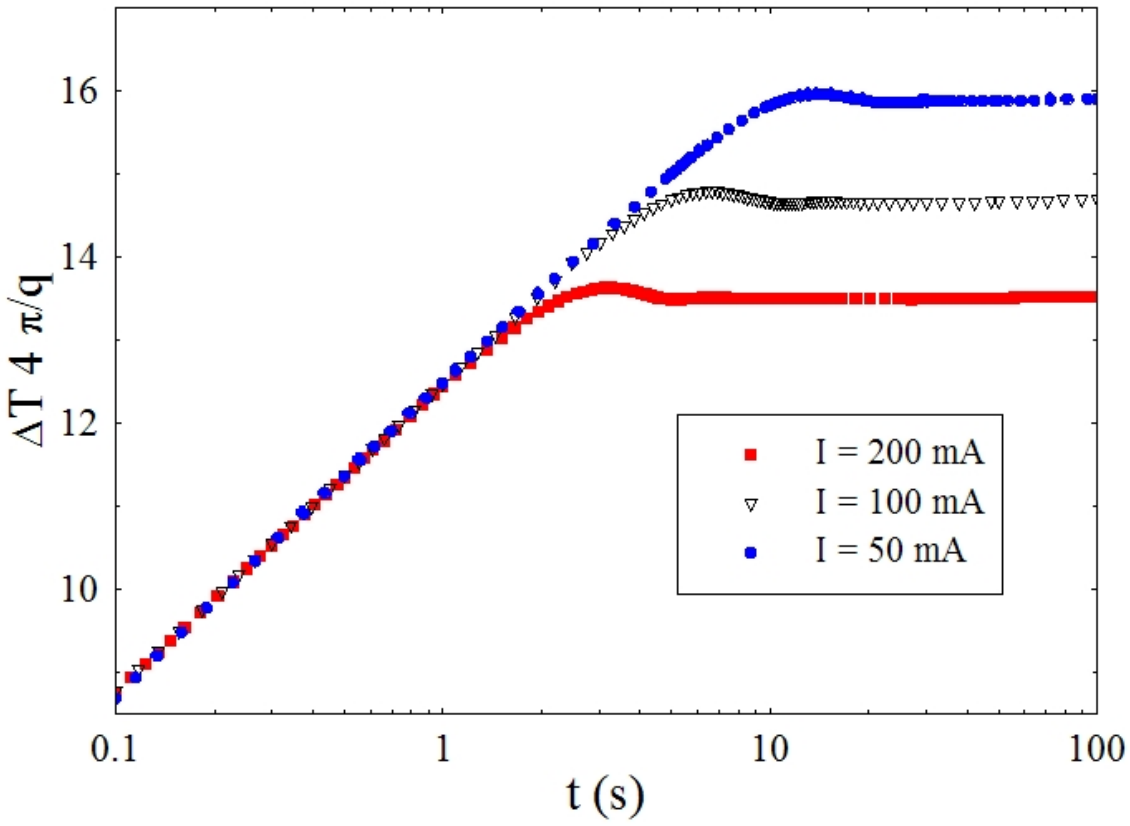

Figure A-9: Comparison of the numerical results for different input currents.

average over the entire wire ($L = 25mm$), the temperature variations at two points at the same distance from the top and the bottom of the wire. In the ideal case these points, for symmetry reasons, should have always the same temperature but because of convection the temporal evolution becomes extremely different after few seconds and this is the same asymmetry as shown in Figure A-6.

Finally in Figure A-9 and Figure A-10 it is clear how the effect of convection is stronger at higher applied power or higher external temperature where the viscosity of water is lower.

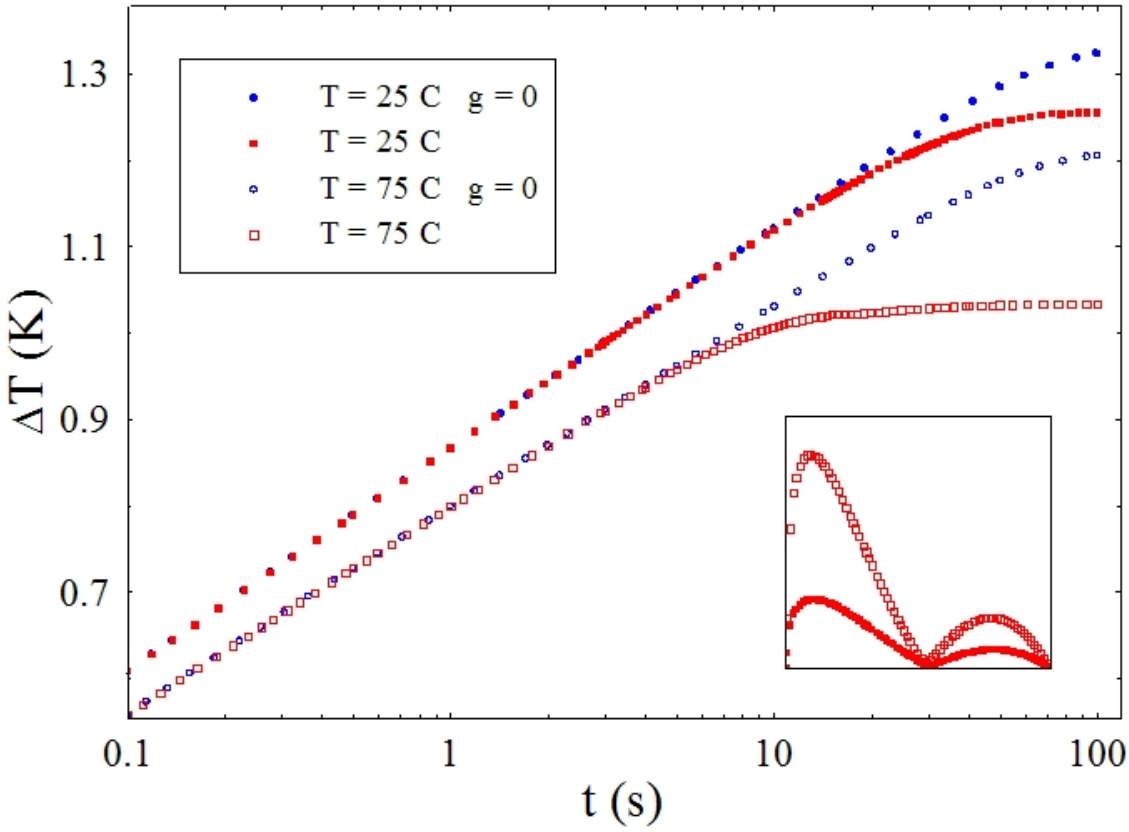

Figure A-10: Comparison of the numerical results for an external temperature of 25 and 75°C. Inset: the magnitude of the velocity field for the two temperatures.

A.2 The transient hot-wire method in colloids: numerical simulations

Similar to the previous work with pure fluids, numerical simulations are performed for the THW method using *FlexPDE Professional 3D*. Once again by exploiting the symmetry of the problem, a 2D cylindrical model is chosen (see Figure A-1) and a self-adapting mesh of triangular elements (derived from an analogue problem [68]).

The Navier-Stokes equations are used along with the Boussinesq approximation, the so-called "Poisson pressure" equation, and the heat and mass diffusion equations as:

$$\begin{aligned}
\nu\nabla\cdot\nabla v_r &= \frac{1}{\rho}\frac{\partial p}{\partial r} + v_r\frac{\partial v_r}{\partial r} + v_z\frac{\partial v_r}{\partial z} + \frac{\partial v_r}{\partial t} \\
\nu\nabla\cdot\nabla v_z &= \frac{1}{\rho}\frac{\partial p}{\partial r} + v_r\frac{\partial v_z}{\partial r} + v_z\frac{\partial v_z}{\partial z} + \frac{\partial v_z}{\partial t} - g\alpha\Delta T \\
\nabla\cdot\nabla(p/\rho) &= \delta\left[\frac{1}{r}\frac{\partial r v_r}{\partial r} + \frac{\partial v_z}{\partial z}\right] + 2\left(\frac{\partial v_r}{\partial r}\frac{\partial v_z}{\partial z} - \frac{\partial v_r}{\partial z}\frac{\partial v_z}{\partial r}\right) - g\alpha\frac{\partial\Delta T}{\partial z} \\
\kappa\nabla\cdot\nabla(\Delta T) &= v_r\frac{\partial\Delta T}{\partial r} + v_z\frac{\partial\Delta T}{\partial z} + \frac{\partial\Delta T}{\partial t} \\
mD_m\cdot\nabla(\Delta c) &= m\cdot(v_r\frac{\partial c}{\partial r} + v_z\frac{\partial c}{\partial z}) + \frac{\partial c}{\partial t} - m\cdot D_m S_T A(1-A)\nabla(\Delta T)
\end{aligned}$$

where c is the concentration and D_m is the mass diffusion coefficient, and A is a coefficient to prevent mass diffusion through the wire region. In contrast with [68], this case has two different areas: the wire (solid) and the sample (liquid). As the routine doesn't allow the implementation of distinct equations for different regions, a parameter `m` which is equal 1 in the liquid area and 0 in the solid one is used. In this way only the Fourier equation has been solved for the wire and it was checked that this imposition didn't affect the solution of the other equations in the liquid part. Also the presence of thermophoresis has been considered, expressed by the Soret

coefficient `sT`. At the boundary the no-slip condition was imposed for the momentum and $\Delta T = 0$, except of course for the axis of rotation where a natural condition (zero flux) has been used.

A.2.1 Case: colloidal suspension without convection

The case of a dispersions in water are analyzed with *alumina* (Aluminium oxide, Nyacol) particles of a mass fraction of around 20% and an effective radius of roughly $50nm$ (measured with Dynamic Light Scattering). The physical properties used in the simulations for the particles are: $\rho_p = 3.89\ g\ cm^{-3}, c_p = 0.88\ J\ g^{-1}\ K^{-1}, \lambda_p = 35\ W\ m^{-1}\ K^{-1}, D = 5.22\ 10^{-6}\ mm^2\ s^{-1}, s_T = -0.023\ K^{-1}$. Where D is the mass diffusion coefficient and the Soret coefficient s_T has been measured with the *Thermal Lens* setup [68] at the Politecnico di Milano. The properties used for the fluid are:

$$\phi_m = \frac{c_m\,\rho_w}{c_m\,\rho_w + \rho_p\,(1 - c_m)} = 6\%,$$

where ϕ_m is the average volume fractions, c_m is the average mass fraction, ρ_w is the density of water, the measured value for the kinematic viscosity is $\nu = 5.6\,mm^2\,s^{-1}$, and the mass expansion coefficient is

$$\beta = \frac{1}{\rho_m}\frac{d\rho_m}{dc_m} = \left(\frac{\rho_p}{\rho_p - \rho_w} - c_m\right)^{-1}$$

. These values are held constant. It is decided for the thermal conductivity to use the Maxwell-Garnett (MG) relation

$$\lambda = \lambda_w \frac{1 + 3\,\phi\,(\lambda_p/\lambda_w - 1)}{\lambda_p/\lambda_w + 2 - \phi\,(\lambda_p/\lambda_w - 1)}$$

with λ_w the thermal conductivity of water and the local volumetric fraction of the particles

$$\phi = \frac{c\,\rho_w}{c\,\rho_w + \rho_p\,(1 - c)}$$

where c is the local mass concentration and both are variables.

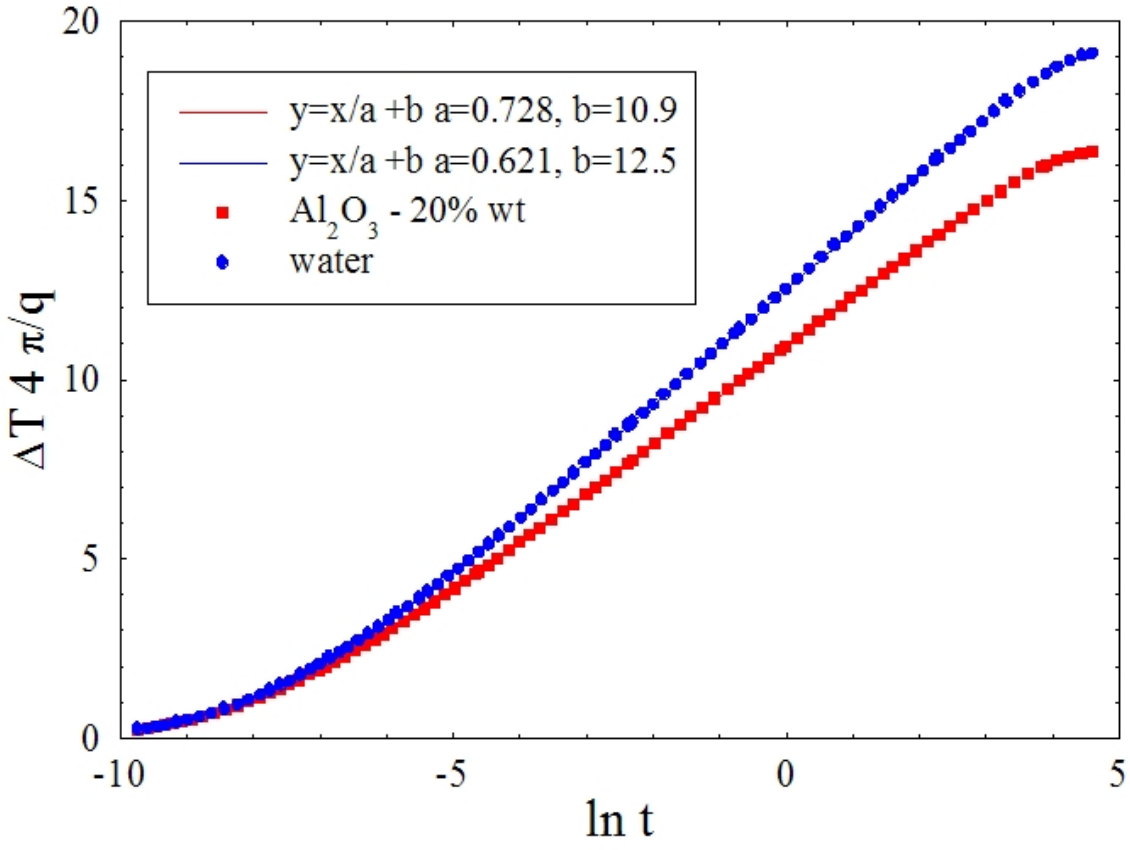

Figure A-11: Comparison of the numerical results for water and alumina at $g = 0$.

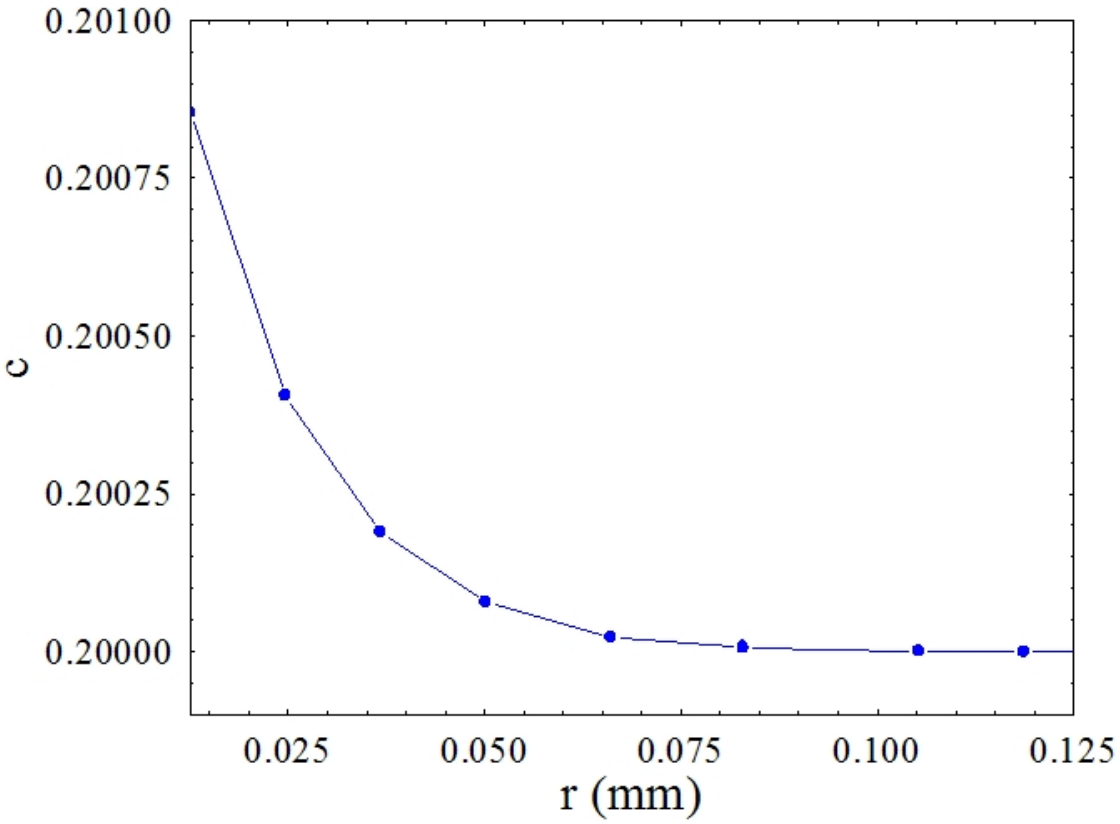

Figure A-12: Concentration profile after 100s at the midpoint of the wire as a function of the radial distance.

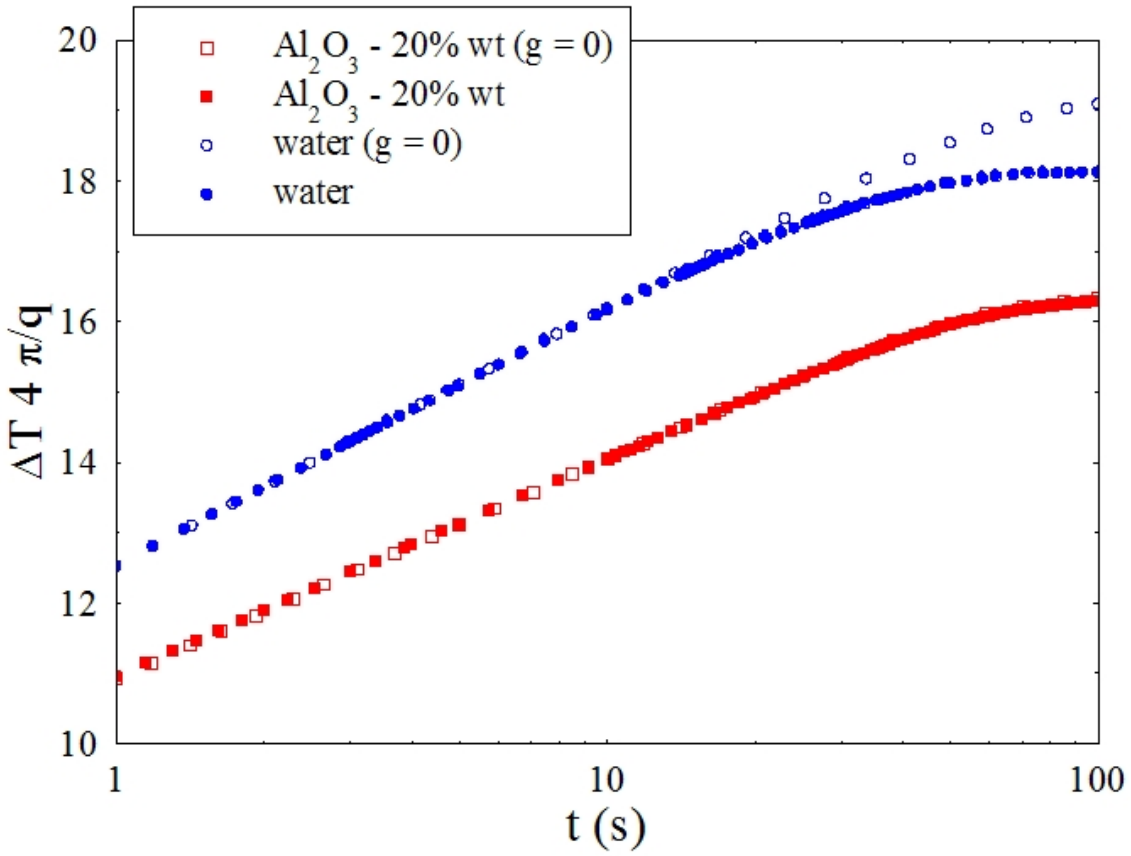

Figure A-13: Comparison of the numerical results for water and alumina with convection.

In Figure A-11 a comparison of the results of the numerical simulations for the alumina dispersion with pure water are shown at $g = 0$: the value of thermal conductivity is obtained by fitting the linear part (in a log scale) of the curves, which gives $0.728\,W\,m^{-1}\,K^{-1}$ and then divide it by the one found for water. This value is found to be exactly the value given by Maxwell-Garnett, which means there should be no influence of thermophoresis on the measurements of heat transfer with the THW method in the ideal case in absence of convection. This is confirmed by the concentration profile around the wire, see Figure A-12, which is too small to affect the thermal conductivity of the sample.

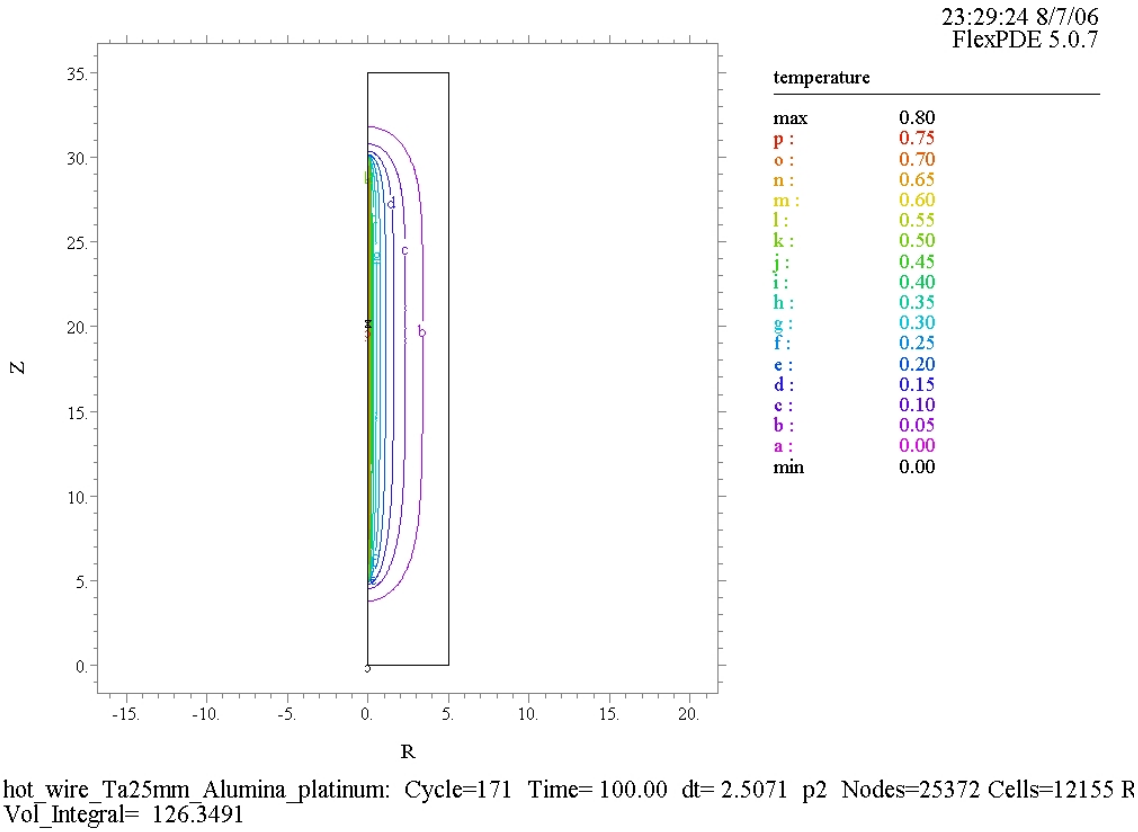

Figure A-14: Temperature field after 100s for a suspension of alumina (20%wt).

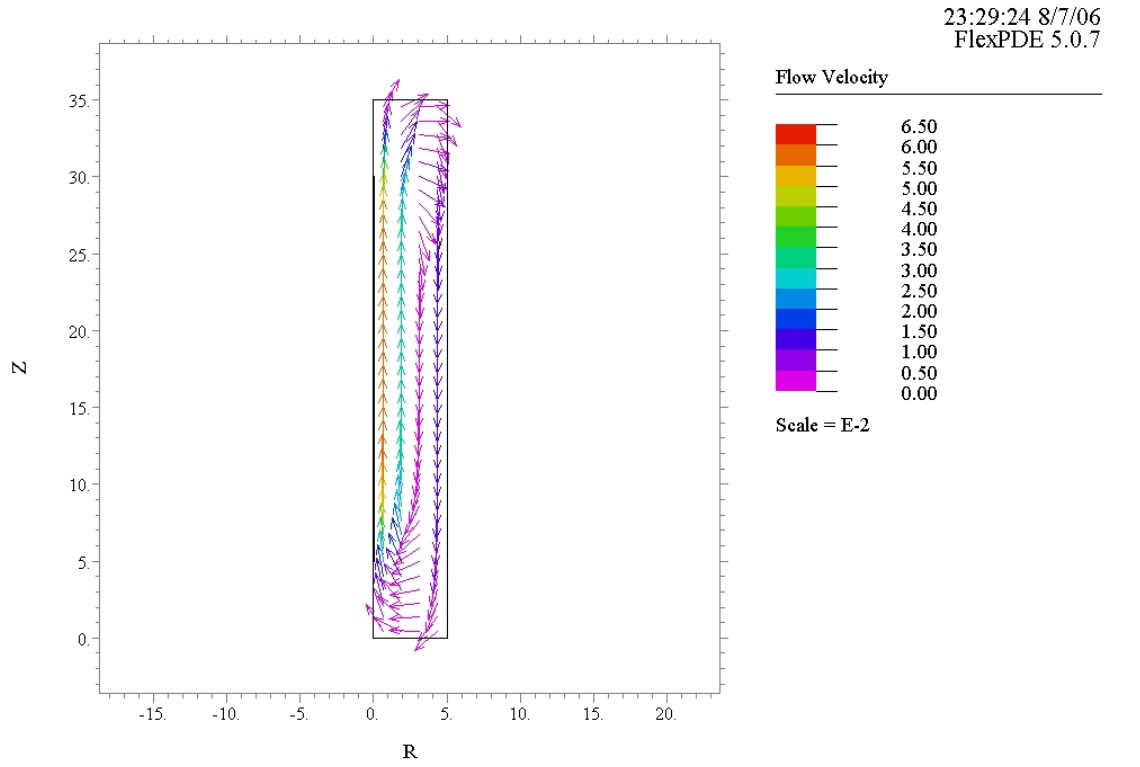

Figure A-15: Velocity field after $100s$ for a suspension of alumina ($20\%wt$).

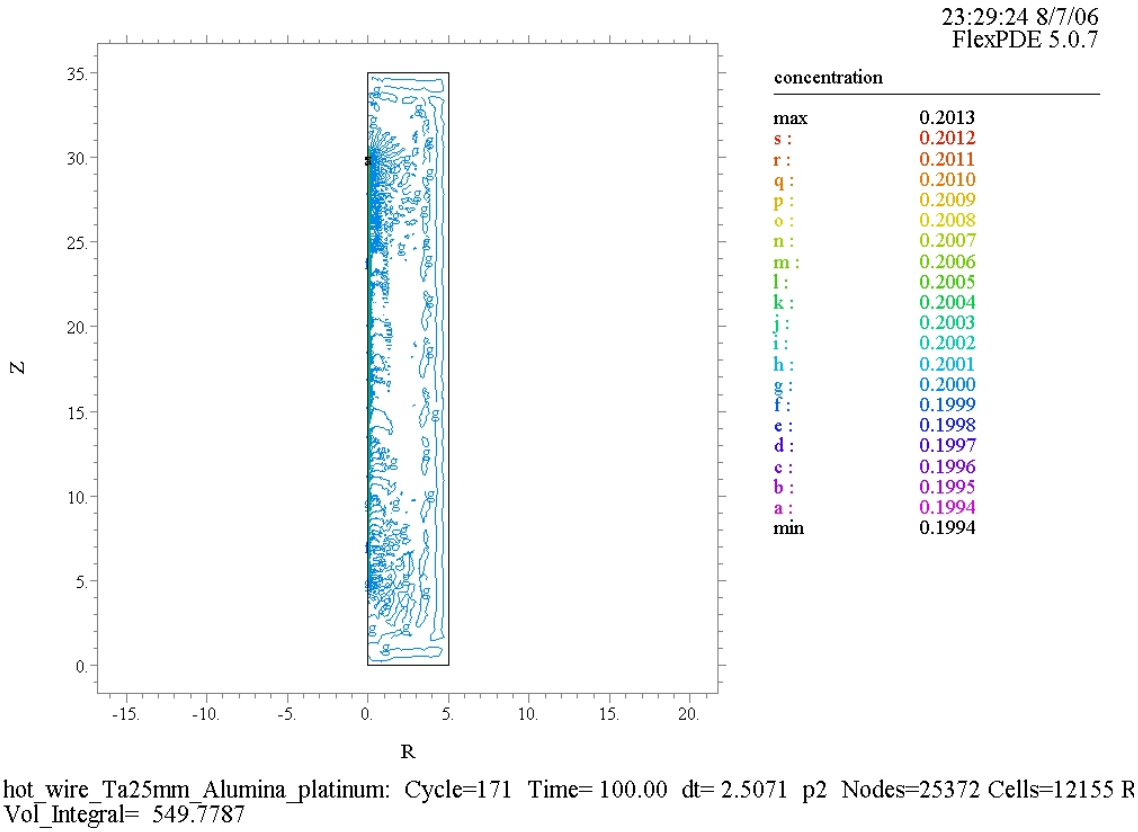

Figure A-16: Concentration field after $100s$ for a suspension of alumina ($20\%wt$).

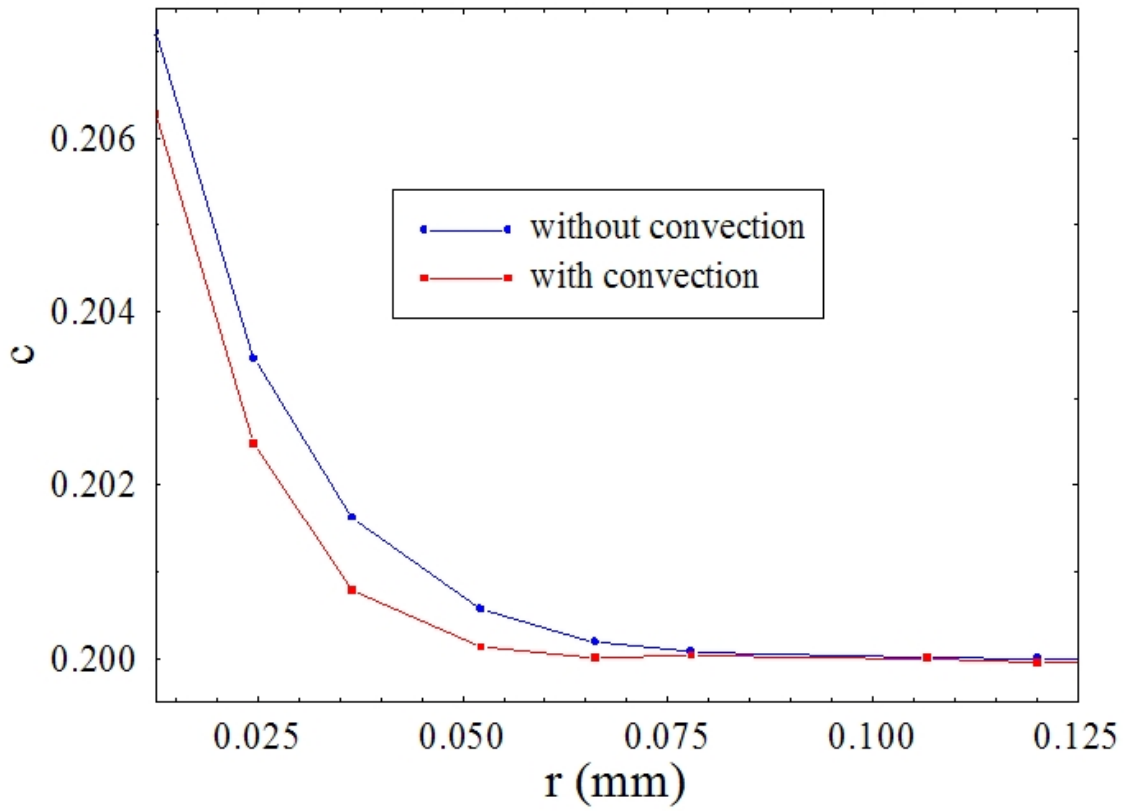

Figure A-17: Concentration profile after $100s$, in the case of a fictitious $s_T = -0.2K^{-1}$, with and without convection.

A.2.2 Case: colloidal suspension with convection

In Figure A-13 the results of the numerical simulations for a suspension of alumina in presence of convection are displayed, compared to those obtained for water. In this case, because of the high value of viscosity, the effect of buoyancy is practically negligible: this is manifested by comparing the thermal field represented in Figure A-14 with that of pure water (Figure A-6) or the intensity of the velocity field (see Figure A-7 and Figure A-15) which is one order of magnitude lower. Furthermore the convective motion slightly affects the concentration profile, see Figure A-16 and Figure A-17, which is essentially developed close to the no-slip region.

Appendix B

Hot-Wire Data Acquisition Code in *MATLAB*

B.1 Routine to Open GPIB

```
%function [curr,volt]=open_gpib()

function [curr,volt]=open_gpib()

curr = visa('ni','GPIB0::7::INSTR');
volt = visa('ni','GPIB0::8::INSTR');

curr.InputBufferSize = 19000;
volt.InputBufferSize = 19000;

curr.OutputBufferSize = 19000;
volt.OutputBufferSize = 19000;



fopen(curr);
fopen(volt);
```

B.2 Routine to Measure Voltage Bias of Wire

```
function voltage=volt_bias(curr,volt)


fprintf(curr,':sour:curr 0.001');
fprintf(volt,':trig:sour ext');
fprintf(volt,':trac:poin 100');
fprintf(volt,':sens:volt:nplc 0.1');
fprintf(volt,':trac:feed sens');
fprintf(volt,':trac:feed:cont next');
fprintf(volt,':trig:sour imm');
pause(1)                                                    10
fprintf(volt,':trac:data?');
point=fscanf(volt);
pause(1)
np = size(point);
n=np(2);
i=1;


while (i<n)
    if (point(i)==',')
        data(i)=' ';                                        20
    else
        data(i) = point(i);
    end
    i=i+1;
end


dataf=sscanf(data,'%f');
voltage=0;
```

```
for i=1:40
    voltage=voltage+dataf(i);
end
voltage=voltage/40;
```

B.3 Routine to Measure Base Temperature

```
function temp_media=measure_temp(curr,volt)

fprintf(volt,':sens:volt:lpass off');   %analog filter off
fprintf(volt,':sens:volt:dfil off');    %digital filter off

%volt_0 = volt_bias(curr,volt);

fprintf(curr,':sour:curr 0.001');
fprintf(volt,':trig:sour ext');
fprintf(volt,':trac:poin 1000');
fprintf(volt,':sens:volt:nplc 0.1');
fprintf(volt,':trac:feed sens');
fprintf(volt,':trac:feed:cont next');
fprintf(volt,':trig:sour imm');
fprintf(curr,':outp on');
pause(10)
fprintf(curr,':outp off');
fprintf(volt,':trac:data?');
point=fscanf(volt);
pause(5)
np = size(point);
```

```
n=np(2);
i=1;

while (i<n)
    if (point(i)==',')
        data(i)=' ';
    else
        data(i) = point(i);
    end
    i=i+1;
end

dataf=sscanf(data,'%f');
res_media=0;
for i=1:400
    res_media=res_media+dataf(i);
end
res_media=res_media/400*1000;
%res_media=(res_media/400 - volt_0)*1000;
temp_media=(res_media - 5.7978)/0.015433;
```

B.4 Routine to Measure at Various Current Settings

```
%function measure(curr,volt,ic_in,ic_fin,pace,nm);

function measure(curr,volt,ic_in,ic_fin,pace,nm);
```

```
for k=ic_in:pace:ic_fin
    acq_data(curr,volt,k,nm);
    pause(10)
end
```

B.5 Routine to Run Basic Data Acquisition

```
%function dataf=acq_data(curr,volt)

function [res_0,temp_0]=acq_data(curr,volt,ic,nm)

fprintf(volt,':sens:volt:lpass off');   %analog filter off
fprintf(volt,':sens:volt:dfil off');    %digital filter off

command = ':sour:curr 0.000';
if (ic>100)
    ic=100;
end
if (ic<1)
    ic=10;
end

i1= floor(ic/100);
i2= floor(ic/10) - i1*10;
i3= ic - i1*100 - i2*10;
command(14) = char(48+i1);
command(15) = char(48+i2);
```

```
command(16) = char(48+i3);

% fprintf(curr,':sour:curr 0.001');
% fprintf(volt,':trig:sour ext');
% fprintf(volt,':trac:poin 1000');
% fprintf(volt,':sens:volt:nplc 0.1');
% fprintf(volt,':trac:feed sens');
% fprintf(volt,':trac:feed:cont next');

ic=ic/1000;
count=0;
res_ave=zeros(588,1);
temp_ave=zeros(588,1);
res_0 = 0;
while (count<nm)
    fprintf(curr,':sour:curr 0.001');
    fprintf(volt,':trig:sour ext');
    fprintf(volt,':trac:poin 1000');
    fprintf(volt,':sens:volt:nplc 0.1');
    fprintf(volt,':trac:feed sens');
    fprintf(volt,':trac:feed:cont next');
    fprintf(volt,':trig:sour imm');
    fprintf(curr,':outp on');
    pause(5)
    fprintf(curr,command);
    pause(15)

    fprintf(curr,':outp off');
    fprintf(volt,':trac:data?');
    point=fscanf(volt);
```

```
pause(5)
np = size(point);
n=np(2);
i=1;

while (i<n)
    if (point(i)==',')
        data(i)=' ';
    else
        data(i) = point(i);
    end
    i=i+1;
end

dataf=sscanf(data,'%f');
res_media=0;
for i=1:200
    res_media=res_media+dataf(i);
end
res_media=res_media/200*1000;
res_0 = res_0 + res_media;

i=200;
ptmin=200;
res_max=res_media*5/1000;
while (dataf(i)<res_max)
    ptmin=i;
    i=i+1;
end
```

```
    res=zeros(588,1);
    t=1:588;
    t=t/588*10;
    t=t';
    i=1;
    ptmax=ptmin+588;
    for k=ptmin+1:ptmax
        res(i)=dataf(k)/ic;
        res_ave(i)=res_ave(i)+res(i);
        temp_ave(i)=temp_ave(i)+(res(i)-res_media)/0.015433;
        i=i+1;
    end

    count=count+1;
    pause(5)
end

res_0 = res_0/count;
temp_0 = (res_0 - 5.7978)/0.015433;
res_ave = res_ave/count;
temp_ave = temp_ave/count;

q=res_ave*power(ic,2)/0.02;

t_norm=temp_ave./q;
t_norm=t_norm*pi*4;

filename ='xxxmA.txt';

filename(1) = char(48+i1);
```

```
filename(2) = char(48+i2);
filename(3) = char(48+i3);

fid = fopen(filename,'w');
for i=1:588
    fprintf(fid,'%f \b %f \b %s \b %f \b %f \n',...
        t(i),t_norm(i),'*',temp_ave(i),q(i));
end
fprintf(fid,'\n \r \n \r');
fprintf(fid,'%s %f','*** temp : ',temp_0);
fclose(fid);
```

B.6 Routine to Close GPIB

```
%function close_gpib(curr,volt)

function close_gpib(curr,volt)

fclose(curr);
fclose(volt);

delete(curr);
delete(volt);
```

Appendix C

Uncertainty Analysis

Evaluating the uncertainty of the heat transfer coefficient and friction factor measurements is done here. The derivation of the equations is facilitated through the use of *MATLAB* and the function capabilities. The initial step is the determination of the governing equations and from that determination of the key variables and their uncertainties.

C.1 Heat transfer coefficient

Heat transfer coefficient is defined from the Newton law of cooling as

$$h = \frac{q''}{T_w - T_b} \tag{C.1}$$

where q'' is the wall heat flux and T_w and T_b are the tube wall and fluid bulk temperatures. The uncertainty for this equation is quite simply

$$\delta h = \sqrt{\left(\frac{\partial h}{\partial q''}\delta q''\right)^2 + \left(\frac{\partial h}{\partial T_w}\delta T_w\right)^2 + \left(\frac{\partial h}{\partial T_b}\delta T_b\right)^2}. \tag{C.2}$$

However, in order to evaluate this equation the uncertainties of the heat flux ($\delta q''$) and temperatures ($\delta T_w, \delta T_b$) are required. These must be derived from other equations.

The heat flux is determined by

$$q'' = \frac{IV}{\pi D_i L} \tag{C.3}$$

where I and V are the current and voltage and D_i and L are the tube inner diameter and length. These values are all directly measured and have known uncertainties. The uncertainty equation for the heat flux is

$$\delta q'' = \sqrt{\left(\frac{\partial q''}{\partial I}\delta I\right)^2 + \left(\frac{\partial q''}{\partial V}\delta V\right)^2 + \left(\frac{\partial q''}{\partial D_i}\delta D_i\right)^2 + \left(\frac{\partial q''}{\partial L}\delta L\right)^2}. \tag{C.4}$$

The inner wall temperature is somewhat more complicated due to the indirect measurement through the outer wall temperature. The inner wall temperature is determined from

$$T_w = T_{w,o} - \frac{IV}{2\pi k_w L}\left(\frac{D_o^2}{D_o^2 - D_i^2}\log\left(\frac{D_o}{D_i}\right) - \frac{1}{2}\right) \tag{C.5}$$

where D_o and $T_{w,o}$ are the tube outer diameter and temperature and k_w is the wall thermal conductivity. The uncertainty is found as

$$\delta T_w = \sqrt{\left(\frac{\partial T_w}{\partial I}\delta I\right)^2 + \left(\frac{\partial T_w}{\partial V}\delta V\right)^2 + \left(\frac{\partial T_w}{\partial D_i}\delta D_i\right)^2 + \left(\frac{\partial T_w}{\partial D_o}\delta D_o\right)^2 + \ldots}$$

$$\overline{\left(\frac{\partial T_w}{\partial L}\delta L\right)^2 + \left(\frac{\partial T_w}{\partial k_w}\delta k_w\right)^2}. \tag{C.6}$$

Finally the bulk temperature is defined as

$$T_b = \frac{IV}{\dot{m} c_p} + T_{b,in} \tag{C.7}$$

where c_p is the specific heat capacity of the fluid, $\dot{m}$ is the mass flow rate and $T_{b,in}$ is the bulk inlet temperature. The uncertainty is defined as

$$\delta T_b = \sqrt{\left(\frac{\partial T_b}{\partial I}\delta I\right)^2 + \left(\frac{\partial T_b}{\partial V}\delta V\right)^2 + \left(\frac{\partial T_b}{\partial \dot{m}}\delta \dot{m}\right)^2 + \left(\frac{\partial T_b}{\partial c_p}\delta c_p\right)^2 + \left(\frac{\partial T_b}{\partial T_{b,in}}\delta T_{b,in}\right)^2}. \tag{C.8}$$

The mass flow rate is found by

$$\dot{m} = \rho Q \tag{C.9}$$

where ρ is the fluid density and Q is the volumetric flow rate. The uncertainty for the mass flow rate is found to be

$$\delta\dot{m} = \sqrt{\left(\frac{\partial\dot{m}}{\partial\rho}\delta\rho\right)^2 + \left(\frac{\partial\dot{m}}{\partial Q}\delta Q\right)^2}. \tag{C.10}$$

All of these equations are solved using *MATLAB* and the final form of the heat transfer coefficient uncertainty is

$$\begin{aligned}
\delta h \;=\; & \frac{1}{2}\Bigg\{ \frac{4}{(T_w - T_b)^2}\left[\frac{V^2}{\pi^2 D_i^2 L^2}\delta I^2 + \frac{I^2}{\pi^2 D_i^2 L^2}\delta V^2 + \frac{I^2V^2}{\pi^2 D_i^4 L^2}\delta D_i^2 + \frac{I^2V^2}{\pi^2 D_i^2 L^4}\delta L^2\right] \\
& + \frac{q''^2}{(T_w - T_b)^4}\Bigg[4\delta T_{w,o}^2 + \frac{V^2\left(\frac{D_i}{D_o^2 - D_i^2} - \frac{1}{2}\right)^2}{\pi^2 k_w^2 L^2}\delta I^2 + \frac{I^2\left(\frac{D_i}{D_o^2 - D_i^2} - \frac{1}{2}\right)^2}{\pi^2 k_w^2 L^2}\delta V^2 + \ldots \\
& \frac{I^2V^2\left(\frac{D_i}{D_o^2 - D_i^2} - \frac{1}{2}\right)^2}{\pi^2 k_w^4 L^2}\delta k_w^2 + \frac{I^2V^2\left(\frac{D_i}{D_o^2 - D_i^2} - \frac{1}{2}\right)^2}{\pi^2 k_w^2 L^4}\delta L^2 + \ldots \\
& \frac{I^2V^2\left(\frac{2D_o\log\left(\frac{D_o}{D_i}\right)}{D_o^2 - D_i^2} - \frac{2D_o^3\log\left(\frac{D_o}{D_i}\right)}{(D_o^2 - D_i^2)^2} + \frac{D_o}{D_o^2 - D_i^2}\right)^2}{\pi^2 k_w^2 L^2}\delta D_o^2 + \ldots \\
& \frac{I^2V^2\left(\frac{2D_o^2 D_i\log\left(\frac{D_o}{D_i}\right)}{(D_o^2 - D_i^2)^2} - \frac{D_o^2}{D_i(D_o^2 - D_i^2)}\right)^2}{\pi^2 k_w^2 L^2}\delta D_i^2\Bigg] \\
& + \frac{4q''^2}{(T_w - T_b)^4}\left[\frac{V^2}{\rho^2 Q^2 c_p^2}\delta I^2 + \frac{I^2}{\rho^2 Q^2 c_p^2}\delta V^2 + \frac{I^2V^2}{\rho^2 Q^2 c_p^4}\delta c_p^2 + \delta T_{b,i}^2\right]\Bigg\}^{1/2}
\end{aligned} \tag{C.11}$$

C.2 Nusselt number

If Nusselt number uncertainty is desired then one must start with the definition of Nusselt number as

$$Nu = \frac{hD_i}{k} \tag{C.12}$$

where k is the fluid thermal conductivity. The uncertainty is defined as

$$\delta Nu = \sqrt{\left(\frac{\partial Nu}{\partial h}\delta h\right)^2 + \left(\frac{\partial Nu}{\partial D_i}\delta D_i\right)^2 + \left(\frac{\partial Nu}{\partial k}\delta k\right)^2}. \tag{C.13}$$

Solving this equation in *MATLAB* finds the uncertainty to be

$$\delta Nu = \sqrt{\left(\frac{D_i^2}{k^2}\right)\delta h^2 + \left(\frac{h^2}{k^2}\right)\delta D_i^2 + \left(\frac{h^2 D_i^2}{k^4}\right)\delta k^2} \tag{C.14}$$

where δh is determined from Equation C.11.

C.3 Friction factor

Friction factor is another important variable under consideration. It is defined as

$$f_f = \frac{1}{2}\frac{\Delta P D_i^3}{\rho Q^2 L} \tag{C.15}$$

where ΔP is the viscous pressure loss. The uncertainty for the friction factor is

$$\delta f_f = \sqrt{\left(\frac{\partial f_f}{\partial \Delta P}\delta \Delta P\right)^2 + \left(\frac{\partial f_f}{\partial D_i}\delta D_i\right)^2 + \left(\frac{\partial f_f}{\partial \rho}\delta \rho\right)^2 + \left(\frac{\partial f_f}{\partial Q}\delta Q\right)^2 + \left(\frac{\partial f_f}{\partial L}\delta L\right)^2}. \tag{C.16}$$

Solving for this equation in *MATLAB* the uncertainty is found to be

$$\delta f_f = \frac{1}{2}\sqrt{\frac{D_i^6}{\rho^2 Q^4 L^2}\delta \Delta P^2 + \frac{9\Delta P^2 D_i^4}{\rho^2 Q^4 L^2}\delta D_i^2 + \frac{\Delta P^2 D_i^6}{\rho^4 Q^4 L^2}\delta \rho^2 + \ldots}$$

$$\overline{\frac{4\Delta P^2 D_i^6}{\rho^2 Q^6 L^2}\delta Q^2 + \frac{\Delta P^2 D_i^6}{\rho^2 Q^4 L^4}\delta L^2}. \tag{C.17}$$

Appendix D

Data Reduction Program in *MATLAB*

D.1 Main Program

```
clear all
clc
%Listing of Data Filenames
filename={'XXMT.csv'};

fileiter=size(filename,1);          %Setting Number of Test Cases
avedata=zeros(fileiter,17);         %Initializing Data Output Matrix

%BEGIN DATA REDUCTION LOOP
for ij = 1:fileiter                                              10
    filenamex=char(filename(ij));

%Data Import from Text File
[t Q V I Tbin  ...
     Tw00 Tw01 Tw02 Tw03 Tw04 ...
     Tw05 Tw06 Tw07 Tw08 Tw09 ...
```

```
    Tw10 Tw11 Tw12 Tw13 Tbout...
    TbHX dPcold dPhot Psys] =...
    textread(filenamex,...
    '%f%f%f%f%f%f%f%f%f%f%f%f%f%f%f%f%f%f%f%f%f%f%f%f%f%f%f',...
    'delimiter',',','headerlines',1);

xloc=[0.2 0.4 0.6 0.8 1 1.2 1.4...
    1.6 1.8 2 2.2 2.4 2.6 2.8]; %Axial Thermocouple Locations
T=[Tw00 Tw01 Tw02 Tw03 Tw04 Tw05...
    Tw06 Tw07 Tw08 Tw09 Tw10 Tw11 Tw12 Tw13]; %Wall Temp Matrix

%Calculating Time Dependent Means of Properties
Im=mean(I);                     %Mean Test Section Current
Vm=mean(V);                     %Mean Test Section Voltage
Tbinm=mean(Tbin)+273.15;        %Mean Bulk Inlet Temperature
Tboutm=mean(Tbout)+273.15;      %Mean Bulk Outlet Temperature
TbHXm=mean(TbHX)+273.15;        %Mean Iso. Bulk Inlet Temp
Qm=mean(Q);                     %Mean Volumetric Flowrate (GPM)
Tm=mean(T)+273.15;              %Mean of Wall Thermocouple Temp


%Setting the Particle Material Type
mat=filenamex(3:4)
if mat == 'zr'                  %use Zirconia Properties
    cppart=0.418;               %Properties from NIST
    rhopart= 5500;
else                            %use Alumina Properties
    cppart=0.880;               %Properties from NIST
    rhopart=3920;
end
```

```
%Setting Particle Loading Volume Fraction
phi=str2num(filenamex(1:2))/1000;

%Setting Basic INPUTS
AV_flow = Qm*0.0000631;              %Calc Mass Flow Rate (kg/s)
D_tube_in = 0.5*.0254-2*.065*.0254; %Inner tube diameter (m)
D_tube_hx = 0.5*.0254-2*.048*.0254; %Cold leg tube diameter (m)
th_tube = .065*.0254;                %Tube thickness (m)
D_tube_out=D_tube_in+2*th_tube;      %Tube OD (m)
L_tube = 111*.0254;                  %Length of tube (m)
L_tube_dp = 118*0.0254;              %Length of tube for dp (m)
Power = Im*Vm;                       %Mean Power (W)
q_flux = Power/(D_tube_in*pi*L_tube);%Heat flux in (W/m^2-K)
V_in = AV_flow/pi/D_tube_in^2*4;     %Inlet velocity (m/s)

%Properties From NIST Water Tables
%Inlet properties
[cp_in, mu_in, k_in, rho_in] = N_property(mean(Tbinm));

%Correcting Fluid Properties for Mixtures
cp_in = (((1-phi)*rho_in*cp_in)+(phi*rhopart*cppart))/...
    (((1-phi)*rho_in)+(phi*rhopart));
rho_in = ((1-phi)*rho_in)+(phi*rhopart);

if mat == 'zr'                       %use Zirconia Properties
    mu_in = mu_in.*exp(11.19*phi/(0.1960-phi));
    k_in = k_in.*(-29.867*phi^2 + 2.4505*phi + 1);%
else                                 %use Alumina Properties
    mu_in = mu_in.*exp(4.91*phi/(0.2092-phi));%
```

```
    k_in = k_in.*(4.5503*phi + 1);
end

%Calculating Hot Section Inlet Mass flowrate and Reynolds
mdot = AV_flow*rho_in;                %Mass flow rate kg/s
Re_in = 4*mdot/mu_in/pi/D_tube_in;   %Inlet Reynolds

%Calculating Hot Section Pressure Drop and Friction Factor
%Mean properties
[cp_ff, mu_ff, k_ff, rho_ff] = N_property((Tbinm+Tboutm)/2);
rho_ff = ((1-phi)*rho_ff)+(phi*rhopart);
mdot2 = AV_flow*rho_ff;               %Mass flow rate kg/s
if mat == 'zr'                        %use Zirconia Properties
    mu_ff = mu_ff.*exp(11.19*phi/(0.1960-phi));
else                                  %use Alumina Properties
    mu_ff = mu_ff.*exp(4.91*phi/(0.2092-phi));%
end
Re_ff = 4*mdot2/mu_ff/pi/D_tube_in;      %Reynolds Number
V_ff = AV_flow/pi/D_tube_in^2*4;         %Inlet velocity
if Re_ff < 30000
    ff_hs = 0.316*Re_ff^-0.25;           %Blasius Relation
else
    ff_hs = 0.184*Re_ff^-0.2;            %McAdams Relation
end

delPhs = ff_hs*L_tube/D_tube_in*rho_ff*V_ff^2/2; %Delta P in Pa

%Measured friction factor
ff_hsm = mean(dPhot)*6894.75728*D_tube_in/...
                L_tube_dp*2/rho_ff/V_ff^2;
```

```
dDi=0.0001;
dL=0.01;
dQ=0.05*AV_flow;
ddelP=mean(dPhot)*0.01;
drho=rho_ff*0.05;
dff_hsm = 1/2*(D_tube_in^6/rho_ff^2/AV_flow^4/...
    L_tube_dp^2*ddelP^2+9*mean(dPhot)^2*D_tube_in^4/...
    rho_ff^2/AV_flow^4/L_tube_dp^2*dDi^2+mean(dPhot)^2*...
    D_tube_in^6/rho_ff^4/AV_flow^4/L_tube_dp^2*drho^2+...
    4*mean(dPhot)^2*D_tube_in^6/rho_ff^2/AV_flow^6/...
    L_tube_dp^2*dQ^2+mean(dPhot)^2*D_tube_in^6/...
    rho_ff^2/AV_flow^4/L_tube_dp^4*dL^2)^(1/2);

%Calculating Cold Section Pressure Drop and Friction Factor
%Isothermal properties
[cp_HX, mu_HX, k_HX, rho_HX] = N_property(mean(TbHXm));
rho_HX = ((1-phi)*rho_HX)+(phi*rhopart);
mdot3 = AV_flow*rho_ff;                 %Mass flow rate kg/s
if mat == 'zr'                          %use Zirconia Properties
    mu_HX = mu_HX.*exp(11.19*phi/(0.1960-phi));
else                                    %use Alumina Properties
    mu_HX = mu_HX.*exp(4.91*phi/(0.2092-phi));%
end
Re_HX = 4*mdot3/mu_HX/pi/D_tube_hx;     %Reynolds Number
V_HX = AV_flow/pi/D_tube_hx^2*4;        %Inlet velocity
if Re_HX < 30000
    ff_HX = 0.316*Re_HX^-0.25;          %Blasius Relation
else
    ff_HX = 0.184*Re_HX^-0.2;           %McAdams Relation
end
```

```
delPhx = ff_HX*L_tube_dp/D_tube_hx*rho_HX*V_HX^2/2; %Delta P in Pa

%Measured friction factor                                          140
ff_HXm = mean(dPcold)*6894.75728*D_tube_hx/...
    L_tube_dp*2/rho_HX/V_HX^2;
dDi=0.0001;
dL=0.01;
dQ=0.05*AV_flow;
ddelP=mean(dPcold)*0.01;
drho=rho_HX*0.05;
dff_HX = 1/2*(D_tube_hx^6/rho_HX^2/AV_flow^4/L_tube_dp^2*...
    ddelP^2+9*mean(dPcold)^2*D_tube_hx^4/rho_HX^2/...
    AV_flow^4/L_tube_dp^2*dDi^2+mean(dPcold)^2*...                 150
    D_tube_hx^6/rho_HX^4/AV_flow^4/L_tube_dp^2*drho^2+...
    4*mean(dPcold)^2*D_tube_hx^6/rho_HX^2/AV_flow^6/...
    L_tube_dp^2*dQ^2+mean(dPcold)^2*D_tube_hx^6/...
    rho_HX^2/AV_flow^4/L_tube_dp^4*dL^2)^(1/2);

%Prediction of Local Nusselt Number
z=xloc;
for i=1:14 %i=1:n
    Tb(i) = (z(i)*(Tboutm-(Tbinm))/L_tube)+(Tbinm);
                                                                   160
    %local properties
    [cp(i), mu(i), k(i), rho(i)] = N_property(Tb(i));

    %Setting Nanofluid Properties
    cp(i) = (((1-phi)*rho(i)*cp(i))+(phi*rhopart*cppart))/...
                        (((1-phi)*rho(i))+(phi*rhopart));
```

```
    rho(i) = ((1-phi)*rho(i))+(phi*rhopart);

    if mat == 'zr' %use Zirconia Properties
        mu(i) = mu(i).*exp(11.19*phi/(0.1960-phi));
        k(i) = k(i).* (-29.867*phi^2 + 2.4505*phi + 1);
    else %use Alumina Properties
        mu(i) = mu(i).*exp(4.91*phi/(0.2092-phi)); %
        k(i) = k(i).* (4.5503*phi + 1); %
    end

    Re(i) = 4*rho(i)*AV_flow/mu(i)/pi/D_tube_in; %local Reynolds
    Pr(i) = mu(i)*cp(i)*1000/k(i);               %local Prandtl
    %Calculating Friction Factor for Gnielinski
    ff(i) = (0.790*log(Re(i))-1.64)^-2;
    %Calculating Nusselt Number for Gnielinski
    Nu(i) = (ff(i)/8)*(Re(i)-1000)*Pr(i)/(1+12.7*...
            ((ff(i)/8)^(1/2))*(Pr(i)^(2/3)-1));...
            %*(1+(D_tube_in/L_tube)^(2/3));
    %Calculating Nusselt Number for Dittus Boelter
    NuDB(i)=0.023*Re(i)^0.8*Pr(i)^0.4;
    htc(i) = Nu(i)*k(i)/D_tube_in;  %local heat transfer coeff.
    Tw(i) = (q_flux/htc(i))+Tb(i);  %local wall temperature
    kw(i)= 0.0127*(Tw(i))+13.23188; %Temp Dep Wall Conductivity
    Two(i)=Tw(i)+Power/(2*pi*kw(i)*L_tube)*(D_tube_out^2/...
        (D_tube_out^2-D_tube_in^2)*log(D_tube_out/...
        D_tube_in)-1/2); %local outer wall temperature
    dTwall(i)=Two(i)-Tw(i);
end

%Correcting Wall Temperature for Conduction
```

```
Twinn=Tm-dTwall;

%Calculating Local Measured Heat Transfer Coefficient
for ii=1:14                                                          200

htcmeas(ii)=q_flux/(Twinn(ii)-(Tb(ii)));

%local properties
[cp2(ii), mu2(ii), k2(ii), rho2(ii)] = N_property(Tb(ii));
Numeas(ii)=htcmeas(ii)*D_tube_in/(k2(ii));

%Uncertainty Analysis for Local HTC and Nusselt
cp2(ii)=cp2(ii)*1000;
dI=0.08;                                                             210
dV=0.004;
dL=0.01;
dTwo=0.5;
dkw=1;
dcp=100;
dDi=0.0001;
dDo=0.0001;
dTin=0.5;

htcerror(ii) = 1/2*(4/(Twinn(ii)-Tb(ii))^2*(Vm^2/pi^2/...            220
    D_tube_in^2/L_tube^2*dI^2+Im^2/pi^2/D_tube_in^2/...
    L_tube^2*dV^2+Im^2*Vm^2/pi^2/D_tube_in^4/L_tube^2*...
        dDi^2+Im^2*Vm^2/pi^2/D_tube_in^2/L_tube^4*dL^2)+...
    q_flux^2/(Twinn(ii)-Tb(ii))^4*(4*dTwo^2+Vm^2/...
    pi^2/kw(ii)^2/L_tube^2*(D_tube_out^2/...
    (D_tube_out^2-D_tube_in^2)*log(D_tube_out/...
```

```
    D_tube_in)−1/2)^2*dI^2+Im^2/pi^2/kw(ii)^2/...
    L_tube^2*(D_tube_out^2/(D_tube_out^2−D_tube_in^2)*...
    log(D_tube_out/D_tube_in)−1/2)^2*dV^2+Im^2*Vm^2/...
    pi^2/kw(ii)^4/L_tube^2*(D_tube_out^2/...                              230
        (D_tube_out^2−D_tube_in^2)*log(D_tube_out/...
    D_tube_in)−1/2)^2*dkw^2+Im^2*Vm^2/pi^2/kw(ii)^2/...
        L_tube^4*(D_tube_out^2/(D_tube_out^2−D_tube_in^2)*...
        log(D_tube_out/D_tube_in)−1/2)^2*dL^2+Im^2*...
    Vm^2/pi^2/kw(ii)^2/L_tube^2*(2*D_tube_out/...
    (D_tube_out^2−D_tube_in^2)*log(D_tube_out/...
    D_tube_in)−2*D_tube_out^3/(D_tube_out^2−...
    D_tube_in^2)^2*log(D_tube_out/D_tube_in)+...
    D_tube_out/(D_tube_out^2−D_tube_in^2))^2*...
    dDo^2+Im^2*Vm^2/pi^2/kw(ii)^2/L_tube^2*...                            240
    (2*D_tube_out^2/(D_tube_out^2−D_tube_in^2)^2*...
    log(D_tube_out/D_tube_in)*D_tube_in−D_tube_out^2/...
    (D_tube_out^2−D_tube_in^2)/D_tube_in)^2*dDi^2)+...
    4*q_flux^2/(Twinn(ii)−Tb(ii))^4*(Vm^2/rho2(ii)^2/...
    AV_flow^2/cp2(ii)^2*dI^2+Im^2/rho2(ii)^2/...
    AV_flow^2/cp2(ii)^2*dV^2+Im^2*Vm^2/rho2(ii)^2/...
        AV_flow^2/cp2(ii)^4*dcp^2+dTin^2))^(1/2);


dNu(ii) =(D_tube_in^2/k2(ii)^2*htcerror(ii)^2+...                         250
            htcmeas(ii)^2/k2(ii)^2*dDi^2+htcmeas(ii)^2*...
        D_tube_in^2/k2(ii)^4*(k2(ii)*0.05)^2)^(1/2);

end


avedata(ij,1:23)=[phi,Qm*0.00006309,Tbinm,Tboutm,...
```

```
    q_flux,mean(Re),Re_HX,mean(NuDB),mean(Numeas),...
    delPhs,mean(dPhot)*6894.75728,delPhx,mean(dPcold)*...
    6894.75728, ff_hs, ff_hsm, dff_hsm, ff_HX, ff_HXm,...
    dff_HX,mean(htcmeas), mean(Pr),mean(htcerror),mean(dNu)];

nuout(ij,1:42)=[NuDB,Numeas,dNu]

Mats(ij,1:2)=mat;
DD1={'mats';'phi';'QmL/s';'Tbinm';'Tb_out';'q_flux';...
    'Re';'Re_HX';'Nu';'Numeas';'delP';'dPhot';'delPhx';...
    'dPcold';'ffhot';'ffhotm';'dff_hot';'ffhx';'ffhxm';...
    'dff_hx';'htcmeas'; 'Pr';'htcerror';'Nuerror'}

 XLSWRITE('ALL.xls',DD1','A1:X1')
 XLSWRITE('ALL.xls',Mats,'A2:A48')
 XLSWRITE('ALL.xls',avedata,'B2:X48')
```

D.2 Properties Program

```
function [cp1, mu1, k1, rho1]=N_property(T1)
%Returns Water properties for pressure of
%0.1MPa (1bars) and temps from 290 to 453K

%Temperature
T=[280 282.5 285 287.5 290  292.5  295   297.5  300   ...
    302.5   305   307.5  310   312.5  315   317.5  320   322.5...
    325 327.5  330   332.5  335   337.5  340   342.5  345.0...
    347.5   350   352.5  355   357.5  360   362.5  365   367.5...
```

```
    370 372.5  375    377.5  380    382.5  385    387.5  390.0...
    392.5      395    397.5  400    402.5  405    407.5  410    412.5...
    415 417.5  420    422.5  425    427.5  430    432.5  435.0...
    437.5      440    442.5  445    447.5  450    452.5  453.03];

%Specific Heat Capacity
cp=[4.1973 4.1928 4.1891 4.1861 4.1836 4.1817 4.1802...
    4.179      4.1781 4.1775 4.1771 4.177  4.177  4.1771...
    4.1774     4.1779 4.1784 4.1791 4.1798 4.1807 4.1816...
    4.1827     4.1838 4.185  4.1863 4.1877 4.1892 4.1908...
    4.1925     4.1943 4.1962 4.1982 4.2004 4.2026 4.205...
    4.2075     4.2101 4.2129 4.2158 4.2188 4.222  4.2254...
    4.2289     4.2325 4.2364 4.2404 4.2446 4.2489 4.2535...
    4.2582     4.2632 4.2683 4.2737 4.2792 4.285  4.291...
    4.2972     4.3037 4.3104 4.3173 4.3245 4.332  4.3397...
    4.3478     4.3561 4.3647 4.3736 4.3829 4.3924 4.4023...
    4.4045];

cp1=interp1(T,cp,T1); % kJ/kg-K

%Viscosity
mu=[0.0014323 0.0013296 0.0012384 0.0011567 0.0010834...
    0.0010173  0.00095752  0.00090319  0.00085367...
    0.0008084  0.00076689  0.00072874  0.00069357...
    0.00066109 0.00063101  0.00060311  0.00057717...
    0.00055301 0.00053047  0.00050941  0.00048969...
    0.00047121 0.00045386  0.00043755  0.00042221...
    0.00040774 0.00039409  0.0003812   0.00036902...
    0.00035748 0.00034655  0.00033619  0.00032635...
    0.000317   0.00030811  0.00029966  0.0002916...
```

```
    0.00028392 0.0002766    0.0002696    0.00026293...
    0.00025654 0.00025043   0.00024459   0.00023899...
    0.00023362 0.00022847   0.00022354   0.0002188...
    0.00021424 0.00020986   0.00020565   0.0002016...
    0.0001977  0.00019394   0.00019031   0.00018682...
    0.00018345 0.0001802    0.00017705   0.00017402...
    0.00017108 0.00016824   0.0001655    0.00016284...
    0.00016026 0.00015776   0.00015534   0.00015299...
    0.00015072 0.00015024];

mu1=interp1(T,mu,T1); %kg/m-s= Pa S

%Thermal Conductivity
k=[0.57454 0.57926 0.58395 0.5886 0.59319  0.59771...
    0.60215    0.60649 0.61073 0.61485 0.61886 0.62274...
    0.6265     0.63012 0.6336 0.63695 0.64016 0.64323...
    0.64617    0.64897 0.65164 0.65418 0.65658 0.65886...
    0.66102    0.66306 0.66498 0.66679 0.66848 0.67008...
    0.67156    0.67295 0.67424 0.67544 0.67655 0.67758...
    0.67852    0.67937 0.68015 0.68086 0.68149 0.68204...
    0.68253    0.68295 0.68331 0.6836 0.68383 0.68399...
    0.6841     0.68415 0.68414 0.68407 0.68395 0.68377...
    0.68353    0.68325 0.6829 0.68251 0.68206 0.68156...
    0.681      0.68039 0.67973 0.67902 0.67825 0.67743...
    0.67655    0.67562 0.67464 0.6736 0.67337];

k1=interp1(T,k,T1); %W/m-K

%Density
rho=[1000.3 1000.2 999.94 999.62 999.22 998.75 998.22...
```

```
997.62      996.96  996.24  995.47  994.65  993.78...
992.86      991.89  990.88  989.82  988.72  987.58...
986.4       985.18  983.92  982.63  981.3   979.93...
978.53      977.1   975.63  974.13  972.6   971.03...
969.44      967.81  966.16  964.47  962.75  961.01...
959.24      957.43  955.6   953.74  951.86  949.94...
948 946.03  944.03  942.01  939.95  937.87  935.77...
933.63      931.47  929.28  927.06  924.82  922.54...
920.24      917.92  915.56  913.17  910.76  908.32...
905.85      903.34  900.81  898.25  895.66  893.04...
890.39      887.7   887.13];
```

rho1=**interp1**(T,rho,T1); $\%kg/m3$

Appendix E

Raw data from convection experiments

	00H2hit	00H2hitm	00H2lit	00H2litm	00H2mit	00H2mitm
Flowrate (GPM)	3.00494	2.1733	3.06269	2.13876	2.97037	2.16391
Voltage (V)	18.67278	18.65394	17.91732	18.02414	18.18814	18.32702
Current (A)	464.9508	464.9247	465.0416	464.9816	464.9652	464.9612
Bulk Inlet Temperature(C)	64.98971	60.50614	22.64198	24.30401	37.69999	41.74975
0.2m Wall Temperature(C)	76.92643	74.53683	36.27494	40.7199	50.61591	56.74614
0.4m Wall Temperature(C)	77.40044	75.23674	36.68983	41.40102	51.06766	57.43918
0.6m Wall Temperature(C)	78.83917	76.96001	38.16023	43.15039	52.55827	59.1828
0.8m Wall Temperature(C)	79.15557	77.52691	38.28732	43.55246	52.75612	59.67458
1.0m Wall Temperature(C)	80.94446	79.58568	40.17383	45.74737	54.62481	61.77469
1.2m Wall Temperature(C)	81.26407	80.17421	40.35535	46.22822	54.88095	62.31103
1.4m Wall Temperature(C)	82.19233	81.37135	41.11659	47.28383	55.72038	63.42
1.6m Wall Temperature(C)	82.23067	81.67714	41.05945	47.50468	55.72001	63.67823
1.8m Wall Temperature(C)	82.72624	82.43108	41.54454	48.25346	56.23802	64.44554
2.0m Wall Temperature(C)	83.80283	83.77626	42.60747	49.60364	57.3328	65.79592
2.2m Wall Temperature(C)	85.14393	85.38461	43.89806	51.15237	58.67855	67.39316
2.4m Wall Temperature(C)	85.38755	85.89222	43.85421	51.39443	58.762	67.76305
2.6m Wall Temperature(C)	86.10437	86.91915	44.41232	52.33759	59.39135	68.74277
2.8m Wall Temperature(C)	86.31836	87.2639	44.96249	53.29815	59.81508	69.30712
Bulk Outlet Temperature(C)	75.65207	75.07867	32.62207	38.82036	48.16604	56.23373
HX Outlet Temperature(C)	64.9397	60.51187	21.94953	23.3907	37.24079	41.24327
Isothermal DP (psi)	2.39482	1.40159	2.98065	1.57596	2.6123	1.49122
Heated DP (psi)	3.12986	1.78977	3.79768	1.95215	3.36358	1.89096
System Pressure (psi)	5.856	4.45594	3.2521	3.12283	3.66034	3.33701

Figure E-1: Water

	09Al2gpm23	09A3gpm21	09A3gpm27hhf	09A3gpm39	09A3gpm63
Flowrate (GPM)	2.14708	3.71554	3.85107	3.59714	3.57432
Voltage (V)	18.0176	17.86031	24.30109	18.17284	18.61698
Current (A)	464.10529	464.11328	620.27004	464.11436	464.05445
Bulk Inlet Temperature(C)	22.82405	21.43268	27.8986	38.80434	63.8074
0.2m Wall Temperature(C)	40.76522	34.75831	50.42508	51.13973	75.07617
0.4m Wall Temperature(C)	41.40868	35.05696	50.90551	51.46299	75.44823
0.6m Wall Temperature(C)	43.19123	36.43843	53.27517	52.79873	76.7955
0.8m Wall Temperature(C)	43.75072	36.57545	53.55975	53.14741	77.36495
1.0m Wall Temperature(C)	46.0893	38.39788	56.81484	54.96446	79.11224
1.2m Wall Temperature(C)	46.55323	38.48939	56.94746	55.12178	79.35514
1.4m Wall Temperature(C)	47.56636	39.15593	58.16805	55.88185	80.19008
1.6m Wall Temperature(C)	47.92721	39.02766	57.88674	55.81818	80.19462
1.8m Wall Temperature(C)	48.74881	39.46218	58.62015	56.25802	80.57566
2.0m Wall Temperature(C)	50.20709	40.51077	60.45831	57.3158	81.5986
2.2m Wall Temperature(C)	51.75584	41.67084	62.44647	58.4985	82.73356
2.4m Wall Temperature(C)	51.97254	41.4593	62.17147	58.47775	82.97719
2.6m Wall Temperature(C)	53.11035	42.05278	63.14805	59.12915	83.67416
2.8m Wall Temperature(C)	54.02716	42.47715	63.81264	59.36877	83.61638
Bulk Outlet Temperature(C)	38.17461	30.08651	43.2501	47.88912	73.13351
HX Outlet Temperature(C)	21.32882	20.52	27.07865	38.21521	63.59562
Isothermal DP (psi)	1.54749	4.10802	4.2043	3.5532	3.16486
Heated DP (psi)	1.8819	5.15152	5.13625	4.52001	4.12396
System Pressure (psi)	3.02007	3.7945	4.4923	4.33714	6.10408

Figure E-2: Nyacol Alumina 0.9 vol%

	18Al2gpm26	18Al3gpm21	18Al3gpm27mhf	18Al3gpm33hhf	18Al3gpm36	18Al3gpm60
Flowrate (GPM)	2.11176	3.48637	3.71442	3.75559	3.60543	3.67032
Voltage (V)	18.08459	17.87957	20.86823	24.45347	18.12009	18.5501
Current (A)	464.11617	464.13844	535.851	620.21515	464.10945	464.09721
Bulk Inlet Temperature(C)	25.91971	21.40127	27.78721	33.40198	35.52497	60.21245
0.2m Wall Temperature(C)	44.47903	35.50469	45.57036	56.4685	48.46948	71.85518
0.4m Wall Temperature(C)	45.14299	35.81661	45.95874	56.96888	48.78125	72.18062
0.6m Wall Temperature(C)	46.9389	37.18	47.78777	59.4234	50.10509	73.47221
0.8m Wall Temperature(C)	47.51333	37.35651	47.99497	59.7354	50.44356	74.01196
1.0m Wall Temperature(C)	49.80852	39.1952	50.45109	62.99287	52.27215	75.78833
1.2m Wall Temperature(C)	50.26745	39.27104	50.55818	63.15393	52.393	75.97945
1.4m Wall Temperature(C)	51.26199	39.9389	51.41532	64.2907	53.0932	76.74103
1.6m Wall Temperature(C)	51.6144	39.8526	51.27172	64.09842	53.04206	76.70914
1.8m Wall Temperature(C)	52.43639	40.30477	51.83576	64.84272	53.47838	77.0918
2.0m Wall Temperature(C)	53.91524	41.35752	53.22519	66.70695	54.52115	78.11155
2.2m Wall Temperature(C)	55.45943	42.51129	54.69912	68.67211	55.67583	79.20907
2.4m Wall Temperature(C)	55.68051	42.31299	54.51399	68.51639	55.61823	79.38452
2.6m Wall Temperature(C)	56.83478	42.93003	55.29438	69.52188	56.24698	80.04375
2.8m Wall Temperature(C)	57.45348	43.26892	55.94786	70.22168	56.48817	80.12054
Bulk Outlet Temperature(C)	41.28559	30.25747	39.45859	49.1903	44.43941	69.20803
HX Outlet Temperature(C)	24.51621	20.52037	26.91552	32.6007	34.8257	59.78618
Isothermal DP (psi)	1.66467	4.34893	4.37949	4.301	4.03712	3.70054
Heated DP (psi)	2.02193	5.40871	5.42377	5.25433	5.10331	4.77444
System Pressure (psi)	3.16892	3.91395	5.19716	5.53237	4.62547	6.7149

Figure E-3: Nyacol Alumina 1.8 vol%

	36Al2gpm24	36Al3gpm24	36Al3gpm39hhf	36Al3gpm41	36Al3gpm59
Flowrate (GPM)	2.1384	3.28003	3.34814	3.36738	3.38854
Voltage (V)	18.10837	18.02803	24.70353	18.3139	18.61091
Current (A)	464.13476	465.12444	620.23816	465.07781	465.11957
Bulk Inlet Temperature(C)	23.68641	24.24426	39.0955	41.51349	59.234
0.2m Wall Temperature(C)	45.98109	41.30078	65.87838	56.5571	72.74825
0.4m Wall Temperature(C)	46.62167	41.65096	66.46589	56.92535	73.1019
0.6m Wall Temperature(C)	48.29552	43.1406	69.02002	58.43503	74.5317
0.8m Wall Temperature(C)	48.7223	43.23788	69.40198	58.59802	75.00121
1.0m Wall Temperature(C)	50.97775	45.20934	72.8344	60.48918	76.81531
1.2m Wall Temperature(C)	51.21864	45.28686	73.01497	60.6322	77.01919
1.4m Wall Temperature(C)	52.15632	45.96563	74.24088	61.34251	77.76243
1.6m Wall Temperature(C)	52.43409	45.96144	74.16273	61.37967	77.83124
1.8m Wall Temperature(C)	53.13548	46.48248	75.00669	61.87477	78.28736
2.0m Wall Temperature(C)	54.58645	47.62865	76.96351	62.96377	79.35771
2.2m Wall Temperature(C)	56.00161	48.78805	79.00559	64.14473	80.52288
2.4m Wall Temperature(C)	56.0483	48.64737	78.9349	64.17745	80.71439
2.6m Wall Temperature(C)	57.21147	49.37382	80.14265	64.88371	81.44306
2.8m Wall Temperature(C)	57.70733	49.6353	80.58697	65.02226	81.46818
Bulk Outlet Temperature(C)	38.62886	34.05324	56.74525	51.24416	68.89603
HX Outlet Temperature(C)	22.43631	23.29163	38.44172	40.81704	58.87414
Isothermal DP (psi)	2.20866	4.51088	4.33627	4.27541	4.06223
Heated DP (psi)	2.61975	5.53466	5.195	5.365	5.17097
System Pressure (psi)	3.2164	4.10653	5.18645	4.95686	6.48639

Figure E-4: Nyacol Alumina 3.6 vol%

	00H22gpm20	00H22gpm40	00H22gpm60	00H23gpm20	00H23gpm40	00H23gpm60	00H24gpm20
Flowrate (GPM)	2.08034	2.07694	2.09386	3.10176	3.21777	3.23872	3.89877
Voltage (V)	18.24232	18.57912	18.87757	18.00325	18.37696	18.81143	18.0497
Current (A)	468.25321	468.56675	468.54142	465.61421	466.04022	468.22107	468.44613
Bulk Inlet Temperature(C)	27.32241	45.8845	62.92734	24.47138	44.98746	64.61695	24.22174
0.2m Wall Temperature(C)	44.1826	61.33645	77.51302	38.19707	57.47591	76.4671	36.65191
0.4m Wall Temperature(C)	44.74066	61.97111	78.19125	38.4462	57.77038	76.80705	36.74138
0.6m Wall Temperature(C)	46.53326	63.71944	79.93023	39.82951	59.16999	78.18583	38.05257
0.8m Wall Temperature(C)	47.00199	64.26776	80.59293	40.04607	59.39551	78.47973	38.06361
1.0m Wall Temperature(C)	49.31427	66.56999	82.83967	42.03153	61.27546	80.29592	39.86
1.2m Wall Temperature(C)	49.86361	67.20125	83.51283	42.28001	61.55684	80.6309	39.95495
1.4m Wall Temperature(C)	50.86178	68.29279	84.64904	43.03529	62.32196	81.47161	40.58396
1.6m Wall Temperature(C)	51.22542	68.69037	85.09655	43.00538	62.32548	81.50864	40.38674
1.8m Wall Temperature(C)	51.97732	69.4376	85.80699	43.45807	62.72522	81.84551	40.69575
2.0m Wall Temperature(C)	53.46722	70.9437	87.27752	44.62602	63.8416	82.92925	41.71109
2.2m Wall Temperature(C)	55.133	72.5897	88.92127	45.93997	65.10668	84.15208	42.85419
2.4m Wall Temperature(C)	55.31439	72.96352	89.48566	45.78854	65.12046	84.3421	42.55684
2.6m Wall Temperature(C)	56.54093	74.22485	90.83136	46.58874	65.91691	85.19349	43.15566
2.8m Wall Temperature(C)	57.23822	74.56683	91.01185	46.85744	66.04466	85.09607	43.84462
Bulk Outlet Temperature(C)	42.28322	60.99272	78.16016	34.29705	54.7069	74.48383	31.92871
HX Outlet Temperature(C)	25.84694	44.83203	62.48355	23.33225	44.22969	64.25673	23.25417
Isothermal DP (psi)	1.50873	1.40297	1.32311	3.07505	2.96851	2.82873	4.7782
Heated DP (psi)	1.88227	1.80357	1.74711	3.9096	3.89219	3.80983	6.21708
System Pressure (psi)	2.50066	2.94688	4.19113	3.75889	3.81128	5.40596	4.45369

Figure E-5: Water Retest

	02zr1gpm30	02zr2gpm28	02zr3gpm31	02zr3gpm37	02zr3gpm40	02zr3gpm63
Flowrate (GPM)	1.05256	1.97399	3.23591	3.1776	3.14237	3.16477
Voltage (V)	18.4147	18.11652	20.90937	24.58307	18.20876	18.60929
Current (A)	463.69928	463.71248	534.60097	620.24427	463.72385	463.7209
Bulk Inlet Temperature(C)	30.17757	28.4696	31.28818	37.23974	40.19891	63.10984
0.2m Wall Temperature(C)	57.2215	46.49989	49.27526	60.93604	53.32542	75.15406
0.4m Wall Temperature(C)	58.55154	47.07186	49.51524	61.29328	53.58902	75.50146
0.6m Wall Temperature(C)	61.12441	48.84714	51.36509	63.81432	54.97188	76.88596
0.8m Wall Temperature(C)	62.34489	49.34029	51.547	64.07715	55.17022	77.14571
1.0m Wall Temperature(C)	65.62477	51.68875	54.0838	67.51872	57.09922	78.94852
1.2m Wall Temperature(C)	66.96229	52.26187	54.32547	67.87998	57.35114	79.25308
1.4m Wall Temperature(C)	68.7517	53.26052	55.22238	69.14545	58.0882	80.0744
1.6m Wall Temperature(C)	70.16564	53.72072	55.21901	69.14262	58.13158	80.15901
1.8m Wall Temperature(C)	71.86951	54.59493	55.86004	70.0307	58.61864	80.58234
2.0m Wall Temperature(C)	74.29244	56.12319	57.34452	72.03663	59.7537	81.68194
2.2m Wall Temperature(C)	76.79373	57.75138	58.96564	74.21324	60.97549	82.89462
2.4m Wall Temperature(C)	78.04988	58.05067	58.84657	74.17127	60.9911	83.11107
2.6m Wall Temperature(C)	80.40835	59.31915	59.82354	75.48213	61.78248	83.96116
2.8m Wall Temperature(C)	81.30343	59.99526	60.42169	76.10372	61.90623	83.78941
Bulk Outlet Temperature(C)	61.00621	44.46611	44.1889	55.14908	50.14591	73.09134
HX Outlet Temperature(C)	28.24339	27.21569	30.4717	36.55966	39.5335	62.9157
Isothermal DP (psi)	0.4523	1.36003	3.20483	3.022	2.92607	2.73728
Heated DP (psi)	0.51691	1.69306	4.02602	3.7604	3.7737	3.62362
System Pressure (psi)	3.95199	4.50467	5.45377	5.60087	5.41823	7.29462

Figure E-6: Nyacol Zirconia 0.2 vol%

	05zr1gpm28	05zr2gpm30	05zr3gpm28	05zr3gpm33mhf	05zr3gpm39hhf	05zr3gpm40	05zr3gpm60
Flowrate (GPM)	1.01515	2.06051	3.55744	3.46943	3.46132	3.38666	3.47349
Voltage (V)	18.44775	18.1832	18.01022	21.1347	24.57007	18.22731	18.57796
Current (A)	463.71327	464.57508	464.59571	539.60519	619.19776	464.54747	464.54
Bulk Inlet Temperature(C)	29.14622	30.08693	28.23168	32.5862	39.18418	39.60241	59.9604
0.2m Wall Temperature(C)	58.72072	48.57727	42.02161	50.9954	62.73373	52.96708	72.24453
0.4m Wall Temperature(C)	60.14585	49.11654	42.15548	51.1709	62.97651	53.20181	72.49383
0.6m Wall Temperature(C)	62.68138	50.8881	43.51732	53.01383	65.41311	54.55386	73.82512
0.8m Wall Temperature(C)	63.89634	51.31437	43.57759	53.137	65.58519	54.70904	74.04297
1.0m Wall Temperature(C)	67.29677	53.66815	45.4835	55.68788	68.9421	56.61359	75.81908
1.2m Wall Temperature(C)	68.57766	54.20186	45.60701	55.88687	69.22975	56.82178	76.05428
1.4m Wall Temperature(C)	70.39178	55.18459	46.24088	56.76519	70.43198	57.52937	76.79289
1.6m Wall Temperature(C)	71.82577	55.61827	46.17488	56.70418	70.32653	57.52046	76.82607
1.8m Wall Temperature(C)	73.50875	56.44731	46.6112	57.29168	71.09794	57.98448	77.22021
2.0m Wall Temperature(C)	75.99534	57.95644	47.68889	58.76514	73.0321	59.08851	78.28266
2.2m Wall Temperature(C)	78.559	59.54968	48.84696	60.3299	75.10884	60.29639	79.4744
2.4m Wall Temperature(C)	79.73114	59.81972	48.67653	60.19639	74.98602	60.2583	79.61338
2.6m Wall Temperature(C)	82.18225	61.03666	49.35125	61.12081	76.20742	61.00588	80.40905
2.8m Wall Temperature(C)	82.9009	61.62327	49.84904	61.55225	76.5203	61.1323	80.42511
Bulk Outlet Temperature(C)	61.32544	45.76329	37.15283	45.05494	55.9053	49.10197	69.35842
HX Outlet Temperature(C)	27.11743	28.85878	27.37513	31.78973	38.51185	38.96035	59.67277
Isothermal DP (psi)	0.44587	1.4817	3.9422	3.69677	3.5525	3.37605	3.22988
Heated DP (psi)	0.4973	1.84638	5.01236	4.63281	4.42264	4.33112	4.23807
System Pressure (psi)	3.78214	4.56177	5.85873	5.88841	6.10362	5.4729	7.67655

Figure E-7: Nyacol Zirconia 0.5 vol%

	09zr2gpm38	09zr3gpm31	09zr3gpm43	09zr3gpm50hhf	09zr3gpm60
Flowrate (GPM)	2.03722	3.1855	3.24266	3.21843	3.22712
Voltage (V)	18.33887	18.18921	18.38689	24.9098	18.67438
Current (A)	464.54793	466.6289	466.55435	620.21681	466.5743
Bulk Inlet Temperature(C)	38.50456	31.62775	43.27469	50.74866	59.89772
0.2m Wall Temperature(C)	57.31303	46.94986	57.53344	75.00809	73.1306
0.4m Wall Temperature(C)	57.83732	47.1713	57.78243	75.40258	73.4212
0.6m Wall Temperature(C)	59.57504	48.53944	59.13909	77.89033	74.74378
0.8m Wall Temperature(C)	59.99302	48.67307	59.32288	78.08654	74.97409
1.0m Wall Temperature(C)	62.24657	50.61906	61.19756	81.46148	76.79803
1.2m Wall Temperature(C)	62.72564	50.78759	61.3865	81.76794	77.03163
1.4m Wall Temperature(C)	63.65355	51.42463	62.05961	82.965	77.76234
1.6m Wall Temperature(C)	64.05099	51.42881	62.07173	82.90725	77.81256
1.8m Wall Temperature(C)	64.79118	51.85876	62.49017	83.67201	78.21078
2.0m Wall Temperature(C)	66.24901	52.97754	63.58277	85.62261	79.27663
2.2m Wall Temperature(C)	67.77864	54.18317	64.78637	87.73328	80.47553
2.4m Wall Temperature(C)	68.03752	54.02866	64.72866	87.68329	80.58213
2.6m Wall Temperature(C)	69.26795	54.82585	65.52694	89.00783	81.42833
2.8m Wall Temperature(C)	69.62152	54.94236	65.5634	89.10601	81.19179
Bulk Outlet Temperature(C)	53.45984	41.16436	52.75321	67.86288	69.44882
HX Outlet Temperature(C)	37.52995	30.81392	42.64694	50.24725	59.56394
Isothermal DP (psi)	1.73875	3.94456	3.81485	3.70913	3.55899
Heated DP (psi)	2.17511	4.97116	4.88016	4.62221	4.61825
System Pressure (psi)	4.0351	4.02895	4.97184	5.91178	6.31908

Figure E-8: Nyacol Zirconia 0.9 vol%

Appendix F

Theoretical Investigation of Gas Nanofluids

Gas nanofluids are of interest to nuclear engineers from the standpoint of advanced gas reactor cooling like the gas cooled fast reactor (GFR) or the high temperature gas cooled reactor (HTGR). Gas nanofluids are also of great interest in fusion reactor divertor cooling. As a part of the current LDRD project, Idaho National Lab (INL) has taken the lead in the design and construction of a gas-nanoparticle suspension convective cooling experiment as shown in Figure F-1. This chapter will cover some initial theoretical background work on gas-particulate flows which are done to help guide the experimental and future theoretical investigations of gas nanofluids.

The author spent a 3-week period at INL in 2005 and contributed this work to the gas nanofluid project underway there. A determination of the key transport phenomena in the INL gas nanofluid experiment is made through a semi-quantitative approach. The current specifications of the experiment (i.e., temperature, pressure, flow, ID, etc.) are used in the analysis. It is important to note that, due to the sensitivity of gas properties to temperature and pressure, gas nanofluid systems can be regarded as continuous, free molecular, or transitional in behavior; thus the results of this analysis are applicable to the described experimental situation only. The insights found lead to the recommendation of certain focal points for the experimental and future theoretical work with gas nanofluids. This chapter is divided into three

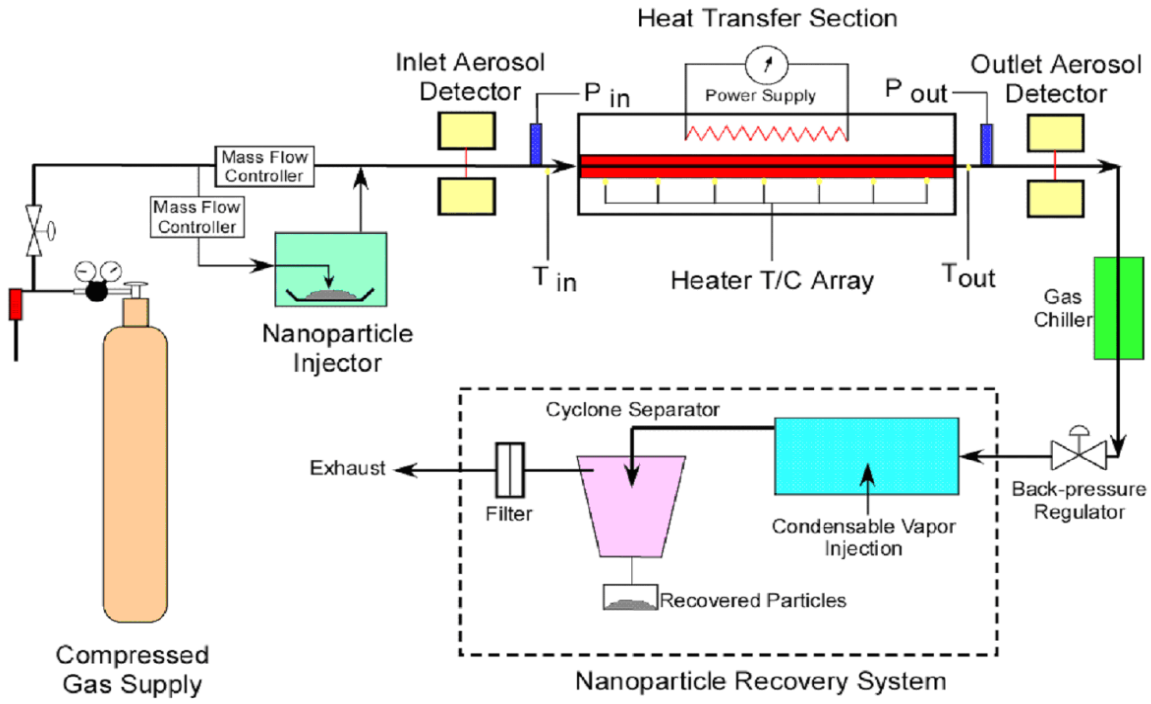

Figure F-1: INL gas loop experiment schematic

sections: Assumptions, Analysis, and Recommendations.

F.1 Assumptions

The main assumption is that the flow situation considered is for the INL gas nanofluid experiment. The experiment is a once-through heated pipe convection heat transfer system. The system has the means to inject, measure, and remove nanometer sized particles at various concentrations. The purpose of the experiment is to determine the potential for using gas nanoparticle dispersions (nanofluids) to enhance convective heat transfer. The experiment uses helium gas as the base fluid and, for the sake of analysis, carbon based nanoparticles. For the analysis the following parameters are set:

Helium Gas State and Properties

- Pressure (P) = 0.2 MPa

- Temperature (T) = 873 K
- Viscosity (μ) $\approx$ 4x10^{-5} Pa-s
- Thermal Conductivity (k) $\approx$ 0.3 W/m-K
- Density (ρ) $\approx$ 0.11 kg/m^3
- Heat Capacity (c) $\approx$ 5193 J/kg-K
- Ideal Gas Constant (R) = 8.31 J/mol-K
- Avogadro's Number (N_{av}) = 6.022x10^{23} atoms/mol
- Effective diameter of single molecule (d_{He}) $\approx$ 0.6x10^{-10} m

Nanoparticle Properties

- Material - Pyro-carbon Spheres
- Particle Diameter (d_p) = 1-100 nm
- Thermal Conductivity (k_p) $\approx$ 4 W/m-K or greater
- Density (ρ_p) $\approx$ 1900 kg/m^3
- Heat Capacity (c_p] $\approx$ 709 J/kg-K

Operating conditions

- Reynolds Number (Re) = 4000
- Pipe diameter (D) = 17.3 mm

F.2 Analysis

The analysis is composed of five parts as follows: 1) assessment of the continuum assumption, 2) evaluation of the internal particle temperature response, 3) evaluation

of the particle/fluid heat transfer response, 4) evaluation of nanoparticle dispersion and turbulence intensification as heat transfer enhancement mechanisms, and 5) discussion of other possible heat transfer enhancement mechanisms.

F.2.1 Continuum Assumption

The common way of determining whether the fluid-particle interaction can be treated as a continuum phenomenon or not is to calculate the Knudsen number (Kn). The Knudsen number is the ratio of the mean free path (λ) of the fluid particles to the characteristic length of the system with which they interact. Here it is the mean free path of the gas atoms divided by the diameter of the nanoparticles as shown:

$$Kn = \lambda / d_p \tag{F.1}$$

$$\lambda = \frac{RT}{\sqrt{2}\pi d_{He} P N_{av}} \tag{F.2}$$

Knudsen values less than 0.01 are considered to be in the continuum; values from 0.01 to 1.0 can be considered near-continuum; values from 1.0 to 10 can be considered transitional; values above 10 are free molecular. Navier-Stokes equations are valid for the continuum regime below 0.01 and can be extended, through the use of slip conditions, up to 0.1. Figure F-2 shows the dependence of the Knudsen number on the diameter of the nanoparticle. From the figure, it is determined that the nanoparticle will see the surrounding gas as a free molecular interaction and therefore not a continuum. However, at lower temperatures and higher pressures, the latter being typical of gas-cooled reactor applications, the interaction is moved to the transitional regime. Other analysis determined the Knudsen number to be very weakly dependent on the base gas.

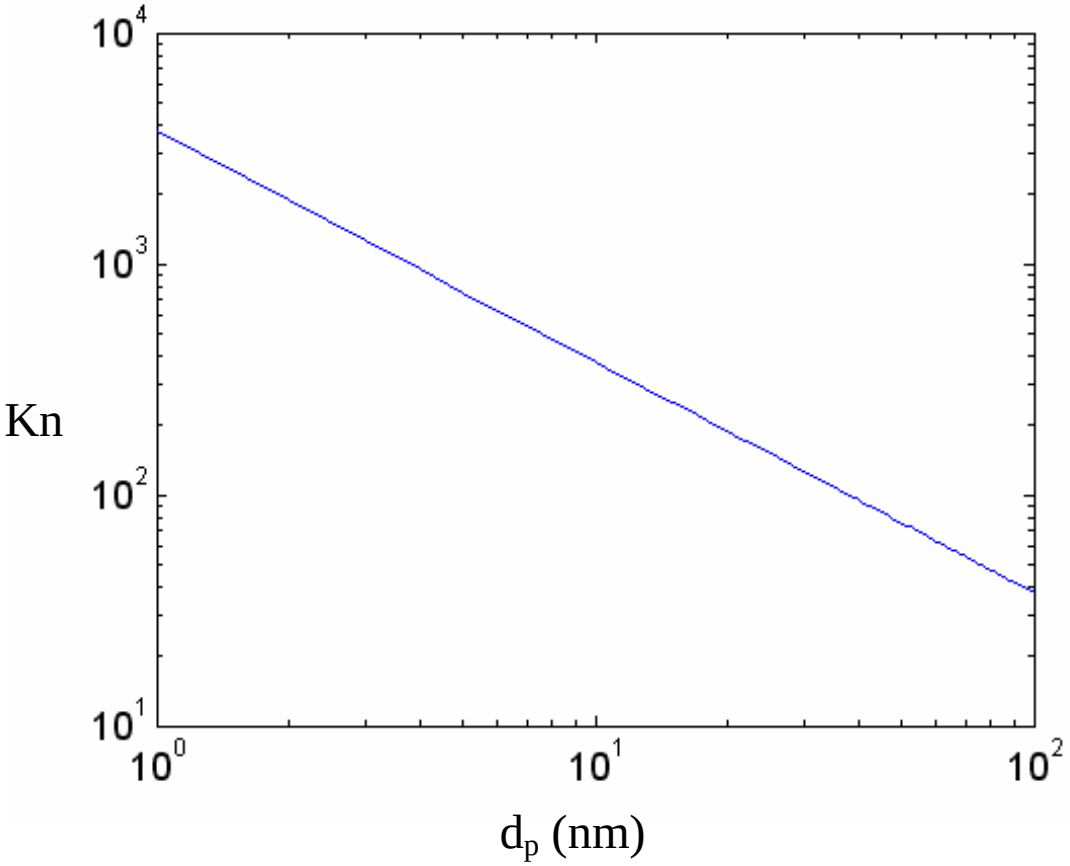

Figure F-2: Knudsen number for nanoparticles in helium gas

F.2.2 Determination of internal particle temperature response

A comparison of the time scale (τ_p) of energy redistribution within the nanoparticle and the timescales of the energy transfer from the particle to the surrounding gas determines whether the temperature distribution inside the nanoparticle can be regarded as uniform. Energy is transferred to and from the particle by conduction and radiation, their time scales being indicated here as (τ_{con}) and (τ_{rad}), respectively.

Energy redistribution within particle

The time scale of the energy transfer can be found as

$$\tau_p \approx \frac{d_p^2}{\alpha_p \cdot 0.12} \tag{F.3}$$

$$\alpha_p = \frac{k_p}{\rho_p c_p} \tag{F.4}$$

as shown from transient conduction solution for spherical systems with low Biot number [76].

Heat conduction from particle to gas

An energy balance for the particle is developed as

$$\rho_p c_p \frac{\pi}{6} d_p^3 \frac{dT_p}{dt} = -\frac{\pi}{2} d_p^2 n_g \bar{c} k_b (T_p - T) \tag{F.5}$$

where the right-hand term, the particle surface heat flux, is from Filippov and Rosner's paper [77], assuming an accommodation coefficient equal to one, $\gamma = 5/3$, and T as the bulk gas temperature. It is also defined that

$$n_g = (P \cdot N_{av})/(R \cdot T) \tag{F.6}$$

is the He atom concentration (atoms/m^3) and

$$\bar{c} = \sqrt{\frac{8k_bT}{\pi n_g}} \tag{F.7}$$

is the average He atom speed and

$$n_g = 0.004/N_{av} \tag{F.8}$$

is the mass of a He atom (kg). From the energy balance equation, the time scale for heat conduction to the gas is

$$\tau_{con} \approx \frac{\rho_p c_p d_p}{3 n_g \bar{c} k_b} \tag{F.9}$$

Heat radiation from particle to surroundings

An energy balance for the particle with radiation heat transfer is developed as

$$\rho_p c_p \frac{\pi}{6} d_p^3 \frac{dT_p}{dt} = -\pi d_p^2 \sigma (T_p^4 - T^4) \tag{F.10}$$

(black body behavior is assumed) $\sigma = 5.67 \cdot 10^{-8}\ W/m^2K^4$. From the energy balance equation, the time scale for radiative heat transfer is

$$\tau_{rad} \approx \frac{\rho_p c_p d_p}{6\sigma T^3} \tag{F.11}$$

Comparison of these time scales gives the relative importance of each mechanism in the overall heat transfer process. Figure F-3 is a plot of the time scales of the three mechanisms and how these vary with nanoparticle diameter.

Two conclusions can be drawn from Fig. F-3 : i) The energy redistribution within the particle is much faster than the energy transfer between particle and gas due to the large particle conductivity. Thus the temperature distribution within the particle is uniform. ii) The dominant heat transfer mechanism from the particle to the gas is conduction. However, due to its long-range nature, particle-to-particle and particle-to-wall radiation can still play a significant role in the overall heat transfer

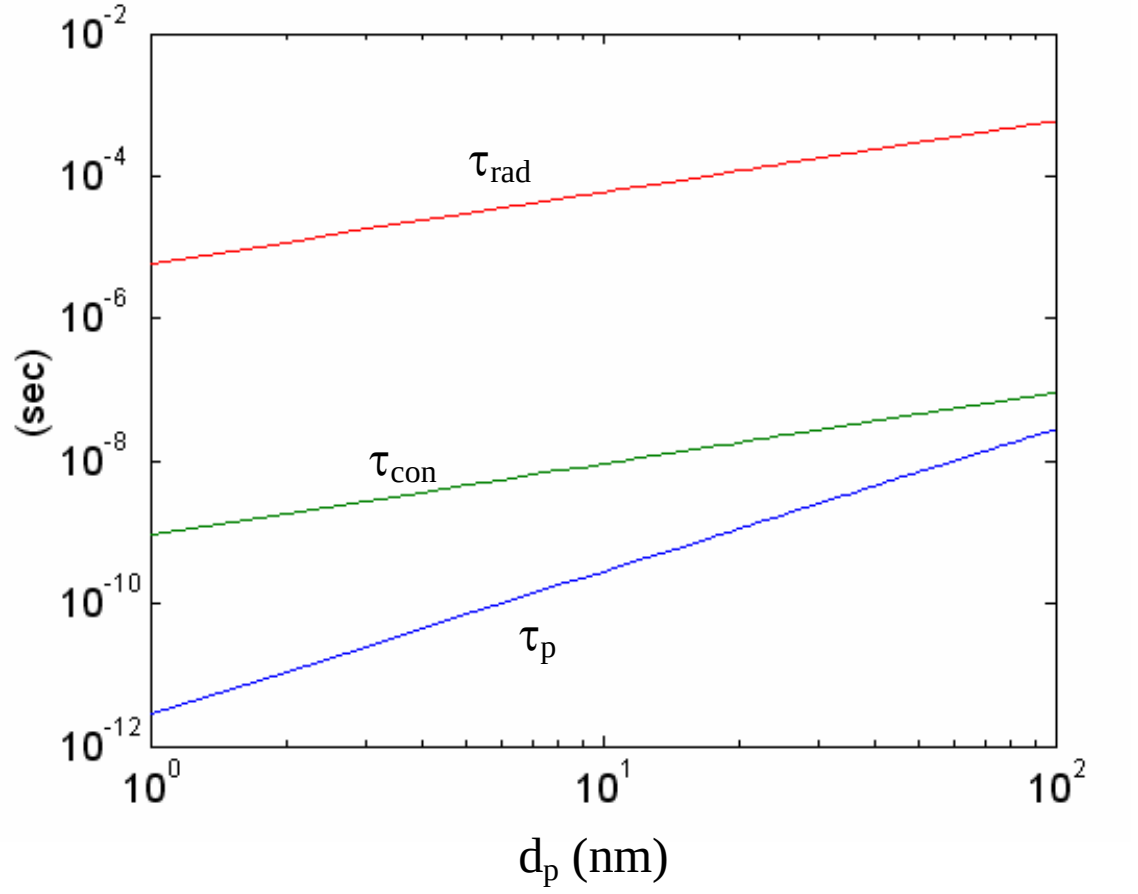

Figure F-3: Time scales for heat transfer mechanisms within and around nanoparticles in helium gas

enhancement in the channel.

F.2.3 Determination of local thermal equilibrium between the particles and the gas

A comparison of the time scale of the heat transfer from the particle to the gas with the time scale of the particle slip motion in the gas can be used to determine the thermal equilibrium characteristics of the mixture. The heat transfer time scale has been determined above. In turbulent flow the dominant slip mechanism is from inertial flight following the abrupt stop of an eddy. The time scale for this process is the so-called relaxation time of the particle

$$\tau_{rel} = \frac{\rho_p d_p^2}{18\mu} C_c \tag{F.12}$$

and

$$C_c = 1 + Kn(\alpha + \beta e^{-\gamma/Kn}) \tag{F.13}$$

is the Cunningham corrective factor, accounting for the non-continuum nature of the particle/gas interaction. The coefficients α, β, and γ are determined experimentally for exact fluid/particle combinations (which is not done here). For this calculation the values $\alpha = 2.34$, $\beta = 1.05$, and $\gamma =$ -0.39 were assumed. It was later found from a recent experiment of a similar system using polystyrene latex particles from 20nm to 270nm that $\alpha = 1.165$, $\beta = 0.483$, and $\gamma = 0.997$ [78]. The Cunningham factors were recalculated with these new values and found to be of the same order as the original calculation. The time scales τ_{rel} and τ_{con} are shown in Figure F-4. Since $\tau_{con} \ll \tau_{rel}$, it is concluded that particles can exchange energy very effectively as they fly within the gas; therefore we can assume that there is local particle/gas thermal equilibrium.

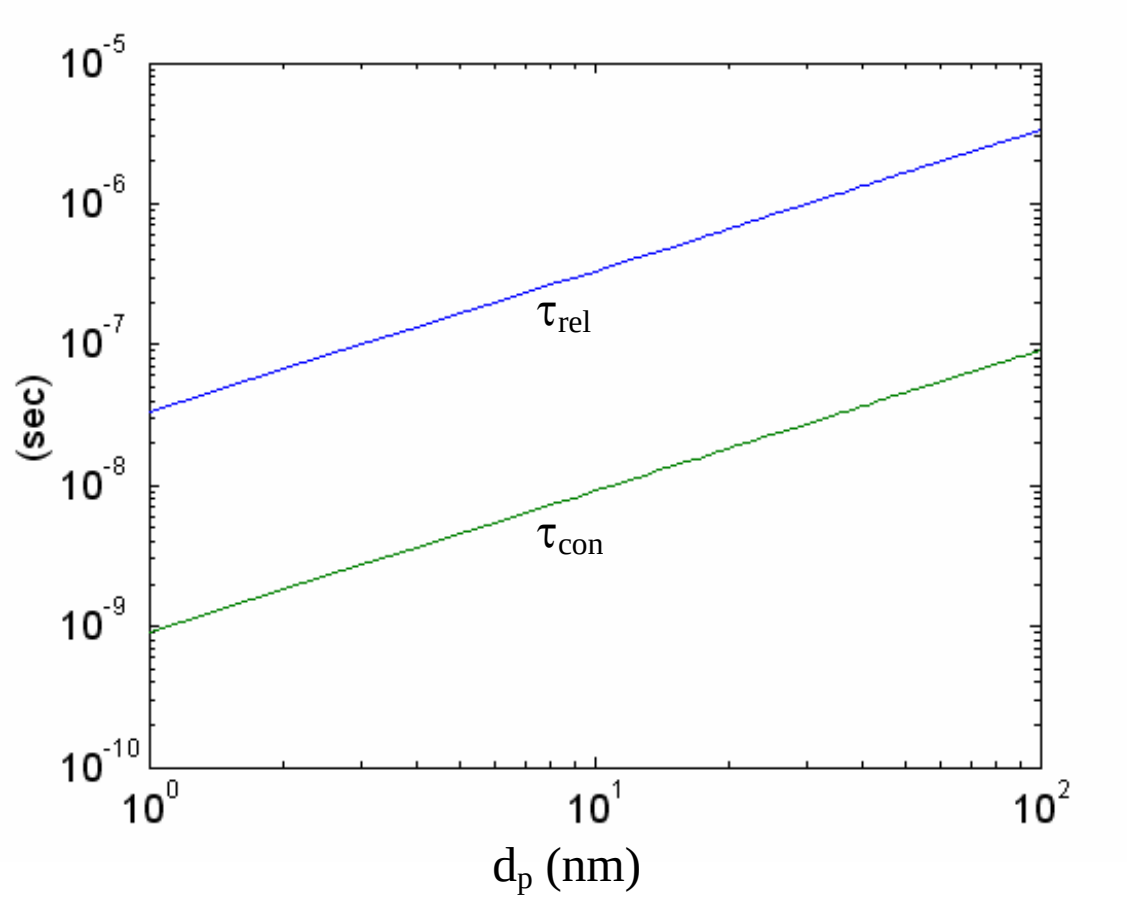

Figure F-4: Comparison of time scales for energy transfer and nanoparticle slip motion in helium gas

F.2.4 Heat transfer enhancement due to particle dispersion and turbulence strengthening

Due to their small size, nanoparticles can be entrained in both large and small turbulent eddies. This is shown by the size (l), velocity (V) and time scales (τ) of the eddies as follows:

Scales for *large* eddies:

- $l_o \sim 0.07 \cdot D \sim 1.2mm$
- $V_o \sim V_{shear} \sim 6m/s$
- $\tau_o \sim l_o/V_o \sim 2 \cdot 10^{-4} sec$

Scales for *small* eddies (using Kolomogorov's scaling laws):

- $l_s/l_o \sim Re^{-3/4} \Rightarrow l_s \sim 2.4\mu m$
- $\tau_s/\tau_o \sim Re^{-1/2} \Rightarrow \tau_s \sim 3 \cdot 10^{-6} sec, V_s \sim l_s/\tau_s \sim 0.7m/s$

It is seen that the particles (1-100nm) are much smaller than the eddy sizes (1.2mm and 2.4μm).

The next step is to determine the stopping distance (S) for the particles entrained in the small and large eddies in order to see how far they can be thrown by the eddy velocities. It is found that

$$S_o = \frac{\rho_p d_p^2}{18\mu} C_c V_o \tag{F.14}$$

for particles entrained by large eddies and

$$S_s = \frac{\rho_p d_p^2}{18\mu} C_c V_s \tag{F.15}$$

for particles entrained by small eddies. The stopping distance is shown in Figure F-5. Figure F-5 suggests that nanoparticles do not significantly project out of the eddies with the possible exception of large nanoparticles, i.e., >100 nm, entrained by small eddies. That is, the nanoparticles move with the turbulent eddies. Thus, contribution

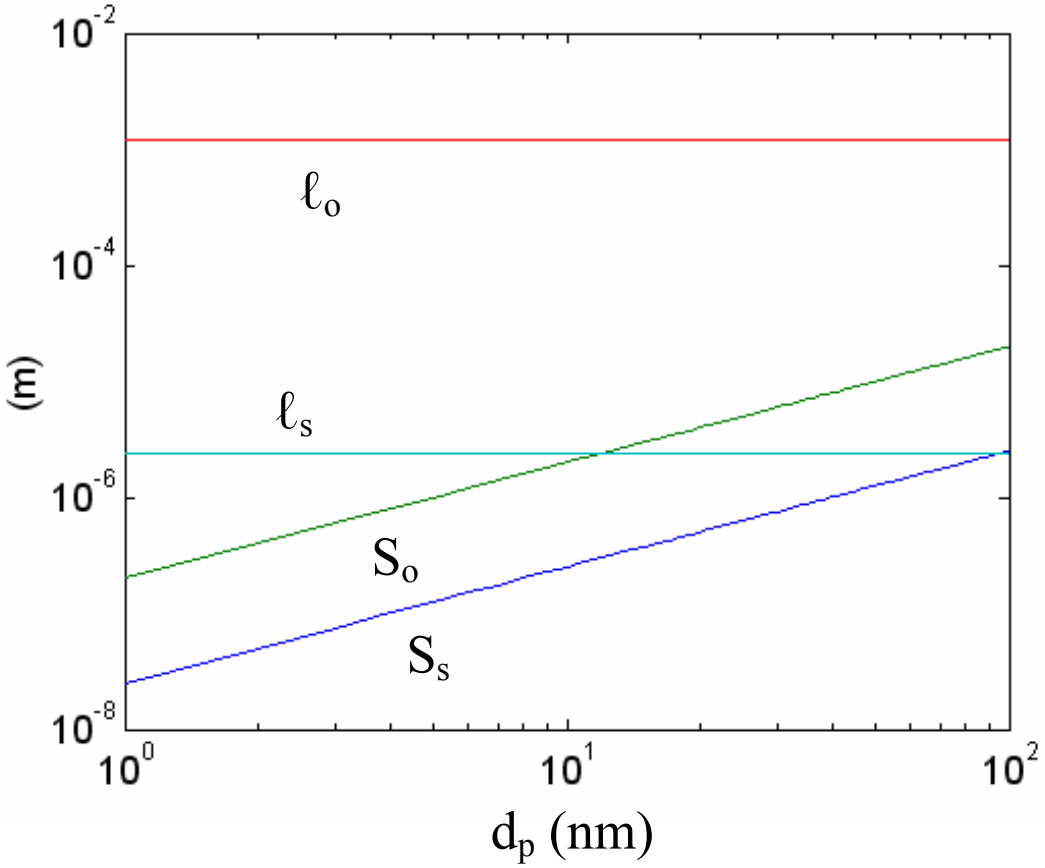

Figure F-5: Comparison of eddy sizes and particle stopping distances

of inertial slip to nanoparticle dispersion is probably negligible. Regarding the question of turbulence intensification, the presence of the nanoparticles will likely increase viscosity, which will delay the onset of turbulence for given mean velocity.

Moreover, Figure F-5 suggests that particles entrained by large eddies may interact with (i.e., break up) small eddies, since their length scales are comparable. Based on order-of-magnitude estimates of the kinetic energy carried by each eddy and using Kolomogorov's scaling laws, one finds that the ratio of the number of small eddies generated per unit time and volume to the number of large eddies generated per unit time and volume is proportional to $Re^{11/4}$, which in our case is about 1010. Therefore, small eddies are much more numerous than large eddies. This means that nanoparticles being projected out of large eddies will affect only a very limited number of small eddies. In summary, an effect on turbulence beyond the obvious effect via the change in viscosity seems unlikely.

F.2.5 Other possible heat transfer enhancement mechanisms

At least three mechanisms remain possible and should be considered in future analysis:

1) thermal conductivity increase due to the presence of the nanoparticles

2) radiative heat transfer from particle to particle and from particle to wall

3) development of thermal conductivity and viscosity gradients, which can develop in the boundary layer as a result of nanoparticle migration (e.g., phoretic effects, shear-rate induced migration, etc.)

F.3 Recommendations

In view of the above considerations, the following recommendations are made for the INL experiments:

a) Measure thermal conductivity and viscosity in static gas-particle systems,

b) Run a few experiments at temperatures for which the effect of radiation heat transfer is expected to be small,

c) Attempt to measure nanoparticle concentration distribution in test section.

Bibliography

[1] A. El Ghzaoui. Measurement of the diffuse double-layer forces between zirconia and α-alumina. *Journal of Applied Physics*, 86(10):5894–5897, 2006.

[2] Yimin Xuan and Qiang Li. Investigation on convective heat transfer and flow features of nanofluids. *Journal of Heat Transfer*, 125(1):151–155, 2003. Compilation and indexing terms, Copyright 2005 Elsevier Engineering Information, Inc.

[3] J.C. Maxwell. *Treatise on Electricity and Magnetism*. Dover Publications, 1954.

[4] A.S. Ahuja. Measurement of thermal conductivity of stationary blood by unsteady-state method. *J Appl Physiol*, 37(5):765–70, 1974.

[5] A.S. Ahuja. Augmentation of heat transport in laminar flow of polystyrene suspensions. I. Experiments and results. *Journal of Applied Physics*, 46:3408, 1975.

[6] A.S. Ahuja. Measurement of thermal conductivity of (neutrally and nonneutrally buoyant) stationary suspensions by the unsteady- state method. *Journal of Applied Physics*, 46:747, 1975.

[7] R.L. Hamilton and O.K. Crosser. Thermal Conductivity of Heterogeneous Two-Component Systems. *Industrial & Engineering Chemistry Fundamentals*, 1(3):187–191, 1962.

[8] J. C. Maxwell Garnett. Colours in Metal Glasses and in Metallic Films. *Royal Society of London Philosophical Transactions Series A*, 203:385–420, 1904.

[9] S. U. S. Choi. Enhancing thermal conductivity of fluids with nanoparticles. In *Proceedings of the 1995 ASME International Mechanical Engineering Congress and Exposition, Nov 12-17 1995*, volume 231 of *American Society of Mechanical Engineers, Fluids Engineering Division (Publication) FED*, pages 99–105, San Francisco, CA, USA, 1995. Argonne Natl Lab, IL, USA, ASME, New York, NY, USA.

[10] D.H. Everett et al. *Basic Principles of Colloid Science*. Royal Society of Chemistry London, 1988.

[11] Hidetoshi Masuda, Akira Ebata, Kazumari Teramae, and Nobuo Hishinuma. Alteration of thermal conductivity and viscosity of liquid by dispersing ultra-fine particles (dispersion of al2o3, sio2, and tio2 ultra-fine particles). *Netsu Bussei*, 4(4):227, 1993.

[12] S. U. S. Choi and Jeffrey A. Eastman. Enhanced heat transfer using nanofluids, April 24, 2001 2001. United States Patent Office.

[13] S. U. S. Choi, Z. G. Zhang, W. Yu, F. E. Lockwood, and E. A. Grulke. Anomalous thermal conductivity enhancement in nanotube suspensions. *Applied Physics Letters*, 79(14):2252, 2001. Compilation and indexing terms, Copyright 2005 Elsevier Engineering Information, Inc.

[14] J. A. Eastman, U. S. Choi, S. Li, L. J. Thompson, and S. Lee. Enhanced thermal conductivity through the development of nanofluids. In *Proceedings of the 1996 MRS Fall Symposium, Dec 2-5 1996*, volume 457 of *Materials Research Society Symposium - Proceedings*, pages 3–11, Boston, MA, USA, 1997. Argonne Natl Lab, IL, USA, Materials Research Society, Pittsburgh, PA, USA. Compilation and indexing terms, Copyright 2005 Elsevier Engineering Information, Inc.

[15] J. A. Eastman, U. S. Choi, S. Li, G. Soyez, L. J. Thompson, and R. J. DiMelfi. Novel thermal properties of nanostructured materials. *Materials Science Forum*, 312:629–634, 1999. Compilation and indexing terms, Copyright 2005 Elsevier Engineering Information, Inc.

[16] J. A. Eastman, S. U. S. Choi, S. Li, W. Yu, and L. J. Thompson. Anomalously increased effective thermal conductivities of ethylene glycol-based nanofluids containing copper nanoparticles. *Applied Physics Letters*, 78(6):718–720, 2001. Compilation and indexing terms, Copyright 2005 Elsevier Engineering Information, Inc.

[17] J. A. Eastman, S. R. Phillpot, S. U. S. Choi, and P. Keblinski. Thermal transport in nanofluids. *Annual Review of Materials Research*, 34:219–246, 2004. Compilation and indexing terms, Copyright 2005 Elsevier Engineering Information, Inc.

[18] Seok Pil Jang and S. U. S. Choi. Role of brownian motion in the enhanced thermal conductivity of nanofluids. *Applied Physics Letters*, 84(21):4316–4318, 2004. Compilation and indexing terms, Copyright 2005 Elsevier Engineering Information, Inc.

[19] P. Keblinski, S. R. Phillpot, S. U. S. Choi, and J. A. Eastman. Mechanisms of heat flow in suspensions of nano-sized particles (nanofluids). *International Journal of Heat and Mass Transfer*, 45(4):855–863, 2002. Compilation and indexing terms, Copyright 2005 Elsevier Engineering Information, Inc.

[20] P. Keblinski, J. A. Eastman, and D. G. Cahill. Nanofluids for thermal transport. *Materials Today*, 8(6):36–44, 2005. Compilation and indexing terms, Copyright 2005 Elsevier Engineering Information, Inc.

[21] Shinpyo Lee and S. U. S. Choi. Application of metallic nanoparticle suspensions in advanced cooling systems. In *Proceedings of the 1996 ASME International Mechanical Engineering Congress and Exposition, Nov 17-22 1996*, volume 342 of *American Society of Mechanical Engineers, Pressure Vessels and Piping Division (Publication) PVP*, pages 227–234, Atlanta, GA, USA, 1996. Argonne Natl Lab, IL, USA, ASME, New York, NY, USA. Compilation and indexing terms, Copyright 2005 Elsevier Engineering Information, Inc.

[22] Sarit K. Das, Nandy Putra, Peter Thiesen, and Wilfried Roetzel. Temperature dependence of thermal conductivity enhancement for nanofluids. *Journal of Heat Transfer*, 125(4):567–574, 2003. Compilation and indexing terms, Copyright 2005 Elsevier Engineering Information, Inc.

[23] Hrishikesh E. Patel, Sarit K. Das, Beena George, T. Sundararajan, A. Sreekumaran Nair, and T. Pradeep. Thermal conductivities of naked and monolayer protected metal nanoparticle based nanofluids: Manifestation of anomalous enhancement and chemical effects. *Applied Physics Letters*, 83(14):2931–2933, 2003. Compilation and indexing terms, Copyright 2005 Elsevier Engineering Information, Inc.

[24] Xinwei Wang, Xianfan Xu, and Stephen U. S. Choi. Thermal conductivity of nanoparticle-fluid mixture. *Journal of Thermophysics and Heat Transfer*, 13(4):474–480, 1999. Compilation and indexing terms, Copyright 2005 Elsevier Engineering Information, Inc.

[25] Bu-Xuan Wang, Le-Ping Zhou, Xiao-Feng Peng, and Xin-Xin Zhang. Enhancing the effective thermal conductivity of liquid withdilute suspensions of nano particles. In *15th Symposium on Thermophysical Properties*, June 23-27 2003 2003.

[26] Huaqing Xie, Jinchang Wang, Tonggeng Xi, Yan Liu, Fei Ai, and Qingren Wu. Thermal conductivity enhancement of suspensions containing nanosized alumina particles. *Journal of Applied Physics*, 91(7):4568, 2002. Compilation and indexing terms, Copyright 2005 Elsevier Engineering Information, Inc.

[27] Huaqing Xie, Jinchang Wang, Tonggeng Xi, Yan Liu, and Fei Ai. Dependence of the thermal conductivity on nanoparticle-fluid mixture on the base fluid. *Journal of Materials Science Letters*, 21(19):1469–1471, 2002. Compilation and indexing terms, Copyright 2005 Elsevier Engineering Information, Inc.

[28] Q. Xue and Wen-Mei Xu. A model of thermal conductivity of nanofluids with interfacial shells. *Materials Chemistry and Physics*, 90(2-3):298–301, 2005. Com-

pilation and indexing terms, Copyright 2005 Elsevier Engineering Information, Inc.

[29] Qing-Zhong Xue. Model for effective thermal conductivity of nanofluids. *Physics Letters A*, 307(5-6):313, 2003.

[30] L. Xue, P. Keblinski, S. R. Phillpot, S. U. S Choi, and J. A. Eastman. Effect of liquid layering at the liquid-solid interface on thermal transport. *International Journal of Heat and Mass Transfer*, 47(19-20):4277–4284, 2004. Compilation and indexing terms, Copyright 2005 Elsevier Engineering Information, Inc.

[31] M. J. Assael, C. F Chen, I. Metaxa, and W. A. Wakeham. Thermal conductivity of suspensions of carbon nanotubes in water. *International Journal of Thermophysics*, 25(4):971–985, 2004. Compilation and indexing terms, Copyright 2005 Elsevier Engineering Information, Inc.

[32] Huaqing Xie, Jinchang Wang, Tonggeng Xi, Yan Liu, and Fei Ai. Thermal conductivity of suspension containing sic particles. *Journal of Materials Science Letters*, 21(3):193–195, 2002. Compilation and indexing terms, Copyright 2005 Elsevier Engineering Information, Inc.

[33] Seok Pil Jang and S. U. S. Choi. Free convection in a rectangular cavity (benard convection) with nanofluids. In *2004 ASME International Mechanical Engineering Congress and Exposition, IMECE, Nov 13-19 2004*, volume 375 of *American Society of Mechanical Engineers, Heat Transfer Division, (Publication) HTD*, pages 147–153, Anaheim, CA, United States, 2004. School of Aerospace and Mechanical Engineering, Hankuk Aviation University, Goyang, Gyeonggi-do, 412-791, South Korea, American Society of Mechanical Engineers, New York, NY 10016-5990, United States. Compilation and indexing terms, Copyright 2005 Elsevier Engineering Information, Inc.

[34] Bock Choon Pak and Young I. Cho. Hydrodynamic and heat transfer study of dispersed fluids with submicron metallic oxide particles. *Experimental Heat Transfer*, 11(2):151, 1998.

[35] Yimin Xuan and Wilfried Roetzel. Conceptions for heat transfer correlation of nanofluids. *International Journal of Heat and Mass Transfer*, 43(19):3701–3707, 2000. Compilation and indexing terms, Copyright 2005 Elsevier Engineering Information, Inc.

[36] Yimin Xuan, Qiang Li, and Weifeng Hu. Aggregation structure and thermal conductivity of nanofluids. *AICHE Journal*, 49(4):1038–1043, 2003. Compilation and indexing terms, Copyright 2005 Elsevier Engineering Information, Inc.

[37] Yimin Xuan and Zhengping Yao. Lattice boltzmann model for nanofluids. *Heat and Mass Transfer/Waerme- und Stoffuebertragung*, 41(3):199–205, 2005. Compilation and indexing terms, Copyright 2005 Elsevier Engineering Information, Inc.

[38] Yimin Xuan and Qiang Li. Heat transfer enhancement of nanofluids. *International Journal of Heat and Fluid Flow*, 21(1):58–64, 2000. Compilation and indexing terms, Copyright 2005 Elsevier Engineering Information, Inc.

[39] Wen Jei Yang. Convective heat transfer in nanofluids. In *Proceedings of the ICHMT - NATOASI Conference on Microscale Heat Transfer: Fundamentals and Applications in Biological and Micromechanical Systems*, 18-30 July 2004 2004.

[40] Dongsheng Wen and Yulong Ding. Experimental investigation into convective heat transfer of nanofluids at the entrance region under laminar flow conditions. *International Journal of Heat and Mass Transfer*, 47(24):5181–5188, 2004. Compilation and indexing terms, Copyright 2005 Elsevier Engineering Information, Inc.

[41] Dongsheng Wen and Yulong Ding. Effective thermal conductivity of aqueous suspensions of carbon nanotubes (carbon nanotube nanofluids). *Journal of Thermophysics and Heat Transfer*, 18(4):481–485, 2004. Compilation and indexing terms, Copyright 2005 Elsevier Engineering Information, Inc.

[42] Dongsheng Wen and Yulong Ding. Effect of particle migration on heat transfer in suspensions of nanoparticles flowing through minichannels. *Microfluidics and Nanofluidics*, 1(2):183–189, 2005. Compilation and indexing terms, Copyright 2005 Elsevier Engineering Information, Inc.

[43] J. Buongiorno. Convective Transport in Nanofluids. *Journal of Heat Transfer*, 128:240, 2006.

[44] Sarit K. Das, Nandy Putra, and Wilfried Roetzel. Pool boiling of nano-fluids on horizontal narrow tubes. *International Journal of Multiphase Flow*, 29(8):1237–1247, 2003. Compilation and indexing terms, Copyright 2005 Elsevier Engineering Information, Inc.

[45] Sarit K. Das, Nandy Putra, and Wilfried Roetzel. Pool boiling characteristics of nano-fluids. *International Journal of Heat and Mass Transfer*, 46(5):851–862, 2003. Compilation and indexing terms, Copyright 2005 Elsevier Engineering Information, Inc.

[46] S. M. You, J. H. Kim, and K. H. Kim. Effect of nanoparticles on critical heat flux of water in pool boiling heat transfer. *Applied Physics Letters*, 83(16):3374–3376, 2003. Compilation and indexing terms, Copyright 2005 Elsevier Engineering Information, Inc.

[47] D. W. Zhou. Heat transfer enhancement of copper nanofluid with acoustic cavitation. *International Journal of Heat and Mass Transfer*, 47(14-16):3109–3117, 2004. Compilation and indexing terms, Copyright 2005 Elsevier Engineering Information, Inc.

[48] S. J. Kim, I. C. Bang, J. Buongiorno, and L. W. Hu. Effects of nanoparticle deposition on surface wettability influencing boiling heat transfer in nanofluids. *Applied Physics Letters*, 89(15):153107, 2006.

[49] J. BUONGIORNO and B. TRUONG. Preliminary study of water-based nanofluid coolants for PWRs. *Transactions of the American Nuclear Society*, 92:383–384, 2005.

[50] S.J. Kim, B. Truong, J. Buongiorno, Hu L.W., and I.C. Bang. Study of two-phase heat transfer in nanofluids for nuclear applications. In *Proceedings of ICAPP 06*, number 5705. American Nuclear Society, American Nuclear Society, May 2006.

[51] J. Buongiorno and Hu L.W. Nanofluid coolants for advanced nuclear power plants. In *Proceedings of ICAPP 05*, number 5705. American Nuclear Society, American Nuclear Society, May 2005.

[52] Manoj K. Chaudhury. Spread the word about nanofluids. *Nature*, 423(6936):131–132, 2003. Compilation and indexing terms, Copyright 2005 Elsevier Engineering Information, Inc.

[53] Darsh T. Wasan and Alex D. Nikolov. Spreading of nanofluids on solids. *Nature*, 423(6936):156–159, 2003. Compilation and indexing terms, Copyright 2005 Elsevier Engineering Information, Inc.

[54] S. Krishnakumar and P. Somasundaran. ESR investigations on the stabilization of alumina dispersions by Aerosol-OT in different solvents. *Colloids and Surfaces A: Physicochemical and Engineering Aspects*, 117(1):37–44, 1996.

[55] Jacob Eapen, Ju Li, and Sidney Yip. *Physical Review Letters*, In Press, 2007.

[56] S.J. Kim. Measurements of contact angle on metal surfaces fouled by nanoparticle deposition. Special problem 22.903, MIT Nuclear Science and Engineering Dept., 2006.

[57] D. Bohne, S. Fischer, and E. Obermeier. Thermal conductivity, density, viscosity, and prandtl-numbers of ethylene glycol-water mixtures. *Berichte der Bunsengesellschaft fuer Physikalische Chemie*, 88(8):739 – 742, 1984.

[58] J. J. Healy, J. J. de Groot, and J. Kestin. The theory of the transient hot-wire method for measuring thermal conductivity. *Physica*, 82C:392–408, 1976.

[59] Y. Nagasaka and A. Nagashima. Absolute measurement of the thermal conductivity of electrically conducting liquids by the transient hot-wire method. *J. Phys. E: Sci. Instrum.*, 14:1435–1440, 1981.

[60] Hans M. Roder. A transient hot wire thermal conductivity apparatus for fluids. *J. Res. Natl. Inst. Stan.*, 86(5):457–493, 1981.

[61] M. Khayet and J. M. Ortiz de Zarate. Application of the multi-current transient hot-wire technique for absolute measurements of the thermal conductivity of glycols. *Int. J. Thermophys.*, 26(3):637–646, 2005.

[62] W.A. Wakeham, A. Nagashima, and JV Sengers. *Measurement of the Transport Properties of Fluids*. Blackwell, 1991.

[63] JJ de Groot, J. Kestin, and H. Sookiazian. Instrument to measure the thermal conductivity of gases. *Physica*, 75:454–482, 1974.

[64] SR De Groot and P. Mazur. *Non-Equilibrium Thermodynamics*. Dover Publications, 1984.

[65] HE Khalifa, J. Kestin, and WA Wakeham. The theory of the transient hot-wire cell for measuring the thermal conductivity of gaseous mixtures. *Physica A*, 97(2):273–286, 1979.

[66] Konstantin Z. Markov and Luigi Preziosi. *Heterogeneous Media: Micromechanics Modeling Methods and Simulations*, chapter 1, pages 1–162. Birkhauser Boston, Cambridge, MA, 2000.

[67] J. Gordon, J. Ma, J. Garg, G.H. McKinley, Chen G., H. Ohtani, D. Sawall, J. Nanda, and J. Remillard. Investigation of thermal and rheological properties of nanofluids (poster). In *Proceedings of the 2006 ASME Energy Nanotechnology*

International Conference, number ENIC2006-19095. Massachusetts Institute of Technology, ASME, 2006.

[68] Roberto Rusconi, Lucio Isa, and Roberto Piazza. Thermal-lensing measurement of particle thermophoresis in aqueous dispersions. *J. Opt. Soc. Am. B*, 21(3):605–616, 2004.

[69] C.H. Li and GP Peterson. Experimental investigation of temperature and volume fraction variations on the effective thermal conductivity of nanoparticle suspensions (nanofluids). *Journal of Applied Physics*, 99(8):84314–84314, 2006.

[70] T. S. Chow. Viscosities of concentrated dispersions. *Phys. Rev. E*, 48(3):1977–1983, 1993.

[71] ASM Handbook. Properties and Selection: Irons, Steels, and High Performance Alloys. *ASM International*, 1:140–194.

[72] J.O. Hinze. *Turbulence*. McGraw-Hill New York, 1975.

[73] MR Maxey. The gravitational settling of aerosol particles in homogeneous turbulence and random flow fields. *Journal of Fluid Mechanics*, 174:441–465, 1987.

[74] H. Etherington. *Nuclear engineering handbook*. McGraw-Hill New York, 1958.

[75] Yulong Ding and Dongsheng Wen. Particle migration in a flow of nanoparticle suspensions. *Powder Technology*, 149(2-3):84–92, 2005. Compilation and indexing terms, Copyright 2005 Elsevier Engineering Information, Inc.

[76] F.P. Incropera and D.P. DeWitt. Fundamentals of heat and mass transfer. *New York: John Wiley & Sons, 1990.*, 1990.

[77] A.V. Filippov and D.E. Rosner. Energy transfer between an aerosol particle and gas at high temperature ratios in the Knudsen transition regime. *International Journal of Heat and Mass Transfer*, 43(1):127–138, 2000.

[78] J.H. Kim, G.W. Mulholland, S.R. Kukuck, and D.Y.H. Pui. Slip Correction Measurements of Certified PSL Nanoparticles Using a Nanometer Differential Mobility Analyzer (Nano-DMA) for Knudsen Number From 0.5 to 83. *Journal of Research of the National Institute of Standards and Technology*, 110(1), 2005.